



**HAL**  
open science

# Application of a non-equilibrium thermodynamics framework derived from nature-inspired themes for modelling and design of processes

Sergio da Cunha

► **To cite this version:**

Sergio da Cunha. Application of a non-equilibrium thermodynamics framework derived from nature-inspired themes for modelling and design of processes. Chemical engineering. Institut National Polytechnique de Toulouse - INPT, 2022. English. NNT: 2022INPT0014 . tel-04191566

**HAL Id: tel-04191566**

**<https://theses.hal.science/tel-04191566v1>**

Submitted on 30 Aug 2023

**HAL** is a multi-disciplinary open access archive for the deposit and dissemination of scientific research documents, whether they are published or not. The documents may come from teaching and research institutions in France or abroad, or from public or private research centers.

L'archive ouverte pluridisciplinaire **HAL**, est destinée au dépôt et à la diffusion de documents scientifiques de niveau recherche, publiés ou non, émanant des établissements d'enseignement et de recherche français ou étrangers, des laboratoires publics ou privés.



Université  
de Toulouse

# THÈSE

En vue de l'obtention du

## DOCTORAT DE L'UNIVERSITÉ DE TOULOUSE

**Délivré par :**

Institut National Polytechnique de Toulouse (Toulouse INP)

**Discipline ou spécialité :**

Génie des Procédés et de l'Environnement

---

**Présentée et soutenue par :**

M. SERGIO DA CUNHA

le mercredi 9 mars 2022

**Titre :**

Application of a non-equilibrium thermodynamics framework derived from nature-inspired themes for modelling and design of processes

---

**Ecole doctorale :**

Mécanique, Energétique, Génie civil, Procédés (MEGeP)

**Unité de recherche :**

Laboratoire de Génie Chimique ( LGC)

**Directeur(s) de Thèse :**

M. VINCENT GERBAUD

MME NATALIYA SHCHERBAKOVA

**Rapporteurs :**

M. KIRILL GLAVATSKIY, UNIVERSITY OF SYDNEY

M. MARC OLIVIER COPPENS, UNIVERSITY COLLEGE LONDRES

**Membre(s) du jury :**

M. PATRICE BACCHIN, UNIVERSITE TOULOUSE 3, Président

M. CHRISTOPHE GOUPIL, UNIVERSITE PARIS 7, Membre

M. DAVID ROUZINEAU, TOULOUSE INP, Invité(e)

MME NATALIYA SHCHERBAKOVA, TOULOUSE INP, Membre

M. VINCENT GERBAUD, TOULOUSE INP, Membre







---

# Table of Contents

---

<b>Summary</b>	iv
<b>Publications and Scientific Presentations</b>	viii
<b>Acknowledgements</b>	ix
<b>List of Tables</b>	xii
<b>List of Figures</b>	xiii
<b>List of Abbreviations and Symbols</b>	xvii
<b>Chapter I Introduction</b>	1
I.1 Context and general introduction	1
I.2 Overview of nature-inspired engineering	4
I.3 Overview of non-equilibrium thermodynamics	10
I.4 Non-equilibrium thermodynamic perspective of nature-inspired mechanisms	19
I.5 Motivation and objectives of the thesis	21
I.6 Organization of the thesis	22
<b>Chapter II A nature-inspired liquid distributor</b>	23
II.1 Literature review	23
II.1.1 <i>The constructal law</i>	23
II.1.2 <i>Liquid distributor designs for distillation columns</i>	27
II.1.3 <i>Performance indicators for liquid distributors</i>	30
II.2 General description of the liquid distributor	33
II.3 Materials and methods	36
II.3.1 <i>Characterization of flow on a wire</i>	36
II.3.2 <i>Characterization of flow along tetrahedron edges</i>	38
II.3.3 <i>Tetra Spline packing</i>	40
II.3.4 <i>Characterization of liquid distributor performance via HETP</i>	42
II.4 Theoretical considerations for distributor design	44
II.5 Experimental results and discussion	60
II.5.1 <i>Industrial packings</i>	60
II.5.2 <i>Tetra Spline packing</i>	61

II.6	Summary	62
<b>Chapter III</b>	<b>Numerical study of diffusioosmosis and diffusiophoresis</b>	<b>65</b>
III.1	Literature review	66
III.1.1	<i>Modelling and simulation</i>	66
III.1.2	<i>Diffusioosmosis: physical mechanism and state of the art</i>	73
III.1.3	<i>Diffusiophoresis: physical mechanism and state of the art</i>	80
III.2	Description of the case studies	83
III.2.1	<i>Diffusioosmosis case study</i>	83
III.2.2	<i>Diffusiophoresis case study</i>	85
III.3	Model for diffusioosmosis	87
III.4	Models for diffusiophoresis	88
III.4.1	<i>Transient Exact Formulation (TEF)</i>	88
III.4.2	<i>Transient Formulation at Constant Velocity (TFCV)</i>	89
III.4.3	<i>High Diffusion Limit (HDL)</i>	92
III.5	Numerical method and solving strategy	93
III.6	Diffusioosmosis results and discussion	98
III.7	Diffusiophoresis results and discussion	101
III.7.1	<i>Influence of initial conditions on long-time behaviour of the system</i>	102
III.7.2	<i>Separation of particles via diffusiophoresis</i>	105
III.7.3	<i>Influence of solute concentration, diffusivity and concentration gradient on diffusiophoretic velocity</i>	106
III.7.4	<i>Influence of solute – interface interactions on diffusiophoretic velocity</i>	111
III.8	Summary	114
<b>Chapter IV</b>	<b>Rebuttal of Ziegler’s MaxEP principle</b>	<b>119</b>
IV.1	Literature review	119
IV.1.1	Onsager’s reciprocal relations	119
IV.1.2	Prigogine’s Minimum Entropy Production Principle	130
IV.1.3	Ziegler’s Maximum Entropy Production Principle	131
IV.2	Derivation of the Orthogonality Principle	135
IV.2.1	<i>Summary of the main flaws and limitations</i>	149

IV.3	A counterexample: coupled reactions far from equilibrium	150
IV.3.1	<i>Preliminary study – assessing the applicability of Onsager’s reciprocal relations to a reaction system</i>	151
IV.3.2	<i>Attesting the inadequacy of MaxEP for coupled reactions</i>	156
IV.4	Other criticisms	159
IV.5	Summary	164
<b>Chapter V</b>	<b>Conclusion and recommendations for future work</b>	167
V.1	Conclusions	167
V.2	Future work	172
	<b>Bibliography</b>	175
	<b>Appendix A. Brief history of thermodynamics</b>	189
	<b>Appendix B. The auxiliary tool for distributor design</b>	199
	<b>Appendix C. Python and C routines for numerical simulations of mixture flow</b>	203



---

## Résumé

---

La Génie Chimique est un sujet riche et passionnant. Que ce soit pour nos vêtements ou nos repas, presque tout autour de nous passe par les mains de l'industrie chimique. Au cours des années, cette discipline a contribué à des découvertes capitales, comme le développement de médicaments, le dessalement de l'eau par osmose inverse, l'invention des colonnes de distillation réactive... Néanmoins, beaucoup de procédés d'usage étudiés en Génie Chimique peuvent être améliorés. En effet, ces procédés utilisent souvent l'hypothèse d'équilibre thermodynamique, et sont loin d'être efficaces. Même les procédés intensifiés, qui font appel au couplage de phénomènes, n'exploitent pas complètement les synergies hors-équilibre en phase de conception ou de contrôle.

Une façon de surmonter ces limitations est de développer des procédés innovants et efficaces en s'inspirant de la nature. Pour cela, il est indispensable de mieux comprendre les mécanismes fondamentaux derrière les procédés biomimétiques. Par conséquent, le présent travail étudie comment la thermodynamique hors-équilibre peut aider à combler ce manque de connaissance. Trois des concepts clés dans la littérature pour impulser la conception de procédés inspirés de la nature étant liés à trois notions importantes de la thermodynamique hors-équilibre, l'usage d'une telle approche semble donc justifiée. Une analogie est faite entre les réseaux de transport hiérarchique, le contrebalancement des forces, l'auto-organisation dynamique et l'équipartition de la production d'entropie + Loi Constructale, le couplage thermodynamique, les structures de dissipation.

Ces notions de thermodynamique hors-équilibre ont motivé trois différents projets de recherche. Le premier porte sur l'évaluation d'un distributeur de liquide pour une colonne à distiller. Cet interne de colonne consiste en un plateau avec des orifices, et des structures filaires sortant de ces orifices comme les branches d'un arbre. Le liquide s'écoule sur la surface de ces fils, se divisant en plusieurs ruisselets avant de tomber sur le garnissage au-dessous. Le choix d'un tel dessin peut être partiellement justifié par la Loi Constructale, un principe censé régir l'évolution des structures d'écoulement vivantes et non-vivantes. Ce principe encourage l'utilisation de structures en arbre pour distribuer un flux d'un point vers une surface. Des calculs théoriques prévoient que cette nouvelle technologie peut empêcher la mauvaise répartition du liquide dans les colonnes. En plus,

des expériences ont montré que cet interne réduit de 40% la hauteur équivalente à un plateau théorique pour un garnissage conçu récemment.

Cette thèse examine aussi deux phénomènes interfaciaux liés aux couplages thermodynamiques : la diffusioosmose et la diffusiophorèse. Ces deux phénomènes sont étudiés via simulation numérique. D'abord, nous essayons de reproduire le comportement d'une membrane à partir de la diffusioosmose afin de déterminer l'impact de trois paramètres sur l'état d'équilibre d'advection-osmose : la différence de concentration de colloïde, les interactions surface-colloïde, et les interactions colloïde-colloïde. Le phénomène de diffusiophorèse est étudié, lui, à l'aide de deux modèles transitoires et un modèle en régime permanent dans la limite de diffusivité infinie. Cette étude s'intéresse à l'impact du gradient de concentration de soluté, de la diffusivité et des interactions interface-soluté sur la vitesse de diffusiophorèse.

Enfin, le dernier projet de recherche conduit au cours de cette thèse met à l'épreuve la validité du principe de Ziegler de Maximisation de la Production d'Entropie, qui est défini comme une généralisation des relations de réciprocity d'Onsager aux systèmes éloignés de l'équilibre. Cette thématique est aussi liée aux couplages thermodynamiques dans la mesure où le principe de Maximisation de la Production d'Entropie se prête à l'explicitation de lois phénoménologiques dans le cas particulier des phénomènes couplés. Cependant, une révision minutieuse de la démonstration du principe proposée par Ziegler montre que celle-ci est erronée. De plus, un contre-exemple simple impliquant deux réactions chimiques éloignées de leur état d'équilibre permet de montrer que le principe lui-même est faux.

---

## Summary

---

Chemical Engineering is a vast and passionate subject. From the clothes we wear to the foods we eat, almost everything surrounding us has passed by the hands of the chemical industry. This discipline has experienced numerous breakthroughs, like advanced pharmaceuticals, water desalination via reverse osmosis, and reactive distillation columns, to name a few. However, many of the typical processes studied by Chemical Engineering have room for improvement. Indeed, these processes are often based on equilibrium hypothesis, far from being efficient. Even intensified processes, which are based on coupled phenomena, do not fully explore non-equilibrium synergies in design/control stages.

One solution to overcome these limitations lies in developing innovative and more efficient processes with nature-inspired ideas. This can only be achieved through a better understanding of underlying fundamental mechanisms and dynamics of the biomimetic processes. Hence, the present work explores how non-equilibrium thermodynamic concepts can help fill in this gap of knowledge. Using non-equilibrium thermodynamics is legitimated by the fact that the three key concepts used in the literature to drive the design of nature-inspired processes are linked to some extent to three important concepts of non-equilibrium thermodynamics. *Hierarchical transport networks*, *force balancing* and *dynamic self-organization* are the concepts mentioned from literature, and *equipartition of entropy production + Constructal Law*, *thermodynamic coupling* and *dissipative structures* are their thermodynamic counterparts.

These non-equilibrium thermodynamics notions prompted three different research projects. The first one is about the assessment of a tree-like liquid distributor for distillation columns. This internal consists of a regular orifice-pan distributor coupled with a wire structure that resembles the branches of a tree. The liquid flows on the outer surface of these wires, splitting into several streamlets before dripping on the packed bed below. Such a design can be partially justified by the Constructal Law, a principle that is claimed to govern the evolution of living and non-living flow structures with respect to time. This principle promotes the use of tree structures to realize point-to-area flow. Theoretical calculations predict that this new technology can help prevent maldistribution

in column operations. Further, experiments show that the internal reduces the height equivalent to a theoretical plate of a recently disclosed packing by 40%.

This work also investigates two interface-driven phenomena related to thermodynamic coupling: diffusioosmosis and diffusiophoresis. Both are linked to thermodynamic coupling since they correspond to fluid or particle flow generated by a secondary thermodynamic force (solute concentration gradient). These phenomena are studied here via numerical simulations. First, an attempt is made to replicate membrane behaviour from diffusioosmosis alone. The simulations explored the impact of three parameters on advection-osmosis equilibrium: colloid concentration difference, colloid-interface interactions, and colloid-colloid interactions. Afterwards, diffusiophoresis is investigated using two transient models and one steady-state model, the latter in the limit of infinite diffusivity. This study focuses on the effect of solute concentration, diffusivity, concentration gradient, and solute-interface interactions on the diffusiophoretic velocity.

Finally, the last research project conducted for this thesis checks the validity of Ziegler's Maximum Entropy Production principle, which attempts to generalize Onsager's reciprocal relations to far-from-equilibrium systems. This topic is also connected to thermodynamic coupling since the Maximum Entropy Production principle attempts to derive the phenomenological relations for coupled phenomena. A careful review of Ziegler's attempt to prove this principle shows that his demonstration is flawed. Further, a simple counterexample using far-from-equilibrium chemical reactions reveals that the principle itself is incorrect.

---

## Publications and Scientific Presentations

---

### Publications

1. Gerbaud, V., Shcherbakova, N., da Cunha, S., 2020. A nonequilibrium thermodynamics perspective on nature-inspired chemical engineering processes. *Chem. Eng. Res. Des.* 154, 316–330.
2. Da Cunha, S., Shcherbakova, N., Gerbaud, V., Bacchin, P., 2020. Modelling and Simulation of 2d-flow Suspension Diffusioosmosis. *Chem. Eng. Trans.* 86, 1147–1152.

### Scientific Presentations

1. *Non-equilibrium thermodynamics and constructal law guidelines for nature-inspired chemical processes.* V. Gerbaud, N. Shcherbakova, S. da Cunha. Nature-inspired Engineering – Cetraro, Italy, September 8-13, 2019.
2. *Modelling and simulation of 2D-flow suspension diffusioosmosis.* S. da Cunha, N. Shcherbakova, V. Gerbaud, P. Bacchin. 15<sup>th</sup> International Conference on Chemical and Process Engineering – Naples, Italy, May 23-26, 2021.

---

## Acknowledgements

---

Finally! I was starting to think I would never write this part. It's very nice by the way to finally be able to use first person singular in the text!

I was struggling on whether to write a very short and straightforward Acknowledgements section (the one in my Master thesis only has 2 paragraphs), or to go for something longer. To be honest, before I never fully understood the purpose of this section: it has no scientific contents, and you can thank the people who helped you in person. Then why write it in your thesis? The answer only came to me today: to ~~procrastinate formatting and proofreading~~ pay an eternal tribute to the people that helped get this three and a half years work done, and to share the credits of this work with them. And I don't say "share credits" in a superficial way. Without the people that I'm mentioning here today, this thesis would not exist, or it would be of much lower quality. Buckle up then, because we are doing a long trip down memory lane.

It all started in 2016, when I had to look for a research internship (stage 3A), a requirement from my Ecole d'ingénieurs. I asked **Elise Provost**, my professor of Chemical Engineering, for some advice. I was majoring in chemistry, but wanted to do something more related to engineering. So she told me about this researcher called **Vincent Gerbaud**, an expert in extractive distillation working in Toulouse. After some phone calls, I landed the internship! It was not going to be about distillation though, but something about flash points. The topic seemed quite interesting, and I was very excited to spend spring at the ville rose.

In Toulouse, I had the chance to work not only with Vincent, but also with **Nataliya Shcherbakova**, a strong mathematician who added rigor to my often clumsy mathematical derivations. Their continuous support and brilliant inputs made the work conducted during my internship quite fruitful. Their passion for research ended up being contagious: by the end of my internship, I was strongly inclined to pursue a PhD. But before that there was a 2-years intermission in Singapore.

And what an intermission! I learned many things and made several friends in that country. It was also in Singapore that I met Professors **Gade Pandu Rangaiah** and **Hidajat Kus**, who supervised the research for my Master thesis. Another great experience with academic research was all I needed to be convinced once and for all to pursue a PhD in

France. Fortunately, leaving Singapore did not mean severing the ties with the people I met there. **Fu Yu**, one of my flatmates, was of great help later during my PhD, often giving me the support and encouragement I needed. Professor Rangaiah also contributed a lot by giving advises and reassurance regarding my work and my career in our online catch-up sessions.

In 2018 I was back in Toulouse, as excited as I was in 2016. Same supervisors, same lab. I thought to myself that the path would be just as smooth as it was two years ago... A rookie's mistake. Research internships are to PhD as the qualifiers of the world cup are to the world cup itself (I'm looking at you, Brazil!). And just as in soccer, having reliable supporters can make a difference. Listing the names of these supporters is unfair, because I'll for sure forget someone. But not listing them would also be unfair, given how important they were to me during these three years.

**Juliano Schorne, Claire Touchard, Manuel Flores, Shumet Sharew and Thomas Neron** were the best office mates I could have asked for. Wasting each other's time with coffee breaks, happy hours, chatting, stories about the coffee in Ethiopia and chess games was surely a very efficient stress reduction system. It also helped (I hope) resetting the brain and getting new ideas when we were mentally exhausted.

There were also other lab mates with whom I wasted lots of time. Let me tell you a little bit about them. **Yohann Chasseray** and **Kalyani Kentheswaran** (from the team ATER) would always listen to me grumbling about the most trivial stuff (what is it about validating a pdf file?!?!?!). **Nancy Prioux** could answer pretty much any question about the lab. She was just like LGC Google, if Google could bake delicious cakes and share it at work. **Timothy Oluwadero** is a wise man, and I always learn something from our conversations. **Michelle Hougbe**, one of the kindest persons I've ever met, can make anyone smile even in the most stressful days. She shared her bureau with **Eduardo Carrera** and **Carlos Montilla**, my latino office neighbours who frequently tried to sabotage my thesis by inviting me to bars à jeux and pool bars. **Benjamin Breig, Paul Lhoste** and **Vivien Daligaux** tried doing the same, but using soccer as the bait.

**Robbie Radjagobalou** couldn't be out of this list. Half of the comics and many of the games I have at my place are his recommendations. I remember fondly the weekend we went to Lisbon to attend the marriage of **Adriana** and **Guilherme Ferreira** (casal 20!). And I remember fondly as well of the times I was invited to their place, always to eat very

delicious food. Visiting them was also a great opportunity to speak in my mother tongue. Not that the lab lacked Lusophones though: **Leticia Pasetto**, **Igor Vargas**, **Almir Ritta** and **Murilo Arrais** were always there for me when I was too tired to speak French.

And because this part of the acknowledgements is all about people who stole my precious working time, my *voleuse de temps* **Josephine Paetzold** has to make her appearance. She arrived by the end of my thesis, when one is supposed to focus on writing his manuscript. And she managed to make it the least of my concerns. Thank you, Joschi, for keeping me calm when I was supposed to feel stressed.

With this long list of time stealers, one could wonder whether I had co-workers who actually worked together with me. And yes, I had some. I gave optimization classes with **Marianne Boix**, learned a lot from her, and always had fun in our quests to find coffee during breaks. Marianne shared her office with **Ir ea Touche**. She, together with **Maxime Pigou**, saved my diffusioosmosis project (I remember that every single time I type “module Load Trilinos” on my terminal!). **David Rouzineau**, **Michel Meyer**, **Benoit Mizzi**, **Beatrice Kawas** and **Mercedes Ali** worked with me on the liquid distributor project. **Patrice Bacchin** and **Kirill Glavatskiy** were co-workers in the project on diffusioophoresis and diffusioosmosis. Without them, these projects would have never existed.

David, Patrice and Kirill were members of the jury for my thesis defense. I thank them, as well as **Marc Olivier Coppens** and **Christophe Goupil**, for carefully reading my manuscript and for attending my defense. I really appreciate your constructive questions and feedbacks. The two last members of the jury were my supervisors, Vincent Gerbaud and Nataliya Shcherbakova. More than supervisors, you are friends who always stood by my side during these past years. You heard my worries, my doubts, my fears, and always managed to reassure me. You’re not only exemplary researchers and professors, but also wonderful human beings.

And finally (yes, this is not an endless acknowledgements section), a huge thank you to my parents, **Helena Sousa** and **Sergio Cunha**, for everything I have and for everything I am.



---

## List of Tables

---

Table II.1 – Geometric characteristics of the TS packing used for HETP experiments with the tree-shaped liquid distributors	41
Table II.2 – Side of the equilateral triangles for 8 regular packings	48
Table II.3 – Summary of constraints considered for liquid distributor design	51
Table II.4 – Characteristics of the tree-like distributors used in experiments	52
Table III.1 – Range of dimensions and parameters used in diffusioosmosis simulations	84
Table III.2 – Range of dimensions and parameters used in diffusiophoresis simulations	86
Table III.3 – Comparison between $v_{DP}$ calculated using different domain sizes	98
Table III.4 – Equilibrium velocities obtained with TFCV for different sets of parameters	108
Table IV.1 – Reaction velocities from MaxEP principle and from kinetics theory for three different pairs of forces	159

---

## List of Figures

---

Figure I.1 – Comparison between Coppens’ NICE framework and Gerbaud’s NET framework	2
Figure I.2 – Articles found on Scopus on March 3rd 2019, with Query (biomim* OR bio*inspired OR nature*inspired): 64713 documents	4
Figure I.3 – Mind-map for the papers on NICE, using Scopus database	5
Figure I.4 – Behaviours of different out-of-equilibrium systems related to the NET framework	20
Figure II.1 – Illustration of a randomly-shaped city (a), the smallest (b) and the 2nd smallest (c) building blocks in the road network	24
Figure II.2 – (a-c) Evolution of a hypothetical street network with respect to time, and (d) gas-supply system for a membrane fuel cell	26
Figure II.3 – Common industrial distributors: (a) perforated pipe; (b) orifice pan; (c) orifice tunnel; and (d) trough	28
Figure II.4 – Constructal distributor	29
Figure II.5 – Areas taken into account for calculating the distribution quality rating index	31
Figure II.6 – (a) isometric, (b) top and (c) bottom views of a tree-structured liquid distributor; (d) pyramid distributing liquid from a single hole on the distributor plate	34
Figure II.7 – Square pyramid resulting from the pattern where each wire splits into 4	35
Figure II.8 – 2D representation of liquid flow on a wire structure	36
Figure II.9 – Illustration of the tetrahedron structure used in experiments	38
Figure II.10 – Cartography of the different flow regimes as a function of We and $d^*$	39
Figure II.11 – The TS packing	40
Figure II.12 – Experimental setup measuring separation efficiency for different distributors	43
Figure II.13 – The length of a spline projected on the cross-section ( $l_w^{proj}$ ) and the distance $d$ between two neighbour outlets	45

Figure II.14 – Triangles projected by a pyramid on the cross-section as the number of layers ( $N_l$ ) increases	46
Figure II.15 – Densest known packings for 3, 6, 10 and 13 equilateral triangles in a circle	48
Figure II.16 – Constraint on the wire diameter ( $d_w/2 < r_c$ )	49
Figure II.17 – Diagram chart illustrating how the Excel auxiliary tool works	51
Figure II.18 – Different designs of liquid distributors used in experiments	53
Figure II.19 – Predicted flow regime in each layer for D1, D2 and D3, considering the binary mixture n-cyclohexane + heptane	54
Figure II.20 – Total liquid flow of 729 distributed over the 28 outlets of a 6-layer pyramid	54
Figure II.21 – Flow partition from the outlets of a N-layer pyramid (dashed circles) after addition of an extra layer (solid circles)	56
Figure II.22 – D3 outlets and imaginary collection zones used to calculate $M_f$	58
Figure II.23 – HETP (a) and pressure drop (b) vs F-factor for 5 different distributors, using Pall rings packing and the test rig described in Section II.3.4	60
Figure II.24 – HETP (a) and pressure drop (b) vs F-factor for 3 different distributors, using Mellapack packing and test rig described in Section II.3.4	61
Figure II.25 – HETP (a) and pressure drop (b) vs F-factor for 3 different distributors, using TS packing and the test rig described in Section II.3.4	62
Figure III.1 – The SIMPLE procedure	71
Figure III.2 – Capillary tube connected to two reservoirs	74
Figure III.3 – Membrane geometry consisting of an array of cylindrical obstacles and used by Bacchin et al. (2019)	78
Figure III.4 – Interface-solute interaction for different attraction parameters and $k_{ic} = 1$ , as a function of the distance from the interface	79
Figure III.5 – (top) Flux across a membrane as a function of the pressure drop and the attraction parameter in eq. (III.25); (bottom) solute concentration and x-velocity profiles corresponding to regular (pRO) and anomalous (pAO) osmosis	80
Figure III.6 – Variation of a polymer's mobility (vertical axis) with respect to the solute-monomer dispersion energy. From Ramírez-Hinestrosa et al. (2020).	83

Figure III.7 – Sketch of the case study (left) and geometry/domain (right) used in diffusioosmosis simulations	84
Figure III.8 – Sketch of the case study (left) and geometry/domain (right) used in diffusiophoresis simulations	85
Figure III.9 – Comparison of colloid concentration profiles in the diffusio-osmosis case study, using meshes with 20,000 elements and 80,000 elements	95
Figure III.10 – Mesh used for the diffusiophoresis case study	96
Figure III.11 – Comparison of axial velocity profiles in the diffusiophoresis case study, using meshes with maximum element size of $0.01 \mu\text{m}$ and $0.016 \mu\text{m}$	97
Figure III.12 – Colloid and velocity profiles at advection – osmosis equilibrium	100
Figure III.13 – 2 particles that move under the same far-field solute concentration profile, but start at different positions	102
Figure III.14 – Colloid – interface force (triangles) and drag force (circles) acting on the particle in different pairs of systems A and B, in transition to fully-developed state according to TFCV predictions	104
Figure III.15 – Resultant force (a) and particle velocity (b) for a pair of systems A,B in transition to fully-developed state according to TEF predictions	105
Figure III.16 – Particle separation via diffusiophoresis	106
Figure III.17 – Comparison between diffusiophoretic velocities obtained via simulation ( $x$ -axis) and via the fitting equation (III.63) ( $y$ -axis)	109
Figure III.18 – (a) Particle mobility vs attraction parameter, according to fluid simulation results in Table III.4; (b) particle mobility vs solute – monomer dispersion energy $\epsilon_{ms}$ , according to molecular simulations (extracted from Ramírez-Hinestrosa et al. (2020))	111
Figure IV.1 – Hypothesis of homogeneous distribution of microstates over two cuboids originating from $\underline{A}^*$	121
Figure IV.2 – Illustration of Prigogine’s MinEP principle when a system is subjected to a fixed force $X_1$ and a free force $X_2$	130
Figure IV.3 – Prigogine’s minEP principle as a consequence of Ziegler’s maxEP principle	135
Figure IV.4 – Illustration of the OP, with vectors $\underline{X}^1, \underline{X}^2, \underline{X}^3$ perpendicular to the level set $\sigma = \sigma_l$	137

Figure IV.5 – Change in velocities following the isosurface $D^*(\underline{a}^*) = D_0$ , for a system with only two forces	147
Figure IV.6 – (a) Far from equilibrium, and (b) near equilibrium comparison between reaction velocities found from kinetics theory and from MaxEP	158
Figure B1 – Screenshots of the different tabs in the Excel auxiliary tool for distributor design	200

---

## List of Abbreviations and Symbols

---

### Abbreviations

CL	Constructal Law
D1	Distributor configuration number 1
D2	Distributor configuration number 2
D3	Distributor configuration number 3
EoS	Equation of State
HDL	High Diffusion Limit
HETP	Height Equivalent to a Theoretical Plate
LEH	Local Equilibrium Hypothesis
LJ	Lennard-Jones
MaxEP	Maximum Entropy Production
minEP	Minimum Entropy Production
NET	Nonequilibrium Thermodynamics
NET1	Equipartition of entropy production + Constructal Law
NET2	Thermodynamic coupling
NET3	Dissipative structures
NICE	Nature-Inspired Chemical Engineering
OP	Orthogonality Principle
PDE	Partial Differential Equation
S <sub>BL</sub>	Liquid sample taken from the bottom of the distillation column
SLIPS	Self-healing slippery liquid-infused porous surfaces
SRLJ	Short-Ranged Lennard-Jones
S <sub>TL</sub>	Liquid sample taken from the top of the distillation column
TEF	Transient Exact Formulation
TFCV	Transient Formulation at Constant Velocity
TS	Tetra Spline

T1	Hierarchical transport networks
T2	Force balancing
T3	Dynamic self-organisation
UDF	User-Defined Function
VDW	Van der Waals
VH	Van 't Hoff

## Symbols

—	First-order tensor
==	Second-order tensor
$\langle \rangle$	Average of a property over a small mixture volume
$\langle \rangle^f$	Continuous fluid phase average
$\langle \rangle^p$	Discrete solid phase average (weighted sum over the particles)
$\langle \rangle^s$	Continuous solid phase average
$\nabla$	Del operator ( $\mu\text{m}^{-1}$ )
$\nabla\phi^\infty$	Far-field solute/colloid concentration gradient ( $\text{m}^{-1}$ )
$A$	Affinity (J/mol); total surface area ( $\text{m}^2$ ); parameter in the distribution quality rating equation
$\underline{A}$	A set of mechanical variables
$a$	Colloid particle size ( $\mu\text{m}$ )
$\underline{a}$	Set nonmechanical state variables and/or external coordinates
$a_{tt}$	Attraction parameter in the solute/colloid – interface interaction potential
$B$	Parameter in the distribution quality rating index equation
$\underline{b}$	Body force acting on a mixture ( $\text{N}/\text{m}^3$ )
$C$	Parameter in the distribution quality rating index equation
$C_b^a$	combination, $a$ choose $b$
$c$	Concentration ( $\text{mol}/\text{m}^3$ )
$\hat{c}_V$	Dimensionless heat capacity

$D$	Diffusion coefficient ( $\mu\text{m}^2/\text{s}$ ); dissipation function (J/s)
$D_Q$	Distribution quality rating index
$d$	Distance between two consecutive outlets of a tree-shaped distributor (mm); distance between the solid interface and a point in the simulation domain ( $\mu\text{m}$ )
$d_w$	Wire diameter (mm)
$d^*$	Dimensionless wire diameter
$\underline{\underline{e}}$	Strain rate tensor ( $\text{s}^{-1}$ )
$F_{ci}$	Resultant force exerted by solute/colloid particles on the interface (N)
$F_{drag}$	Drag force (N)
F-factor	Product between the superficial gas velocity and the vapor density in a distillation column ( $\text{Pa}^{1/2}$ )
$f$	Helmholtz free energy density ( $\text{J}/\text{m}^3$ ); function
$f^c$	Conditional probability density
$f^U$	Joint probability density
$g$	Gravity ( $\text{m}^2/\text{s}$ ); probability density function for the microstate of a system in the phase space ( $\underline{q}, \underline{p}$ )
$\mathcal{H}$	Hamiltonian (J)
$H$	Height (m)
$J, \underline{J}$	Thermodynamic flux
$\underline{\underline{K}}$	Covariance matrix in the Gaussian distribution
$k_B$	Boltzmann constant ( $\text{m}^2 \cdot \text{kg}/\text{K} \cdot \text{s}^2$ )
$k_{ic}$	Magnitude of interface – solute or interface – colloid interactions
$L$	Length (m)
$L_{ij}$	Linear coefficient linking the flux $i$ to the thermodynamic force $j$
$l_c$	Capillary length (mm)
$l_{ic}$	Range of the interactions between interface and solute/colloid ( $\mu\text{m}$ )
$l_w^{proj}$	Length projected by a spline on the cross-section of the column (mm)



$l_w$	Wire length (mm)
$M$	Molar mass (kg/mol)
$M_f$	Maldistribution factor
$m$	Mobility (s/kg)
$N$	Number of moles (mol); number of cells used to calculate the maldistributor factor; number of molecules
$N_l$	Number of layers in a tree-like liquid distributor
$N_r$	Number of ramifications for the wires in a tree-like distributor
$n$	Number of particles per volume of solution ( $\text{m}^{-3}$ )
$P$	Pressure ( $\text{N}/\text{m}^2$ ); probability
$p$	Pressure ( $\text{N}/\text{m}^2$ ); probability
$\underline{p}$	Generalized momenta in the Hamiltonian
$Q$	Heat (J)
$Q_i$	Liquid flowrate through cell $i$ in maldistribution factor equation ( $\text{m}^3/\text{s}$ )
$Q_{\text{mean}}$	Average liquid flowrate through cells in the maldistribution factor equation ( $\text{m}^3/\text{s}$ )
$\underline{q}$	Heat flux ( $\text{J}/\text{m}^2 \cdot \text{s}$ ); microscopic coordinates in the Hamiltonian
$q_l$	Volumetric flow on wire's surface divided by the perimeter of the cross-section ( $\text{m}^2/\text{s}$ )
$R$	Gas constant ( $\text{J}/\text{mol} \cdot \text{K}$ ); radius of the phoretic particle ( $\mu\text{m}$ )
$\underline{\underline{R}}$	Matrix that gives the linear dependency of the thermodynamic forces on the fluxes
$r$	Production rate; radial distance in spherical coordinates (m)
$r_c$	Minimum radius of curvature of a spline (mm)
$S$	Entropy (J/K)
$s$	Specific entropy ( $\text{J}/\text{kg} \cdot \text{K}$ )
$T$	Temperature (K)
$t$	Time (s)

$U$	Internal energy (J)
$u$	Specific internal energy (J/kg)
$\underline{u}$	Velocity ( $\mu\text{m/s}$ )
$V$	Volume ( $\text{m}^3$ ); velocity on street-like networks (m/s)
$V_l$	Volumetric liquid flowrate ( $\text{m}^3/\text{s}$ )
$V_p$	Colloid/solute particle volume ( $\text{m}^3$ )
$v$	Reaction velocity ( $\text{mol}/\text{m}^3 \cdot \text{s}$ )
$v$	Specific volume ( $\text{m}^3/\text{kg}$ )
$\underline{v}$	Velocity of the centre of mass (m/s)
$v_{DP}$	Diffusiophoretic velocity ( $\mu\text{m/s}$ )
$W$	Work (J)
$w$	Mass fraction
$We$	Weber number
$X, \underline{X}$	Thermodynamic force
$x$	State variable

## Greek letters

$\alpha$	Fluctuation of a state variable; angle between the vertical axis and the segment connecting both ends of a spline
$\beta$	Index for phenomena that are odd under time-reversal
$\underline{Y}$	Partial derivatives of the internal energy with respect to the variables $\underline{a}$
$\underline{Y}^i$	Irreversible contribution to $\underline{Y}$
$\underline{Y}^r$	Reversible contribution to $\underline{Y}$
$\gamma$	Surface tension (N/m)
$\delta$	Liquid film thickness (mm); thickness of the diffusive layer ( $\mu\text{m}$ )
$\epsilon_{ms}$	Solute – monomer dispersion energy
$\eta_f$	Liquid viscosity (Pa.s)
$\eta_p$	Particle contribution to suspension viscosity (Pa.s)

$\theta$	Spline angle with respect to the vertical axis; polar angle in spherical coordinates
$\kappa$	Index for phenomena that are even under time-reversal
$\mu$	Chemical potential (J/mol)
$\xi(\underline{X})$	Entropy production rate as a function of the thermodynamic forces (J/K. m <sup>3</sup> . s)
$\Pi_{cc}$	Particle pressure (N/m <sup>2</sup> )
$\Pi_{cc,mc}$	Mechanical contribution to particle pressure (N/m <sup>2</sup> )
$\Pi_{ic}$	Colloid/solute – interface interaction potential
$\rho$	Density (kg/m <sup>3</sup> )
$\sigma$	Volumetric rate of entropy production (J/K. m <sup>3</sup> . s)
$\underline{\underline{\sigma}}$	Total stress tensor (N/m <sup>2</sup> )
$\sigma_0$	Reflection coefficient
$\underline{\underline{\tau}}$	Deviatoric stress tensor (N/m <sup>2</sup> )
$\Phi$	Dissipation function (J/K. m <sup>3</sup> . s)
$\phi$	Solid phase volume fraction
$\phi_m$	Mean far-field volume fraction
$\Psi$	Thermodynamic potential (J)
$\psi$	Microscopic quantity corresponding to $(F - \mathcal{H})/T$ (J/K)
$\Omega$	Domain of volume integrations; degeneracy of quantum states
$\omega$	Constant in the expression for entropy of a perfect gas

---

## Chapter I. Introduction

---

### I.1 Context and general introduction

Chemical engineering deals with the processing of matter and energy, which requires processing of information as well. It also puts an emphasis on the development of technologies used for the large-scale chemical production and on the manufacture of products with desired properties through chemical processes. Interactions within and between processes are important, as well as dynamics. Nature also manipulates energy, matter and information. It does so via structures and processes whose performance, efficiency and resilience can and should be envied by human-made activities. And yet, few lessons have been taken from nature and implemented in chemical industry. One of the possible reasons for that was the lack of consistent frameworks that can guide researchers towards new nature-inspired processes.

Fortunately, the new engineering challenges of the XXIst century, such as renewable energies and small-scale technologies, boosted nature-inspired chemical engineering (NICE) studies. And an interesting NICE framework emerged from them. In 2012, Coppens (Coppens, 2012) suggested that the backbone for nature-inspired reactor and catalysis engineering should consist of three themes: *Hierarchical Transport Networks* (T1), *Force Balancing* (T2) and *Dynamic Self-Organization* (T3). Despite being first proposed in the context of reactor and catalysis, this framework can actually be employed to NICE as a whole (UCL, 2021). It is worth noting that a fourth theme, *Ecosystems, Networks and Modularity* (T4), has been recently added to the framework (Coppens, 2021; UCL, 2021).

Analogies exist between the mechanisms listed by Coppens and the field of non-equilibrium thermodynamics (NET). Indeed, T1, T2 and T3 can be associated to the concepts of *equipartition of entropy production + Constructal Law* (NET1), *thermodynamic coupling* (NET2) and *dissipative structures* (NET3) (Gerbaud et al., 2020). Figure I.1 illustrates both T1-T3 and NET1 – NET3 frameworks.

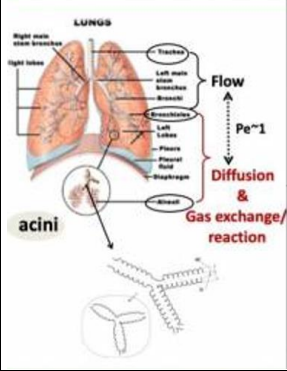
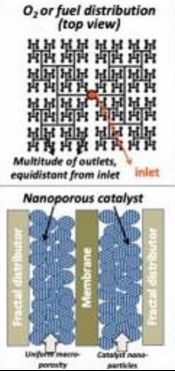

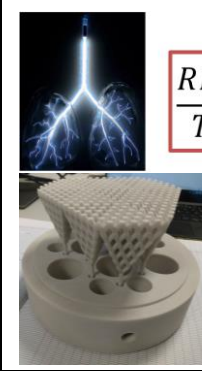
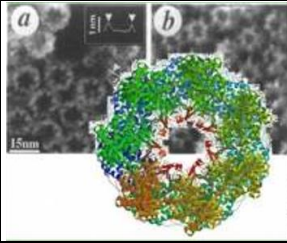

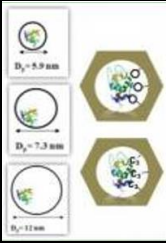
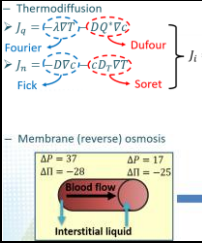

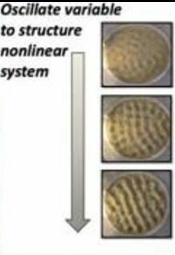
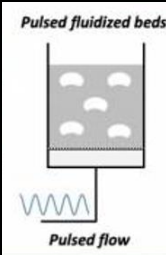
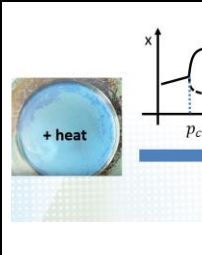
Natural modeling	Nature-inspired concept	Nature-inspired design	Thermodynamic analogy
<b>T1: Transport Networks</b>			<b>NET1: Equipartition of Entropy Production + CL</b>
 <p>LUNGS</p> <p>Flow <math>\propto Pe^{-1}</math></p> <p>Diffusion &amp; Gas exchange/reaction</p> <p>acini</p>	 <p><math>O_2</math> or fuel distribution (top view)</p> <p>Multitude of outlets, equidistant from inlet</p> <p>Nanoporous catalyst</p> <p>Fractal distributor</p> <p>Membrane</p> <p>Fractal distributor</p>	 <p>Cathode</p> <p>PEM</p> <p>Carbon Black</p> <p>Electrolyte</p> <p>Liquid Water</p>	 $\frac{RI^2}{T} = cst$
<b>T2: Force Balancing</b>			<b>NET2: Thermodynamic Coupling</b>
 <p>Enzyme</p> <p>Tune: pore curvature surface chemistry</p>	 <p><math>D_p = 5.9 \mu m</math></p> <p><math>D_p = 7.3 \mu m</math></p> <p><math>D_p = 11 \mu m</math></p>	 <p>Thermodiffusion</p> <p>Fourier</p> <p>Fick</p> <p>Dufour</p> <p>Soret</p> $J_i = \sum_k L_{ik} X_k$ <p><math>J_n = -D_T c - c D_T T = 0</math></p> <p>Membrane (reverse) osmosis</p> <p>Blood flow</p> <p>Interstitial liquid</p> <p><math>\Delta P = 37</math></p> <p><math>\Delta \Pi = -28</math></p> <p><math>\Delta P = 17</math></p> <p><math>\Delta \Pi = -25</math></p>	
<b>T3: Dynamic Self-Organisation</b>			<b>NET3: Dissipative Structures</b>
 <p>Oscillate variable to structure nonlinear system</p>	 <p>Pulsed fluidized beds</p> <p>Pulsed flow</p>	 <p>Bénard cells</p> <p>+ heat</p> <p><math>P_{crit}</math></p> <p><math>p</math></p>	

Figure I.1 – Comparison between Coppens’ NICE framework and Gerbaud’s NET framework. Illustrations on T1-T3 extracted from UCL (2021). Figures on the right-column adapted from Lloyd-Jones (2019), SUEZ (2021) and Nick Moore (2016). CL stands for Constructal Law.

It is important to make these analogies because chemical engineering processes are mostly designed and operated on the basis of phase equilibrium hypotheses in reaction and separation engineering. Besides, transport phenomena, which are the core of chemical engineering unit operations, are usually described with linear phenomenological laws, and process regulation is often done via linear control theory to maintain quasi-steady state operation. Most of these concepts are more than 50 years old and are antipodal with

nature's way of life: an ever adapting, out-of-equilibrium state with nonlinear dynamics. These disparities between industry and nature are what makes the NET framework for chemical engineering promising.

The merits of this framework are brought to the fore thanks to the three projects derived from it and discussed in this thesis. Each project is whole on its own, but the NET framework is the thread that links them. The first one concerns a nature-inspired liquid distributor, and it relates to NET1. Indeed, the choice of a tree-like configuration for the distributor that will be discussed in Chapter II can be partially justified by the Constructal Law, which is concerned with the evolution of flow architectures (Bejan and Lorente, 2004). Further, the project on modelling and simulation of diffusiophoresis and diffusioosmosis (Chapter III) is derived from NET2. Both these phenomena are instances of thermodynamic coupling, in which gradient of solute concentration induces particle flow (diffusiophoresis) or fluid flow (diffusioosmosis). Finally, the rebuttal of Ziegler's principle (Chapter IV) falls in the NET2 theme, since the principle attempts to predict the phenomenological laws of thermodynamic couplings.

The versatility of these projects gives the thesis a cross-disciplinary nature, without making it uncoherent. Indeed, the thesis as a whole can be seen as an application of the NET framework described in Section I.4. Alternatively, this work may also be seen as a thesis on transport phenomena at different scales. The project on liquid distributor studies this concept on the process scale, without focusing much on the physics underlying the liquid flow along the distributor. The impact of liquid distribution on distillation performance is assessed with a more heuristic and experimental approach, without using a rigorous model to describe the physics of the flow. In contrast, for the project on diffusioosmosis and diffusiophoresis a detailed description of the transport equations is given. These phenomena are studied via numerical simulations in a microscopic scale that corresponds to membrane channels (diffusioosmosis) or to micro-sized phoretic particles. Finally, the critical review of Ziegler's Maximum Entropy Production Principle investigates the phenomenological laws of coupled transport phenomena. It is a purely theoretical work at the most fundamental scale of transport phenomena.

The remainder of this chapter will bring additional context to the thesis. The next sections give an overview of nature-inspired engineering and non-equilibrium thermodynamics. The motivation and objectives of each project, as well as the organization of the manuscript, are given by the end of the chapter.

## I.2 Overview of nature-inspired engineering

Nature-inspired engineering is a relatively old research field. Back in 1948, the electrical engineer Georges de Mestral invented the hook-and-loop fastener, inspired by the microstructure of the burs of burdock (Merlin and Ménézo, 2018). Since then, biomimetics has boosted the design of several innovative materials. The SLIPS (self-healing slippery liquid-infused porous surfaces) constitute an interesting example (Wong et al., 2011). These surfaces can be used in the handling of biomedical fluids, fuel transportation and self-cleaning windows. SLIPS are inspired by the slipping peristome of the *Nepenthes* pitcher, a carnivorous plant. This region has a microstructure that allows for water retention, and insects wandering on it often slip towards the plant's digestive juices due to aquaplaning. Other applications of biomimetics to Material Science include surface coating, nanocomposites, adherent surfaces, and more (Merlin and Ménézo, 2018).

Despite the advances of biomimetics in the Material Science domain, some other subjects still struggle to develop nature-inspired ideas. That is the case for process engineering, as depicted in Figure I.2. Process engineering here will be used to refer to the branch of chemical engineering that accounts for works on thermodynamics, transport phenomena, unit operation and manufactory scale.

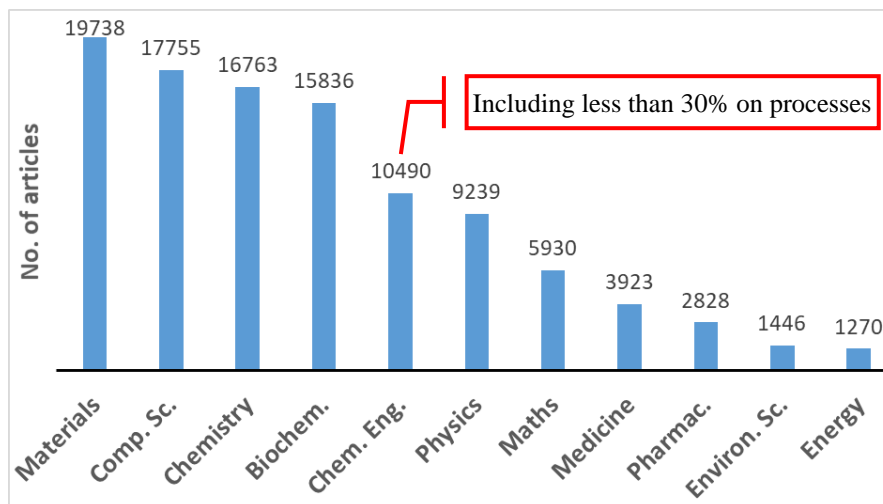


Figure I.2 – Articles found on Scopus on March 3<sup>rd</sup> 2019, with Query (*biomim\* OR bio\*inspired OR nature\*inspired*): 64713 documents

The landscape of nature-inspired works on Chemical Engineering (excluding Material Science) is presented in Figure I.3. This mind-map was generated using the Gargantex website (CNRS, 2018), with data from the Scopus database. Each node corresponds to a

recurrent keyword from the abstracts of the papers. The edges represent common co-occurrences of these words. We can distinguish 6 well-defined clusters: reactions, surface/coating, biomaterials, nano/microstructured materials, nanoparticles/enzymes and bone tissue engineering. Further, the unnamed bright yellow cluster assembles works on photocatalysis and biomimetic syntheses. Finally, the papers on Process Engineering are mostly scattered in the unnamed light-blue cluster on top of Figure I.3, showing that nature-inspired works in this area are scarce.

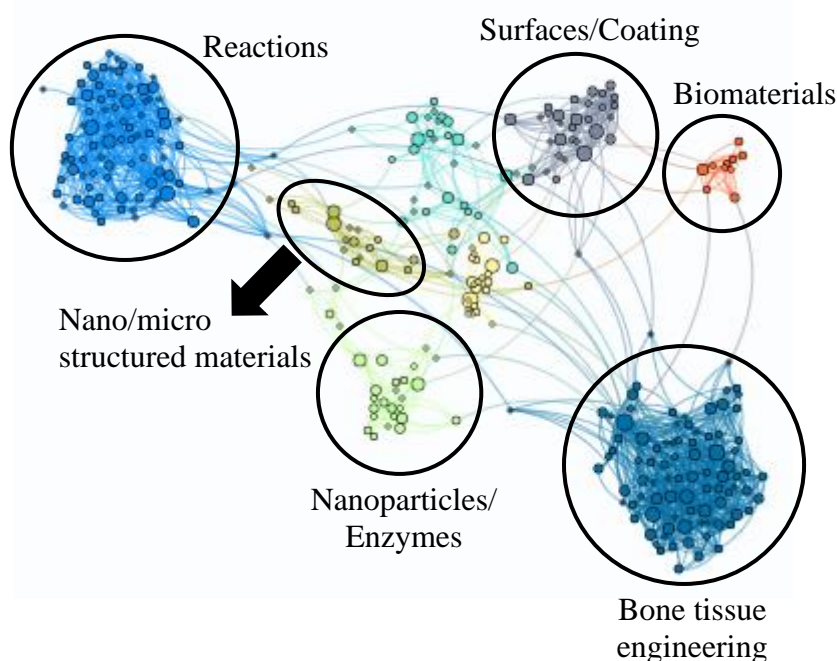


Figure I.3 – Mind-map for the papers on NICE, using Scopus database with Query  $((((TITLE-ABS-KEY(biomim*) OR TITLE-ABS-KEY(bio-inspired) OR TITLE-ABS-KEY(nature-inspired) OR TITLE-ABS-KEY("bio inspired") OR TITLE-ABS-KEY("inspired by nature") OR TITLE-ABS-KEY("inspired by the nature") OR TITLE-ABS-KEY("nature inspired") AND TITLE-ABS-KEY(process))) AND (LIMIT-TO(SRCTYPE,"j")) AND (LIMIT-TO(SUBJAREA,"CENG") OR EXCLUDE(SUBJAREA,"MATE")) AND (LIMIT-TO(DOCTYPE,"ar")) AND (LIMIT-TO(LANGUAGE,"English"))))$

Some works on nature-inspired ideas for process engineering will be reviewed in the following paragraphs. This short review aims to expose the reader to the concepts of diffusiophoresis, diffusioosmosis and Constructal Law, and to show some of their applications. These concepts are connected to the projects presented in Chapter II (the nature-inspired liquid distributor) and Chapter III (modelling and simulation of diffusioosmosis and diffusiophoresis). Furthermore, some papers related to the NICE



framework proposed by Coppens (2012) are also reviewed below. These works elucidate the themes T1-T3 from which the NET framework was derived (see Figure I.1).

Synthetic microswimmers (Elgeti et al., 2015) are an interesting first example of nature-inspired ideas for process engineering. They are self-propelled, artificial microbodies that can move through liquid media. In the future, such swimmers may be used to operate cells, to remove toxins from the human body or even as a drug-delivery system. Various transport mechanisms involved in the motion of microorganisms are adapted for artificial microswimmers, such as the propulsion mechanisms of sperm cells and artificial cilia (Elgeti et al., 2015). Diffusiophoresis (particle transport due to solute concentration gradient) is another mechanism used to drive the motion of synthetic swimmers. This phenomenon is also associated to various natural processes, including protein transport across membrane pores and viral DNA transport in living cells (Velegol et al., 2016).

Baring similarities with diffusiophoresis, osmosis (fluid flow due to concentration difference across an interface) is another phenomenon that arises in nature and has practical applications. For example, kidneys perform very well in separating urea from our blood. Every day, human kidneys filter around 200L of water, and only 0.8 - 2 L are wasted as urine (Marbach, 2018; Mount Sinai Health System, 2021). This biological filtration consumes less than 1% of the energy used in commercial dialysis equipment (Marbach, 2018), showing the gap for improvement in human-based engineering. The natural dialysis task is completed in the kidneys thanks to a U-shaped structure called loop of Henle. Water, urea and salt flow inside this structure, which is immersed in interstitial fluid. The walls of the descending limb in the loop are permeable to water, whereas the walls of the ascending limb have micropumps that pump the salt to the interstitium. This salt pump increases salt concentration in the interstitial fluid, causing the water in the descending limb to flow out of the structure via osmosis. As a result, salt and most of the water are filtered out; only urea and some water are retained. From this idea, a kidney-inspired filtration device was recently conceived which uses classic permeable membranes and charged membranes to mimic the walls of the descending and ascending limbs, respectively (Marbach, 2018). Future applications include seawater pre-treatment (prior to desalinization), and dialysis.

The inventions listed in this section are objective instances of nature-inspired engineering. But this field has also produced general frameworks and theories of practical application, such as the Constructal Law (CL) (Bejan and Lorente, 2004). CL is a principle claimed

to dictate how the architecture of living and non-living flow structures evolve in time. It is about survival in time by increasing efficiency, territory and compactness. Considering a global flow resistance  $R$ , global internal size  $V$ , and global external size  $L$ , survival is achieved by minimizing/maximizing one of the parameters when the other two are held constant. The formal statement of the principle is (Bejan and Lorente, 2004):

*For a finite-size system to persist in time (to live), it must evolve in such a way that it provides easier access to the imposed currents that flow through it.*

*For a system with fixed global size and global performance to persist in time (to live), it must evolve in such a way that its flow structure occupies a smaller fraction of the available space.*

*In order for a flow system with fixed global resistance ( $R$ ) and internal size ( $V$ ) to persist in time, the architecture must evolve in such a way that it covers a progressively larger territory.*

The above three-parts statement shows the importance of the CL to engineers. Indeed, the three features being evoked (easiest flow access, compactness or more free space, maximal spreading) are the drivers for the conception of transport networks. When designing the pipe network for a chemical plant, engineers want to minimize the pressure drop (i.e., the resistance to the flow) in order to lower the cost of pumping. However, transport of corrosive fluids requires expensive materials, such as titanium or zirconium alloys. In those cases, engineers may prefer to minimize the capital cost of construction (i.e., minimize the material used for transport) by accepting a fixed maximum pressure drop. This is similar to the second part of the CL statement. Finally, road networks are conceived to connect the different parts of a city. The optimal configuration in this case is the one covering the maximum territory available, following the third principle of the CL.

Fractal tree structures emerge from CL, when it is necessary to connect one point with an infinite number of points covering a surface/volume. Fractal structures also facilitate scale-up. Two examples are the vascular and the respiratory networks in the human body. Tree-shaped networks are also found to dissipate energy uniformly (West et al., 1997) and to operate near optimality in terms of momentum and heat flow resistance (Bejan and Tondeur, 1998; Coppens, 2012). Despite providing interesting alternatives for the design of flow structures, CL has been criticized for its vague formulation (Smith, 2013).

Attempts to transform the law in a deterministic approach for optimal flow structure design have failed in several applications (Kuddusi and Eğrican, 2008).

In nature, fractals and other highly symmetric structures are often associated to hierarchical transport, when the flow network bridges scales in order to distribute a current. In chemical engineering, such structures may facilitate scaling, as the only characteristic length pertinent to design is that of the basic building unit (Coppens, 2005). This feature is the motivation for the first research theme in the NICE framework proposed by Coppens: Hierarchical Transport Networks (T1) (Coppens, 2005, 2012). T1 was used in the design of a new oxygen distribution system in polymer electrolyte membrane fuel cell. This fractal distribution system provided better oxygen distribution over the cathode's surface, decreasing catalyst consumption. Further, creating smaller-scale transport hierarchies by introducing macroporosity in the catalyst layer improved the access of reactant to the active sites within (see Figure I.1). Another application of T1 was in the design of a scalable fractal-like gas injector for a fluidized bed. This injector avoids the formation of large bubbles in the bed, stabilizing the gas-liquid suspension and therefore improving gas-solid contact. Such a device can be easily scaled-up by increasing the number of fractal generations (Coppens, 2005).

The second research theme proposed by Coppens is called Force Balancing (T2) (Coppens, 2012). It draws inspiration from complex structures, such as enzymes and DNA double-helices, that are formed and stabilized due to the action of several forces of different natures. This theme has often been applied to enhance the catalytic activity of proteins. For example, it was found that one can increase the catalytic activity of the lysozyme and myoglobin by confining these proteins between concave, hydrophilic walls. The curvature radius of these walls should be close to the protein's characteristic length (Sang and Coppens, 2011). Besides, T2 inspired a new anti-fouling system for microfiltration membranes, which consists roughly in adding a chitosan layer on the membrane surface. Like the anti-fouling mechanism of cell membranes, this layer imparts steric hindrance and a hydration coating to the membrane, which prevents adsorption of *E. coli* bacteria and polymer formation/deposition (Coppens, 2021).

The third theme in Coppens' framework is Dynamic Self-Organization (T3). The term refers to organized natural structures that appear as a result of stimuli from their surroundings. The classical example is that of sand waves (see Figure I.1). Sand waves (the organized structure) are formed through oscillatory wind tides (an intermittent

stimulus). Inspired by this phenomenon, Coppens and van Ommen (2003) proposed the use of oscillating gas flow in fluidized beds. They found that oscillating the gas inlet flowrate (an intermittent stimulus) creates a regular bubble pattern (the organized structure) at the lower part of the bed. This helps increasing control over the otherwise chaotic hydrodynamics of the bed. Furthermore, it prevents channelling and clumping, improving processes such as combustion and drying (Coppens, 2012).

Finally, the last theme of the NICE framework (T4 – Ecosystems, Networks, and Modularity) is related to the synergy created by the interaction of different living systems (Coppens, 2021). In animals for example, cells can assemble into tissues, and eventually into organs that are capable of executing complex tasks. The characteristics of such organs cannot be reduced to the sum of individual cell properties; instead, the synergy from the interactions between the constituting cells gives the final structure much richer features. It has been suggested that T4 could be used in the control of the hydrodynamics of fluidized beds. The idea behind this proposal is that the behaviour of complex structures presenting several nonlinear coupled interactions can be modulated between chaotic and ordered via the tuning of some relevant parameters. Therefore, there might exist an appropriate control loop capable of fine tuning the hydrodynamics of a fluidized bed (Coppens, 2021).

Several nature-inspired works were briefly reviewed in this section. Because researchers strive for innovation, it is only natural to dwell on the thinking process behind each of the inventions described here. The hook-and-loop fastener mentioned in the beginning of the section was most likely an *observation-driven* invention. By observation-driven, it is meant that the inventor was not “trying to invent” anything when he “stumbled” upon the source of his inspiration. The inventor of the hook-and-loop fastener probably only thought of creating a new type of fastener after observing the burdock burs. Some people may refer to this thinking process as serendipity, but this term will be avoided here. Serendipity has connotations of “by chance”, “by luck”, whereas inventions require work, experience and conscious/unconscious thinking.

After the hook-and-loop fastener, SLIPS (Wong et al., 2011) were mentioned. These slippery surfaces were likely an *application-driven* invention. Indeed, some of the authors were already working with hydrophobic and nanostructured surfaces before year 2011. It is likely that they were actively searching ideas for a surface with strong liquid-repelling properties, and the pitcher-inspired concept was a result of this brainstorming. The

kidney-inspired filtration described by Marbach (2018) is also likely an application-driven invention. The author was already working with osmosis, membranes and other related phenomena prior to year 2018.

The last type of thinking process involved in the inventions described here will be called *application-driven-framework-oriented*. The inventions emerging from CL and Coppens' T1-T4 principles all fit in this category. The inventors certainly had a goal in mind prior to their inventions, but their creative process uses a pre-conceived framework. Another framework for chemical engineering, which led to this thesis' projects, is the NET1 – NET3 framework presented in Gerbaud et al. (2020) and depicted in Figure I.1.

This concludes a brief review of the current nature-inspired engineering landscape. The next section gives an overview of non-equilibrium thermodynamics, focusing on entropy production and the definition of thermodynamic fluxes and forces. This section is particularly helpful for readers not familiar with thermodynamic coupling.

### I.3 Overview of non-equilibrium thermodynamics

Many historians of science attribute the first developments in the field of thermodynamics to Count Rumford and Sadi Carnot. The former proved experimentally that heat could be indefinitely generated from friction, which casted doubts on the prevailing theory that heat was a substance (Count of Rumford, 1798). The latter came up with the concept of reversible cycles for engines, and theorized that the maximum efficiency of an engine depends only on the temperature of the hot and cold bodies serving as driving force for the heat flow (Carnot, 1824). These works laid the basis for the First and Second Law of Thermodynamics, whose mathematical expression would be given years later by Rudolf Clausius:

$$\Delta U = Q + W \text{ (closed system)} \quad (\text{I.1})$$

$$\Delta S \geq 0 \text{ (isolated system)} \quad (\text{I.2})$$

For a more detailed account of the historical works leading to the First and Second Law of Thermodynamics, refer to Appendix A.

In eq. (I.1),  $U$  refers to the internal energy of a system,  $Q$  is the heat exchanged with the surroundings, and  $W$  is the work exerted on/by the surroundings. Term  $S$  in eq. (I.2) is the entropy, and this equation implies that an isolated system maximizes  $S$  when it reaches

equilibrium. Internal energy and entropy are state functions; hence, they can be defined with some set of state variables. For example, the state of a perfect single component gas at equilibrium is fully described by its temperature ( $T$ ), volume ( $V$ ) and number of moles ( $N$ ). The internal energy and entropy of perfect gas at equilibrium can be written as:

$$U = \hat{c}_V NRT \quad (\text{I.3})$$

$$S = NR \ln \left[ \frac{VT^{\hat{c}_V}}{\omega N} \right] \quad (\text{for } VT^{\hat{c}_V} / \omega N \gg 1) \quad (\text{I.4})$$

In eqs. (I.3) and (I.4),  $\hat{c}_V$  is the dimensionless heat capacity at constant volume, and  $\omega$  is a constant that depends upon the type of gas. For example, for a monoatomic gas  $\omega = 1.776 \times 10^{-44} \times m^{-3/2}$  (in SI units), with  $m$  being the mass of the gas particle.

These equations can be used when temperature and gas concentration are homogeneous. However, systems out-of-equilibrium may present temperature and concentration gradients. For instance, a gas cylinder heated at one end and cooled at the other does not have a particular temperature describing its state. And yet, it has a certain entropy and a certain internal energy. How can these quantities be calculated in this case?

A logical suggestion is to assume eqs. (I.3) and (I.4) are valid for smaller portions of the domain in which temperature is well-defined. The modified equations would be of integral form:

$$U = \int_V \hat{c}_V cRT \, dV \quad (\text{I.5})$$

$$S = \int_V cR \ln \left[ \frac{T^{\hat{c}_V}}{\omega c} \right] dV \quad (\text{I.6})$$

where  $c$  is gas concentration (moles per volume).

There are two key hypotheses behind eqs. (I.5) and (I.6): (i) temperature is locally well-defined; (ii) despite the system not being at equilibrium, eqs. (I.3) and (I.4) are valid locally. In other words, if one looks at a very small portion of the domain, its properties are homogeneous and it resembles a system at equilibrium.

These hypotheses constitute a particular application of the more general local equilibrium hypothesis (LEH). LEH assumes that (Jou et al., 2010):

- (i) variables that are well-defined at equilibrium states (e.g. temperature, pressure) remain locally well-defined when the system is out-of-equilibrium;
- (ii) equations relating state functions and state variables at equilibrium remain valid (locally) when the system is out-of-equilibrium.

LEH is a key assumption in most of the NET developments. It allows one to write the local form of the Gibbs equation (Jou et al., 2010):

$$ds = \frac{du}{T} + \frac{pdv}{T} - \frac{1}{T} \sum_i \frac{\mu_i}{M_i} dw_i \quad (\text{I.7})$$

where  $s$ ,  $u$  and  $v$  are respectively specific entropy, specific internal energy and specific volume (in terms of mass);  $w_i$  is the mass fraction of component  $i$ ;  $\mu_i$  and  $M_i$  are respectively the chemical potential and the molecular weight of component  $i$ ; and  $p$  is the pressure.

The volumetric rate of entropy production  $\sigma$  is obtained from the entropy balance equation together with eq. (I.7) (Jou et al., 2010):

$$\sigma = \sum_j v_j \frac{A_j}{T} + \underline{J}_u \cdot \underline{\nabla} \left( \frac{1}{T} \right) - \sum_i \underline{J}_i \cdot \underline{\nabla} \left( \frac{\mu_i}{M_i T} \right) - \underline{\underline{\tau}} : \left( \frac{\underline{\nabla} \underline{v}}{T} \right) \quad (\text{I.8})$$

where  $v_j$  is the rate of reaction  $j$  (in moles per volume per second),  $\underline{J}_u$  is the internal energy flux,  $\underline{J}_i$  is the diffusive mass flux of component  $i$ ,  $A_j$  is the affinity of reaction  $j$ ,  $\underline{\underline{\tau}}$  is the deviatoric stress tensor, and  $\underline{v}$  is the velocity of the centre of mass. The single dot product is the scalar product between two vectors, and the double dot product is defined as  $\underline{\underline{A}} : \underline{\underline{B}} = \sum_{i,j} A_{ij} B_{ij}$ . For the sake of simplicity, eq. (I.8) assumes that external body forces, if present, are identical to all components.

The Second Law of Thermodynamics re-written for a continuous body out-of-equilibrium is:

$$\sigma \geq 0 \quad (\text{I.9})$$

Note that, whereas eq. (I.8) is derived assuming LEH, eq. (I.9) does not need such an assumption.

It is suitable to decompose the stress tensor and the gradient of the velocity in eq. (I.8) into a mean normal tensor and a traceless deviatoric term. Using this decomposition yields:

$$\sigma = \sum_j v_j \frac{A_j}{T} + \underline{J}_u \cdot \underline{\nabla} \left( \frac{1}{T} \right) - \sum_i \underline{J}_i \cdot \underline{\nabla} \left( \frac{\mu_i}{M_i T} \right) - \tau^0 \left( \frac{1}{T} \underline{\nabla} \cdot \underline{v} \right) - \underline{\underline{\tau}}' : \frac{1}{T} (\underline{\nabla} \underline{v})^S \quad (\text{I.10})$$

where  $\tau^0 = (1/3)\text{Tr}(\underline{\underline{\tau}})$  is the mean normal viscous stress tensor,  $\underline{\underline{\tau}}' = \underline{\underline{\tau}} - \tau^0 \underline{\underline{I}}$  is the deviatoric viscous stress tensor, and  $(\underline{\nabla} \underline{v})^S = \frac{1}{2} [\underline{\nabla} \underline{v} + (\underline{\nabla} \underline{v})^T] - \frac{1}{3} (\underline{\nabla} \cdot \underline{v}) \underline{\underline{I}}$ .

Entropy production is generally written as a bilinear expression involving fluxes ( $J_k$ ) and forces ( $X_k$ ):

$$\sigma = \sum_k J_k X_k \quad (\text{I.11})$$

Looking back at eq. (I.10), one can identify reaction velocity  $v_j$  as a flux, and  $\frac{A_j}{T}$  as its associated force. Further, the internal energy flux  $\underline{J}_u$  has a corresponding force  $\underline{\nabla} \left( \frac{1}{T} \right)$ , and diffusive flux  $\underline{J}_i$  is associated to the force  $\underline{\nabla} \left( \frac{\mu_i}{M_i T} \right)$ . Finally,  $\tau^0$  and  $\underline{\underline{\tau}}'$  can be interpreted as deformation velocities in the body,  $\left( \frac{1}{T} \underline{\nabla} \cdot \underline{v} \right)$  and  $\frac{1}{T} (\underline{\nabla} \underline{v})^S$  being the respective forces.

The identification of fluxes and forces as described above is quite intuitive. Nevertheless, the choice of fluxes and forces is not unique. Other definitions may be preferable according to the nature of the system being studied. For example, one may be interested in decomposing the internal energy flux  $\underline{J}_u$  into a diffusive part and a conductive part:

$$\underline{J}_u = \overbrace{\underline{\underline{q}}}^{\text{conduction}} + \overbrace{\sum_i \frac{h_i}{M_i} \underline{J}_i}^{\text{diffusion}} \quad (\text{I.12})$$

In eq. (I.12),  $h_i$  stands for the partial specific enthalpy (per mole) of component  $k$ . Inserting it into eq. (I.10) yields (de Groot and Mazur, 1984):

$$\sigma = \sum_j v_j \frac{A_j}{T} + \underline{q} \cdot \underline{\nabla} \left( \frac{1}{T} \right) - \sum_i \underline{J}_i \cdot \frac{1}{M_i T} \underline{\nabla}^T \mu_i - \tau^0 \left( \frac{1}{T} \underline{\nabla} \cdot \underline{v} \right) - \underline{\underline{\tau}}' : \frac{1}{T} (\underline{\nabla} \underline{v})^S \quad (\text{I.13})$$

There is now a new flux  $\underline{q}$  corresponding to the “purely conductive” heat flow (as in the case of rigid bodies), and a new force  $\underline{\nabla}^T \mu_i = (h_i/T) \underline{\nabla} T + T \underline{\nabla} (\mu_i/T)$  that stands for the



chemical potential gradient in the absence of temperature gradients. Many other possibilities exist for redefining fluxes and forces in eq. (I.10). For example, one could make linear combinations of the reactions taking place in the system to derive alternative affinities and reaction velocities.

Eq. (I.13) shows that thermodynamic forces can usually be calculated if the state of the system (temperature profile, concentration profile, ...) is known. The fluxes are unknown quantities *a priori*, but they can be related to the forces via phenomenological relations. A classic example is that of heat conduction in a rod. Heat flow in this case is given by Fourier's law of heat conduction:

$$\begin{aligned} \underline{q} &= -\kappa \underline{\nabla} T \Rightarrow \\ \Rightarrow \overbrace{\underline{\tilde{q}}}^{flux} &= \kappa T^2 \overbrace{\underline{\nabla} \left( \frac{1}{T} \right)}^{force} \end{aligned} \quad (\text{I.14})$$

In eq. (I.14),  $\kappa$  is the thermal conductivity. This equation shows that heat flux is proportional to its driving force, although the linear coefficient relating them depends on the local temperature. Linear flux-forces relationships are valid when the system is near equilibrium, i.e. when the forces are sufficiently small. For example, the affinity of a reaction becomes lower as it approaches equilibrium composition. When affinity is sufficiently low ( $A/RT \ll 1$ ), one can assume that reaction velocity and affinity obey a linear relation (Prigogine, 1962).

Other than temperature gradients, gradients in chemical potential could also drive heat flow. This is known as the Dufour effect (de Groot and Mazur, 1984), and it is an example of thermodynamic coupling. Near equilibrium, this contribution is also linear:

$$\underline{q} = \overbrace{L_{qq} \underline{\nabla} \left( \frac{1}{T} \right)}^{\text{Fourier's law}} + \overbrace{L_{qj} \frac{1}{M_1 T} \underline{\nabla}^T \mu_1}_{\text{Dufour effect}} \quad (\text{I.15})$$

In eq. (I.15) it is considered that only component 1 can generate the Dufour effect. Further,  $L_{qq}$  stands for the linear ratio  $\kappa T^2$  linking heat flux to the gradient of  $1/T$ , and  $L_{qj}$  is the linear coefficient of the Dufour effect.

Apart of driving heat flow, gradients in chemical potential can also drive diffusion flux. The relation between gradients in chemical potential and diffusive flow is obtained from Fick's law of diffusion. In addition, diffusion can be driven by temperature gradients

because of the Soret effect (de Groot and Mazur, 1984). These two contributions are included in eq. (I.16):

$$\underline{J}_1 = \overbrace{\frac{L_{jj}}{M_1 T} \nabla^T \mu_1}^{\text{Fick's law}} + \overbrace{L_{jq} \nabla \left( \frac{1}{T} \right)}^{\text{Soret effect}} \quad (\text{I.16})$$

The expressions that give the flux-force relationships, such as eqs. (I.14) – (I.16), are called phenomenological equations. Using them, one can fully describe the evolution of a system. One of the challenges in current research on NET is to derive a general and consistent principle from which these relations can be deduced. Such formalism already exists in classical mechanics, where the dynamics of any system can be derived from the Least Action Principle.

Onsager (1931a, 1931b) proposed one of the first variational principles in NET. The main result from his works is the Onsager's reciprocal relations, which are related to the linear coefficients of thermodynamic coupling. Assuming that flux-force relationships are linear, like equations (I.15) and (I.16), the phenomenological law for a flux  $J_k$  is:

$$J_k = \sum_j L_{kj} X_j \quad (\text{I.17})$$

Onsager's theorem states that:

$$L_{kj} = L_{jk} \quad (\text{I.18})$$

Eq. (I.18) shows that the linear coefficients for the Dufour and Soret effects are equivalent (i.e.,  $L_{qj} = L_{jq}$ , see eqs. (I.15) and (I.16)). It is valid for any pair of phenomena, provided they are: (i) of the same tensorial order, and (ii) of the same parity with respect to microscopic time-reversal (de Groot and Mazur, 1984). For example, reactions can couple between them because they correspond to 0<sup>th</sup>-order (scalar) fluxes and forces. Further, reaction extents are even under time-reversal, so eq. (I.18) holds. Nevertheless, reactions cannot couple with heat conduction because the latter is a 1<sup>st</sup>-order (vectorial) phenomenon. Besides, eq. (I.18) does not hold for the coupling between reactions and the scalar viscous term in eq. (I.13), since the velocity appearing in the viscous term is odd under time-reversal.

A more general form of eq. (I.18) was proposed by Casimir (1945). This form accounts for even and odd parities under time-reversal. Let  $\kappa$  be the category of phenomena

corresponding to even variables (e.g. heat flux associated with the transport of internal energy), and let  $\beta$  be the category of phenomena corresponding to odd variables (e.g. viscous dissipations associated with velocity gradients). The modified Onsager's relations for thermodynamic coupling are written as (Casimir, 1945; de Groot and Mazur, 1984):

$$L_{kj}^{\kappa\kappa} = L_{jk}^{\kappa\kappa} \quad (\text{I.19a})$$

$$L_{kj}^{\beta\beta} = L_{jk}^{\beta\beta} \quad (\text{I.19b})$$

$$L_{kj}^{\kappa\beta} = -L_{jk}^{\kappa\beta} \quad (\text{I.19c})$$

where  $\kappa\kappa$  represents even couplings,  $\beta\beta$  represents odd couplings, and  $\kappa\beta$  represents couplings associated with variables of different parities.

It was previously stated that there exist different choices of fluxes and forces corresponding to the same system. For example, eqs. (I.10) and (I.13) differ on the definitions of heat flux and forces  $X_i$ . However, eqs. (I.19a-c) hold for both these choices. A fundamental question follows from this observation: how should fluxes and forces be defined so that eqs. (I.19a-c) are valid?

To answer this, one should seek the definition of forces and fluxes used by Onsager and Casimir. In Onsager (1931b), the fluxes are derived from the concept of fluctuations. The macrostate of a system at equilibrium can be defined by some set of macroscopic variables. For example, the macrostate of a reactive mixture at equilibrium is well-defined by the equilibrium concentrations of reactants/products, the pressure of the mixture and its temperature. However, the properties measured at equilibrium are only an average of the real properties of the system. The actual concentrations of reactants/products are not always exactly equal to the equilibrium values. Instead, they fluctuate around a mean value, though the fluctuations are in general several orders of magnitude smaller than this mean value.

Onsager defines the fluxes as the average time derivatives of these fluctuations. Therefore, if reaction extent is used to measure fluctuations, reaction velocity is the corresponding flux. The forces are defined as conjugate variables of these fluxes with

respect to entropy. In summary, if a system is fully described by a set of fluctuations  $\underline{\alpha}$ , fluxes and forces are defined by Onsager as:

$$J_i = \frac{\partial \tilde{\alpha}_i(t)}{\partial t} \quad (\text{I.20a})$$

$$X_i = \frac{\partial S}{\partial \alpha_i} \quad (\text{I.20b})$$

In eq. (I.20a),  $\tilde{\alpha}_i(t)$  refers to an average evolution of the fluctuation  $\alpha_i$ . Knowing the initial fluctuation  $\alpha_0$  is not sufficient to determine its evolution in time, since it also depends on the initial microstate. This is why an average evolution  $\tilde{\alpha}_i(t)$  is used to define the fluxes.

Note that eq. (I.20) assumes that the system is homogeneous (the forces can be defined for the whole system, instead of being locally defined). Further, eq. (I.18) was first derived assuming that the fluctuations  $\alpha_i$  are even functions of the velocities. Casimir (1945) proposed an extension of Onsager's theory without the latter assumption. Indeed, when considering odd and even fluctuations, eqs. (I.19a-c) replace eq. (I.18). He also attempts to prove the validity of Onsager's reciprocal laws for continuous systems, when forces are defined locally, although his approach seems incomplete.

De Groot and Mazur (1984) present a more solid approach to the demonstration of Onsager's law for continuous systems. Even though they restrict the analysis to anisotropic heat flow and heat flow / diffusion coupling, their developments show that Onsager's law remain valid for vectorial phenomena in continuous media. In this case,  $\underline{J}_i$  is no longer a time derivative of a fluctuation, but instead it is the flux that appears in the conservation law of some state variable  $x_i$ . Force  $\underline{X}_i$  on the other hand is the gradient of the partial derivative of the specific entropy with respect to  $x_i$ . Therefore, for a continuous system containing  $n$  macroscopic degrees of freedom, vectorial fluxes and forces are such that:

$$\frac{dx_i}{dt} = -\underline{\nabla} \cdot \underline{J}_i + r_i \quad (\text{I.21a})$$

$$\underline{X}_i = \underline{\nabla} \left( \frac{\partial s}{\partial x_i} \right) \quad (\text{I.21b})$$

where  $r_i$  is the production rate of  $x_i$ .

Onsager's reciprocal relations can also be written as a variational principle for continuous media. Consider a set of fluxes  $\underline{J}$  and their corresponding forces  $\underline{X}$  in a continuous system. Further, let us define a dissipation function  $\Phi$  that depends only on the fluxes, and equals the volumetric rate of entropy production in the system. Near equilibrium, this function is quadratic:

$$\Phi(\underline{J}) = \sum_i \sum_j \gamma_{ij} J_i J_j \quad (\text{I.22})$$

In this case, there exists a variational principle that is equivalent to Onsager's reciprocal relations. For given force profiles  $\underline{X}^*(\underline{x})$ , the corresponding flux profiles satisfy the following variation problem (Onsager, 1931a):

$$\max_{\underline{J}} \int_{\Omega} [\underline{J} \cdot \underline{X}^* - \Phi(\underline{J})] dV \quad (\text{I.23})$$

From eqs. (I.22) and (I.23), one obtains the following relation, which is equivalent to eq. (I.18):

$$\underline{J}^* = \left( \underline{\gamma} + \underline{\gamma}^T \right)^{-1} \cdot \underline{X}^* \quad (\text{I.24})$$

Later works kept looking for general extremization principles in NET. In 1961, Ziegler proposed a generalization of Onsager's principle for non-linear fluxes-forces relations (Ziegler, 1961, 1983a). The rebuttal of Ziegler's principle is one of the results of this thesis, so his work will be discussed in detail in Chapter IV. Gambar and Markus (1994) derived linear flux-force relationships using a field theory approach in which the dynamics of a continuous system is described via a variational formulation. The Lagrangian used by the authors depend on certain field quantities derived from partial derivatives of the specific entropy with respect to relevant state variables. Onsager's reciprocal relations are derived assuming that entropy production is invariant under a gauge transformation that preserves the Lagrangian. Another formulation using Lagrange field theory was proposed by Glavatskiy (2015a). The Lagrangian contains two sets of field variables: one corresponding to the real system, and the other corresponding to a mirrored system. The mirrored system evolves backwards in time; its entropy production is always negative. The second law of thermodynamics and linear phenomenological relations result from this formulation. This analysis was later extended for systems with thermodynamic inertia, using a modified Lagrangian (Glavatskiy, 2015b). This extended

variational approach yields the Maxwell-Cattaneo-Vernotte equation for heat conduction with relaxation. Further, it provides a modified statement of the second law of thermodynamics: the averaged entropy production over a certain wave period (and not the instantaneous entropy production) is always positive.

### **I.4 Non-equilibrium thermodynamic perspective of nature-inspired mechanisms**

From the discussion in the previous sections, it is easier to understand the relationship shown in Figure I.1 between Coppens' T1-T3 framework for NICE and Gerbaud's NET1 – NET3 principles (Coppens, 2012; Gerbaud et al., 2020). The Hierarchical Transport Networks (T1) principle may give rise to fractal-like flow architectures similar those found from the CL theory. Further, transport networks operating near equilibrium minimize energy dissipation when the thermodynamic forces (e.g. temperature difference for a heat exchanger) are uniformly distributed (Tondeur and Kvaalen, 1987). This theorem, known as *equipartition of entropy production*, is used together with CL theory in the thermodynamic counterpart of T1, called NET1.

The second theme in Coppens' framework, Force Balancing (T2), can be adapted to the NET framework as the Thermodynamic Coupling (NET2) principle. In the same way complex structures can be stabilized in nature due to the action of different elementary forces, fluxes can be maintained or eliminated in systems due to the action of different thermodynamic forces. This phenomenon arises regardless of whether the system is near equilibrium or far from equilibrium. One example is the coupling between solute diffusion and heat explained in Section I.3.

Finally, the Dynamic Self-Organisation theme (T3) proposed by Coppens refers to the emergence of organized structures in nature. In thermodynamics, organization is linked to Dissipative Structures (NET3). Out-of-equilibrium systems can present spatiotemporal organization as long as energy and/or mass is continuously provided to them. The formation of Bénard cells (see bottom-right image in Figure I.1) is a classic example. Heating a horizontal layer of fluid from below creates a vertical gradient of temperature. If this gradient is too low, no significant change is observed in the system. However, after a certain threshold of temperature gradient, the fluid forms a regular pattern of convection cells.

Note that, despite the NET framework being derived from the themes T1-T3, there is no bijective relation between them. In other words, each of these frameworks may give rise to research projects and engineering solutions that could not be derived from the other. For example, the confinement of enzymes in narrow channels to increase their catalytic activity (see Section I.2) was an idea derived from T2 that could not be conceived from NET2. Alternatively, countercurrent heat exchangers are more efficient as they distribute the thermodynamic force (temperature difference between the fluids) more evenly than co-current exchangers. This idea could have stemmed from NET1 (according to the principle of equipartition of entropy production), but not from T1.

Figure I.4 shows the behaviours of different systems associated with each of the NET principles evoked above. The blue solid lined at the left side of the sketch corresponds to an isolated system that is initially out-of-equilibrium. The entropy of the system increases as it evolves towards its equilibrium state. Thermodynamic coupling may occur if there are multiple fluxes/forces in the system. Near equilibrium, this coupling is captured by the linear flux-forces relationship given in the figure.

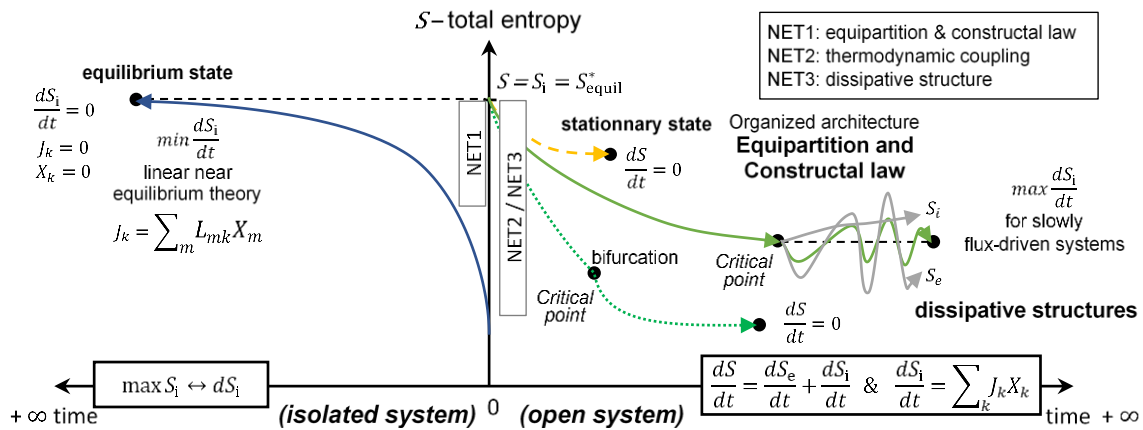


Figure I.4 – Behaviours of different out-of-equilibrium systems related to the NET framework. Adapted with permission from Gerbaud et al. (2020).

The right side of Figure I.4 depicts three different open systems that evolve from an equilibrium state to an out-of-equilibrium state. The yellow dashed line represents a system that is only slightly perturbed from its equilibrium state. If it corresponds to a transport network, then Equipartition of Entropy Production and Constructal Law can be used to minimize energy dissipation. Next, the green solid line and the green dotted line portray dissipative structures. The Bénard cells mentioned earlier in this section correspond to the green dotted line, because this structure reaches a stationary form.

Nevertheless, it is also possible for dissipative structures to change with respect to time, as depicted by the green solid line. For example, systems exhibiting Self-Organized Criticality (Pruessner, 2012), such as tectonic plates, are fed with a continuous energy input, which is released via intermittent avalanches (earthquakes). These systems never reach a steady state; instead, they oscillate near a critical state.

### I.5 Motivation and objectives of the thesis

Although being connected by the NET framework (Gerbaud et al., 2020), each of the three topics investigated in this thesis has its own individual motivations, in relation to the chemical engineering field.

Liquid distributor is an important internal in packed distillation columns. If not chosen wisely, distributors can contribute to several issues during distillation operation, such as entrainment and foaming. But the main operational issue related to this internal is maldistribution. Liquid maldistribution is associated with a reduction in packing efficiency, which translates into HETP increasing by a factor as high as 3 in some cases (Kister et al., 2008). The tree-like liquid distributor discussed in Chapter II (Meyer and Rouzineau, 2020) addresses this issue.

Diffusiophoresis and diffusioosmosis emerge frequently in nature and industry. Therefore, the modelling of these phenomena (Chapter III) is of utmost importance. Indeed, the more one knows about a phenomenon, the easier it gets to find new applications for it and optimize the existing ones. For example, it was through a diligent study of diffusioosmosis that Ajdari and Bocquet (2006) figured out a way to significantly increase osmotic flowrates in capillary tubes.

Finally, Ziegler's Maximum Entropy Production Principle (MaxEP) (Ziegler, 1961, 1983a) has found wide acceptance in modern literature, and it is used by several authors without second thoughts. However, some clues point to the fact that Ziegler's theory may have severe limitations that are often neglected by its advocates. This is a great motivation for revisiting this principle.

Hence, the specific objectives of this thesis are:

1. To study the performance of a new nature-inspired liquid distributor (Chapter II)
2. To model a membrane via diffusioosmosis (Chapter III)



3. To study the (instantaneous) equilibrium states of diffusiophoresis, estimate diffusiophoretic velocity as a function of system parameters, and compare the results with limiting cases already discussed in the literature (Chapter III)
4. To prove the existence of fully-developed, out-of-equilibrium states for diffusiophoretic systems (Chapter III)
5. To show that the only stable equilibrium state in diffusiophoresis corresponds to null velocity (Chapter III)
6. To study the effect of weak and strong interface – solute attraction forces on diffusiophoretic velocities (Chapter III)
7. To dispute Ziegler’s MaxEP principle (Chapter IV)

### **I.6 Organization of the thesis**

The rest of this thesis is organized as follows. Chapter II describes the main features of the nature-inspired liquid distributor. It also discusses theoretical and experimental performance results. Chapter III describes the case studies chosen for diffusiophoresis and diffusioosmosis, as well as the model adopted to describe these systems. Simulation results are reviewed and discussed in detail. Chapter IV contains the critics to Ziegler’s MaxEP principle. Finally, Chapter V summarizes the main findings of this work and recommends several topics for further study.

---

# Chapter II. A nature-inspired liquid distributor

---

In this chapter, a solution to liquid maldistribution in distillation column is assessed. Such a solution consists in increasing the number of initial irrigation points without increasing the number of holes on the distributor's plate. This can be achieved by incorporating an innovative tree-like structure (Meyer and Rouzineau, 2020) that guides the liquid dripping from each hole and separates it into several branches.

Section II.1 lays the groundwork for the remainder of the chapter. It discusses the theory behind the design of the novel liquid distributor, reviews classic distributor configurations and presents some performance indicators used in the following sections to assess the new distributor. Section II.2 overviews the novel distributor concept, and the following section reviews previous works that will be useful for distributor design. Section II.3 also reviews design and performance of a new type of packing, called Tetra Spline (TS) packing (Kawas et al., 2021), which is used in the test rig described by the end of the section.

Section II.4 discusses criteria for choosing distributor design and it details the three configurations chosen according to these criteria. In the next section, their performance is assessed via distillation experiments that measure separation efficiency. The results are later compared with Sulzer's perforated pipe and regular orifice-pan distributors. Finally, Section II.6 reviews the main findings of this chapter.

## II.1 Literature review

### II.1.1 *The constructal law*

Darwin's theory of evolution states that the living species inhabiting the planet have evolved from older forms (and will continue to evolve), the evolution being driven by natural selection. The fundamental idea behind this theory is almost elementary: living beings strive to survive, and any inheritable modification that increases an individual's capability to survive and/or to reproduce will be spread within the species through the individual's offspring.

Bejan proposed that a similar reasoning could be applied to flow structures (Bejan and Lorente, 2004). For example, it seems reasonable to assume that the lungs, responsible

## Chapter II. A nature-inspired liquid distributor

for oxygen transport from the air to the alveoli, have evolved through time so that the current configuration needs less energy to function. The theory that emerged from this assumption is called the Construal Law (CL). Its full statement (Bejan and Lorente, 2004) has already been cited in Chapter I, but it will be restated below for completeness:

*For a finite-size system to persist in time (to live), it must evolve in such a way that it provides easier access to the imposed currents that flow through it.*

*For a system with fixed global size and global performance to persist in time (to live), it must evolve in such a way that its flow structure occupies a smaller fraction of the available space.*

*In order for a flow system with fixed global resistance ( $R$ ) and internal size ( $V$ ) to persist in time, the architecture must evolve in such a way that it covers a progressively larger territory.*

Tree shapes will usually arise in nature when transport is made from a single point to an area/volume, or vice-versa. Inspired by this, Bejan proposed a systematic procedure to design optimal flow structures, using building blocks called constructs (Bejan, 1996). In a subsequent paper (Bejan, 1997), the author used this procedure to study the problem of cooling a heat generating surface through a heat sink, using a fixed amount of a high conductivity material. This case study could be applied to the cooling of electronic devices. For this problem, a heat sink at temperature  $T$  is available at a point  $M$  on the edge of the heat generating surface with area  $A$  (Figure II.1a).

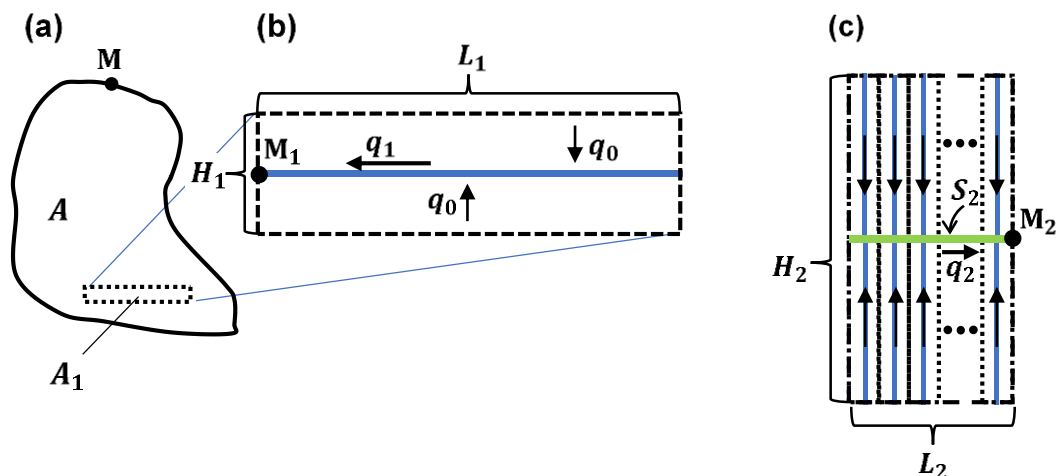


Figure II.1 – Illustration of a randomly-shaped heat generating surface (a), the smallest (b) and the 2<sup>nd</sup> smallest (c) building blocks in the transport network; adapted from Bejan (1996)

## Chapter II. A nature-inspired liquid distributor

The designer can embed part of the surface with a highly conductive material in order to facilitate heat dissipation to the sink. The goal is to minimize the temperature  $T_{max}$  of the hot spot. The allocation of high conductivity material is optimized in several levels. The smallest levels, corresponding to the elemental constructs, are supposed to be rectangular, with dimensions  $L_1 \times H_1$  yet to be determined. Their surface area equals  $A_1$ , and a single strip of high conductive material passes through each of them. If  $H_1 \ll L_1$ , heat flow  $q_0$  in the low conductivity material (thermal conductivity  $k_0$ ) can be assumed to be perpendicular to this high conductive path. Within the region of high conductivity  $k_p$ , heat ( $q_1$ ) flows along this path towards the heat sink  $M_1$ . Figure II.1b illustrates these elemental constructs.

It is suitable to shape the element so that its hot spot temperature is minimized. The resulting shape is such that:

$$\frac{H_1}{L_1} = 2 \left( \frac{k_0 H_1}{k_p D_1} \right)^{\frac{1}{2}} \quad (\text{II.1})$$

where  $D_1$  is the width of the strip. The hypothesis  $H_1 \ll L_1$  made earlier is equivalent to  $(k_0/k_p) \ll (D_1/H_1)$ . In other words, the ratio between the smaller and the larger conductivities must be smaller than a certain threshold for the hypothesis of vertical heat flow to hold outside the strip.

The second-generation construct (surface area  $A_2$ ) also has a high conductivity strip passing through it. The exit points (heat sinks)  $M_1$  need to be connected to the second-generation strip  $S_2$  so that the heat can easily access  $M_2$  (see Figure II.1c). Now, one can minimize the temperature of the hot spot in this second element. The optimal aspect ratio for the second-generation neighbourhood is:

$$\frac{H_2}{L_2} = 2 \quad (\text{II.2})$$

Following a similar reasoning, it is possible to generalize the aspect ratio of the  $n^{\text{th}}$ -generation neighbourhood ( $n > 1$ ) as follows:

$$\frac{H_n}{L_n} = \begin{cases} 1, & \text{if } n \text{ is odd} \\ 2, & \text{if } n \text{ is even} \end{cases} \quad (\text{II.3})$$

Figure II.2a–c depicts the network generated by CL up to the 5<sup>th</sup> generation.

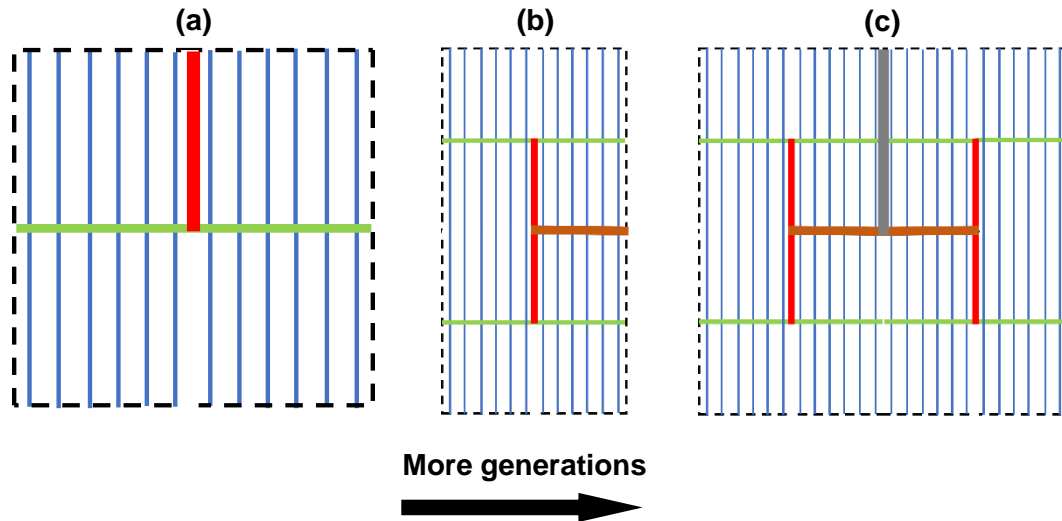


Figure II.2 – (a-c) Evolution of a hypothetical cooling network with respect to the number of generations (Bejan, 1997)

The claim that higher order constructs decrease thermal resistance has been disputed by Ghodoossi (2004), who revisited the problem with a more rigorous approach. The author also discusses the application of CL to liquid transport from a porous surface to an outlet point. The problem consists in the design of a structure with high-permeability channels to realize liquid transport from a porous surface to an outlet M. The channels have different permeabilities, all of which are higher than the permeability of the porous surface. It is assumed that the flow follows Darcy's law, and the goal is to minimize the maximum pressure difference between the surface and point M. Ghodoossi (2004) shows that previous CL architectures proposed for this problem only decrease flow resistance because the fraction of the surface occupied by the highly permeable material increases as the complexity increases. That is, the improvement as one goes towards high-order constructs comes from the fact that the volume fraction of high-permeable material increases, and not from the extra branching levels.

Another attempt to apply the CL design procedure is found in an innovative configuration for ground coupled heat exchangers (Kobayashi et al., 2013). The authors have compared the classic serpentine design with Y and T-shaped tree heat exchanger configurations. They have modelled the ground as an insulated cube, and the heat exchanger as a pipe network immersed in this cube. Results show that Y-tree shapes have higher exchange rates compared with T-trees and serpentine. The paper also claimed that an increase in the number of bifurcations yields higher heat transfer rates. However, in this case the configurations with more bifurcations occupy larger volume fractions of the cube. Hence,

it is not clear whether the increase in exchange rate comes from a more homogeneous distribution, or simply from the added heat transfer area due to the incorporation of extra pipe branches.

Other cases where constructal design fails to decrease flow resistance are discussed in Kuddusi and Eđrican (2008). These examples show that constructal theory fails in its attempt to propose a deterministic method for the design of optimal flow structures. Nevertheless, the CL statement as given by Bejan and Lorente (2004) is still quite relevant for engineers. It should not be extrapolated to a “magical” design method, but rather interpreted as a motivation to use nature-inspiration in the creation of artificial flow structures. Natural flow architectures have likely evolved through the years, towards more resilient and efficient structures. Therefore, it is reasonable to get inspiration from nature when developing artificial flow networks.

### *II.1.2 Liquid distributor designs for distillation columns*

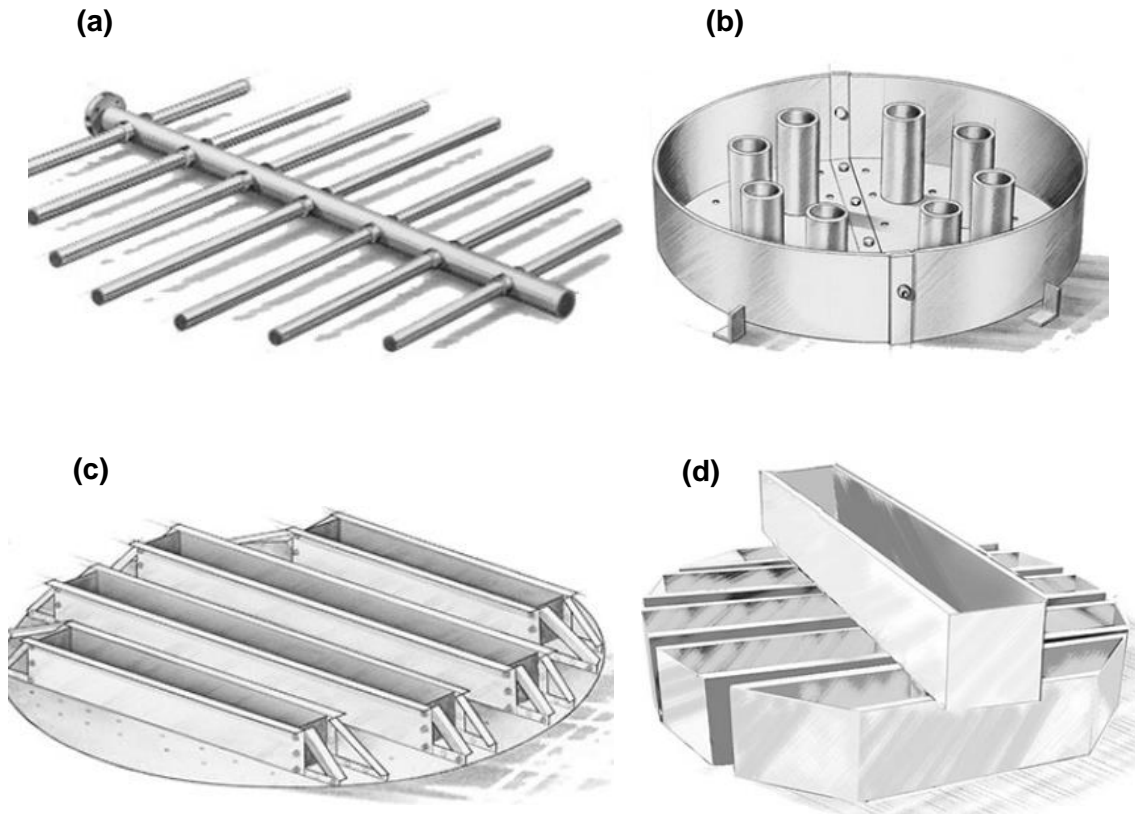
Liquid distributors and redistributors are critical components in packed distillation columns. They are used to ensure an even distribution of liquid throughout the cross-section of the column. Ideally, such equipment should provide a large number of evenly distributed irrigation points and a large area for upward countercurrent vapor flow. Further, their design should aim for large turndown ratios to give room for operational fluctuations and changes in nominal flow rates (due to increase/decrease in demand, for example). However, these requirements are often conflicting in practice, and different types of distributors are available in market according to the designer priority.

Distributors are usually divided in two categories, according to the driving force for the liquid flow within: pressure or gravity. The most classic example of pressure distributors is the perforated pipe (Kister, 1990; Kister et al., 2008). It consists of several perforated pipes branching out from a main tube. The liquid stream is pumped through the main tube, where it splits into different streams as the liquid flows along the branches. Discharge takes place through the holes on the underside of the branching pipes. This device provides a large area for upward vapor flow. However, the high liquid pressure drop induces either smaller number of holes or smaller size of holes, decreasing quality of distribution or making it prone to fouling.

Gravity distributors allow for smaller liquid pressure drops, though they generally provide smaller areas for the upward vapor flow. The driving force for liquid discharge is the

## Chapter II. A nature-inspired liquid distributor

weight of the liquid head built up on the distributor. Some gravity distributors, such as orifice pan and orifice tunnel types (Kister, 1990; Kister et al., 2008), can be used as self-collecting redistributors. For this application, a hat needs to be installed on the top of the vapor risers to prevent the liquid from flowing through them. Both types are prone to plugging when hole diameter is small ( $<12\text{mm}$ ). Orifice pan distributors usually have higher turndown ratio ( $\sim 4:1$ ) compared with orifice tunnel types ( $\sim 2.5:1$ ). The gravity distributors aforementioned direct the vapor flow through risers and discharge the liquid through holes on the base plate. As an alternative, instead of directing the vapor stream, trough distributors (Kister, 1990; Kister et al., 2008) direct the liquid stream to troughs in which the liquid heads are built up. Vapor flows through the gaps between the troughs, and the area available for this flow is generally higher compared to orifice pan and orifice tunnel distributors. Figure II.3 illustrates the industrial distributors aforementioned.



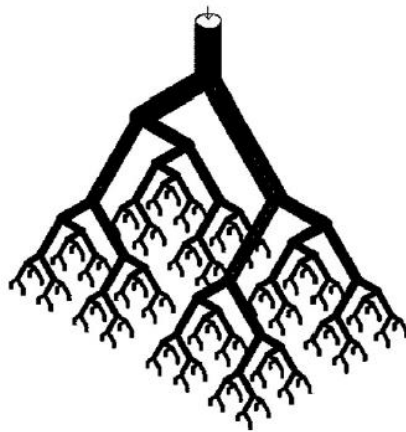
*Figure II.3 – Common industrial distributors: (a) perforated pipe; (b) orifice pan; (c) orifice tunnel; and (d) trough. Courtesy of Koch-Glitsch.*

The distributors shown in Figure II.3 are well-established in the chemical industry and have been operated for decades. Recently, Eck and Kirsten (2019) proposed a new design for self-collecting liquid redistributors, with the addition of a droplet dumping tray just above the distributor tray. Usually, when droplets fall from the bottom of a packed bed

## Chapter II. A nature-inspired liquid distributor

directly onto the liquid layer formed on the distributor tray below, foam can be formed. The inventors claim that adding the so-called droplet dumping tray just above this liquid layer helps prevent foam formation. In addition, Franz and Geipel (2019) improved on classic nozzle distributors by using flat-jet nozzles and adding a drain element to them. In one of the configurations listed by the inventors, guide plates intercept liquid from the end of the flat jets at small angles. The liquid then drops from the edge of the plate. Such drain element also protects the liquid against the rising vapor flow, and a significant reduction in entrainment can be achieved.

The inventions above approach relevant issues in distillation operation, namely entrainment and foaming. Yet another issue that can cause malfunction in packed columns is maldistribution. The liquid maldistribution is associated with a reduction in packing efficiency, which translates into HETP increasing by a factor as high as 3 in some cases (Kister et al., 2008). This issue may be caused by uneven liquid distribution over the different distributor outlets. For this reason, Zhang and Lv (2012) proposed a constructal distributor design capable of distributing the fluid evenly among 128 outlet points. The proposed configuration has a tree shape, with cylindrical tubes conducting the flow. Each channel splits into two in the subsequent layer, forming the structure shown in Figure II.4. The angle between the tubes and the vertical axis, as well as diameter and length ratios between tubes in adjacent layers, are optimized to minimize pressure drop.



*Figure II.4 – Constructal distributor. Reprinted from Zhang and Lv (2012), with permission from Elsevier.*

Other authors have proposed and optimized similar constructal-based designs for liquid distributors, always minimizing energy dissipation but using different design variables and constraints (Fan et al., 2009; Tondeur et al., 2009). The downside common to all these



devices is the high energy dissipation from friction with the walls of the tubes, which makes them not suitable for distillation applications.

### *II.1.3 Performance indicators for liquid distributors*

In the previous section it was stated that maldistribution is a major issue in packed distillation columns, and that this issue may be caused by underperformance of the liquid distributor. Therefore, the quality of the liquid distribution should be one of the most relevant criteria to assess distributors. Here three assessment methods will be discussed: the distribution quality rating index (Moore and Rukovena, 1987; Kister, 1990), the maldistribution factor (Hoek et al., 1986; Lämmermann et al., 2016) and the height equivalent of a theoretical plate (HETP). The two first methods evaluate the quality of the distribution itself, whereas the third one is an indirect method that evaluates the effect of the distribution on the separation efficiency.

The distribution quality rating index ( $D_Q$ ) was proposed by Moore and Rukovena in 1987, and is defined as follows (Moore and Rukovena, 1987; Kister, 1990):

$$D_Q = 0.4(1 - A) + 0.6B - 0.33(C - 0.075) \quad (\text{II.4})$$

This approach considers the irrigation points as drip circles whose areas are proportional to the liquid flowrate through them. Further, the sum of circle areas equals the cross-sectional area of the column. Parameter  $A$  is the fraction of the cross-section that is not covered by drip circles. To evaluate  $B$ , one needs to partition the cross-section of the column in 12 sectors with the same area. Sectors can be ring-like or trapezoid-like (Hanusch et al., 2019). The smallest ratio of total circle area in a sector to the sector area ( $B_1$ ) and the smallest ratio of a sector area to its total circle area ( $B_2$ ) are calculated.  $B$  is defined as the minimum between  $B_1$  and  $B_2$ . Finally,  $C$  is the total overlap area of the circles divided by the cross-sectional area of the column.

Typical values of index  $D_Q$  are 0.1 to 0.7 (Kister et al., 2008). The geometric representation of parameters  $A$ ,  $B$  and  $C$  is illustrated in Figure II.5. In this figure, the black dots correspond to the irrigation points. The white area inside the larger circle contour and not covered by the smaller blue circles is used to calculate  $A$ . The grey surface on the top of the figure represents the sector used to estimate  $B$ , and dark blue regions are the intersections that give  $C$ .

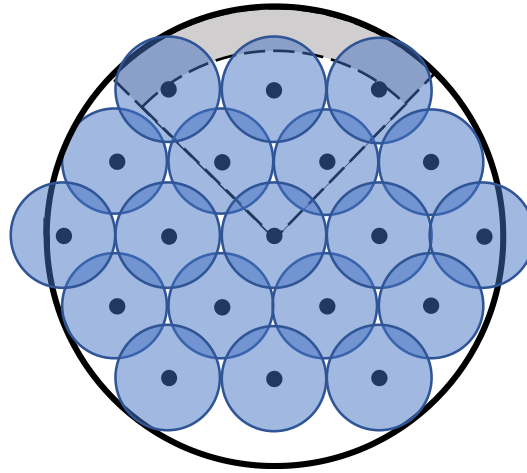


Figure II.5 – Areas taken into account for calculating the distribution quality rating index (A is the cross-section fraction not covered by blue circles; B is the grey sector fraction covered by circles; C is the cross-section fraction covered by dark-blue intersections)

Despite being a common criterion to assess liquid distribution,  $D_Q$  presents several inconsistencies. Firstly, it does not account for drip point density. According to this criterion, the distributor with 19 outlets in Figure II.5 is equally good regardless of whether the distillation tower has 0.15m or 12m diameter. Another problem with  $D_Q$  is that it reaches a maximum value of 1.02 for a single outlet at the centre of the cross-section. Further, if instead of a single outlet there were two even outlet flows placed very close to each other and almost coincident with the centre of the cross-section, the quality of the distribution should not change. Nevertheless, this new 2-outlets configuration changes  $D_Q$  to 0.06. If 3 outlets are arranged with uniform flow and close to the centre of the cross-section,  $D_Q$  further decreases to -0.06. This incongruence takes place when outlet points are very close to each other, which is why the index behaves inconsistently for high drip point numbers (Bozzano et al., 2014).

The maldistribution factor ( $M_f$ ) is a more consistent alternative to  $D_Q$ . This index is similar to a coefficient of variation, measuring the deviation from a perfectly homogeneous distribution. It is usually employed to assess liquid distribution in a packed bed, although it can also be used for liquid distributors (Hanusch et al., 2019). To calculate it, one needs a liquid collector divided in  $N$  cells of equal area. The collector should be placed below the bed/distributor, and  $M_f$  is calculated by measuring the liquid flow collected by each of these  $N$  cells (Hoek et al., 1986; Marcandelli et al., 2000).

## Chapter II. A nature-inspired liquid distributor

Let  $Q_i$  be the liquid flowrate captured by cell  $i$ , and  $Q_{mean}$  the average flowrate over the  $N$  cells. In this case:

$$M_f = \sqrt{\frac{1}{N(N-1)} \sum_i \left( \frac{Q_i - Q_{mean}}{Q_{mean}} \right)^2} \quad (\text{II.5})$$

$M_f$  varies between 0 and 1. A zero value indicates a perfectly homogeneous distribution, whereas 1 corresponds to the case where all the liquid flows through only one region.

Although eq. (II.5) does not depend explicitly on the drip point density, this factor is accounted for if the number of cells  $N$  is chosen according to the cross-section area of the column. For example, let us consider two columns of diameter 0.15 m and 12 m, both using distributors with 19 drip points placed according to Figure II.5. For the small column,  $N$  should be small (say 21), whereas for the large column it should be higher (134 400 if it is proportional to the cross-sectional area of the column, i.e. if keeping the same cell area). With these values,  $M_f \approx 0.073$  for the smaller distributor, whereas  $M_f \approx 0.23$  for the larger one.

Hoek et al. (1986) used the criterion in eq. (II.5) to assess liquid distribution in various types of packing. They employed a collector with 681 cells of 2.56 cm<sup>2</sup> in order to capture the distribution on the scale of the packing elements. All the experiments were conducted without upward vapor flow. Average  $M_f$  was 0.7 for random packing, and 0.4 for structured packing. For random packings, the authors found that  $M_f$  remains approximately the same for bed heights between 0.4 m and 2 m. Further,  $M_f$  is smaller (i.e., distribution is better) when packing elements are smaller in size, and the index does not depend on the wettability of the material. For structured packings,  $M_f$  decreases significantly with respect to the depth of the bed, showing that these structures are capable of distributing the flow quite well after a certain number of layers. The authors also compared two beds of the same height, made of Plastic BX and Mellapak 500-Y. They showed that the former packing distributes the liquid better, although this could be due to the difference in the number of layers present in each bed. Plastic BX has a smaller layer height, so one can fit more layers using this packing. Finally,  $M_f$  in both structured and random packings significantly decreases when liquid flowrate is increased.

Later experiments made by Marcandelli et al. (2000) in a column of 0.3m diameter confirm the conclusions in the previous paragraph. The experiments were conducted

## Chapter II. A nature-inspired liquid distributor

using a collector with 9 cells of 78.5 cm<sup>2</sup>, so fluctuations in the scale of the packing elements were not captured by their assessment. Overall,  $M_f$  values in experiments without countercurrent gas flow remained in the range 0.4 – 0.7. In addition, the authors remarked that even small upward vapor flowrates can significantly improve liquid distribution, with  $M_f$  ranging between 0.005 and 0.4 in these cases. This study also investigated the influence of the initial distribution on the maldistribution factor for a bed height of 1.3 m. It was found that an increase in the number of irrigation points on the distributor is associated with a decrease in  $M_f$ .

The last performance indicator covered in this section is the HETP. It is the height over which a change in composition corresponding to one ideal separation stage is observed. This criterion corresponds to the efficiency of the column, being the most practical among the 3 discussed in this section. To measure HETP of a packed distillation column, one can operate it at total reflux to separate a binary mixture, and measure the compositions at the top and bottom of the packed bed. Knowing these compositions, the McCabe-Thiele method can be used to estimate the number of theoretical stages in the column. Finally, HETP is obtained by dividing the height of the packed bed by the number of theoretical stages. More details on HETP measurements are given in Section II.3.4. Note that an improvement of initial liquid distribution does not necessarily yield a decrease in HETP. Indeed, it has been observed that irrigation densities beyond 100 pts/m<sup>2</sup> do not bring significant improvement to industrial packing efficiency (Kister, 1990; Kister et al., 2008).

### II.2 General description of the liquid distributor

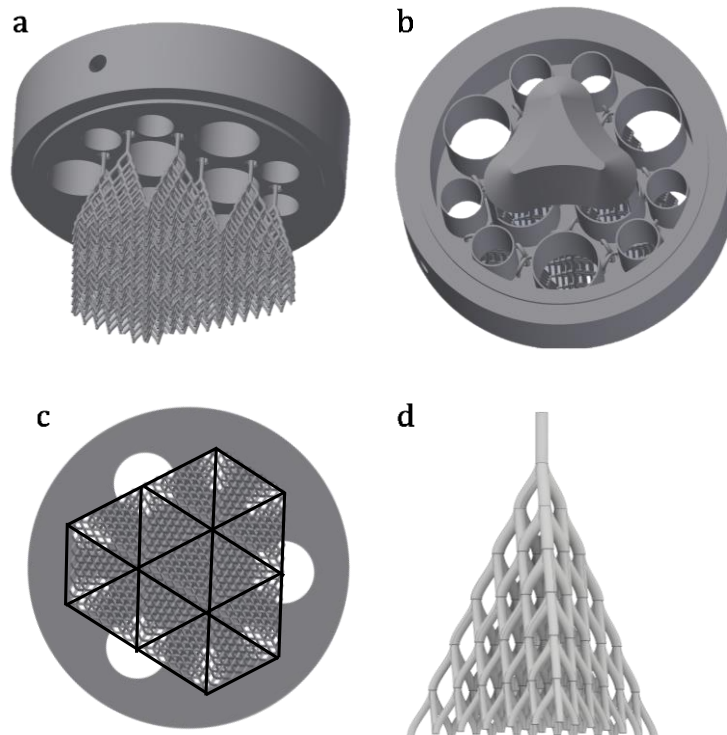
As mentioned in Section II.1.2 and II.1.3, the performance of a liquid distributor generally increases with respect to the number of irrigation points. However, designing a liquid distributor with a high number of holes could make it prone to fouling, as the diameter of the holes would have to be smaller. The solution proposed by Meyer and Rouzineau (2020) and discussed here is to increase the number of irrigation points without increasing the number of holes on the distributor's plate. This can be achieved by incorporating a tree-like structure that guides the liquid dripping from each hole and separates it into several branches.

Similar tree-like structures for liquid distributors had been conceived before with the help of the Constructal theory, such as the one developed by Zhang and Lv (2012) and

## Chapter II. A nature-inspired liquid distributor

illustrated in Figure II.4. However, this and the other constructal designs mentioned in Section II.1.2 are unsuitable for distillation applications because they would result in large liquid heads, due to the friction inside the tubes. The workaround is to conceive a tree distributor with the liquid flowing outside the branches. This is the key innovation in the invention disclosed by Meyer and Rouzineau (2020).

In the arrangement proposed by them, the liquid does not drip directly from the distributor plate holes to the packed bed below. Instead, it flows along the outer surface of wires, driven by gravity. Each wire later splits into 3 different branches, spreading the irrigation along the cross-section of the column. Wires are shaped as splines instead of a straight form, to ensure a smooth transition between different branching levels (Dejean et al., 2020) that prevents exaggerated liquid bead formation at level junctions. Further, wire diameter is allowed to vary along the tree-structure levels. Figure II.6 shows an example of a liquid distributor that was designed according to such criteria. The distributor displayed in Figure II.6 and the others used in this work were designed using Autodesk Inventor software (Autodesk, 2019).



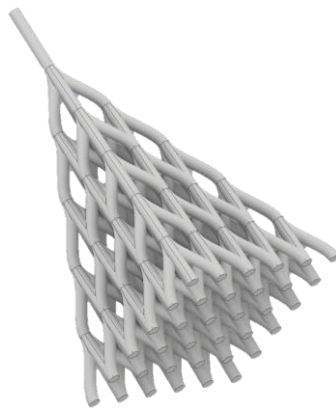
*Figure II.6 – (a) isometric, (b) top and (c) bottom views of a tree-structured liquid distributor; (d) pyramid distributing liquid from a single hole on the distributor plate*

The distributor depicted in Figure II.6 distributes the liquid from 13 primary irrigation points. The plate above the wire network is an orifice-pan structure, similar to the one in

## Chapter II. A nature-inspired liquid distributor

Figure II.3b. Figure II.6b shows the 12 chimneys for the upward vapor flow in this orifice-pan portion. Only the 3 at the centre are covered by a hat, as in the experiments discussed in the next sections the liquid falling from above is mostly concentrated in the centre of the column. However, hats can be added to the top of the other chimneys if necessary. A liquid head is formed on the orifice-pan structure, as the liquid does not pass through the chimneys. This head is discharged through small gaps on the underside of the plate, between the holes and the vertical wires (see Figure II.6a). The liquid discharged from the plate then splits into several branches as it flows down the wire structure. Figure II.6c depicts the bottom view of the distributor. There are 262 potential irrigation points, which can be divided in 13 triangular sectors (one per plate hole). These triangles are actually the bases of pyramid-like structures similar to the one shown in Figure II.6d.

The pyramid in Figure II.6d exhibits 6 branching levels. The top wire captures the liquid falling from the plate, and the following branches distribute it over a larger area. In this structure, each wire splits into 3 branches. A regular tetrahedron is obtained because all the wires have the same length and form the same angle with respect to the vertical axis. Another regular arrangement can be conceived with 4 branches instead of 3 in the offspring of each wire. This structure is show in Figure II.7.



*Figure II.7 – Square pyramid resulting from the pattern where each wire splits into 4*

It would be naive to assume that all the wires in the arrangements shown in Figure II.6d or in Figure II.7 are wet during column operation. Indeed, experimental results for liquid flow down a tetraspline structure (i.e., a straight wire with 3 ramifications) suggest that the stream sometimes splits over 2 out of the 3 offspring branches (Dejean et al., 2020). However, the number of redundancies over the different branching levels helps preventing large dry areas. Redundancies refer to the reconnections happening along the

several branching levels (see Figure II.8). They ensure that the offspring (children, grandchildren, ...) of a dry wire can still be wet, as there are other paths for the liquid to reach these wires.

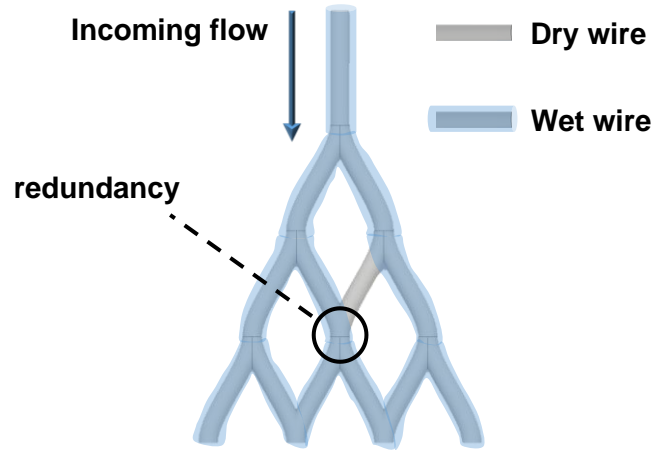


Figure II.8 – 2D representation of liquid flow on a wire structure

### II.3 Materials and methods

#### II.3.1 Characterization of flow on a wire

In order to assess the suitability of a liquid distributor such as the one shown in Figure II.6, one must first study the characteristics of liquid flow on wires. Dejean et al. (2020) made several experiments on the flow of liquid films along the surface of vertical wires and against an uprising gas flow. In their experimental setup, liquid inlet flow is controlled by a syringe pump. A connector controls the injection diameter, and the liquid film thickness on the wire is measured using a high velocity camera. Wire length is kept below 20 mm to avoid instabilities, and the upward gas flow is controlled using a needle valve and a flowmeter. Gas (air) is first humidified in a different chamber, in order to avoid evaporation of the liquid on the wire. Moreover, gas flowrates are set so that the corresponding F-factors in the wire chamber do not exceed  $3 \text{ Pa}^{1/2}$ . As a reminder, F-factor is defined as the product between the superficial gas velocity and the square root of the vapor density.

Dejean's work shows that gas flowrate and injection diameter have little effect on film thickness ( $\delta$ ). Further, it reveals an increase in  $\delta$  (from 0.47 mm to 0.78 mm for a 150 mL/min water flow) as wire diameter decreases from 2 mm to 0.5 mm. The wire material also impacts  $\delta$ , with polyamide (PA12) wires providing much thinner films than

## Chapter II. A nature-inspired liquid distributor

aluminium and stainless-steel wires. Finally, the type of liquid being used in the experiments affects film thickness and flow regime at small flowrates. For water, flow regime shifts from partial wetting (with the presence of liquid beads) to full wetting (without beads) for liquid flowrates above around 20 mL/min. For ethanol, full wetting regime is obtained even for liquid flowrates as low as 5 mL/min. Above 40 mL/min, film thickness is approximately the same for both liquids.

The value of  $\delta$  can be estimated from Nusselt's solution for a flow with uniform film thickness down a cylindrical wire (Duprat, 2009; Dejean et al., 2020). This solution is obtained by solving the Navier-Stokes equation with no-slip boundary condition at the surface of the wire, and assuming zero tangential stress on the liquid-air interface. Integration of the resulting velocity profile over the film width yields eq. (II.6), which can be used to calculate  $\delta$ :

$$\frac{\rho g}{3\eta_f} \delta^3 \psi(\delta/R) = q_l \quad (\text{II.6})$$

Here,  $q_l$  is the volumetric flow divided by the perimeter of the cross-section of the wire,  $\rho$  and  $\eta_f$  are the density and viscosity of the liquid, and  $g$  is the standard gravity. Function  $\psi$  is given by:

$$\psi(x) = \frac{3(4(x+1)^4 \ln(x+1) - x(x+2)(3x(x+2)+2))}{16x^3} \quad (\text{II.7})$$

For silicone oil film with a viscosity of 48 mPa.s on a wire of diameter 3 mm, the thickness calculated with eqs. (II.6) and (II.7) agrees quantitatively with experimental measures in a volumetric flow range of 0 – 120 mL/min (Duprat, 2009). For higher viscosities (up to 485 mPa.s) and thinner wires (between 0.4 and 0.64 mm diameter), this agreement is only shown for very small flowrates ( $\leq 1.2$  mL/min). Dejean et al. (2020) performed a similar study using water instead of silicone oils. Their study used volumetric flowrates between 0 and 160 mL/min, and wire diameters between 0.5 mm and 2 mm. The only experiments that agreed quantitatively with eqs. (II.6) and (II.7) were the ones performed with large wire diameter (= 2 mm). The experiments performed using smaller diameters (1 mm and 0.5 mm) showed significant deviations from the predicted thickness. However, qualitative agreements are still observed, as both experiments and model show an increase in film thickness when wire diameter is decreased.



### II.3.2 Characterization of flow along tetrahedron edges

Dejean et al. (2020) also studied liquid flow along a tetrahedron structure made of wires. This tetrahedron, depicted in Figure II.9, resembles the repeating pattern of the Tetra Spline (TS) structured packing described in Kawas et al. (2021). In this figure,  $d_w$  is the wire diameter,  $l_w$  is wire length and  $\theta$  is the angle of the tetrahedron edges with respect to the vertical axis.

Three different liquids were used for experiments: demineralized water, ethanol and a 50-50 ethanol-water mixture. The setup for experiments is similar to the one described in Section II.3.1, where the single wire is replaced by the tetrahedron element. However, instead of investigating film thickness, authors were more interested in the different flow regimes taking place when studying the structure. Three main regimes were observed: capillary, inertial and wetting. Capillary flow takes place when surface tension dominates over other forces. This regime is characterized by the formation of droplet streams, and liquid flows only on 1 of the 3 edges. Inertial flow is observed when inertia controls the flow, rendering surface tension negligible. In this state, the wires are not capable of changing flow direction. Finally, wetting is achieved when inertia and surface tension are of the same order of magnitude. In this case, the flow is smoothly repartitioned over 2 or 3 edges.

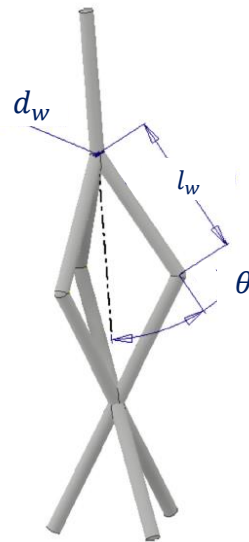


Figure II.9 – Illustration of the tetrahedron structure used in experiments. Adapted with permission from Dejean et al. (2020).

Generally, high flowrates and low wire diameters favour inertial regime, whereas low flowrates and low wire diameters favour capillary flow. Wire length does not play a

## Chapter II. A nature-inspired liquid distributor

significant role in the flow regime, although it was observed that for  $l_w < 10\text{mm}$  the liquid flow englobes the entire structure instead of splitting over the edges. Similarly, for  $\theta < 30^\circ$  separation of the liquid stream cannot be achieved. Further, for  $\theta > 40^\circ$  the liquid stream detaches from the wires.

The remaining parameters studied by the authors were gas countercurrent flowrate and liquid type. It was found that gas countercurrent does not affect flow regime along the tetrahedron for F-factors smaller than  $3 \text{ Pa}^{1/2}$ . Liquid type however has a major impact on the flow. Wetting flow can be obtained for some ethanol flowrates at relatively small wire diameters. The minimum wire diameter required to achieve the wetting regime is higher for the 50-50 ethanol-water mixture. Finally, wetting could not be observed for the experiments using pure water, probably because wire diameters were not large enough. A cartography of the flow regimes is shown in Figure II.10.

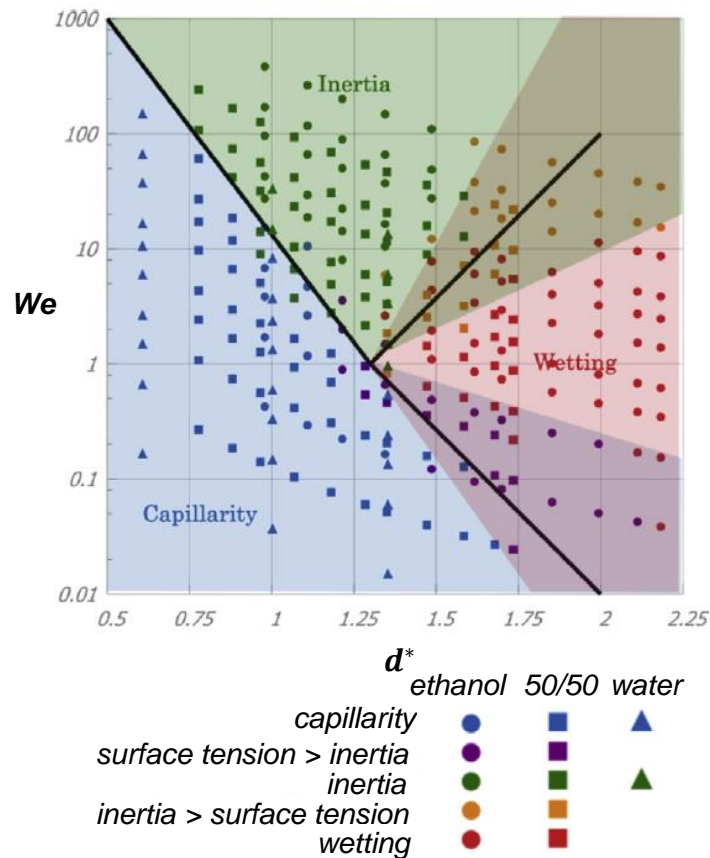


Figure II.10 – Cartography of the different flow regimes as a function of  $We$  and  $d^*$ , reproduced with permission from Dejean et al. (2020). Blue, green and red regions are respectively the capillary, inertial and wetting flow zones. Purple and orange represent intermediate zones.

## Chapter II. A nature-inspired liquid distributor

This figure summarizes experimental observations for 3 different liquids (ethanol, water and 50-50 ethanol-water mixture) at various flowrates and wire diameters.

$$We = \frac{\rho V_l}{\gamma d_w^3}; \quad d^* = \frac{d_w}{l_c} \quad (\text{II.8})$$

In eq. (II.8),  $\rho$  is the liquid density,  $V_l$  is the volumetric flowrate,  $\gamma$  is the surface tension and  $l_c$  is the capillarity length, defined as follows:

$$l_c = \sqrt{\frac{\gamma}{\rho g}} \quad (\text{II.9})$$

The wetting region in Figure II.10 corresponds to  $d^*$  and  $We$  in the following range:

$$d^* \geq 1.3 \quad (\text{II.10})$$

$$10^{-0.815(d^*-1.3)} \leq We \leq 10^{1.429(d^*-1.3)} \quad (\text{II.11})$$

### II.3.3 Tetra Spline packing

One of the packings used in the experiments to evaluate the performance of the novel liquid distributor was the Tetra Spline (TS) packing (Kawas et al., 2021), depicted in Figure II.11. This packing consists of a wire structure replicating the pattern in the left sketch in Figure II.11, with the mixture flowing outside the wires. The liquid is expected to flow along the surface of these wires, improving distribution and providing a large contact area for mass and heat exchange. Different from the tetrahedron unit depicted in Figure II.9, in this packing the wires are shaped as splines to improve the liquid repartition. Further, the layers alternate between regular and unregular tetrahedrons in order to prevent gas chimneys in the packing.

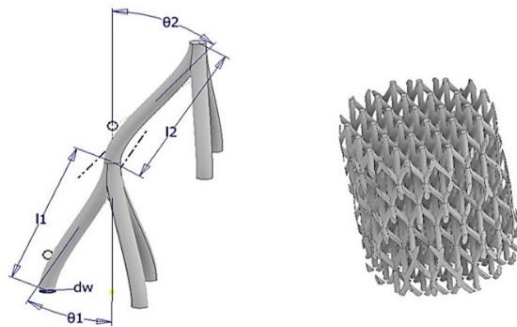


Figure II.11 – The TS packing, reproduced with permission from Kawas et al. (2021)

## Chapter II. A nature-inspired liquid distributor

The packed bed was fabricated via 3D-printing, using either polyamide or stainless steel as material. HETP experiments with this new packing were conducted by Kawas et al. (2021) using wire diameters ( $d_w$ ) in the range 0.5 mm – 2.75 mm, and specific surface area ( $A_g$ ) in the range 139 m<sup>2</sup>/m<sup>3</sup> – 387 m<sup>2</sup>/m<sup>3</sup>. Mellapak 250Y was used as reference packing for comparison.

Packing material was found to influence the efficiency of the column only for smaller wire diameters. At  $d_w = 1.5$  mm, the stainless-steel packing showed ~10% decrease in HETP compared to the polyamide packing. At  $d_w = 2.25$  mm, no significant difference was observed. Further, Kawas et al. (2021) found that larger wire diameters and specific surface areas result in lower HETP. The former is consistent with the results in Figure II.10 showing an improvement in liquid distribution over the tetrahedron structure when wire diameter is increased. The low HETP values obtained for high specific surface area are clearly due to the increase in mass/heat exchange area.

Overall, the packing efficiency of TS was found comparable to that of Mellapak 250Y. Many of the TS configurations performed better than the reference packing at low vapor flowrates (F-factor < 1 Pa<sup>1/2</sup>). Three of them outperformed Mellapak 250Y for all the vapor flowrates used in experiments, which correspond to F-factors between 0 and 2.5 Pa<sup>1/2</sup>. The values of  $d_w$  (mm), void fraction ( $\epsilon$ ) and  $A_g$  (m<sup>2</sup>/m<sup>3</sup>) for these best configurations were: (1.5, 0.89, 281); (2.25, 0.89, 182); (1.5; 0.92, 205). The two first configurations were printed using polyamide, whereas the third was printed using stainless steel.

For the evaluation of the nature-inspired liquid distributor in the next sections, some of the HETP experiments were done with a TS packed bed made of polyamide. Its configuration is characterized by  $d_w = 1.5$  mm, void fraction of 0.92 and a specific area of 205 m<sup>2</sup>/m<sup>3</sup>. The geometric features of this TS bed are summarized in Table II.1. The wire lengths and angles given in this table correspond to the features depicted on the left sketch in Figure II.11.

*Table II.1 - Geometric characteristics of the TS packing used for HETP experiments with the tree-shaped liquid distributors*

$l_1$ (mm)	$l_2$ (mm)	$\theta_1$ (°)	$\theta_2$ (°)	$d_w$ (mm)	$\epsilon$	$A_g$ (m <sup>2</sup> /m <sup>3</sup> )
12	12	30	40	1.5	0.92	205

### *II.3.4 Characterization of liquid distributor performance via HETP*

Liquid distributor performance can be evaluated through its impact on the HEPT value of a standard distillation column. Fractionation Research, Inc. suggests standardized methods to measure the HETP in packed columns. Measurements are preferably made when operating a column at total reflux to separate a binary mixture. Samples from the top and bottom liquid streams are taken, and their composition is used to calculate the number of theoretical plates. This calculation uses an iterative procedure where theoretical liquid composition for each stage (from top to bottom) is calculated via vapor-liquid equilibrium equations. Corresponding theoretical vapor compositions are determined by mass balance. The method uses the stream composition measured at the top of the column as the starting point. It then iterates from the top to the bottom until light key theoretical molar fraction becomes smaller than the molar fraction measured at the bottom. More details are available in Bessou et al. (2010).

In this work, experiments with different liquid distributors were conducted, using a packed distillation column to separate 35 kg of a mixture of cyclohexane (25 wt%) + heptane. This binary mixture is recommended by Fractionation Research Inc., and it has been previously used in the literature (Subawalla et al., 1997; Olujić et al., 2000). The setup is shown in Figure II.12. The column shell is made of glass, with inner diameter of 150 mm. A packed bed of 1 m height is placed in the column, just below the liquid distributor. Three different packings were used in the experiments: Mellapak 250Y, Pall Rings and the TS packing described in Section II.3.3.

This column operates at total reflux. Initially, a mixture of cyclohexane and heptane is placed in the thermosyphon reboiler. Reboiler duty (1 – 23 kW) is set by adjusting steam flowrate. As shown in Figure II.12, pressure drop is measured between the top and the bottom of the packings in order to manage the control valve (heat duty) via a pressure feedback and achieve a steady state. At the top, the condenser chosen for the experiment was a coil glass condenser, using cooling water at room temperature.

## Chapter II. A nature-inspired liquid distributor

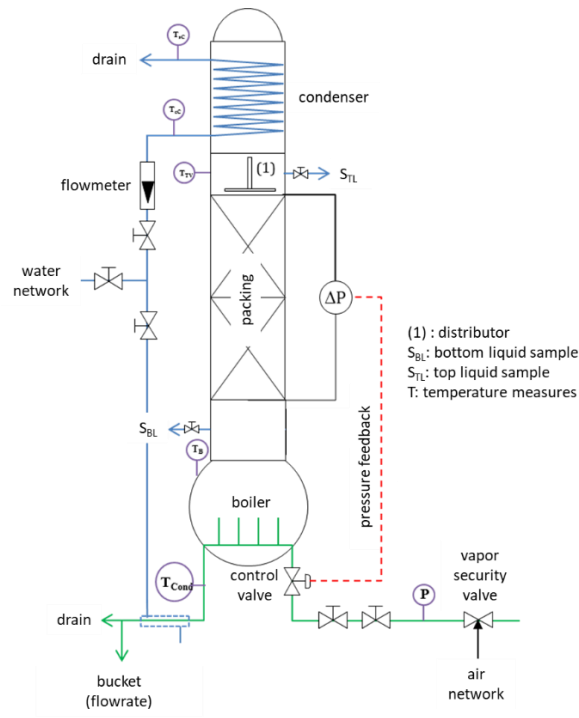


Figure II.12 – Experimental setup measuring separation efficiency for different distributors. Reproduced with permission from Kawas et al. (2021).

Liquid samples are taken from the top ( $S_{TL}$ ) and the bottom ( $S_{BL}$ ) of the column every 20 minutes. A capillary tube is placed on the bottom of the liquid distributor to ensure that only liquid is taken for the  $S_{TL}$  (without any traces of gas). For the  $S_{BL}$  liquid sample, a flange-gutter system is installed just below the packed bed. Steady state is considered to be achieved when three consecutive liquid samples have identical compositions. These compositions are measured via densitometry analysis, and they are later used to calculate HETP using the method described in Bessou et al. (2010).

For Pall Rings packing, 5 different distributors were tested using the setup described above: a perforated pipe distributor provided by Sulzer with 5 drip points, an orifice-pan distributor with 13 holes, and 3 different tree-like configurations (D1, D2, D3). The Mellapak 250Y and TS packings were used with only 3 distributors: Sulzer's perforated pipe distributor, the orifice-pan distributor, and tree-like distributor configuration D1.

The hole diameter is 2.7 mm for the orifice-pan distributor, and its design is very similar to the top plate in Figure II.6a. This orifice-pan distributor was designed using Inventor (Autodesk, 2019) and fabricated in the laboratory. For Sulzer's perforated pipe distributor, diameter is 3.2 mm for the central hole and 5.2 mm for the remaining 4 holes. The tree-like distributors were designed using Autodesk Inventor software (Autodesk,

2019), and fabricated using a 3D printer and polyamide (PA12) as material. Details for the configurations D1-D3 are shown later in Section II.4.

### II.4 Theoretical considerations for distributor design

Designing a distributor with a tree-like structure like the one shown in Figure II.6 requires careful analysis. The first step in this analysis is to define whether a new distributor will be designed from scratch, or if the tree-like structure will be used to retrofit an existing orifice distributor. In the former scenario, specifications for the top-plate depicted in Figure II.6a (such as hole diameter, number of holes and chimneys, etc.) can be chosen by the designer. In the latter scenario, the existing distributor is reused, and only the wire structures in Figure II.6d or Figure II.7 need to be fabricated.

The key design variables are: number of layers ( $N_l$ ),  $d_w$  (for each layer),  $l_w$ ,  $\theta$  and the number of ramifications at the end of each wire ( $N_r$ , 3 or 4). Note that, while the designer has the freedom to vary  $d_w$  with respect to the layer level,  $l_w$ ,  $\theta$  and  $N_r$  need to be kept constant. Indeed, if one of these 3 parameters is changed between consecutive layers, neighbour wires will no longer reconnect together to form the redundancies shown in Figure II.8. In the remaining of this section, configurations with  $N_r = 4$  are excluded. This design choice is made beforehand and justified by the experiments made by Dejean et al. (2020). Their results show that the tetrahedron with 3 ramifications in Figure II.9 sometimes can only split the upstream fluid into 2 streams, suggesting that a fourth child branch is probably superfluous.

Several constraints need to be accounted for in the design of a tree-shaped distributor. The first, most intuitive one is that the distributor should fit in the column. This constraint is easily incorporated in the design of orifice-pan distributors: it suffices to set a plate diameter inferior to the inner diameter of the column. However, it becomes a more complicated issue when designing a tree-shaped distributor. For example: can a distributor with 13 plate holes, 6 layers,  $d_w = 4$  mm,  $l_w = 10$  mm,  $\theta = 30^\circ$  and  $N_r = 3$  fit in a column with inner diameter of 150 mm? The answer depends on how the holes are arranged over the top plate.

As discussed in Section II.2, for  $N_r = 3$  each hole is followed by a tetrahedron such as the one depicted in Figure II.6d. The base of this pyramid is an equilateral triangle (see Figure II.6c and Figure II.14) whose length can be calculated as a function of  $N_l$ ,  $l_w$ ,  $\theta$

## Chapter II. A nature-inspired liquid distributor

and  $d_w$  of the last layer. This relation can be obtained through simple geometric considerations. First, one needs to calculate the length projected by a spline ( $l_w^{proj}$ ) on the cross-section of the column. This quantity is shown in Figure II.13, and it is given by:

$$l_w^{proj} = l_w \sin(\alpha) \quad (II.12)$$

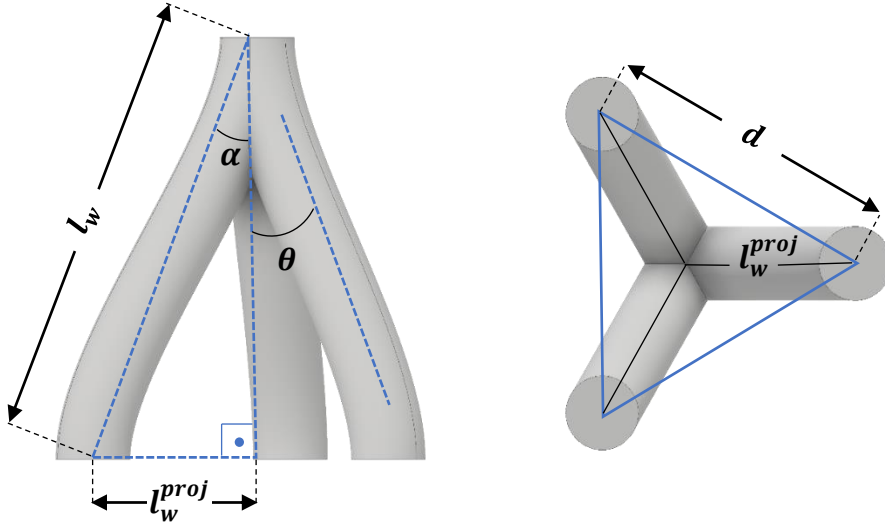


Figure II.13 – The length of a spline projected on the cross-section ( $l_w^{proj}$ ) and the distance  $d$  between two neighbour outlets

Knowing  $l_w^{proj}$ , the distance  $d$  between two consecutive outlets (see right sketch in Figure II.13) can be calculated:

$$d = l_w^{proj} \sqrt{3} \quad (II.13)$$

Figure II.14 depicts the triangles formed by the base of pyramids with different number of layers. The length of these solid blue edges is proportional to  $N_l$ , and given by:

$$L_{\Delta} = N_l d \quad (II.14)$$

Lastly, one can correct eq. (II.14) and account for the extra space occupied by the outlets on the edges (the dashed blue segments in Figure II.14). The length of these dashed edges is given by:

$$L'_{\Delta} = L_{\Delta} + d_w \sqrt{3} \quad (II.15)$$

Putting eqs. (II.12)-(II.14) into eq. (II.15) yields:

$$L'_{\Delta} = \sqrt{3}(N_l l_w \sin(\alpha) + d_w) \quad (II.16)$$



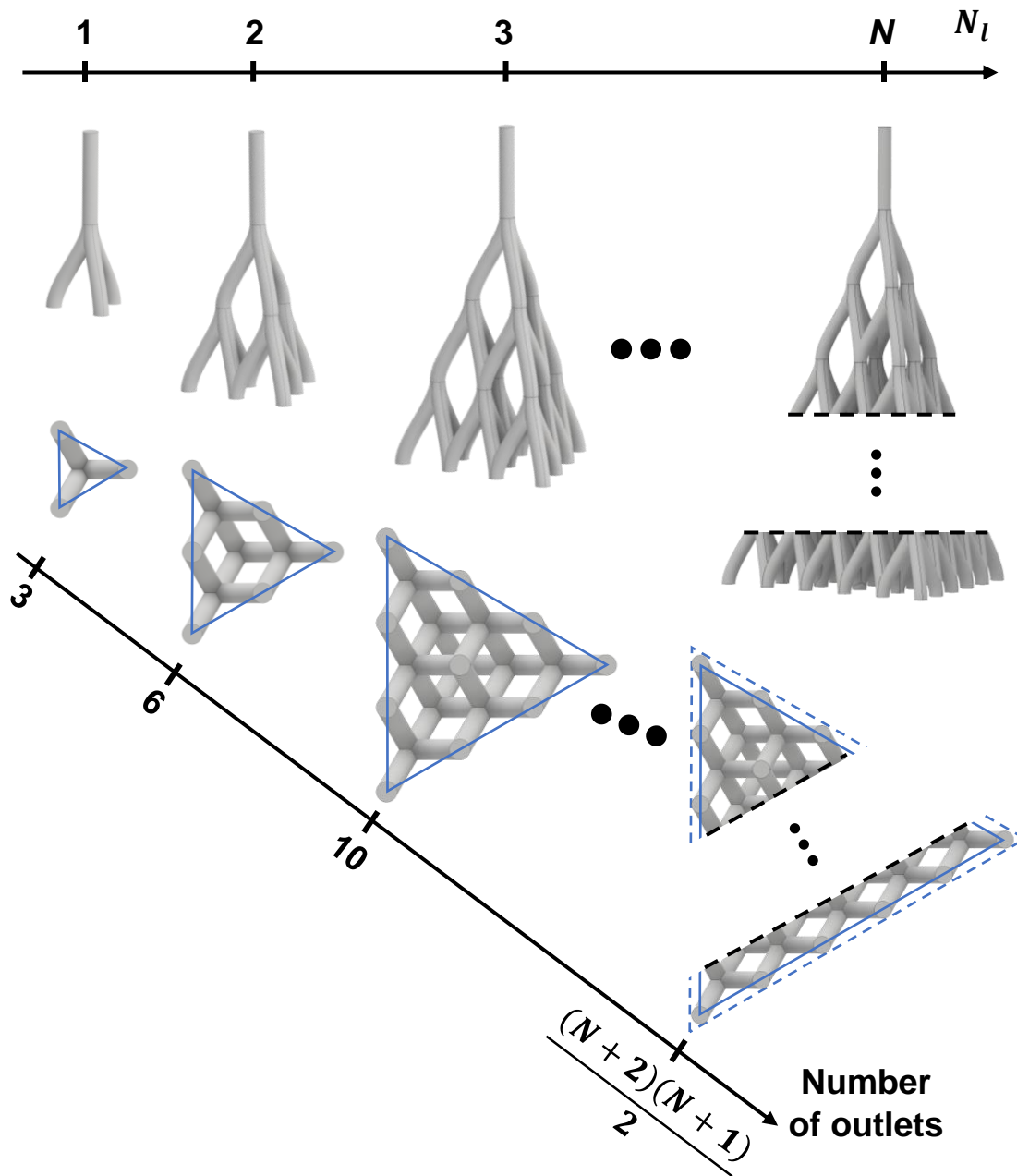


Figure II.14 – Triangles projected by a pyramid on the cross-section as the number of layers ( $N_l$ ) increases

Here it is important to point out that the angle  $\alpha$  depicted in Figure II.13 is not equivalent to the spline angle  $\theta$  shown in Figure II.11 and Figure II.13. Indeed,  $\alpha$  is the angle between the vertical axis and the segment connecting both ends of the spline, whereas  $\theta$  is the inclination of the spline (with respect to the vertical) on its middle point. The relation between  $\alpha$  and  $\theta$  can be obtained using the law of sines:

## Chapter II. A nature-inspired liquid distributor

$$\alpha = \theta - \arcsin \left[ \frac{\sin(\theta)}{4} \right] \quad (\text{II.17})$$

Eqs. (II.16) and (II.17) together give the length of the triangle occupied by the base of the pyramid as a function of the design variables  $N_l, l_w, \theta$  and  $d_w$ . Recalling the problem mentioned earlier in this section, we wish to know if a distributor with 13 plate holes, 6 layers,  $d_w = 4$  mm,  $l_w = 10$  mm,  $\theta = 30^\circ$  and  $N_r = 3$  can fit in a column with inner diameter of 150 mm. Using eqs. (II.16) and (II.17), the length of the triangles each pyramid projects on the cross-section is  $L'_\Delta = 47.2$  mm. The question now comes down to whether 13 of such triangles can fit in a circle of diameter 150 mm without overlapping.

This question is a particular case of a larger class of optimization problems known as the packing problems. Much of the densest known packings of equilateral triangles inside a circle can be found in the website WolframAlpha (Wolfram|Alpha, 2020), as well as in a private webpage on Github (Friedman, 2021). Some of these packings are regular and some are unregular, depending on how many triangles one tries to fit inside the circle. Figure II.15 shows 2 regular (with 6 and 13 triangles), and 2 unregular packings (with 3 and 10 triangles). Configurations with regular packings are more suitable for liquid distribution for many reasons. First, the distribution of plate holes, which coincides with the barycentres of the triangles, is easier to implement for regular geometries. Second, liquid distribution is more homogeneous. Finally, when the number of triangles is large ( $\geq 13$ ), many of the edges in the packing are coincident (see the packing with 13 triangles in Figure II.15). That enables the outlets from different pyramids to reconnect, which can save some space in the column. Table II.2 summarizes the length of the triangles for 8 known regular packings, using units of circle radius. From this table, the maximum side length of 13 triangles in a circle of diameter 150 mm is 49.1 mm. And since  $L'_\Delta = 47.2$  mm  $<$  49.1 mm, the distributor mentioned in the previous paragraph can fit in the column.

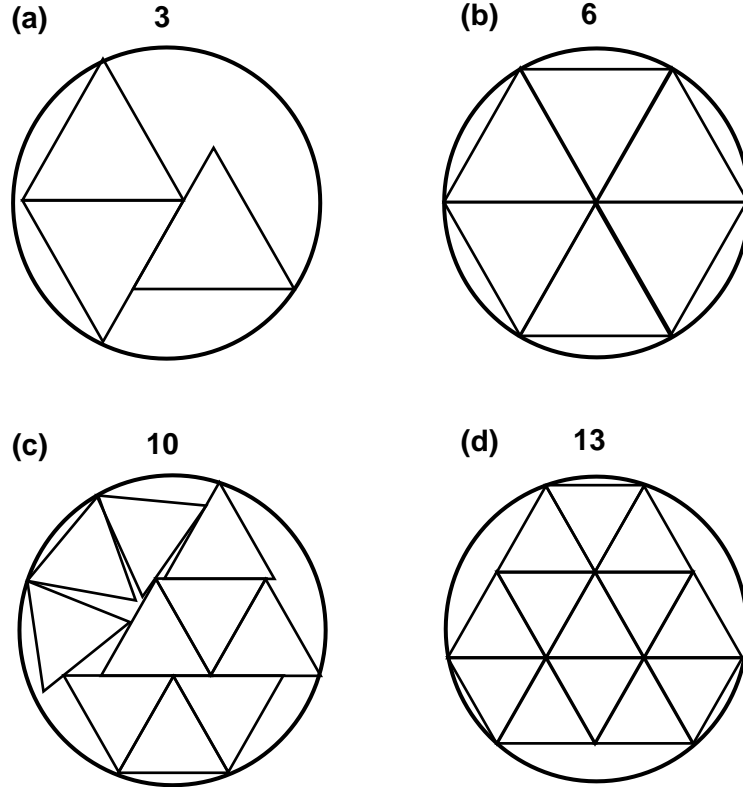


Figure II.15 – Densest known packings for 3, 6, 10 and 13 equilateral triangles in a circle ( Wolfram|Alpha, 2020; Friedman, 2021)

Table II.2 – Side of the equilateral triangles for 8 regular packings (Friedman, 2021; Wolfram|Alpha, 2020)

triangles	1	2	6	7	13	18	20	24
side ( $\times R$ )	$\sqrt{3}$	$2/\sqrt{3}$	1	$2 \sin\left(\frac{\pi}{7}\right)$	$\sqrt{3/7}$	$\sqrt{2/13}$	0.533	0.5

Until this point in the section, most of the discussion was focused on the constraint *the distributor has to fit in the column*. A second noteworthy geometric constraint is on the maximum wire diameter. If wire diameter is too large, the outlets of the 3 ramifications in Figure II.13 may overlap. To avoid this, the following constraint must be considered:

$$d_w < d \tag{II.18}$$

Here the term  $d$  corresponds to the distance shown in Figure II.13, and it can be calculated in terms of  $l_w$  and  $\theta$  with the help of eqs. (II.12), (II.13) and (II.17).

One can write another constraint for the maximum wire diameter involving  $l_w$  and  $\theta$ . The wires are conceived extruding a circular shape along a spline. Therefore, the radius of the

## Chapter II. A nature-inspired liquid distributor

wire cannot exceed the minimum radius of curvature ( $r_c$ ) of the spline. Figure II.16 shows this constraint. The dimensions on the bottom image are shown in mm.

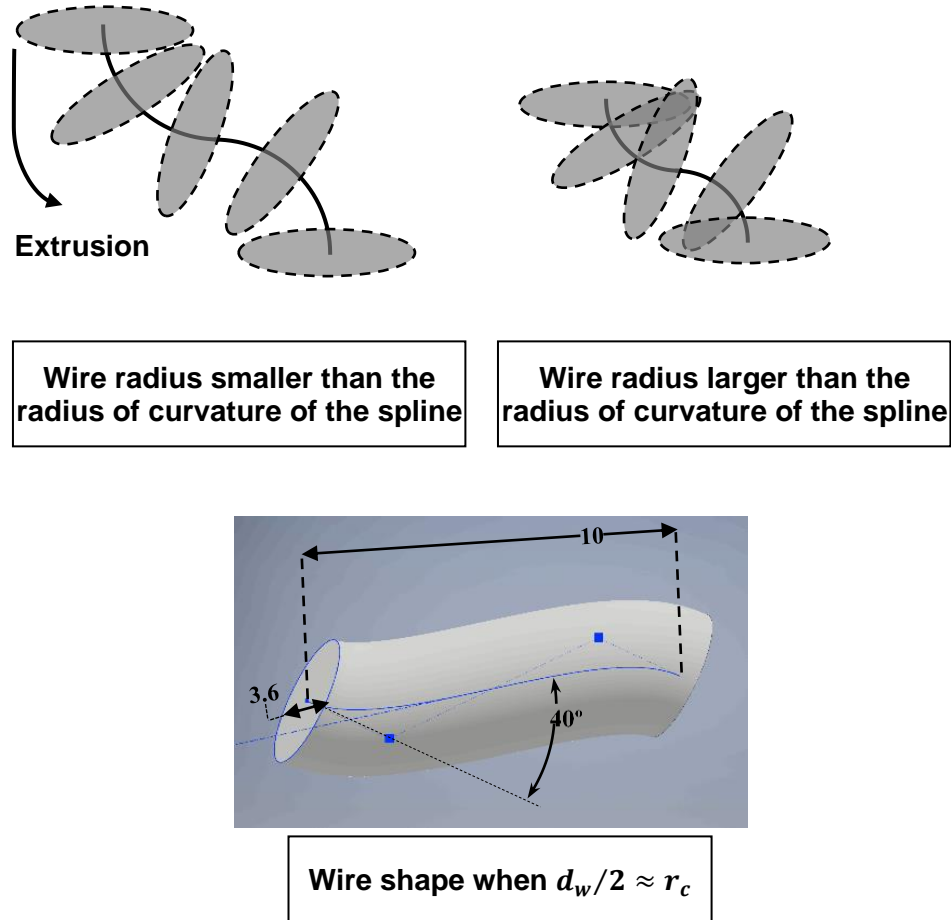


Figure II.16 – Constraint on the wire diameter ( $d_w/2 < r_c$ )

The splines used to generate a wire are curves interpolated from the end points and controlled by 2 vertexes, shown as blue squares in the bottom image of Figure II.16. Inventor software does not disclose the exact interpolation equation it uses for the spline, so  $r_c$  cannot be derived analytically from the equation of the curve. However, the software provides the radius of curvature of the spline at any given position. This radius of curvature is minimal at the end points, and fitting by trial-and-error lead to the following relation:

$$r_c = \frac{3l_w}{32 \sin(\alpha)} \quad (\text{II.19})$$

## Chapter II. A nature-inspired liquid distributor

The fourth and final geometric constraint regards the height of the distributor, defined as the distance between the base of the tree-structure and the bottom of the plate above. Its maximum height depends on the allowance in the column, so the designer is free to set this constraint accordingly. In the design of D1 – D3, the distributors that were printed and used in the experiments, it was imposed that their heights should not exceed 200 mm.

In addition to constraints imposed by the geometry of the equipment, some constraints are imposed to ensure reasonable liquid distribution over the wires. Wire length is restricted to the interval  $10 \text{ mm} \leq l_w \leq 20 \text{ mm}$ . The lower wire length limit prevents the formation of a membrane englobing multiple wires, as mentioned in Section II.3.2, whereas the upper limit prevents the appearance of the instabilities mentioned in Section II.3.1. Further, spline angle is constrained to  $30^\circ \leq \theta \leq 40^\circ$ . Here again, the lower limit prevents formation of liquid membranes englobing multiple wires, whereas the upper limit prevents liquid detachment from the wires (see Section II.3.2).

Finally, a third performance constraint relates to the position of each layer with respect to the mapping shown in Figure II.10. The average flow per wire in a certain level can be calculated dividing the downwards liquid flow by the number of wires in this layer. This number is not the same as the number of outlets; some outlets are common to 2 or 3 wires, as shown in Figure II.14. Instead, for  $N_r = 3$ , the number of wires in a level is equal to 3 times the number of outlets from the previous level, since every outlet splits into 3 children in the subsequent layer.

Knowing the number of wires and the wire diameter per layer, one can assign a certain position on the mapping shown in Figure II.10 to each level of the distributor. Preferably, the distributor should be designed so that all these positions are within wetting flow regime. Table II.3 summarizes the main constraints to be considered during the design of a tree-like liquid distributor.

Table II.3 – Summary of constraints considered for liquid distributor design

Type of constraint	Constraint	Variables implied
Geometric	Distributor has to fit in the column	$N_l, l_w, \theta, d_w$
	Outlets of ramifications cannot overlap	$l_w, \theta, d_w$
	Wire radius < spline’s radius of curvature	$l_w, \theta, d_w$
	Distributor height < allowance	$N_l, l_w, \theta$
Performance	$10\text{mm} \leq l_w \leq 20\text{mm}$	$l_w$
	$30^\circ \leq \theta \leq 40^\circ$	$\theta$
	Flow regime is preferably wetting	$N_l, d_w$

All the aforementioned design considerations were implemented in an Excel file, whose goal is to facilitate the design and screening of performant configurations. The logic steps for the Excel calculations are illustrated in the diagram chart in Figure II.17.

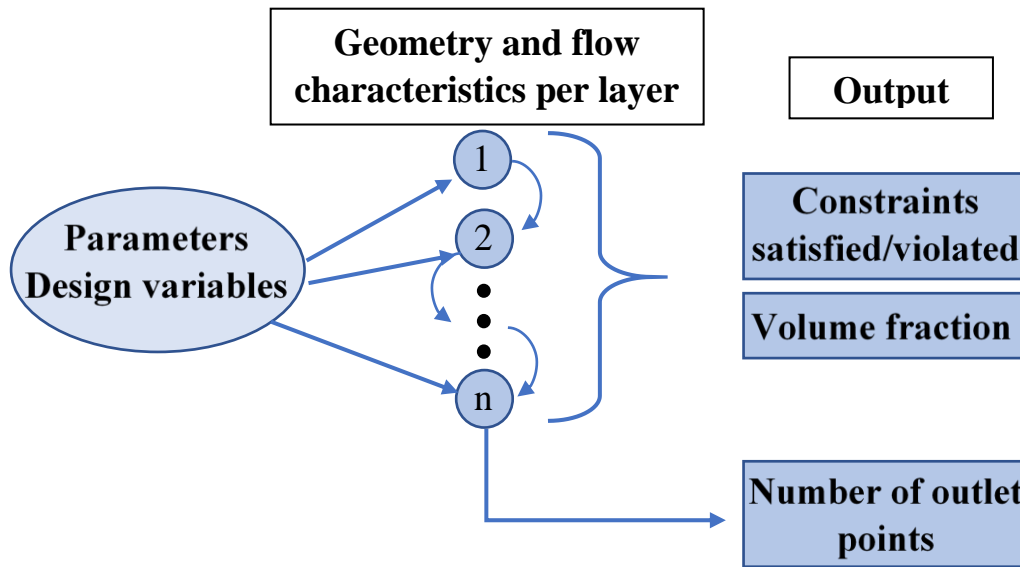


Figure II.17 – Diagram chart illustrating how the Excel auxiliary tool works

Column diameter, number of initial irrigation points, total liquid flow and mixture parameters are given by the user. Further, the user chooses to provide either the exact values of the design variables ( $d_w, l_w, \theta, N_l$ ) or their range. In the latter case, the spreadsheet performs a feasibility analysis to find combinations of values yielding proper configurations. For a given combination of decision variable values, the design tool calculates the geometric features (number of wires, height,  $L'_\Delta$ ) and flow characteristics ( $\delta$ , average flowrate and We per wire) on each layer.

## Chapter II. A nature-inspired liquid distributor

The results are used to check which constraints (according to Table II.3) are satisfied/violated. The remaining outputs are the final number of outlet points and the volume fraction occupied by the wire structures. The former is calculated according to the formula in Figure II.14, whereas the occupancy is estimated using the total number of wires in the structure and eq. (II.20) for the volume of a single wire. This volume,  $V_w$ , is the product of the cross-section of the wire and the length of the spline, whose formula was obtained via a linear fit.

$$V_w = \frac{\pi d_w^2}{4} \left( 1.073 - 0.073 \cos(\theta) \right) l_w \quad (\text{II.20})$$

Note that this procedure overestimates the volume fraction occupied by the distributor in the column, since it neglects wire intersections such as the one on the top of the structure in Figure II.13. Finally, screenshots of the Excel design tool developed in this study are shown in Appendix B, along with more details regarding its mode of operation.

Considering the design aspects discussed so far, and with the help of the design tool mentioned above, 3 distributor configurations (D1 – D3) were selected for experimental investigation. Figure II.18 illustrates these configurations, and their geometric features are given in Table II.4.

*Table II.4 – Characteristics of the tree-like distributors used in experiments*

	<b>D1</b>	<b>D2</b>	<b>D3</b>
No. of holes	13	13	13
Hole diameter (mm)	6.0	6.0	6.8
$N_l$	6	6	6
$d_w$ (mm)	[2.5, 2.5, 2.5, 2.25, 2.0, 1.75, 1.5]	[2.5, 2.5, 2.5, 2.25, 2.0, 1.75, 1.5]	[4.0, 4.0, 4.0, 4.0, 4.0, 4.0, 4.0]
$l_w$ (mm)	12	10	10
$\theta$ (°)	30	36.2	36.2
Distributor height (mm)	71.4	64.7	64.7

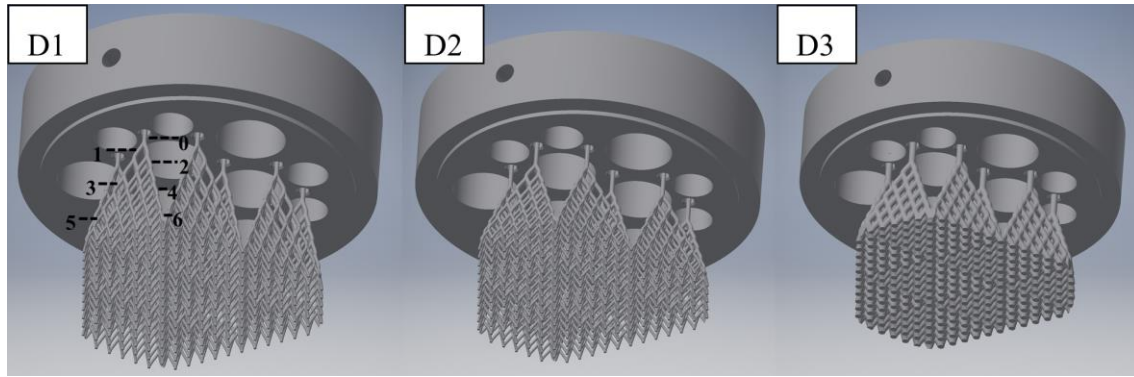


Figure II.18 – Different designs of liquid distributors used in experiments

In Table II.4, the number of holes correspond to the number of plate holes from which the pyramid structures stem. The branching levels  $N_l$  correspond to the number of times the distributor splits. Each level is located at a certain height, and they are numerated in Figure II.18 for D1. The 0th level just below the plate is the part of the distributor containing only vertical wires. Values for  $d_w$  in Table II.4 are the wire diameters in order from the 0th to the 6th branching level. Terms  $l_w$  and  $\theta$  are the length and inclination of the wires. Further, the distributor height is measured from the bottom part of the plate until the base of the last branching level. Note that the pyramids stemming from the plate holes are not completely separate from one another. Instead, D1 – D3 were designed so that the outlets of neighbour pyramids reconnect on the base of the structure. This can be achieved by placing the plate holes on the barycentres of the triangles shown in Figure II.15d, and carefully choosing a combination of  $\theta$  and  $l_w$ . If the distributor is designed in this way, the overlapping edges of the triangles in Figure II.15d will correspond to the positions where the outlets from different pyramids reconnect.

The configuration D1 was conceived at an early stage of this work, and its design does not cope with the last constraint given in Table II.3 (the wetting regime constraint). Configuration D2 replicates the wire diameters and the number of layers in D1, but with smaller  $l_w$  and larger  $\theta$ . It was conceived to have a minimum height while performing similarly to D1. Finally, configuration D3 is conceived with the same height as D2, but with different wire diameter in order to improve performance. Figure II.19 maps the flow regime on the layers of D1, D2 and D3. The data shown in this figure are theoretical predictions obtained when replacing  $V_l$  in eq. (II.8) by the average flow per wire on each layer. Further, the fluid considered in this mapping is a mixture of n-cyclohexane + heptane, which is used later for experiments.



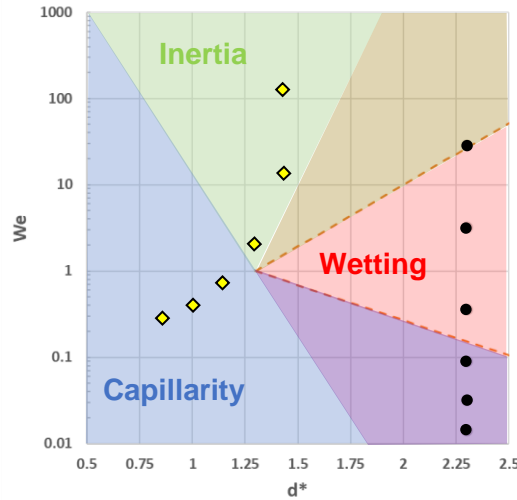


Figure II.19 – Predicted flow regime in each layer for D1, D2 (yellow diamonds with black contour) and D3 (black circles), considering the binary mixture *n*-cyclohexane + heptane; Weber number decreases as layer levels increase

The remaining design considerations are the drip point density and the indexes  $D_Q$  and  $M_f$  mentioned in Section II.1.3. Distributors D1 – D3 have a theoretical drip point density of  $\sim 14800$  pts/m<sup>2</sup>. This density is considerably larger than the 736 pts/m<sup>2</sup> provided by the 13 primary irrigation holes on the top-plate. However, whereas the top plate distributes the flow evenly among its 13 holes, distribution over the 262 outlets at the base of the distributor (Figure II.6c) is uneven.

To see how liquid is distributed at the base of a tree-like distributor, let us first focus on how a single pyramid (Figure II.6d) splits the flow coming from one of the 13 holes. At the base of a 6-layer pyramid, there are in total 28 outlets (see the formula in Figure II.14). If we assume that flow is evenly partitioned over the 3 children branches of every wire, a total flow of  $3^6 = 729$  would be distributed over the 28 outlets according to Figure II.20.

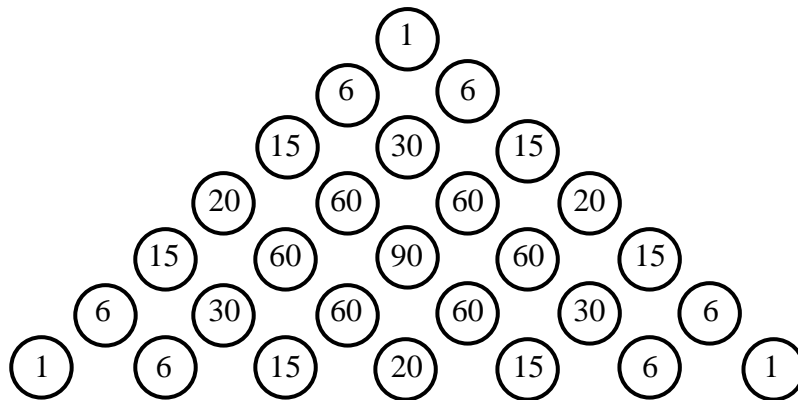


Figure II.20 – Total liquid flow of 729 distributed over the 28 outlets of a 6-layer pyramid

## Chapter II. A nature-inspired liquid distributor

Readers familiar with combinatorics will quickly recognize the values on the edges of the triangle shown in Figure II.20 as the binomial coefficients of the 6th power. A more careful analysis shows that the Pascal's triangle is retrieved if we divide each row by its lead coefficient (i.e., divide first row by 1, second row by 6, third row by 15, and so on). This pattern can be generalized for a pyramid with  $n$  layers and a flow of  $3^n$  by induction.

**Theorem.** *If liquid is split into 3 identical parts over all junctions of a pyramid with  $N$  layers, then for a total inlet flow of  $V_l$  the flow on each of the outlets obeys the following relation:*

$$\frac{V_l^{i,j}}{V_l} = \frac{C_i^N \times C_j^i}{3^N} \quad (\text{II.21})$$

where  $V_l$  is the total liquid flowrate through the pyramid,  $0 \leq i \leq N$  is row index of the outlet,  $0 \leq j \leq i$  is the column index of the outlet, and  $C_a^b$  are binomial coefficients:  $C_a^b = \binom{b}{a} = \frac{b!}{a!(b-a)!}$ .

Remark. Before proving this theorem, let us clarify its statement. In eq. (II.21),  $i$  refers to the position of the outlet along the rows (from top to bottom), and  $j$  is its position along the columns (from left to right). Outlets are depicted in Figure II.20 for  $N = 6$ . The position  $(i, j) = (0,0)$  corresponds to the top outlet with a flow  $V_l^{0,0} = 1$ . The position  $(4,1)$  corresponds to the fifth row and second column, for which  $V_l^{4,1} = 60$ . The reader can obtain the results shown in Figure II.20 for any position  $(i,j)$  with the help of eq. (II.21), after setting  $V_l = 729$  and  $N = 6$ .

*Proof.* The first step is to show that the theorem is valid for  $N = 1$ . That is indeed the case; for 1 layer, there are only 3 outlets as depicted by the left structure in Figure II.14. If the liquid is identically partitioned between the 3 ramifications, then the flow on each outlet is  $V_l^{i,j} = V_l/3$ . This is in agreement with eq. (II.21), since  $C_0^0 = C_0^1 = C_1^1 = 1$ .

Now, let us assume that eq. (II.21) is valid for an arbitrary number of layers  $N$ , and attempt to demonstrate its validity for  $N + 1$  layers. Without loss of generality, we shall assume the total flow to be  $V_l = 3^{N+1}$ . The flowrates on the outlets of the  $N$ -layers pyramid would then be given by  $V_{l,N}^{i,j} = 3C_i^N \times C_j^i$ , where the second subscript in the left-hand side indicates the number of layers. If an extra layer is added to this pyramid, the flow will be further partitioned according to the illustration in Figure II.21.

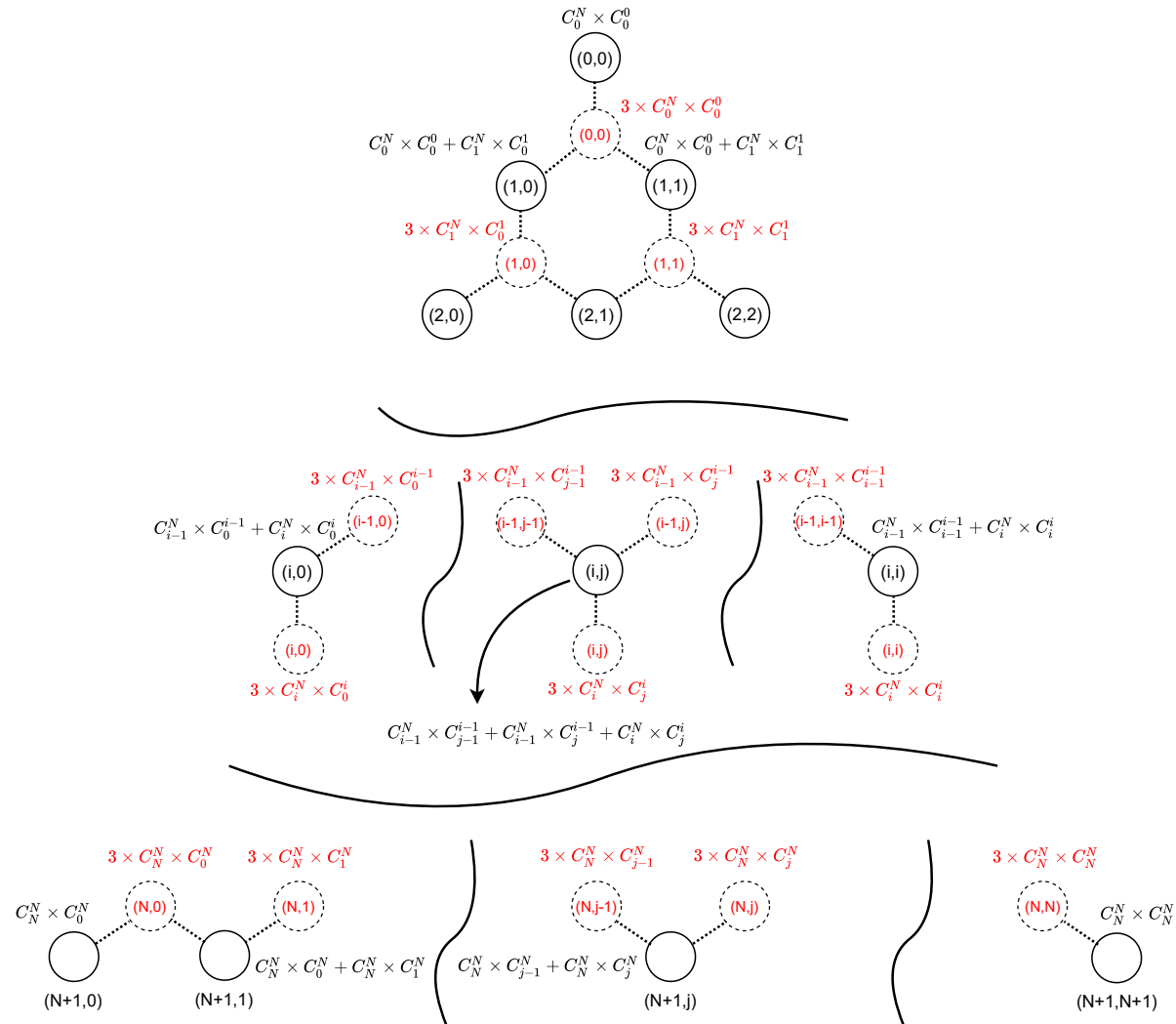


Figure II.21 – Flow partition from the outlets of a  $N$ -layer pyramid (dashed circles) after addition of an extra layer (solid circles)

## Chapter II. A nature-inspired liquid distributor

The outflow on the vertexes  $(0,0)$ ,  $(N+1,0)$ ,  $(N+1,N+1)$  are given by:

$$V_{l,N+1}^{0,0} = C_0^N \times C_0^0 = 1 \Rightarrow V_{l,N+1}^{0,0} = C_0^{N+1} \times C_0^0 \quad (T1)$$

$$V_{l,N+1}^{N+1,0} = C_N^N \times C_0^N = 1 \Rightarrow V_{l,N+1}^{N+1,0} = C_{N+1}^{N+1} \times C_0^{N+1} \quad (T2)$$

$$V_{l,N+1}^{N+1,N+1} = C_N^N \times C_N^N = 1 \Rightarrow V_{l,N+1}^{N+1,N+1} = C_{N+1}^{N+1} \times C_{N+1}^{N+1} \quad (T3)$$

The three equations above are in agreement with eq. (II.21) for  $N + 1$  layers and  $V_l = 3^{N+1}$ . Now, for an arbitrary outlet on one of the 3 edges:

$$\begin{aligned} V_{l,N+1}^{i,0} &= C_{i-1}^N \times C_0^{i-1} + C_i^N \times C_0^i = C_{i-1}^N + C_i^N = \frac{N!}{(i-1)!(N-i+1)!} + \frac{N!}{i!(N-i)!} \Rightarrow \\ &\Rightarrow V_{l,N+1}^{i,0} = \frac{N!i}{i!(N-i+1)!} + \frac{N!(N-i+1)}{i!(N-i+1)!} = \frac{(N+1)!}{i!(N+1-i)!} \times 1 \Rightarrow \\ &\Rightarrow V_{l,N+1}^{i,0} = C_i^{N+1} \times C_0^i \end{aligned} \quad (T4)$$

$$\begin{aligned} V_{l,N+1}^{i,i} &= C_{i-1}^N \times C_{i-1}^{i-1} + C_i^N \times C_i^i = C_{i-1}^N + C_i^N = \frac{(N+1)!}{i!(N+1-i)!} \times 1 \Rightarrow \\ &\Rightarrow V_{l,N+1}^{i,i} = C_i^{N+1} \times C_i^i \end{aligned} \quad (T5)$$

$$\begin{aligned} V_{l,N+1}^{N+1,j} &= C_N^N \times C_{j-1}^N + C_N^N \times C_j^N = C_{j-1}^N + C_j^N = 1 \times \frac{(N+1)!}{j!(N+1-j)!} \Rightarrow \\ &\Rightarrow V_{l,N+1}^{N+1,j} = C_{N+1}^{N+1} \times C_j^{N+1} \end{aligned} \quad (T6)$$

Eqs. (T4)–(T6) are also in agreement with eq. (II.21) for  $N + 1$  layers and  $V_l = 3^{N+1}$ . The remaining step to complete this proof is to show that an arbitrary interior outlet  $(i, j)$  also obeys eq. (II.21). According to Figure II.21, the flow on this outlet is given by:

$$\begin{aligned} V_{l,N+1}^{i,j} &= C_{i-1}^N \times C_{j-1}^{i-1} + C_{i-1}^N \times C_j^{i-1} + C_i^N \times C_j^i = \\ &= \frac{N!}{(i-1)!(N-i+1)!} \frac{(i-1)!}{(j-1)!(i-j)!} + \frac{N!}{(i-1)!(N-i+1)!} \frac{(i-1)!}{j!(i-1-j)!} + \frac{N!}{i!(N-i)!} \frac{i!}{j!(i-j)!} = \\ &= \frac{N!}{(N-i+1)!} \frac{1}{(j-1)!(i-j)!} + \frac{N!}{(N-i+1)!} \frac{1}{j!(i-1-j)!} + \frac{N!}{(N-i)!} \frac{1}{j!(i-j)!} = \\ &= \frac{N!}{(N-i+1)!} \frac{j}{j!(i-j)!} + \frac{N!}{(N-i+1)!} \frac{(i-j)}{j!(i-j)!} + \frac{N!}{(N-i+1)!} \frac{(N-i+1)}{j!(i-j)!} \end{aligned}$$

Simplifying the above expression yields:

$$V_{l,N+1}^{i,j} = \frac{N!}{(N-i+1)!} \frac{(N+1)}{j!(i-j)!} = \frac{(N+1)!}{(N+1-i)!} \frac{1}{j!(i-j)!} = \frac{(N+1)!}{i!(N+1-i)!} \frac{i!}{j!(i-j)!}$$

Hence:

$$V_{l,N+1}^{i,j} = C_i^{N+1} \times C_j^i \quad (\text{T7})$$

*Q.E.D.*

Qualitatively, Figure II.20 and eq. (II.21) show that irrigation is lower near the edges and vertices of the triangles depicted in Figure II.14, growing near their barycenters. Visual observations corroborate this conclusion. However, despite this non-uniform distribution, one should still expect the quality of liquid distribution to be improved when the wire structure is added to the orifice-pan distributor. This can be verified by calculating the distribution quality indicators  $D_Q$  and  $M_f$  discussed in Section II.1.3.

Theoretical  $M_f$  is obtained from eq. (II.5), dividing the cross-section in 21 imaginary collection zones identical to the ones shown in Lämmermann et al. (2016) (see Figure II.22). Instead of using experiments to measure the flowrate through each zone, these are calculated by analysing how the outlets are distributed over the different zones. For the simpler orifice-pan configuration with 13 holes, it is assumed that flow is evenly partitioned among the outlets. For the more complex tree-like structure, Figure II.20 is used to estimate the outlet flow on each of the 262 dripping points. Further, because the orientation of the imaginary collector affects the distribution of the outlet points over the zones,  $M_f$  values are averaged using 5 random collector orientations.

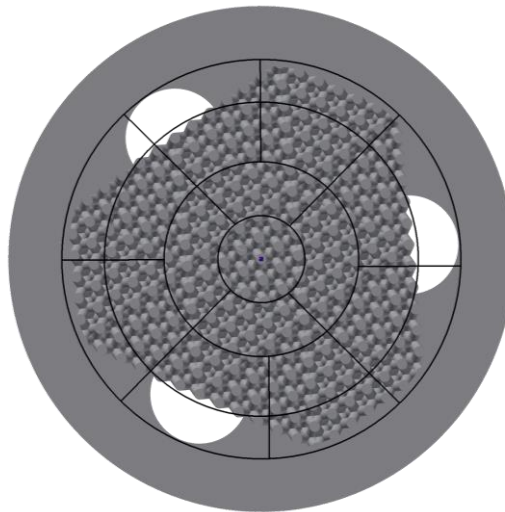


Figure II.22 – D3 outlets and imaginary collection zones used to calculate  $M_f$

## Chapter II. A nature-inspired liquid distributor

Because D1, D2 and D3 have the same number of layers and a similar outlet structure, the theoretical  $M_f$  value is the same for all of them. It varies between 0.135 and 0.137 according to the orientation of the collector, with an average  $M_f = 0.136$ . This is a significant improvement compared to  $M_f = 0.236$  for the orifice-pan distributor. For comparison, Sulzer's perforated pipe distributor with 5 irrigation points has a theoretical maldistribution factor  $M_f = 0.421$ .

Analogously, one should expect an increase in the distribution quality index  $D_Q$  when the number of outlets is increased from 13 to 262. Nevertheless, the opposite happens:  $D_Q$  decreases from 0.40 (orifice-pan) to 0.27 (D1 – D3). This is likely due to the inconsistencies in the index that appear when the outlet points are very close to each other, as explained in Section II.1.3.

A last theoretical aspect important for this nature-inspired distributor is scalability. As mentioned in Section I.2, tree structures generally facilitate scaling, which is remarkably useful in chemical engineering. However, scaling up the distributor described in Section II.2 is not straightforward. Let us assume a fixed liquid flux (flow per column cross-section area) for two columns with different sizes. The larger column experiences a larger liquid flow, as the fluxes are equal for these two columns. If the number of initial irrigation points is the same, maintaining the same quality of distribution would imply increasing the number of branching generations  $N_l$  in the larger column. However, this could result in a distributor whose height is larger than the maximum allowance (see Table II.3). Further, the wires in the last layers of the distributor, which experience the smallest flows, are more likely to be in the capillarity flow zone (Figure II.10). This could affect the quality of the distribution in the larger column. That does not mean the distributor presented in this Chapter is not scalable; rather, it means scaling up should be done carefully, considering all the constraints in Table II.3. One alternative to facilitate the scaling up is to increase the number of initial irrigation points. Doing so would decrease the number of branching levels necessary for the larger column, avoiding the allowance and the flow regime issues.

## II.5 Experimental results and discussion

### II.5.1 Industrial packings

Experiments to measure HETP and pressure drop were performed according to the procedure described in Section II.3.4. Five different types of distributors (D1 – D3, orifice-pan with 13 irrigation points, and Sulzer’s distributor with 5 irrigation points) were compared in a column packed with Pall rings. Figure II.23 shows the results obtained from these tests.

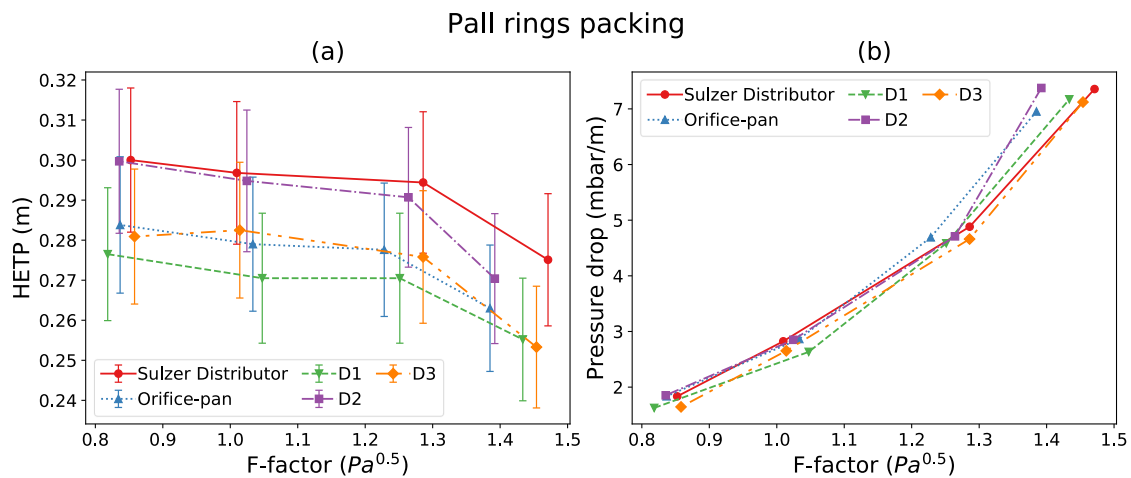


Figure II.23 – HETP (a) and pressure drop (b) vs  $F$ -factor for 5 different distributors, using Pall rings packing and the test rig described in Section II.3.4

The relative error for all HETP measures is estimated around 6%. One source of error is the densitometry accuracy of  $\pm 0.001 \text{ g/cm}^3$ . The second one are deviations in molar fraction in the Wilson activity coefficient model (mean deviation of  $\pm 0.0008$ ; maximum deviation of  $\pm 0.0025$ ) used for vapor-liquid equilibrium computations in the HETP calculation procedure described in the beginning of Section II.3.4. Figure II.23a shows that column efficiency is approximately the same for all liquid distributors. The reason is that the lowest drip point density ( $283 \text{ pts/m}^2$  for Sulzer’s distributor) is already too high. Indeed, it has been shown that densities beyond  $100 \text{ pts/m}^2$  do not bring significant improvement in industrial packing efficiency (Kister, 1990; Kister et al., 2008).

Differences in pressure drop are negligible comparing the 5 distributors, as depicted in Figure II.23b. This is because the main source of energy loss is friction against the packing. Although some distributors are bulkier than others (see for example D3 in Figure

II.18), their height is only 7% the length of the packed bed. Besides, the pressure above the packed bed is measured just below the distributor plate, so the only parts of the distributors that are considered in pressure drop measurements are the tree-like wire structures.

Experiments using Mellapak 250Y bed confirm that the tree-like distributors do not decrease HETP of industrial packings (see Figure II.24). This result does not imply that distribution itself is not improved: as shown in Section II.4, theoretical maldistribution factor is decreased from 0.236 to 0.136 with the addition of the trees to an orifice-pan distributor with 13 points. However, such an improvement is not reflected in a better distillation performance when Pall rings or Mellapak 250Y are employed.

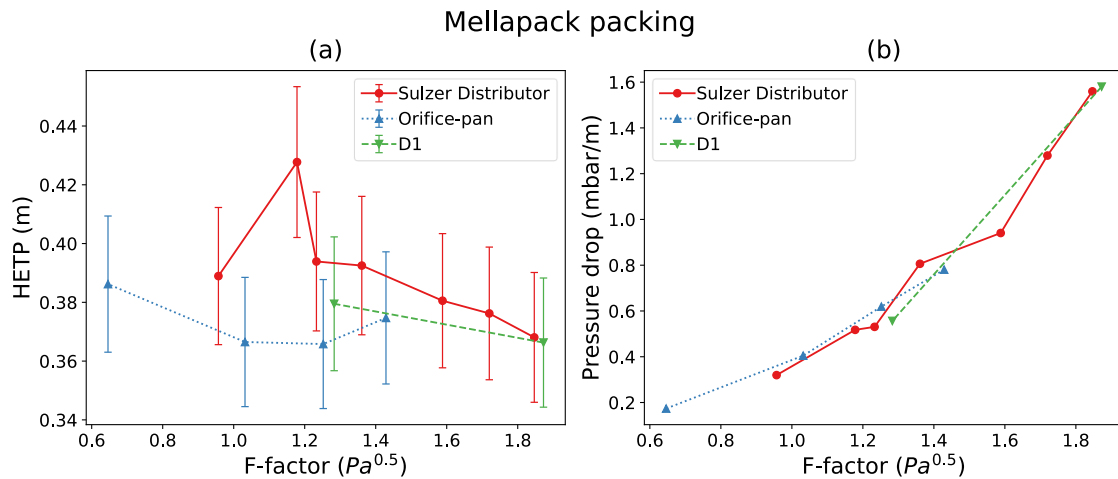


Figure II.24 – HETP (a) and pressure drop (b) vs F-factor for 3 different distributors, using Mellapak 250Y packing and the test rig described in Section II.3.4

Other applications possibly more sensitive to liquid maldistribution, such as multiphase reactions and chemical absorption, could benefit from this improvement. In addition, the next section shows that the tree distributors are capable of reducing HETP when coupled with the TS structured packing (Kawas et al., 2021).

### II.5.2 Tetra Spline packing

Distillation performance was also assessed for different liquid distributors using the Tetra Spline (TS) packing described in Section II.3.3. Three different liquid distributors were used for experiments: the orifice-pan type with 13 irrigation points, Sulzer’s distributor with 5 irrigation points, and the tree-shaped distributor D1 with 262 irrigation points. The latter was printed together with the packing itself. The results are shown in Figure II.25.



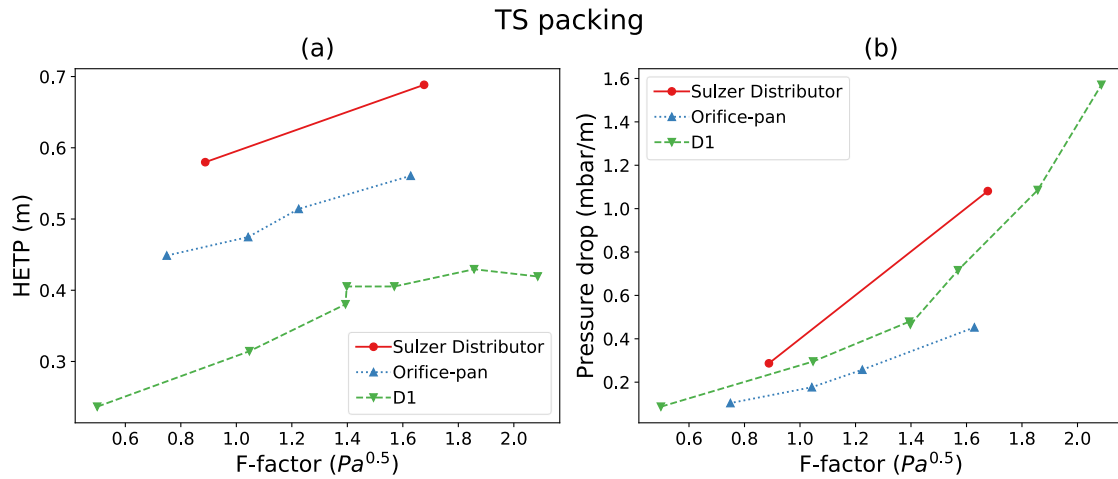


Figure II.25 – HETP (a) and pressure drop (b) vs F-factor for 3 different distributors, using TS packing and the test rig described in Section II.3.4

The errors for HETP measurements in Figure II.25 lie within  $\pm 6\%$ . The vertical error bars were omitted from the figure because these errors are small compared to the range of HETP values obtained. A comparison of the HETP plots in Figures Figure II.23a – Figure II.25a shows that the TS structured packing is much more sensitive to the initial distribution than the industrial packings. It greatly benefits from the tree-shaped distributor, which reduces HETP by up to 50% at low F-factors.

Further, the pressure drops measured using the TS packing are significantly smaller than those measured using Pall Rings, and comparable to those obtained for Mellapack 250Y. For the range of pressure drops in Figure II.25b, small variations are observed according to the type of liquid distributor used. The Sulzer distributor increases the pressure drop slightly. Vapor flow obstruction due to the wire structure in D1 is probably the reason for it causing slightly larger pressure drops than the orifice-pan distributor.

## II.6 Summary

This chapter presented the new liquid distributor invented by Meyer and Rouzineau (2020) and evaluated its performance. A general description of this invention is given in Section II.2. In brief, the top of this distributor is similar to a regular orifice-pan type, but wires are added below. These wires form a tree structure that guides the liquid dripping from the holes and distributes it over the cross-section of the column. After the description, some studies on liquid flow regimes along wire structures were reviewed, and the test rig for HETP measurements was described.

## Chapter II. A nature-inspired liquid distributor

Section II.4 presented the three different tree-like configurations that were selected for experiments. The design stage involved careful consideration of various geometric and performance constraints. A 4th distributor was printed, which served as benchmark for comparison with the previous ones. It consisted in an orifice-pan distributor with 13 holes. Theoretical liquid distribution was assessed by using the maldistribution factor  $M_f$ . The tree-like distributor invention improved liquid distribution over the cross-section of the column. For a 13-holes orifice-pan distributor with  $M_f = 0.236$ , adding the tree structure with 6 layers can in theory decrease the maldistribution factor up to  $M_f = 0.136$ . At the end of the section, scalability of the liquid distributor was discussed. The scale-up of tree structures is generally straightforward; most of the times, it is done simply via an increase in the number of branching generations. However, some of the constraints summarized in Table II.3 make this task considerably harder for the tree-shaped distributor discussed in this chapter.

Finally, Section II.5 provided experimental results for separation performance with different types of packings and distributors. For the industrial packings Pall Rings and Mellapak 250Y, the improvement in initial liquid distribution does not result in better separation efficiency. This is not completely unexpected, as for most industrial packings increasing the number of initial irrigation points above 100 pts/m<sup>2</sup> does not improve packing efficiency (Kister, 1990; Kister et al., 2008). Nevertheless, significant improvement in packing efficiency is obtained when tree-like distributors are used along with the TS structured packing disclosed in Kawas et al. (2021). The efficiency of such packing is highly dependent on initial liquid distribution, and the wire structure in the new distributor configuration can decrease HETP by 0.18 m.



---

## Chapter III. Numerical study of diffusioosmosis and diffusiophoresis

---

In this chapter, diffusioosmosis and diffusiophoresis are studied via numerical simulations. Both case studies consider an aqueous mixture flowing near an interface. The mixture is a colloidal suspension (heterogeneous mixture, particle size larger than 1nm) in the diffusioosmosis case study, and a solution of small solute molecules (homogeneous mixture, particle size smaller than 1nm) in the diffusiophoresis case study. Further, the interface corresponds to the surface of a (static) membrane in the diffusioosmosis work, whereas in the diffusiophoresis study it represents a (moving) solid particle. Solute – interface and colloid – interface interactions are described as an attraction-repulsion potential ( $\Pi_{ic}$ ), and colloid – colloid interactions ( $\Pi_{cc}$ ) consist of two contributions: hard-sphere repulsion and van der Waals (VDW) attraction.

This chapter investigates, among other things, the influence of concentration difference,  $\Pi_{ic}$  and  $\Pi_{cc}$  on the diffusioosmosis of a colloidal suspension that flows through a membrane. Besides, it answers the question of whether diffusiophoretic systems depend on their initial states after long periods of time. The chapter also presents simulation results that illustrate the potential application of diffusiophoresis for particle separation. Finally, it evaluates the influence of solute concentration, diffusivity, concentration gradient and  $\Pi_{ic}$  on phoretic velocities.

The remainder of the chapter is organized as follows. Section III.1 introduces the equations used later for the modelling of mixture flow in the presence of a solid interface. Further, this section reviews relevant works on diffusioosmosis and diffusiophoresis, whose results will be reused for a comparative analysis later in the chapter. Section III.2 describes the case studies that are simulated, as well as the goals of these studies. The numerical models used for simulations are presented in Sections III.4 and III.3, respectively for diffusiophoresis and diffusioosmosis. In the next section, boundary conditions and technical aspects of the simulations, such as mesh type and solvers, will be detailed. Sections III.6 and III.7 present simulation results and discussion for diffusioosmosis and diffusiophoresis, respectively. Finally, Section **Error! Reference source not found.** summarizes the main results of this chapter.

### III.1 Literature review

#### III.1.1 Modelling and simulation

##### III.1.1a Modelling

Suspension flow modelling is a long-time challenge, and a number of approaches have been proposed in the literature. The most intuitive one is the Euler-Lagrangian approach. In its simplest form, the Navier-Stokes equations are solved for the fluid phase in an Eulerian grid, whereas Newton's law is used in each of the particles to predict their motion. Position, velocity and volume of the particles are tracked and updated at every time iteration. Other than the Euler-Lagrangian, another common approach to study 2-phase flows is the Euler-Euler. In this approach, one does not keep track of individual particles. Instead, the properties of these particles (e.g. velocity) are considered continuous. Because of this assumption, it is possible to derive differential equations for the particle phase that are similar to the ones describing the fluid phase. Euler-Euler approach can be subdivided into two categories: two-fluid models and mixture models (Loth, 2000; Van Der Sman, 2009). The modelling in this dissertation falls in the latter category, so the following discussion will be restricted to mixture models.

Such models can be obtained by averaging momentum and mass balance equations for the fluid and particle phases. Nott et al. (2011) used a rigorous averaging procedure to derive the suspension balance model (SBM), assuming that fluid and particles are incompressible. SBM is summarized by the following equations:

$$\underline{\nabla} \cdot \langle \underline{u} \rangle = 0 \quad (\text{III.1})$$

$$\langle \underline{b} \rangle - \underline{\nabla} \cdot \left( (1 - \phi) \langle \underline{p} \rangle^f \right) + 2\eta_f \underline{\nabla} \cdot \langle \underline{e} \rangle + \underline{\nabla} \cdot \phi \langle \underline{\sigma} \rangle^s = 0 \quad (\text{III.2})$$

$$\frac{\partial n}{\partial t} = -\underline{\nabla} \cdot (n \langle \underline{u} \rangle^p) \quad (\text{III.3})$$

Eq. (III.1) represents the mass balance of the mixture. Term  $\underline{u}$  stands for velocity, and the brackets  $\langle \rangle$  indicate that this quantity is averaged over a small volume containing particles and fluid. Eq. (III.2) is the momentum balance for the mixture. The superscripts  $f$  and  $s$  next to the brackets indicate whether the average is taken over the fluid or the solid phase, respectively. No superscripts indicates that the average is taken over both phases (fluid + solid). In eq. (III.2),  $\phi$  is the volume fraction of particles at a given position, and it can be

### Chapter III. Numerical study of diffusioosmosis and diffusiophoresis

defined as the average of a particle phase indicator function over a small volume around that position. Term  $\underline{b}$  refers to the body force,  $p$  is the pressure, and  $\eta_f$  represents the viscosity of the fluid. Finally,  $\underline{\underline{\sigma}}$  is the total stress tensor and  $\underline{\underline{e}}$  is the strain rate tensor. Eq. (III.3) is an averaged conservation equation for the solid phase, and  $n$  stands for the number of particles per volume of solution. Both superscripts  $s$  and  $p$  indicate average over the solid phase; the difference between them is that the former indicates an integral average, whereas the latter corresponds to a discrete average, i.e. a weighted sum of the property taken over the nearby particles.

To use the SBM equations as a model to simulate suspension flow, one needs to formulate closure relations for  $\langle \underline{u} \rangle^p$  and for the particle contribution to the suspension stress  $\phi \langle \underline{\underline{\sigma}} \rangle^s$ . The particle average velocity  $\langle \underline{u} \rangle^p$  can be estimated using relations for the drag force acting on a colloidal particle. This force ( $F_{drag}$ ) is proportional to the relative velocity between the particle and the mixture:  $F_{drag} = -(\langle \underline{u} \rangle^p - \langle \underline{u} \rangle)/m(\phi)$ , where  $m(\phi)$  is the mobility of the colloids in solution. For interface-driven flows, if one assumes that the sum of forces acting on each particle is 0, then drag force is balanced by the gradient of the so-called particle pressure and by the external force exerted by the interface on the colloid particles:  $F_1 = -\frac{V_p}{\phi} \underline{\nabla} \Pi_{cc} - k_B T \underline{\nabla} \Pi_{ic}$ . Therefore the particle average velocity writes (Bacchin et al., 2019):

$$\langle \underline{u} \rangle^p = \langle \underline{u} \rangle - m(\phi) \left( \frac{V_p}{\phi} \underline{\nabla} \Pi_{cc} + k_B T \underline{\nabla} \Pi_{ic} \right) \quad (III.4)$$

In Eq. (III.4),  $V_p$  is the volume of the colloid particles,  $\Pi_{cc}$  is known as the particle pressure,  $k_B$  is Boltzmann's constant,  $T$  is the temperature and  $\Pi_{ic}$  corresponds to the interface – particles (or interface – colloid) interaction potential.

The closure relation for the particle stress term in Eq. (III.2) assumes that such a term can be decomposed in shear stress and normal stress terms (Clausen, 2013):

$$\phi \langle \underline{\underline{\sigma}} \rangle^s = 2\eta_f \eta_p(\phi) \langle \underline{\underline{e}} \rangle - \Pi_{cc,mc} \underline{\underline{I}} \quad (III.5)$$

Eq. (III.5) considers that the shear stress contribution is proportional to the strain rate tensor of the mixture, and the normal stress term is isotropic and equal to the mechanical contribution to the particle pressure. The divergence of this isotropic stress can be lumped together with the term  $\underline{\nabla} \left( (1 - \phi) \langle p \rangle^f \right)$  in Eq. (III.2) in an overall bulk pressure  $p'$

### Chapter III. Numerical study of diffusioosmosis and diffusiophoresis

(Miller et al., 2009). Further, it is assumed that the only external body force acting on the mixture comes from the interface – colloid interactions. Eq. (III.2) can therefore be rewritten as follows:

$$-\frac{k_B T}{V_p} \phi \underline{\nabla} \Pi_{ic} - \underline{\nabla} p' + 2\eta_f (1 - \eta_p(\phi)) \underline{\nabla} \cdot \underline{\underline{e}} = 0 \quad (\text{III.6})$$

From Eq. (III.6) one can observe that the model captures the effect of the colloids in the suspension flow as a variation in the effective viscosity of the mixture. Substituting  $\langle \underline{u} \rangle^p$  in eq. (III.3) by its expression in eq. (III.4), and using  $n = \phi/V_p$ , yields:

$$\frac{\partial \phi}{\partial t} = -\underline{\nabla} \cdot [\phi \langle \underline{u} \rangle - m(\phi)(V_p \underline{\nabla} \Pi_{cc} + k_B T \phi \underline{\nabla} \Pi_{ic})] \quad (\text{III.7})$$

Eq. (III.7) models the flux of colloids in the solution. It comprises two convective terms, associated with the velocity field and the interface – colloid interactions. It also contains an extra term proportional to the gradient of the particle pressure, which captures a thermodynamic (Brownian) contribution as well as a mechanical contribution to the flux of colloids.

With a suitable definition of colloid diffusion coefficient  $D$ , the final set of balance equations is equivalent to the one used in Bacchin et al. (2019):

$$\underline{\nabla} \cdot \underline{u} = 0 \quad (\text{III.8})$$

$$\eta_f \nabla^2 \underline{u} - \underline{\nabla} p - \frac{k_B T}{V_p} \phi \underline{\nabla} \Pi_{ic} = 0 \quad (\text{III.9})$$

$$\frac{\partial \phi}{\partial t} = -\underline{\nabla} \cdot (\underline{J}_\phi) = -\underline{\nabla} \cdot \left( -D \underline{\nabla} \phi - \frac{k_B T}{6\pi\eta_f a} \phi \underline{\nabla} \Pi_{ic} + \phi \underline{u} \right) \quad (\text{III.10})$$

In eqs. (III.8)–(III.10), the average brackets were dropped for simplicity. Eq. (III.8) is equivalent to eq. (III.1). Eq. (III.9) is derived from eq. (III.6) after the following considerations: (i)  $\eta_p(\phi) \approx 0$  (low concentrations); (ii) using the relation  $\underline{\nabla} \cdot \underline{\underline{e}} = \nabla^2 \underline{u}/2$ . Further, the term  $\underline{J}_\phi$  in eq. (III.10) is the volume flux of colloids in  $\text{m}^3/(\text{m}^2 \cdot \text{s})$ . This equation can be derived from eq. (III.7):

- (i) assuming constant mobility  $m(\phi) = 1/6\pi\eta_f a$ , where  $a$  is the particle size;

### Chapter III. Numerical study of diffusioosmosis and diffusiophoresis

- (ii) neglecting the mechanical contribution  $\Pi_{cc,mc}$  to the particle pressure, which is reasonable at low concentrations and/or low shear rates;
- (iii) using the Van 't Hoff (VH) law to compute the particle pressure, as given in eq. (III.11);
- (iv) defining a diffusion coefficient  $D$  according to the Stokes-Einstein equation (III.12).

$$\Pi_{cc} = \frac{\phi k_B T}{V_p} \quad (\text{van 't Hoff}) \quad (\text{III.11})$$

$$D = m k_B T = \frac{k_B T}{6\pi\eta_f a} \quad (\text{III.12})$$

The sum  $\nabla p + (k_B T/V_p)\phi\nabla\Pi_{ic}$  in eq. (III.9) is the divergence of the “thermodynamic pressure tensor” defined in Bacchin et al. (2019). The viscous term in the same equation is an irreversible contribution to the momentum balance of the mixture, due to internal friction. The irreversible processes responsible for particle transport are lumped together in eq. (III.10).

Eqs. (III.8)–(III.10) are commonly used by other authors to study diffusiophoresis and diffusioosmosis when the particles in solution consist of small solute molecules (Michelin and Lauga, 2014; Popescu et al., 2016; Marbach et al., 2020). The difference is that  $D$  replaces the coefficient  $k_B T/6\pi\eta_f a$  multiplying the interface contribution to the solute flux in eq. (III.10). Further, the diffusion coefficient  $D$  of small molecules does not follow eq. (III.12). Finally, these authors work with solute concentration in number of molecules per volume (i.e., replacing  $\phi$  by  $V_p \times n$ ). These modifications eliminate the dependency of eqs. (III.8)–(III.10) on the solute particle size. The mixture velocity  $\underline{u}$  in this case corresponds to the velocity of the fluid, as the volume occupied by solute molecules is negligible. In this chapter, the model for diffusioosmosis (Section III.3) represents a colloidal suspension flow, whereas the diffusiophoresis models in Section III.4 consider infinitely small solute particles. However, for convenience the equations for diffusiophoresis keep the volume fraction notation  $\phi$  instead of using  $n$ .

Other differences between suspensions and mixtures with small solute molecules may arise depending on the equation of state (EoS) used to model suspension particle pressure. The VH EoS in eq. (III.11) is a 1<sup>st</sup>-order approximation of the particle pressure  $\Pi_{cc}$ . A more accurate equation for repulsive interactions was proposed by Carnahan and Starling



### Chapter III. Numerical study of diffusioosmosis and diffusiophoresis

(1969), which agrees well with the 7 first virial coefficients for hard spheres (Russel et al., 1989). This EoS, given in eq. (III.13), does not change the form of the mass balance equation (III.10). However, it impacts the colloid diffusion coefficient, which now depends on the colloid volume fraction. This modified diffusion coefficient is given by eq. (III.14).

$$\Pi_{cc} = \frac{k_B T}{V_p} \phi \frac{\overbrace{1 + \phi + \phi^2 - \phi^3}^{f_{cs}(\phi)}}{(1 - \phi)^3} \quad (\text{Carnahan Starling}) \quad (\text{III.13})$$

$$D = \frac{k_B T}{6\pi\eta_f a} f'_{cs}(\phi) \quad (\text{III.14})$$

In eq. (III.14),  $f'_{cs}$  is the derivative with respect to  $\phi$  of the function  $f_{cs}$  given in eq. (III.13).

Van der Waals (VDW) attractive interactions can also impact colloid distribution at high concentrations. The attractive part of the VDW interaction potential (Jönsson and Jönsson, 1996; Bacchin et al., 2002) can be combined with eq. (III.13), resulting in a more realistic particle pressure EoS with both repulsive and attractive contributions:

$$\Pi_{cc} = \frac{k_B T}{V_p} \left( \phi \frac{\overbrace{1 + \phi + \phi^2 - \phi^3}^{f_{cs}(\phi)}}{(1 - \phi)^3} - \frac{\overbrace{z_n A_H \phi^3}^{f_{vdw}(\phi)}}{36 k_B T (\phi_{cp} - \phi_{cp}^{1/3} \phi^{2/3})^2} \right) \quad (\text{Carnahan + VDW}) \quad (\text{III.15})$$

$$D = \frac{k_B T}{6\pi\eta_f a} \left( f'_{cs}(\phi) + f'_{vdw}(\phi) \right) \quad (\text{III.16})$$

The VDW contribution in eq. (III.15) assumes that, at high concentrations, the colloids are arranged in a regular lattice. Term  $z_n$  is the number of neighbouring particles in a cell lattice,  $A_H$  is the Hamaker constant and  $\phi_{cp}$  is the closed-packing concentration.

#### III.1.1b Numerical simulation using FiPy and ANSYS Fluent

There are many fluid dynamics software that can solve the partial differential equation (PDE) system (III.8)–(III.10). The simulations may be more or less complicated depending on the set of boundary conditions, the flow regime (transient vs stationary) and the EoS used to model  $\Pi_{cc}$ . As it will be shown in Section III.1.2, interface-driven flows with static interface, such as suspension flow through a capillary tube, generally have fixed boundary conditions (e.g. colloid concentration at both ends of the tube).

### Chapter III. Numerical study of diffusioosmosis and diffusiophoresis

These simpler cases can be solved with open-source PDE solvers, such as FiPy (Guyer et al., 2009). FiPy is a library implemented in Python, and it uses a more abstract and user-friendly syntax than many popular PDE solvers, such as Matlab's PDE Toolbox. For example, the colloid balance equation in eq. (III.10) can be written in one line with the help of abstract terms defined in the library:

```
eq0 = TransientTerm() + ConvectionTerm(velocity-pi_ci.faceGrad) ==  
DiffusionTerm(coeff=diffusioncoeff2)
```

The arguments for the convection and diffusion terms are FiPy variables whose values are initialized or assigned elsewhere by the user. These terms are discretized according to the finite volume method.

One of the main drawbacks of choosing FiPy rather than a fluid dynamics software is that it does not have built-in subroutines to solve systems of PDEs automatically. I.e., even though one can easily use it to solve eq. (III.10) for a given velocity field, solving the system (III.8)–(III.10) simultaneously requires the user to write a code according to an algorithm of his choice. For example, the Navier-Stokes equations (III.8), (III.9) can be solved for a given concentration profile via the SIMPLE algorithm (Caretto et al., 1973), which consists in a compute-and-correct procedure summarized in Figure III.1.

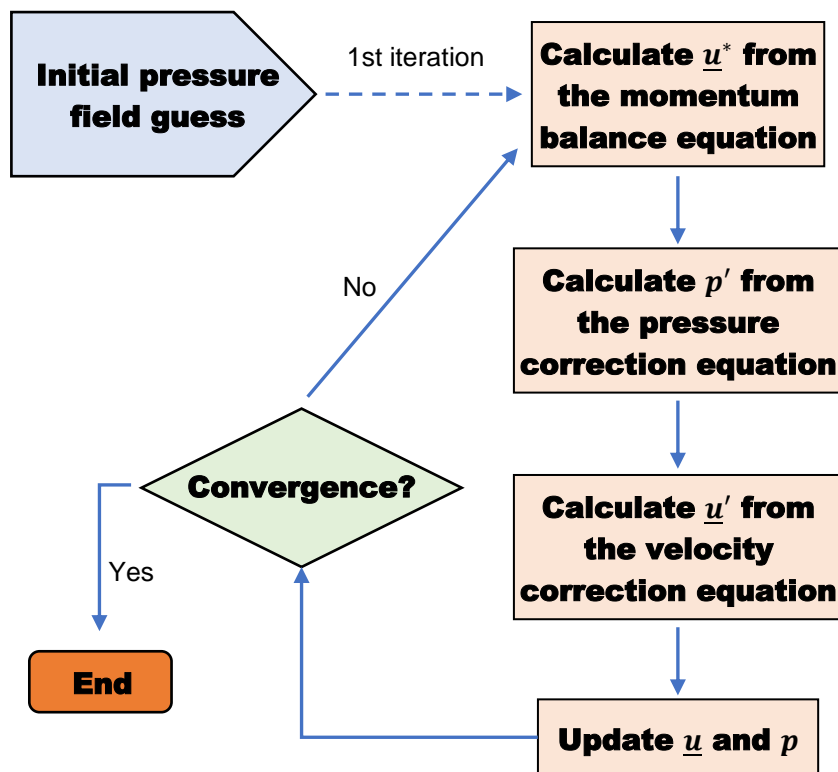


Figure III.1 – The SIMPLE procedure

### Chapter III. Numerical study of diffusioosmosis and diffusiophoresis

In this procedure, the pressure profile of current iteration ( $p^*$ ) is replaced in the discrete version of eq. (III.9) and intermediate velocities  $\underline{u}^*$  are calculated by solving the momentum balance equation. These intermediate velocities  $\underline{u}^*$  do not necessarily satisfy the continuity equation (III.8); correction terms  $\underline{u}'$  and  $p'$  are considered so that  $\underline{u} = \underline{u}^* + \underline{u}'$  satisfies eq. (III.8) in its discrete form. To calculate these terms, one must first replace  $\underline{u} = \underline{u}^* + \underline{u}'$  and  $p = p^* + p'$  in the discrete momentum balance equations. For each control volume, the velocities  $\underline{u}_n$  of its neighbours are approximated by  $\underline{u}_n^*$ . By doing so, one obtains a system of linear equations relating the corrections  $\underline{u}_p'$  on each control volume to the pressure correction profile  $p'$ . The equation that gives  $\underline{u}'$  as a function of  $p'$  will be hereafter called the velocity-correction equation.

Finally, writing  $\nabla \cdot (\underline{u}^* + \underline{u}') = 0$  in its discrete form, replacing  $\underline{u}^*$  by the intermediate profile already calculated, and writing  $\underline{u}'$  in terms of  $p'$ , one can calculate the pressure correction profile. The final equation that gives  $p'$  as a function of the already calculated  $\underline{u}^*$  will be called the pressure-correction equation. Once  $p'$  has been calculated, it can be replaced into the velocity-correction equation in order to compute  $\underline{u}'$ . The continuous equations counterpart to the discrete velocity and pressure-corrections are given in eqs. (III.17) and (III.18). In these equations,  $u_x, u_y, u_z$  are the components of the velocity field, and  $T, H_x, H_y, H_z$  are scalar fields that depend on the viscosity and on local mesh characteristics.

$$\underline{\nabla} \cdot T \underline{\nabla} p' - \underline{\nabla} \cdot \underline{u}^* = 0 \quad (\text{III.17})$$

$$\begin{aligned} u_x &= -H_x \frac{\partial p'}{\partial x} \\ u_y &= -H_y \frac{\partial p'}{\partial y} \\ u_z &= -H_z \frac{\partial p'}{\partial z} \end{aligned} \quad (\text{III.18})$$

This algorithm can be implemented in Python using FiPy equation terms and variables. However, this library only handles collocated grids. This means that the control volumes for all conservation equations are the same, with the variables defined at their centres. Therefore, special interpolation procedures are necessary so that the velocities interpolated on the cell faces satisfy the continuity equation and avoid pressure checkerboarding (Pascau, 2011; Ansys Inc., 2021).

### Chapter III. Numerical study of diffusioosmosis and diffusiophoresis

One of the issues with FiPy is that the linear solvers compatible with the library are slow compared to commercial software. Besides, the mesh module provided by the library is limited, and does not allow curved boundaries. Commercial software such as ANSYS (Ansys Inc., 2020) do not have these limitations.

ANSYS provides complete geometry and meshing modules that allow the user to create complex domains and manage most aspects of the meshing, according to the particularities of the problem. Further, its fluid simulation software (Fluent) already has built-in algorithms (including SIMPLE) to solve the Navier-Stokes equation. But the main advantage of using Fluent over FiPy is the significant decrease in time required for simulation. Another key feature in Fluent is the dynamic mesh option, which allows the user to simulate a flow with moving boundaries, such as the falling of a solid sphere immersed in a fluid.

#### *III.1.2 Diffusioosmosis: physical mechanism and state of the art*

Diffusioosmosis is an interface-driven phenomenon upon which a solute concentration gradient generates fluid flow relative to the fixed interface. Capillary osmosis was one of the first instances of diffusioosmosis studied in the literature. Derjaguin et al. (1947) observed that solutions in a capillary tube can flow through it if a gradient in solute concentration is applied. The flow arises from repulsion/attraction forces exerted on the solute by the tube's wall. To better understand the mechanism behind the flow, let us imagine a mixture of fluid and solute in a capillary tube of radius  $R$ . Interactions between the solute and the wall (e.g. adsorption) can create a solute concentration distribution normal to the wall. These interactions however are limited to a thin layer (thickness  $\delta \ll R$ ), and outside it one should expect solute concentration to be constant in the direction normal to the wall. Because the length of the thin layer (hereafter called diffusive layer) is much smaller than  $R$ , at the scale of this layer the wall can be considered flat. Figure III.2 illustrates the system under this approximation.

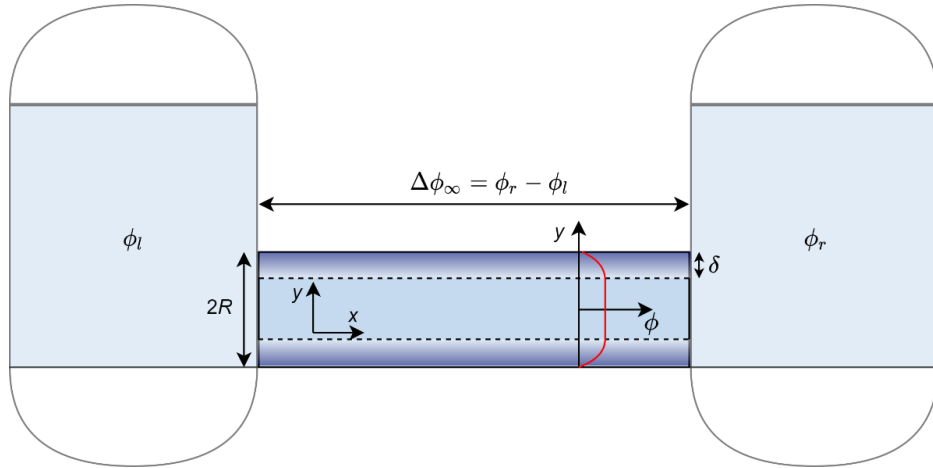


Figure III.2 – Capillary tube connected to two reservoirs; the red curve represents the variation of solute concentration along the  $y$ -direction

The concentration profile in the bulk  $\phi_0(x)$  can be set by connecting the openings of the capillary to reservoirs with different concentrations  $\phi_l$  and  $\phi_r$ . As mentioned before, the wall interacts with solute particles via attractive/repulsive forces along the  $y$ -direction. These forces are transmitted to the fluid, for example via viscous drag (Oster and Peskin, 1992). The resultant force on the solvent is commonly written as the gradient of an interaction potential, times the solute concentration. In eq. (III.9), the term  $(k_B T/V_p)\phi \nabla \Pi_{ic}$  corresponds to such a force. It will follow the  $y$ -direction if the interface is the wall of the capillary tube in Figure III.2.

Momentum balance in the diffusive layer then reveals the appearance of a pressure profile along the  $y$ -direction, which counters this force. The pressure profile changes with respect to the  $x$ -direction as well, since the solute concentration in the bulk (and therefore the magnitude of the solute – interface interaction forces) depends on  $x$ . In other words, the force applied on the solute by the walls of the capillary ends up creating a hydrostatic pressure gradient along the  $x$ -direction. This gradient is the driving force for the flow in the diffusive layer, which entrains the fluid in the bulk (Anderson, 1989).

Diffusioosmosis is now gaining attention of researchers in the micro/nanofluidics field. Fluid flow through confined system has many applications, including lab-on-a-chip analyses and microelectronics cooling (Laser and Santiago, 2004). Electroosmosis is commonly used to drive the flow, and it is preferred over diffusioosmosis because it is capable of generating larger flowrates. Nevertheless, solvophobic channel surfaces could induce hydrodynamic slip at the solid-fluid interface, which in turn amplifies significantly the diffusioosmotic flowrates in narrow channels (Ajdari and Bocquet, 2006). In addition,

### Chapter III. Numerical study of diffusioosmosis and diffusiophoresis

biological systems may employ several processes in which diffusioosmosis plays a major role. Bonthuis and Golestanian (2014) modelled the flow of a solution across a funnel-shaped membrane protein channel. Including diffusioosmotic effects and calculating the forces exerted on the channel's walls, they were able to predict the two conformational states (closed and opened) that the channel can adopt.

Diffusioosmosis can also be seen as the mechanism driving the flow through membranes. Traditionally, membranes are modelled as a boundary of 0 thickness separating two homogeneous mixtures with different solute concentrations. The difference in concentration generates a difference in the so-called osmotic pressure, which drives solvent flow across the membrane. If instead one is interested in describing the flow at the membrane scale, interface-solute interactions have to be included in the momentum balance equations, which drive diffusioosmosis near the membrane wall.

Anderson and Malone (1974) showed that the osmotic flow through porous membranes can be partially predicted with the diffusioosmosis theory. Assuming long, cylindrical pores, the authors derived an expression for the osmotic reflection coefficient  $\sigma_0$  as a function of solute characteristics. The definition of osmotic reflection coefficient and its expression are given in eqs. (III.19) and (III.20):

$$J_v = L_p \left[ \Delta p_\infty - \sigma_0 \frac{k_B T}{V_p} \Delta \phi_\infty \right] \quad (\text{III.19})$$

$$\sigma_0 = 1 - \frac{8}{R^4} \int_0^R 2y dy \int_y^R \frac{d\xi}{\xi} \int_0^\xi \gamma e^{-\Pi_{ic}(\gamma)} d\gamma \quad (\text{III.20})$$

Eq. (III.19) is a classical expression in membrane science that defines the osmotic reflection coefficient for an ideal solution. In this equation,  $J_v$  is the volumetric flow of solvent across the membrane,  $\Delta p_\infty$  is pressure difference and  $\Delta \phi_\infty$  is volume fraction difference between the reservoirs. This definition is valid regardless of membrane geometry. When  $\sigma_0 = 1$ , the flow is proportional to the difference between hydrostatic pressure drop and osmotic pressure drop; this case represents an ideal semipermeable membrane. The cases where  $0 < \sigma_0 < 1$  correspond to leaky membranes, and  $\sigma_0 = 0$  indicates that the membrane interacts in the same way with solute and solvent molecules (i.e. a non-selective membrane). Reflection coefficients lower than 0 ( $\sigma_0 < 0$ ) are rare, but have been reported in the literature for electrolyte solutions flowing through a charged membrane (Sasidhar and Ruckenstein, 1982). They indicate that the tendency for osmotic

### Chapter III. Numerical study of diffusioosmosis and diffusiophoresis

flow is inverted, i.e. the solvent tends to move towards the region of lower solute concentration (anomalous osmosis).

Eq. (III.20) gives osmotic reflection coefficient for a membrane made of long and cylindrical pores. The development leading to this equation mixes concepts from thermodynamics and fluid mechanics. The resulting expression is a function of the pore radius  $R$  and the dimensionless interface – solute interaction potential  $\Pi_{ic}$  (see Section III.1.1). The integrals in this equation are taken along the radial direction, with 0 corresponding to the centre of the pore and  $R$  corresponding to its wall.

To obtain eq. (III.20), Anderson and Malone (1974) neglected inertial terms in the Navier Stokes equations, which is reasonable since the Reynolds number for a flow in a capillary tube tends to be much lower than 1. They also neglected the gradient of the radial velocity in the momentum balance of the fluid along the radial direction (long pores), as well as axial variations of the axial velocity in the momentum balance of the fluid along the axial direction. Finally, the authors assumed that the solute concentration follows a Boltzmann distribution along the radial direction, and between the bulk and the pore ends. This last assumption is valid if the activity coefficient of the solute and the molar volume of the mixture remain approximately constant.

Assuming that the solute particles are perfect spheres of radius  $a$ , and that their interactions with the channel walls are restricted to steric exclusion, it can be shown (Anderson and Malone, 1974) that the expression in eq. (III.20) results in:

$$\sigma_0 = \left(1 - \left(1 - \frac{a}{R}\right)^2\right)^2 \quad (\text{III.21})$$

In the limit  $a \rightarrow 0$ , the membrane is incapable of retaining the solute, and the reflection coefficient equals 0. But as  $a \rightarrow R$ , the solute particles cannot enter the pores, and the membrane is now perfectly semipermeable. Further, when considering an adsorptive potential outside of the exclusion zone, their model predicts negative reflection coefficients (anomalous osmosis) for small solute particles.

Following the steps of Anderson and Malone (1974), Marbach et al. (2017) also tried a mechanical approach to model osmotic flow. They modelled the system in a 1D geometry where the membrane is depicted by a potential acting on the solute, along the same direction as the flow. One of the key results in this work is the generalization of eq. (III.19)

### Chapter III. Numerical study of diffusioosmosis and diffusiophoresis

for non-ideal mixtures at high solute concentrations. In this regime, the diffusive term in the solute transport equation is modified, and eqs. (III.19) and (III.20) are re-derived using perturbation theory:

$$J_v = L_p \left( \Delta P_\infty - \sigma_0 \Delta \Pi_\infty^o \right) \quad (\text{III.22})$$

$$\sigma_0 = 1 - \frac{\int_{-\frac{L}{2}}^{\frac{L}{2}} \frac{1}{\lambda(\phi_0)} dx}{\int_{-\frac{L}{2}}^{\frac{L}{2}} \frac{\phi_l}{\phi_0 \lambda(\phi_0)} dx} \quad (\text{III.23})$$

$\Pi^o$  in eq. (III.22) is an osmotic pressure defined with respect to the Helmholtz free energy density  $f$ :

$$\Pi^o(T, \phi) = \phi \frac{\partial f}{\partial \phi} - f(T, \phi) + f(T, 0) \quad (\text{III.24})$$

In eq. (III.23),  $\phi_0$  is the solute concentration profile that would arise if solute concentration at the right-end of the pore was equal to the solute concentration at the left-end of the pore (i.e., the 0<sup>th</sup>-order approximation of the actual solute concentration profile). Term  $\lambda$  represents the solute mobility, which may depend on solute concentration. Finally,  $\phi_l$  is the solute concentration at the left-end of the pore. The limit case  $\phi_0 \ll \phi_l$  corresponds to a highly selective pore that prevents solute entrance. In this case,  $\sigma_0 \approx 1$  and the membrane is perfectly semipermeable.

Despite providing interesting qualitative insights to the osmosis phenomenon, there are some limitations to the approach proposed by Marbach et al. (2017). The first is that osmosis is modelled using 1D analysis, which can result in errors. For example, 1D treatment of osmosis across a pore wrongly predicts that the solvent velocity inside the pore is 0 everywhere when osmotic pressure drop is equal to the hydrostatic pressure drop (Anderson and Malone, 1974). Further, 1D models may violate the 2<sup>nd</sup> law of thermodynamics by predicting a spontaneous flow through a pore with similar bulk concentrations in both ends, when the pore ends have different diameters (Anderson and Malone, 1974). The second limitation of the approach proposed by Marbach et al. (2017) is that it treats osmosis and diffusioosmosis as separate phenomena. In other words, in their approach the osmotic flow does not stem directly from diffusioosmotic transport.



### Chapter III. Numerical study of diffusioosmosis and diffusiophoresis

Bacchin et al. (2019) attempted to overcome the former limitations by using a 2D approach where the membrane is modelled as an array of cylinders, according to Figure III.3. In this figure, the blue arrows represent the net flow across the membrane, and the small circles are the solute/colloid particles.

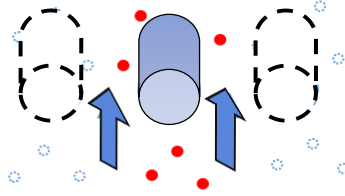


Figure III.3 – Membrane geometry consisting of an array of cylindrical obstacles and used by Bacchin et al. (2019)

The transport equations used for numerical calculations in their work are the ones shown in eqs. (III.8)–(III.10), and the solute-interface interaction potential  $\Pi_{ic}$  is given by:

$$\Pi_{ic} = k_{ic} \times \left[ \overbrace{(1 + a_{tt})e^{-\frac{d}{l_{ic}}}}^{\text{repulsion}} - \overbrace{a_{tt}e^{-\frac{d}{2l_{ic}}}}^{\text{attraction}} \right] \quad (\text{III.25})$$

Eq. (III.25) models  $\Pi_{ic}$  as the sum of a repulsive and an attractive term. In this equation,  $k_{ic}$  represents the magnitude of interface-solute interactions,  $a_{tt}$  is an attraction parameter,  $d$  is the distance between the cylindrical obstacle and a point in the domain, and  $l_{ic}$  is the interaction range. This potential is illustrated in Figure III.4 for  $k_{ic} = 1$ . The repulsion term in the  $\Pi_{ic}$  is similar to the negative exponential function used in DLVO theory to model repulsion between electric double layers (Bhattacharjee et al., 1998). Because an exponential decay is a stiff function, this repulsion term may also model steric exclusion if  $l_{ic}$  is of the same order of magnitude as the solute particles size. Further, the attraction term may account for solute adsorption near the solid walls (Bacchin et al., 2019).

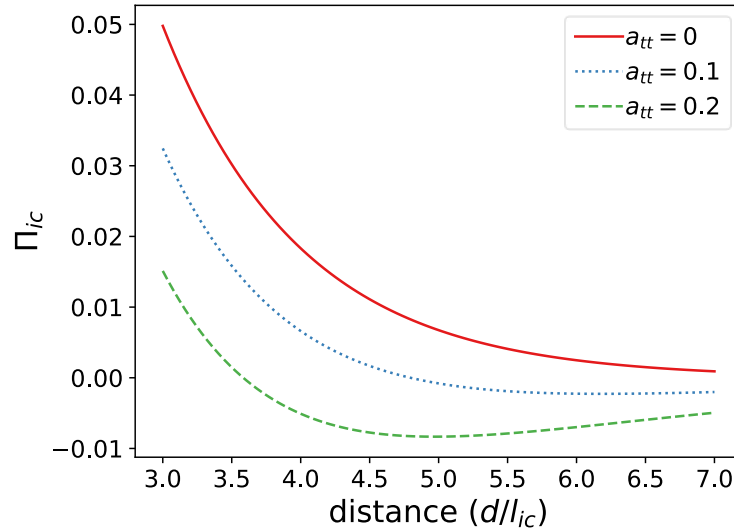


Figure III.4 – Interface-solute interaction for different attraction parameters and  $k_{ic} = 1$ , as a function of the distance from the interface

The main result in the work by Bacchin et al. (2019) is a unified mechanical description for regular and anomalous osmosis. Indeed, when no attraction forces are considered ( $a_{tt} = 0$  in eq. (III.25)), numerical results show the tendency for mixture flow towards higher solute concentrations. However, large attraction parameters can invert this tendency, similar to the predictions made by Anderson and Malone (1974) when accounting for solute adsorption in a pore geometry. Both these cases are depicted in Figure III.5, reproduced from Bacchin et al. (2019).

In this figure, the top plot shows how the flux across the membrane changes as pressure drop or  $a_{tt}$  are varied. The blue dashed line represents the reference case, where solute concentration is zero (pure water). For the other two curves, positive fluxes correspond to flow towards lower solute concentrations. In the absence of hydrostatic pressure drop, regular osmosis is observed when  $a_{tt} = 0$  (pRO), and anomalous osmosis takes place when  $a_{tt} = 0.2$  (pAO). The colour maps below this plot depict the dimensionless  $x$ -velocity and solute concentration profiles for these two points. In these colour maps, the white circles correspond to the cylindrical obstacles depicted in Figure III.3, and the domain coordinates are given in dimensionless units. The characteristic length used for normalization is the space  $\delta$  between two cylindrical obstacles ( $2 \mu\text{m}$ ), and dimensionless pressures are obtained using the normalizing term  $k_B T / V_p$  (982 Pa). Finally, velocities are normalized with respect to the ratio  $k_B T / 6\pi\eta_f a \delta$  ( $10.9 \mu\text{m/s}$ ).

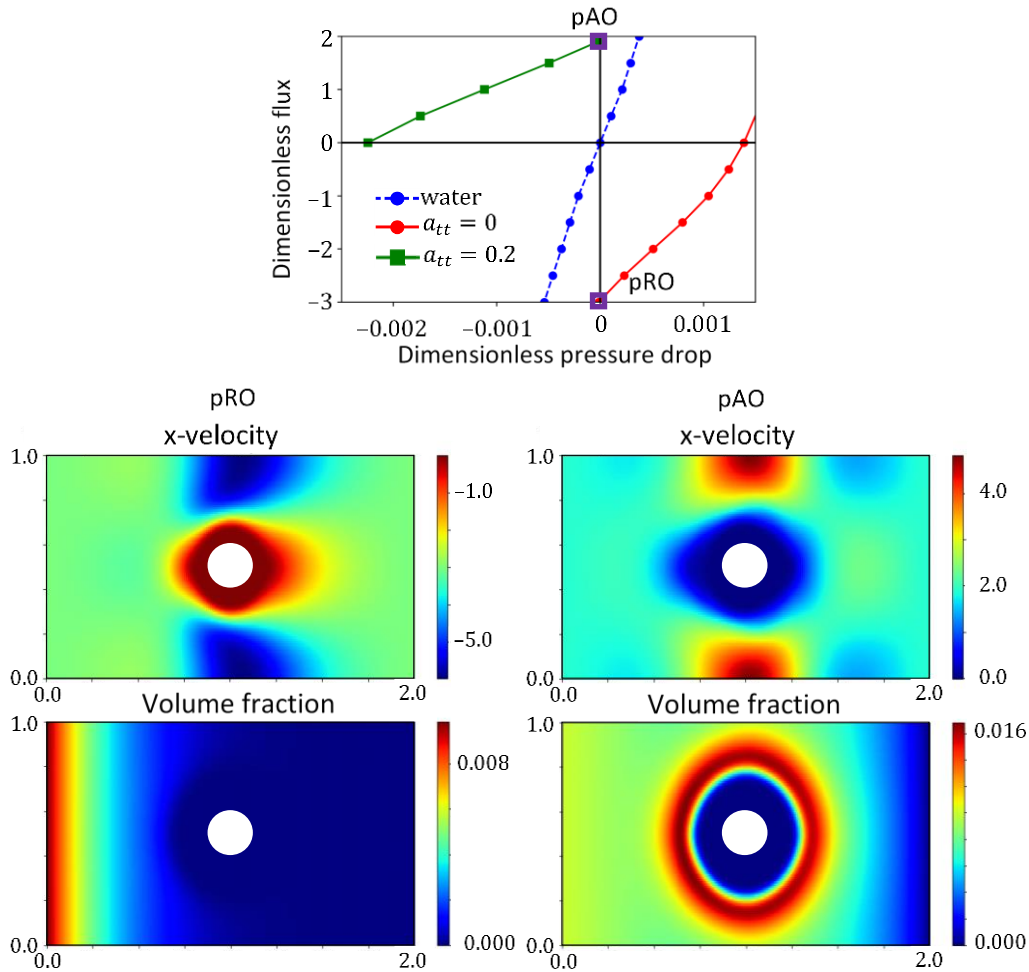


Figure III.5 – (top) Flux across a membrane as a function of the pressure drop and the attraction parameter in eq. (III.25); (bottom) solute concentration and x-velocity profiles corresponding to regular (pRO) and anomalous (pAO) osmosis. Extracted with permission from Bacchin et al. (2019).

### III.1.3 Diffusiophoresis: physical mechanism and state of the art

Like diffusioosmosis, diffusiophoresis is another interface-driven phenomenon upon which a solute concentration gradient drives a flux. The key difference is that the term diffusioosmosis describes a system with a fixed interface around which the fluid flows, whereas diffusiophoresis refers to the movement of the interface itself, driven by solute-interface forces.

Diffusiophoresis was first described by Derjaguin and co-authors in 1947. They studied the displacement of wax beads in a water/methanol/glucose solution contained in a cylinder connected to two reservoirs of different glucose concentration, 0 at the top and positive at the bottom (Derjaguin et al., 1947, 1993; Churaev et al., 1987). The glucose gradient creates a linear density distribution, and one should expect all the beads to remain

### Chapter III. Numerical study of diffusioosmosis and diffusiophoresis

at a level in the cylinder corresponding to 0 buoyancy. However, glucose molecules interact repulsively with the wax beads, and because of the glucose concentration gradient, the resultant force of the glucose-bead interaction points towards the top. Hence the beads will move up until an equilibrium is reached between this force and the buoyancy of the particles.

More recently, Popescu et al. (2016) made a concise review of self-diffusiophoresis, the phenomenon upon which an immersed particle creates itself the gradient of solute serving as the driving force for its motion. One of the mechanisms through which the particle can create this gradient is if its surface catalyses the formation/degradation of solute. A degree of asymmetry (e.g. anisotropic chemical activity over the surface) is necessary for motion to take place. Still in the context of self-diffusiophoresis, Michelin and Lauga (2014) proposed a framework for finding the phoretic velocity of Janus particles, i.e. particles having two or more distinct physical properties. Using this framework, the authors found that advection (convection) affects self-phoresis in a non-monotonic way: a maximum in phoretic velocity was found in their study for Péclet numbers of  $O(1)$ .

Neglecting the convection and transient terms in the solute transport equation (III.26), Marbach et al. (2020) found semi-analytical solutions for the diffusiophoresis velocity, corresponding to a null resulting force acting on the surface. The simplest system considered in their work consists of a solid sphere immersed in a mixture with neutral solute. Assuming an interface-solute potential  $\Pi_{ic}$  that depends only on the distance to the particle's surface, as well as a constant solute gradient  $\nabla\phi^\infty$  far from the particle, the solution of eq.(III.26) in spherical coordinates is given by eq. (III.27). Finally, the diffusiophoretic velocity of the particle under these assumptions is given in eq. (III.28).

$$\underline{\nabla} \cdot (\underline{J}_\phi) = \underline{\nabla} \cdot \left( -D\underline{\nabla}\phi - D\phi\underline{\nabla}\Pi_{ic} \right) = 0 \quad (\text{III.26})$$

$$\phi = \phi_0(r) + R\nabla\phi^\infty \cos(\theta) f(r) \quad (\text{III.27})$$

$$v_{DP} = \frac{R^2}{3\eta_f} \nabla\phi^\infty \times \frac{k_B T}{V_p} \int_R^\infty f(r) (-\Pi'_{ic}) \left( \frac{r}{R} - \frac{R}{3r} - \frac{2r^2}{3R^2} \right) dr \quad (\text{III.28})$$

In eq. (III.27),  $\theta$  is the polar angle,  $R$  is the radius of the particle,  $r$  is the radial distance,  $\phi_m = \lim_{r \rightarrow \infty} \phi(r, \theta = \pi/2)$ , and we consider that the solute concentration gradient far

### Chapter III. Numerical study of diffusioosmosis and diffusiophoresis

from the sphere is parallel to the azimuthal direction  $\theta = 0$ . Further,  $\Pi'_{ic}$  in eq. (III.28) corresponds to the derivative of  $\Pi_{ic}$  with respect to  $r$ .

The authors have also derived semi-analytical solutions for local surface forces acting on spherical particles in various systems (neutral solute and porous/impermeable particle, electrophoresis, and others). One of the main results presented shows that, despite the resultant force acting on the particle's gravity centre being 0 at diffusiophoresis and electrophoresis, local stresses along the particle's surface are zero only in electrophoresis.

Finally, Ramírez-Hinestrosa et al. (2020) studied the diffusiophoresis of a polymer in a mixture via molecular dynamic simulations. The interactions between the various particles in the system (monomers, solute and solvent molecules) were modelled with the 12-6 Lennard-Jones potential, except for monomer – monomer interactions. The authors assumed that the solvent + solute mixture behaves ideally, setting solute – solute, solute – solvent and solvent – solvent dispersion energy to 1. Solvent – monomer dispersion energy was set to 1 as well. Under these assumptions, Ramírez-Hinestrosa et al. (2020) assessed how polymer size and solute – monomer interactions affect polymer mobility. They found that the corresponding diffusiophoresis velocity depends weakly on the size of the polymer.

Besides, it was shown that the effect of solute – monomer dispersion energy ( $\epsilon_{ms}$ ) on the mobility of the particle is non-monotonic. Mobility, defined by the ratio between diffusiophoretic velocity and the solute chemical potential gradient, is negative when monomers have more affinity with solvent molecules than solute molecules (i.e.,  $\epsilon_{ms} < 1$ ). In other words, the polymer moves towards lower solute concentration regions when it has lower affinity to solute particles. When  $\epsilon_{ms} > 1$ , the solute molecules are adsorbed around the polymer, and the direction of particle displacement is inverted. The mobility of the polymer continues to increase with respect to  $\epsilon_{ms}$  until a certain threshold, after which it starts decreasing, possibly due to the immobilization of the diffusive layer surrounding the polymer. Figure III.6 illustrates this finding. In this figure,  $\tau$  and  $m$  are units for time and mass, LJ stands for Lennard-Jones and SRLJ stands for short-ranged Lennard-Jones.

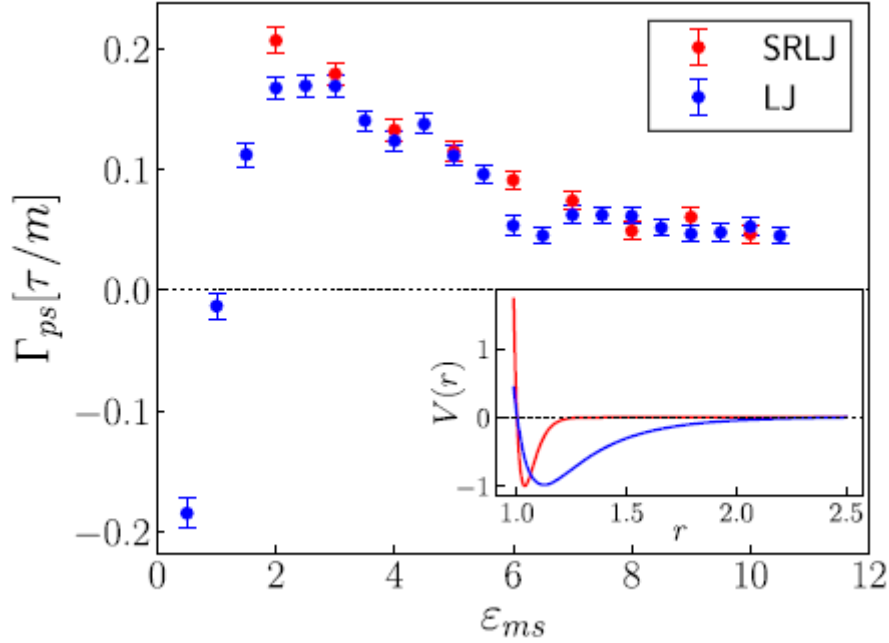


Figure III.6 – Variation of a polymer’s mobility (vertical axis) with respect to the solute-monomer dispersion energy. From Ramírez-Hinestrosa et al. (2020), reproduced with permission from AIP.

## III.2 Description of the case studies

### III.2.1 Diffusioosmosis case study

As reviewed in Section III.1, diffusioosmosis is the flow of fluid with respect to a fixed interface (for example the walls of a capillary tube), driven by solute concentration gradient. In this chapter, the system used to study diffusioosmosis is the same as the one considered by Bacchin et al. (2019) and briefly discussed in Section III.1.2: it consists of a mixture of colloids and water flowing through an array of cylinders that mimics a membrane. Colloid concentration is fixed on the inlet and outlet, replicating a channel that connects two large reservoirs with certain colloid volume fractions ( $\phi_l$  and  $\phi_r$ ). It is assumed that the cylinders are impermeable to both colloids and solvent, and no-slip condition is imposed for the mixture at the cylinder’s wall (Figure III.7).

### Chapter III. Numerical study of diffusioosmosis and diffusiophoresis

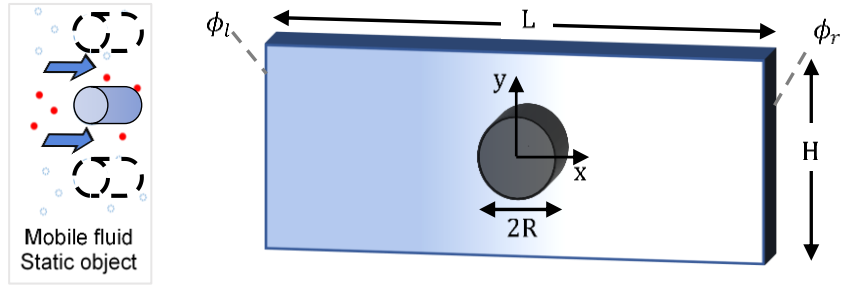


Figure III.7 – Sketch of the case study (left) and geometry/domain (right) used in diffusioosmosis simulations

The array of obstacles is simulated using a single cylinder, together with symmetry conditions on the top and bottom boundaries of the domain. The coordinate system origin is set at the centre of the cylinder. The blue rectangle in Figure III.7 corresponds to the simulation domain, and its size can be arbitrarily chosen as long as  $L \gg R$ .

The study of diffusioosmosis focuses on the advection-osmosis equilibrium, when the pressure difference prevents flow between the left and the right reservoirs. The first goal of this work is to determine whether diffusioosmosis predicts an increase in equilibrium pressure drop when the difference in colloid concentration  $\Delta\phi$  across the membrane is increased. Further, the influence of interface – colloid and colloid – colloid interactions (see  $\Pi_{ic}$  and  $\Pi_{cc}$  in Section III.1.1) on the suspension flow is investigated. Among other things, the study intends to simulate moderate colloid adsorption near the membrane through modulation of interface – colloid interactions, and to assess the drawback from using simplistic models in the description of colloid – colloid interactions.

The range of parameters used in diffusioosmosis simulations is given in Table III.1:

Table III.1 – Range of dimensions and parameters used in diffusioosmosis simulations

$\phi_l$	[0.01, 0.1]	$L(\mu\text{m})$	4	$k_{ic}$	100
$\phi_r$	0	$H(\mu\text{m})$	2	$l_{ic}(\mu\text{m})$	0.1
$\frac{k_B T}{6\pi\eta_f a}$ ( $\mu\text{m}^2/\text{s}$ )	21.8	$R(\mu\text{m})$	0.2	$a_{tt}$	[0, 0.2]
$\eta_f$ (Pa.s)	$10^{-3}$	$k_B T/V_p$ (Pa)	999		

In Table III.1,  $\eta_f$  is the viscosity of the fluid (water viscosity), and  $k_B T/6\pi\eta_f a$  corresponds to the diffusion coefficient of colloid particles obtained via the Stokes-

### Chapter III. Numerical study of diffusioosmosis and diffusiophoresis

Einstein equation (III.12). The parameter  $k_B T/V_p$  (Boltzmann constant multiplied by temperature and divided by the volume of a solute particle) appears in the momentum balance equation, see eq. (III.9). The value for this parameter is retrieved assuming a temperature of 303 K and a spherical solute particle of radius  $a = 0.01 \mu\text{m}$ . Finally,  $k_{ic}$ ,  $l_{ic}$  and  $a_{tt}$  are the parameters of the solute – interface interaction potential in eq. (III.25), which can model both repulsion and attraction behaviours. This interaction potential will be adopted throughout the simulations in both diffusiophoresis and diffusioosmosis case studies, unless stated otherwise. The range of  $a_{tt}$  values, as well as the values of parameters  $k_{ic}$  and  $l_{ic}$ , correspond to those used in the diffusioosmosis study by Bacchin et al. (2019).

#### III.2.2 Diffusiophoresis case study

Differently from diffusioosmosis, diffusiophoresis refers to the motion of a solid interface in a solution, driven again by solute concentration gradient. The system used to study diffusiophoresis is depicted in Figure III.8. It consists of a spherical particle (black sphere) immersed in a mixture of solute (red circles) and water. Solute concentration gradient is kept constant very far from the sphere. The particle is assumed to be impermeable to solute and solvent alike, and a no-slip condition is imposed for the fluid at the particle's surface.

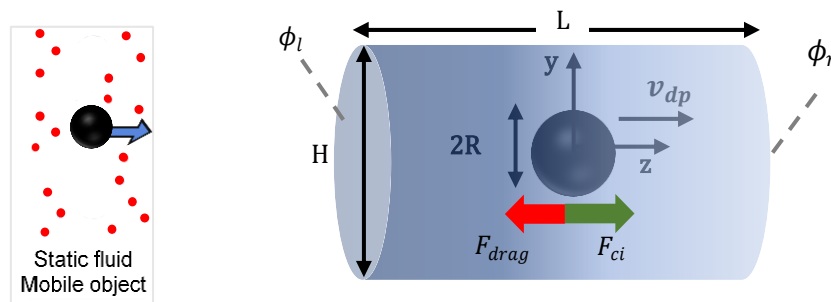


Figure III.8 – Sketch of the case study (left) and geometry/domain (right) used in diffusiophoresis simulations

This setup is axisymmetric with respect to the z-axis passing through the centre of the sphere and parallel to the solute gradient. Therefore, a rectangular simulation domain on the y-z plane translates into a cylindrical 3D domain. The origin of the coordinate system is set at the centre of the cylinder, and as an initial condition, we place the centre of the sphere at the origin. The sphere may or may not move away from the centre of the cylinder, depending on the model used for simulation. The cylinder in this figure



### Chapter III. Numerical study of diffusioosmosis and diffusiophoresis

corresponds to the simulation domain, and its size can be arbitrarily chosen as long as  $H, L \gg R$ . A solute gradient  $\nabla\phi^\infty = (\phi_r - \phi_l)/L$  is imposed by fixing solute volume fraction at  $z = -L/2$  ( $\phi = \phi_l$ ) and at  $z = L/2$  ( $\phi = \phi_r$ ). Values of parameters used for simulations are given in Table III.2.

Table III.2 – Range of dimensions and parameters used in diffusiophoresis simulations

$\nabla\phi^\infty$ (m <sup>-1</sup> )	[-625, -200]	$L$ (μm)	16	$k_{ic}$	[10, 100]
$\phi_m$	[0, 0.05]	$H$ (μm)	16	$l_{ic}$ (μm)	[0.01, 0.1]
$D$ (μm <sup>2</sup> /s)	[21.8, ∞)	$R$ (μm)	0.2	$a_{tt}$	[0, 0.2]
$\eta_f$ (Pa. s)	$10^{-3}$	$k_B T/V_p$ (Pa)	984		

The particle is subjected to the force applied by the solute on its interface ( $F_{ci}$ ), and to the viscous drag force  $F_{drag}$  opposing particle motion. The direction of these forces depends on the nature of solute – interface interactions. If repulsive interactions dominate, the left side of the domain (richer in solute) “pushes harder” than the right side, so  $F_{ci}$  is positive and the drag force is negative, as depicted in Figure III.8. Alternatively, if attractive interactions dominate, the left part of the mixture “pulls harder” than the right part, and the forces will be oriented oppositely.

In Table III.2,  $D$  is the diffusion coefficient of the solute particles, and  $\phi_m$  is the mean value of the far-field profile, given by  $\phi_m = (\phi_l + \phi_r)/2$ . Here, it is important to recall that the diffusiophoresis case study considers infinitely small solute molecules. That is the reason why  $D$  can take any value in the range shown in Table III.2, but only one value (given by eq. (III.12)) in Table III.1 corresponding to diffusioosmosis. Still, concentrations are given in volume fraction for the sake of simplicity. A volume fraction  $\phi = 0.01$  actually corresponds to a solute concentration of 0.0040 mol/m<sup>3</sup>.

The case study depicted in Figure III.8 will be used to meet some of the objectives listed in Section I.5 (and recalled in this paragraph). Diffusiophoretic velocities  $v_{DP}$  will be calculated for several combinations of the parameters listed in Table III.2. The goal of these simulations is to regress an expression for  $v_{DP}$  as a function of these parameters. Further, dynamic simulations will show whether there exist fully-developed, out-of-equilibrium states for which velocity and concentration profiles change with respect to time, but no longer depend on the initial conditions of the system. The last goal to be achieved through this case study is to show that there is only one possible stable

equilibrium state in diffusiophoresis, which corresponds to an equilibrium of forces at null velocity.

### III.3 Model for diffusioosmosis

This section presents the model used to solve the suspension flow near a membrane made of cylindrical obstacles, as depicted in Figure III.7. In diffusiophoresis, the interface is free to move, and it experiences different far-field solute concentrations as it travels through the mixture. This inherent transient feature is not present in diffusioosmosis, where the interface is fixed. In this phenomenon, the flow around the interface will eventually reach a steady state if the boundary conditions are stationary. The set of equations describing steady state diffusioosmotic flow is:

$$\underline{\nabla} \cdot \underline{u} = 0 \quad (\text{III.29})$$

$$\eta_f \nabla^2 \underline{u} - \underline{\nabla} p - \frac{k_B T}{V_p} \phi \underline{\nabla} \Pi_{ic} = 0 \quad (\text{III.30})$$

$$\underline{\nabla} \cdot \left[ -D \underline{\nabla} \phi - \frac{k_B T}{6\pi\eta_f a} \phi \underline{\nabla} \Pi_{ic} + \phi \underline{u} \right] = 0 \quad (\text{III.31})$$

$$\underline{u}|_{\text{interface}} = \underline{0}; \underline{J}_\phi \cdot \underline{n}|_{\text{interface}} = 0 \quad (\text{III.32})$$

Here,  $\underline{u}$  is the velocity of the mixture,  $\eta_f$  is the viscosity of the fluid,  $p$  is pressure,  $\Pi_{ic}$  is the solute-particle interaction potential, and  $\underline{J}_\phi$  is the colloid volume flux.

The conditions imposed to the other boundaries depend mostly on the geometry of the problem being studied, and therefore were omitted from the set of equations above. For the cylindrical channels of capillary tubes (see Figure III.2) and also for flat walls, it is common to assume fully-developed flow on the outlet and zero shear stress far from the surface ( Churaev et al., 1987; Ajdari and Bocquet, 2006). The former boundary condition can no longer be used if there is not a well-defined direction for the flow, for instance if the osmotic flow happens around a small spherical surface (McDermott et al., 2012). Further, the condition of no stress far from the surface becomes meaningless when the flow is confined in very narrow channels whose width is comparable to the range of surface-solute interactions (Keh and Ma, 2007; Rasmussen et al., 2020).

### III.4 Models for diffusiophoresis

There are several alternatives to model the diffusiophoretic system depicted in Figure III.8. The ones presented in the following sections are derived from the mixture model discussed in Section III.1.1. Simulation results from these models are shown later in Section III.7, along with the main conclusions drawn from them.

#### III.4.1 Transient Exact Formulation (TEF)

It was stated in Section III.1.1 that the set of equations commonly used to study diffusiophoresis when solute particles consist of small molecules is ( Michelin and Lauga, 2014; Popescu et al., 2016; Marbach et al., 2020):

$$\underline{\nabla} \cdot \underline{u} = 0 \quad (\text{III.33})$$

$$\eta_f \nabla^2 \underline{u} - \underline{\nabla} p - \frac{k_B T}{V_p} \phi \underline{\nabla} \Pi_{ic} = 0 \quad (\text{III.34})$$

$$-\underline{\nabla} \cdot [\underline{J}_\phi] = -\underline{\nabla} \cdot [-D \underline{\nabla} \phi - D \phi \underline{\nabla} \Pi_{ic} + \phi \underline{u}] = \frac{\partial \phi}{\partial t} \quad (\text{III.35})$$

Here,  $\underline{u}$  is the velocity of the fluid, and solute concentration (in no. of molecules per volume) equals  $\phi/V_p$ . Note that  $D$  replaces  $k_B T/6\pi\eta_f a$  in eq. (III.10).

The fundamental difference between diffusiophoresis and diffusioosmosis lies in the boundary conditions for each phenomenon. Diffusiophoresis refers to the displacement of a particle in a solution due to the interactions between its surface and the solute molecules. It is common to assume that the solute profile is well-established far from the particle and that the latter moves under the influence of a distant solute gradient  $\nabla \phi^\infty$  (Anderson and Prieve, 1984, 1991; Churaev et al., 1987; Anderson, 1989; Khair, 2013; Marbach et al., 2020; Ramírez-Hinestrosa et al., 2020; Rasmussen et al., 2020). The boundary conditions (BCs) for eqs. (III.33)–(III.35) are then listed as six equalities:

$$\begin{aligned} \underline{u}|_{interface(t)} &= \underline{v}_0; \quad \underline{u}|_\infty = \underline{0}; \quad \frac{d\underline{v}_0}{dt} = \frac{\underline{F}}{M} \\ (\underline{J}_\phi - \underline{v}_0 \phi) \cdot \underline{n}|_{interface(t)} &= 0 \\ \phi|_{t=0} &= \phi_0(\underline{x}) \\ \phi|_{r \rightarrow \infty} &= \phi^\infty(\underline{x}) \end{aligned} \quad (\text{III.36})$$

### Chapter III. Numerical study of diffusioosmosis and diffusiophoresis

The first equality in eq. (III.36) corresponds to the no-slip condition; subscript *interface*( $t$ ) refers to the moving (time-dependent) surface of the particle, and  $v_0$  refers to its velocity. The next BC means that the fluid is at rest far from the particle. Third equality is Newton's second law applied to the particle of mass  $M$ .

$$\underline{F} = \int_{\Omega} \frac{k_B T}{V_p} \phi \underline{\nabla} \Pi_{ic} dV + \int_{\delta\Omega} \eta_f (\underline{\nabla} \underline{u} + \underline{\nabla} \underline{u}^T) \cdot \underline{n} dS - \int_{\delta\Omega} p \underline{n} dS \quad (\text{III.37})$$

The fourth BC in eq. (III.36) guarantees that solute molecules cannot enter the particle ( $\underline{n}$  is the unit vector normal to the particle's surface). The BC  $\phi|_{t=0} = \phi_0(\underline{x})$  represents the initial condition of the colloid concentration profile. Finally, the last BC stresses that the solute concentration profile is not perturbed far from the particle. The distance  $r$  at the left-hand side is the distance from the centre of the spherical particle. Because the gradient of solute far from the particle is considered constant,  $\phi^\infty$  depends on the position  $\underline{x}$ . It is a linear concentration profile, and not a constant.

Eqs. (III.33)–(III.36) define the dynamics of diffusiophoresis, and one is often interested in the equilibrium state, for which  $\underline{F} = 0$ . According to eq. (III.37), the particle is subjected to the action of 3 forces: colloid – interface interaction force (1st term) and hydrodynamic forces due to viscous stress (2nd term) and due to pressure (3rd term). The volumetric integral is taken over the entire domain, whereas the surface integrals are taken over the particle's surface  $\partial\Omega$ .

Several questions arise from the transient formulation presented above. For given initial conditions (position and velocity of the particle; solute concentration profile), is it possible for the particle to reach an equilibrium state where the sum of forces equals zero? If such a state can be reached, does it persist during a long time or is it a momentary state? These and other questions will be addressed later via numerical simulation.

#### III.4.2 Transient Formulation at Constant Velocity (TFCV)

Eqs. (III.33)–(III.37) are the exact description of the case study. However, such a model has a high computation cost, since the problem is transient and the domain needs to be remeshed at every time step. To avoid remeshing, one can assume that the velocity  $\underline{v}_0$  of the particle is constant. The origin can then be set at the centre of the particle by defining

### Chapter III. Numerical study of diffusioosmosis and diffusiophoresis

new coordinates  $\underline{x}^* = \underline{x} - \underline{v}_0 t$ . For this new moving frame, eqs. (III.33)–(III.36) can be re-written as follows:

$$\underline{\nabla}^* \cdot \underline{u}^* = 0 \quad (\text{III.38})$$

$$\eta_f \nabla^{*2} \underline{u}^* - \underline{\nabla}^* p^* - \frac{k_B T}{V_p} \phi^* \underline{\nabla}^* \Pi_{ic}^* = 0 \quad (\text{III.39})$$

$$-\underline{\nabla}^* \cdot [-D \underline{\nabla}^* \phi^* - D \phi^* \underline{\nabla}^* \Pi_{ic}^* + \phi^* \underline{u}^*] = \frac{\partial \phi^*}{\partial t} - \underline{\nabla}^* \phi^* \cdot \underline{v}_0 \quad (\text{III.40})$$

$$\begin{aligned} \underline{u}^*|_{interface} &= \underline{v}_0; \underline{u}^*|_{\infty} = \underline{0} \\ \underline{J}_{\phi'} \cdot \underline{n}|_{interface} &= 0 \end{aligned} \quad (\text{III.41})$$

$$\begin{aligned} \phi|_{t=0} &= \phi_0(\underline{x}^*) \\ \phi^*|_{r \rightarrow \infty} &= \phi^\infty(\underline{x}^*) + \underline{\nabla}^* \phi^*|_{\infty} \cdot \underline{v}_0 \times t \end{aligned}$$

In eqs (III.38)–(III.41), the starred operator  $\underline{\nabla}^*$  indicates that the derivatives are taken with respect to the new coordinates, relative to the moving frame. Further, the far-field boundary condition assumes constant solute concentration gradient ( $\underline{\nabla}^* \phi^*|_{\infty}$ ) far from the sphere. Starred scalar/vector fields  $f^*$  are defined according to eq. (III.42), and the right-hand side of eq. (III.40) results from eq. (III.43).

$$f^*(\underline{x}^*, t) \equiv f(\underline{x}^* + \underline{v}_0 t, t) \quad (\text{III.42})$$

$$\left[ \frac{\partial \phi}{\partial t} \right]^* = \frac{\partial \phi^*}{\partial t^*} - \underline{\nabla}^* \phi^* \cdot \underline{v}_0 \quad (\text{III.43})$$

The vector field  $\underline{u}^*$  does not correspond to the velocity of the fluid with respect to the sphere. Indeed, the first boundary condition shows that  $\underline{u}^*$  does not go to  $\underline{0}$  at the particle's surface. Therefore, one may find it useful to define a new variable  $\underline{w}$ , corresponding to the velocity of the fluid with respect to the sphere, as follows:

$$\underline{w} = \underline{u}^* - \underline{v}_0 \quad (\text{III.44})$$

### Chapter III. Numerical study of diffusioosmosis and diffusiophoresis

Inserting eq. (III.44) into eqs. (III.38)–(III.41) yields the final set of equations:

$$\underline{\nabla}^* \cdot \underline{w} = 0 \quad (\text{III.45})$$

$$\eta_f \nabla^{*2} \underline{w} - \underline{\nabla}^* p^* - \frac{k_B T}{V_p} \phi^* \underline{\nabla}^* \Pi_{ic}^* = 0 \quad (\text{III.46})$$

$$-\underline{\nabla} \cdot [J_{\phi}'] = -\underline{\nabla}^* \cdot [-D \underline{\nabla}^* \phi^* - D \phi^* \underline{\nabla}^* \Pi_{ic}^* + \phi^* \underline{w}] = \frac{\partial \phi^*}{\partial t} \quad (\text{III.47})$$

$$\begin{aligned} \underline{w}|_{interface} &= 0; \quad \underline{w}|_{\infty} = -\underline{v}_0 \\ J_{\phi}' \cdot \underline{n}|_{interface} &= 0 \\ \phi|_{t=0} &= \phi_0(\underline{x}^*) \\ \phi^*|_{r \rightarrow \infty} &= \phi^{\infty}(\underline{x}^*) + \underline{\nabla}^* \phi^*|_{\infty} \cdot \underline{v}_0 t \end{aligned} \quad (\text{III.48})$$

The term  $J_{\phi}'$  corresponds to the solute flux perceived by the particle. Eqs. (III.45)–(III.48) can be simulated using a fixed mesh. The translation of the particle is captured by the transient BC given in the fourth equality of eq. (III.48). However, this set of equations is not equivalent to the dynamic formulation described previously, because here we assume constant particle velocity. Despite that, this formulation can capture instantaneous equilibrium states. That is, for a given  $\underline{v}_0$ , one can run a simulation with eqs. (III.45)–(III.48) and check if  $\underline{F} = 0$  at some time  $t$ . It is also possible to distinguish whether a certain equilibrium state is instantaneous or lasting. Indeed, if a simulation using this formulation shows that the force acting on the surface remains very close to 0 during a large time interval, that means the actual dynamic system will also sustain an equilibrium state during the same interval.

Comparing eqs. (III.45)–(III.47) and (III.29)–(III.31), one can notice that the formulations for diffusioosmosis and diffusiophoresis are very similar. However, because of the last BC in eq. (III.48) it is impossible for the diffusiophoretic model described in this section to reach a true steady state. Besides, in the diffusioosmotic case study the solute consists of colloid particles, so the diffusion coefficient  $D$  depends on the equation of state for colloid-colloid interactions, as discussed in Section III.1.1.

### III.4.3 High Diffusion Limit (HDL)

In the limit of very high diffusion coefficients ( $D \rightarrow \infty$ ), convective solute transport and the transient term  $\partial\phi/\partial t$  in the solute transport equation can be neglected. The equations describing this formulation are:

$$\underline{\nabla} \cdot \underline{w} = 0 \quad (\text{III.49})$$

$$\eta_f \nabla^2 \underline{w} - \underline{\nabla} p - \frac{k_B T}{V_p} \phi \underline{\nabla} \Pi_{ic} = 0 \quad (\text{III.50})$$

$$\underline{\nabla} \cdot [\underline{J}_\phi] = \underline{\nabla} \cdot [-D \underline{\nabla} \phi - D \phi \underline{\nabla} \Pi_{ic}] = 0 \quad (\text{III.51})$$

$$\begin{aligned} \underline{w}|_{interface} &= 0; \quad \underline{w}|_\infty = -\underline{v}_0 \\ \underline{J}_\phi \cdot \underline{n}|_{interface} &= 0 \\ \phi|_{r \rightarrow \infty} &= \phi^\infty(\underline{x}) \end{aligned} \quad (\text{III.52})$$

These equations are written with respect to the moving frame centred in the particle, which is why the velocity is set to zero on the particle's surface. However, the starred fields and operators that appeared in the TFCV model are no longer necessary in HDL. This happens because HDL is a steady-state formulation, and hence the substitution  $\underline{x}^* = \underline{x} - \underline{v}_0 t$  is meaningless. In other words, one can assume (without loss of generality) that the set of equations (III.49) – (III.52) is being solved for  $t = 0$ , so that  $\underline{x}^* = \underline{x}$ .

The HDL formulation is commonly used in the literature (Sharifi-Mood et al., 2013; Popescu et al., 2016; Marbach et al., 2020), mainly because it decouples the solute transport equation from the momentum balance of the mixture. In other words, one can solve eq. (III.51) to find the solute concentration profile before computing the velocity and pressure fields. Besides, HDL does not require time iterations: the velocity and solute concentration profiles are established instantaneously for any given far-field BC  $\phi^\infty(\underline{x})$ .

Considering a potential  $\Pi_{ic}$  that depends only on the distance to the particle's surface, and also considering a constant solute gradient  $\nabla\phi^\infty$  far from the particle, the solution of eq. (III.51) in spherical coordinates is (Marbach et al., 2020):

$$\phi = \phi_0(r) + R \nabla \phi^\infty \cos(\theta) f(r) \quad (\text{III.53})$$

$$\phi_0(r) = \phi_m e^{-\Pi_{ic}} \quad (\text{III.54})$$

### Chapter III. Numerical study of diffusioosmosis and diffusiophoresis

for  $f(r)$  such that:

$$2rf' + r^2f'' - 2f + 2r\Pi'_{ic}f + r^2f'\Pi'_{ic} + r^2f\Pi''_{ic} = 0 \quad (\text{III.55})$$

In eq. (III.53),  $\theta$  is the polar angle,  $R$  is the radius of the particle,  $r$  is the radial distance,  $\phi_m = \lim_{r \rightarrow \infty} \phi(r, \theta = \pi/2)$ , and we consider that the solute concentration gradient far from the sphere is parallel to the azimuthal direction ( $\theta = 0$ ). The function  $f(r)$  in eq. (III.53) is defined by eq. (III.55), where the superscript (') indicates derivative with respect to  $r$ . Note that there is no general solution for this differential equation. Nevertheless, one can still derive an expression for the diffusiophoresis velocity of the particle in terms of  $f$ , setting  $\underline{F} = 0$  in eq. (III.37) (Marbach et al., 2020):

$$v_{DP} = \frac{R^2}{3\eta_f} \nabla\phi^\infty \frac{k_B T}{V_p} \int_R^\infty f(r) (-\Pi'_{ic}) \left( \frac{r}{R} - \frac{R}{3r} - \frac{2r^2}{3R^2} \right) dr \quad (\text{III.56})$$

Eq. (III.53) corresponds to an unnumbered equation in the first paragraph of Section 3 in Marbach et al. (2020). Eqs. (III.54) and (III.55) are not given in Marbach's paper, but it can be found by inserting eq. (III.53) into eq. (III.51) and later using the BCs to get rid of unknown constants. Finally, eq. (III.56) is eq. (3.23) in Marbach et al. (2020).

#### III.5 Numerical method and solving strategy

Previous works (Bacchin, 2017; Bacchin et al., 2019) have used the open-source FiPy library for Python (see Section III.1.1) to simulate a suspension flowing under the influence of some interface – colloid interaction potential. In these works, the inside of the cylindrical obstacle in Figure III.7 was meshed together with the rest of the domain, and a penalization method was used to account for the no-slip boundary condition on the particle's surface. Here, the same approach was used to simulate diffusioosmosis, but ANSYS Fluent® software (Ansys Inc., 2020) was chosen to perform diffusiophoresis simulations. As explained in Section III.1.1, Fluent supports dynamic meshing, which is a required feature to implement the TEF model described in Section III.4.1. Further, transient models such as TEF and TFCV described in Sections III.4.1 and III.4.2 sometimes require a significant amount of time to depart from the initial condition, especially when solute diffusion coefficient is small. By using Fluent, computation time is significantly reduced, and transient simulations can be run within less than 24h for a large number of time steps (up to 400) and refined mesh (up to  $1.3 \times 10^6$  elements).



### Chapter III. Numerical study of diffusioosmosis and diffusiophoresis

The python code written to simulate the diffusioosmosis case study is annexed in Appendix C. It uses various classes from the FiPy library to declare the differential equations (III.29)–(III.32), together with an adaptation of the SIMPLE algorithm (Figure III.1) to solve them. The range of colloid concentrations used as boundary conditions was shown in Table III.1. The velocity at the left boundary is imposed, and normal velocity gradients are set to 0 at the right boundary. Finally, symmetry BC is imposed at the top and bottom boundaries (see Figure III.7). Further, because FiPy mesh module cannot create interior walls, the cylindrical obstacle has to be meshed along with the rest of the domain in Figure III.7, and BCs cannot be imposed to the cylinder's wall. To solve this issue, a penalization method is implemented according to eq. (III.57), which adds a large source term to the momentum balance equation in the region occupied by the cylinder (Guyer et al., 2012).

$$\eta_f \nabla^2 \underline{u} - \underline{\nabla} p - \frac{k_B T}{V_p} \phi \underline{\nabla} \Pi_{ic} + X_{\|x\| \leq R} \times LV \underline{u} = 0 \quad (\text{III.57})$$

In this equation,  $LV$  is a large value, and  $X_{\|x\| \leq R}$  is the indicator function, which is 1 for mesh elements whose centres are inside the cylinder, and 0 otherwise. This penalization brings the velocity of the mixture down to 0 in the cylinder and on the cylinder's wall.

It was mentioned in Section III.1.1 that FiPy uses the finite volume method to discretize the differential equations. The spatial discretization scheme used to interpolate colloid concentration at the cell faces, for the purpose of calculating convective fluxes, is the first-order power law scheme (Guyer et al., 2012). Besides, the interpolation of the pressure at cell faces, required to compute the discrete pressure term in the momentum balance equation, follows a second-order linear scheme.

The mesh used in all diffusioosmosis simulations was a structured mesh with  $2 \times 10^4$  squared elements. This mesh was validated by comparing simulation results with the results from another structured mesh with  $8 \times 10^4$  elements. Figure III.9 shows the comparison of the colloid concentration profiles using both meshes, for  $\phi_l = 0.01$  and a velocity of  $10.9 \mu\text{m/s}$ . The maximum deviation between both profiles is  $1.5 \times 10^{-4}$ , which is insignificant compared to the absolute range of variation in colloid concentration ( $\phi_l - \phi_r = 0.01$ ).

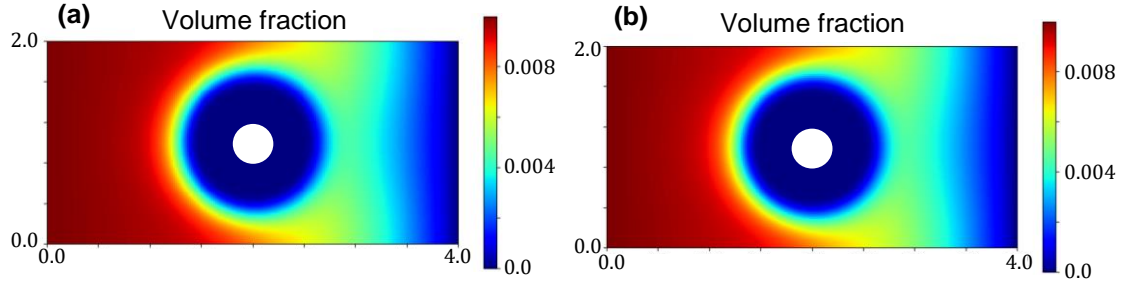


Figure III.9 – Comparison of colloid concentration profiles in the diffusioosmosis case study, using meshes with 20,000 elements (a) and 80,000 elements (b)

Whereas the python implementation requires the user to code his model, Fluent comes with a series of built-in models for fluid and mixture flow. For diffusiophoresis simulations, the laminar model was chosen to simulate fluid flow, and a user-defined scalar was defined to describe solute transport (Ansys Inc., 2021). The extra term  $-(k_B T/V_p)\phi \nabla \Pi_{ic}$  appearing in the momentum balance equation for the mixture, which corresponds to the force exerted by the interface on the solute, is captured via a source term. Further, the additional term  $-D\phi \nabla \Pi_{ic}$  in the solute transport equation, which represents the transport due to interface – solute forces, is captured via a user-defined function (UDF). UDFs are also necessary to prescribe the motion of the sphere in the TEF model. More details on these UDFs are given in Appendix C.

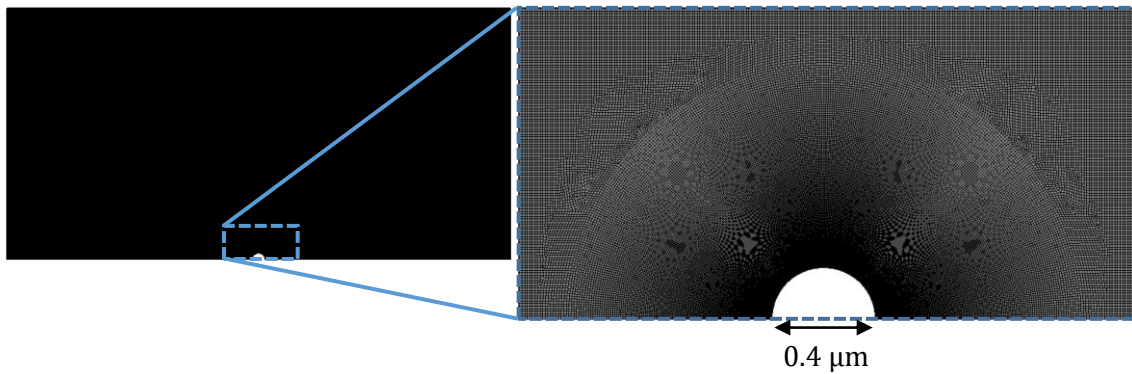
Once the model is correctly implemented in Fluent, the user can choose the solver. Unlike the diffusioosmosis simulations that focused on the steady-state regime, the diffusiophoresis case (Figure III.8) is fundamentally transient since the sphere experiences different solute concentrations as it moves. Due to this difference, the Coupled algorithm (Ansys Inc., 2021) was used to solve the diffusiophoretic transport equations. Differently from the SIMPLE algorithm, this method solves the momentum and continuity equations simultaneously. Therefore, it can converge faster, reducing significantly the number of iterations necessary at any given time step.

The ranges of solute concentration  $\phi_m$  and far-field solute concentration gradient  $\nabla \phi^\infty$  used to define the far-field solute concentration profile were shown in Table III.2. For the TEF model, the velocity at the left and right boundaries is set to 0 as the fluid far from the sphere is considered at rest. Further, no-slip BC is imposed at the wall, whose velocity is updated based on the forces exerted on the sphere. The colloid concentration values at the left and right boundaries are calculated from  $\phi_m$  and  $\nabla \phi^\infty$ . On the other hand, both

### Chapter III. Numerical study of diffusioosmosis and diffusiophoresis

TFCV and HDL models place the sphere at the origin of the reference frame. Therefore, null velocity is imposed for the fluid on the surface of the sphere. The velocity at the left and right boundaries is imposed, and it is kept the same throughout the simulation. The initial concentrations at the left and right boundaries are calculated from  $\phi_m$  and  $\nabla\phi^\infty$ , but they are updated for the TFCV model according to the last equality in eq. (III.48). Finally, in the 3 diffusiophoretic models, axis-symmetry BC is imposed on the axial axis passing through the centre of the sphere, symmetry BC is imposed on the shell of the cylindrical domain in Figure III.8, and zero solute flux is imposed on the walls of the sphere.

The mesh used in all diffusiophoresis simulations is shown in Figure III.10. It consists of a structured zone with regular squared elements far from the sphere, an inflation layer around the sphere, and an unstructured mesh region between these zones. The total number of elements is 1 317 824, and maximum element size was set to  $0.01 \mu\text{m}$  (5% of the radius of the sphere). The different mesh zones are clearer in the right extract of Figure III.10, which zooms in a small portion of the domain around the sphere. When the entire domain is displayed (left image), the elements are not visible and the entire mesh has a solid dark aspect, due to the limited pixel resolution.



*Figure III.10 – Mesh used for the diffusiophoresis case study*

This mesh was validated by comparing simulation results with the results from a similar mesh with maximum element size of  $0.016 \mu\text{m}$ . Figure III.11 shows the comparison of the axial velocity profiles for both meshes, using the TFCV model with  $\nabla\phi^\infty = -6.25 \times 10^{-4} \mu\text{m}^{-1}$ ,  $\phi_m = 0.005$ ,  $D = 218 \mu\text{m}^2/\text{s}$  and setting the velocity at the inlet and outlet to zero. Note that the deviation between these profiles is negligible compared to the absolute range of variation in velocity ( $\approx 47.3 \mu\text{m}/\text{s}$ ). A second type of validation was performed by slightly displacing the sphere from the centre of the domain, while

### Chapter III. Numerical study of diffusioosmosis and diffusiophoresis

keeping the same  $\phi_m$ . It was found that this modification could change the calculated diffusiophoretic velocities significantly, especially when drag and solute-sphere interaction forces are in the order of  $10^{-14}$  N or lower. However, this discrepancy vanishes if the inflation layer is at least 4 times thicker than the radius of the sphere. This condition was taken into account in the mesh shown in Figure III.10.

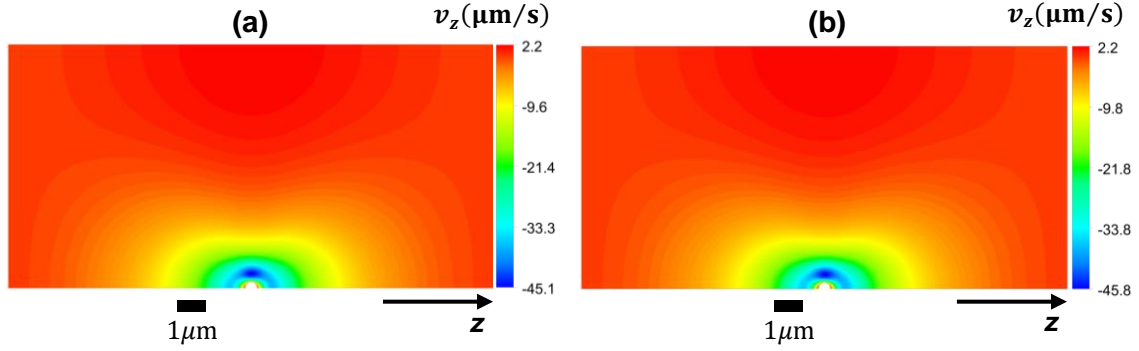


Figure III.11 – Comparison of axial velocity profiles in the diffusiophoresis case study, using meshes with maximum element size of  $0.01 \mu\text{m}$  (a) and  $0.016 \mu\text{m}$  (b)

A third kind of mesh validation can be performed by comparing simulation results with analytical results. Marbach et al. (2020) have derived a semi-analytical expression for the diffusiophoretic velocity in the HDL model, given by eqs. (III.55) and (III.56). Note that the differential equation (III.55) does not have a general explicit solution. However, a careful study of these equations led to the finding of a specific interface – solute interaction potential  $\Pi_{ic}$  that results in a fully analytical expression for diffusiophoretic velocity. Such a convenient  $\Pi_{ic}$  is given by eq. (III.58), and the corresponding analytical solutions for eqs. (III.55) and (III.56) are given in eqs. (III.59) and (III.60):

$$\Pi_{ic} = \frac{1}{2} \ln \left[ \frac{r^4}{r^4 + R^4} \right] \quad (\text{III.58})$$

$$f(r) = \frac{r}{R} + \frac{R^3}{r^3} \quad (\text{III.59})$$

$$v_{DP} = \frac{R^2}{6\eta_f} \nabla \phi^\infty \times \frac{k_B T}{V_p} \quad (\text{III.60})$$

The potential in eq. (III.58) together with eq. (III.60) can be used to quickly assess numerical implementations of the HDL model presented in Section III.4.3. This has significant importance due to the relative popularity of the model in the literature (Sharifi-Mood et al., 2013; Popescu et al., 2016; Marbach et al., 2020).

### Chapter III. Numerical study of diffusioosmosis and diffusiophoresis

For values of  $R$ ,  $\eta_f$  and  $k_B T/V_p$  given in Table III.2, and for  $\nabla\phi^\infty = -6.25 \times 10^{-4} \mu\text{m}^{-1}$ , one obtains a theoretical diffusiophoresis velocity  $v_{DP} = -4.09 \mu\text{m/s}$ . From numerical simulation, the value obtained is  $v_{DP} = -3.86 \mu\text{m/s}$ , corresponding to a relative error of -5.6%. The source of the error is not the meshing itself, but rather the size of the simulation domain, which is too small for a logarithmic potential. Indeed, doubling  $H$  and  $L$  given in Table III.2 (without changing mesh element size) results in a new simulated velocity of  $-3.97 \mu\text{m/s}$ , and error is reduced to -2.9%. This variation of  $v_{DP}$  is much smaller when an exponential potential such as the one in eq. (III.25) is used. The reason for this difference is that the logarithmic potential in eq. (III.58) decays in  $1/r^4$ , which makes it act over longer distances compared to a potential that decays exponentially. Table III.3 summarizes the changes in  $v_{DP}$  considering different domain sizes and interface – solute interaction potential. The results for the exponential potential considered  $\nabla\phi^\infty = -6.25 \times 10^{-4} \mu\text{m}^{-1}$ ,  $\phi_m = 0.02$  and  $l_{ic} = 0.1 \mu\text{m}$ .

Table III.3 – Comparison between  $v_{DP}$  calculated using different domain sizes

	$v_{DP} (\mu\text{m/s})$	
	$H = 16 \mu\text{m}, L = 16 \mu\text{m}$	$H = 32 \mu\text{m}, L = 32 \mu\text{m}$
$\Pi_{ic} = \frac{1}{2} \ln \left[ \frac{r^4}{r^4 + R^4} \right]$	-3.86	-3.97
$\Pi_{ic} = 100 \times e^{-\frac{d}{l_{ic}}}$	29.1	29.5

### III.6 Diffusioosmosis results and discussion

In this section, simulation results are presented for the diffusioosmotic case study discussed in Section III.2.1, using the model described in Section III.3. Mixture velocity and colloid concentration profiles corresponding to advection–osmosis equilibrium are displayed in rows in Figure III.12. Only two different colloid concentration values were imposed at the left boundary:  $\phi_l = 0.01$  in the first line and  $\phi_l = 0.1$  in the subsequent lines. At the right boundary,  $\phi_r$  was kept at 0 in all simulations, as indicated in Table III.1. Besides, the first three rows of results in this figure were obtained assuming eq. (III.12) (a diffusion coefficient from van 't Hoff equation of state), whereas the results in the last row assumed eq. (III.16) (a diffusion coefficient from Carnahan-Starling + van der Waals equations of state). Finally, the simulations corresponding to the first two lines

### Chapter III. Numerical study of diffusioosmosis and diffusiophoresis

in Figure III.12 considered  $a_{tt} = 0$  in eq. (III.25), whereas in the remaining ones  $a_{tt} = 0.2$  was used.

Comparing the first and second lines in Figure III.12, one observes that an increase in  $\Delta\phi$  between the reservoirs increases the velocity of the mixture. This phenomenon is expected since the body force on the mixture ( $\phi\nabla\Pi_{ic}$ , see eq. (III.30)) is proportional to the colloid concentration. Interestingly, the appearance of the velocity and colloid concentration profiles does not change significantly upon an increase in colloid concentration. But a shift in the absolute values of velocities and concentration is observed. Finally, the pressure drop along the x-axis for the case  $\phi_l = 0.01$  (first line) is of +1.26 Pa. The positive value indicates that the left boundary has a higher pressure than the right one. This pressure difference is what equilibrates the osmotic tendency for the mixture to flow towards higher solute concentrations. When concentration at the left boundary is increased (line 2), this tendency is enhanced, and a higher pressure drop (+4.07 Pa) is required to attain the advection–osmosis equilibrium.

The osmotic reflection coefficient  $\sigma_0$  of the membrane can be calculated for both simulations using eq. (III.19): it equals 0.128 when  $\phi_l = 0.01$  and 0.0414 when  $\phi_l = 0.1$ . This dependency of  $\sigma_0$  on solute concentration has been reported by previous experiments. Its theoretical interpretation in literature is usually associated with solute–solute interactions that affect solute mobility and/or the stress tensor of the mixture (Adamski and Anderson, 1983; Marbach et al., 2017). However, these interactions were not accounted for in the first two simulations of Figure III.12.

The two simulations discussed above considered purely repulsive interface – colloid interactions, using the  $\Pi_{ic}$  potential in eq. (III.25) with  $a_{tt} = 0$ . When long-range attraction is included ( $a_{tt} = 0.2$  in Figure III.12, line 3), colloids concentrate around the cylinder, forming the red ring. The velocity profiles are more complex in this case, with the appearance of extra vortices. Furthermore, the flow is partially inverted after increasing the attraction parameter  $a_{tt}$  (line 3 vs line 2). Blue areas in the velocity profiles on the second row become red on the third row, and vice-versa. The pressure drop corresponding to the third line of results is -13.85 Pa. It is negative because the flow tends to move towards low colloid concentrations (from left to right) when  $a_{tt} = 0.2$ , so a higher pressure at the right boundary is necessary to attain equilibrium.

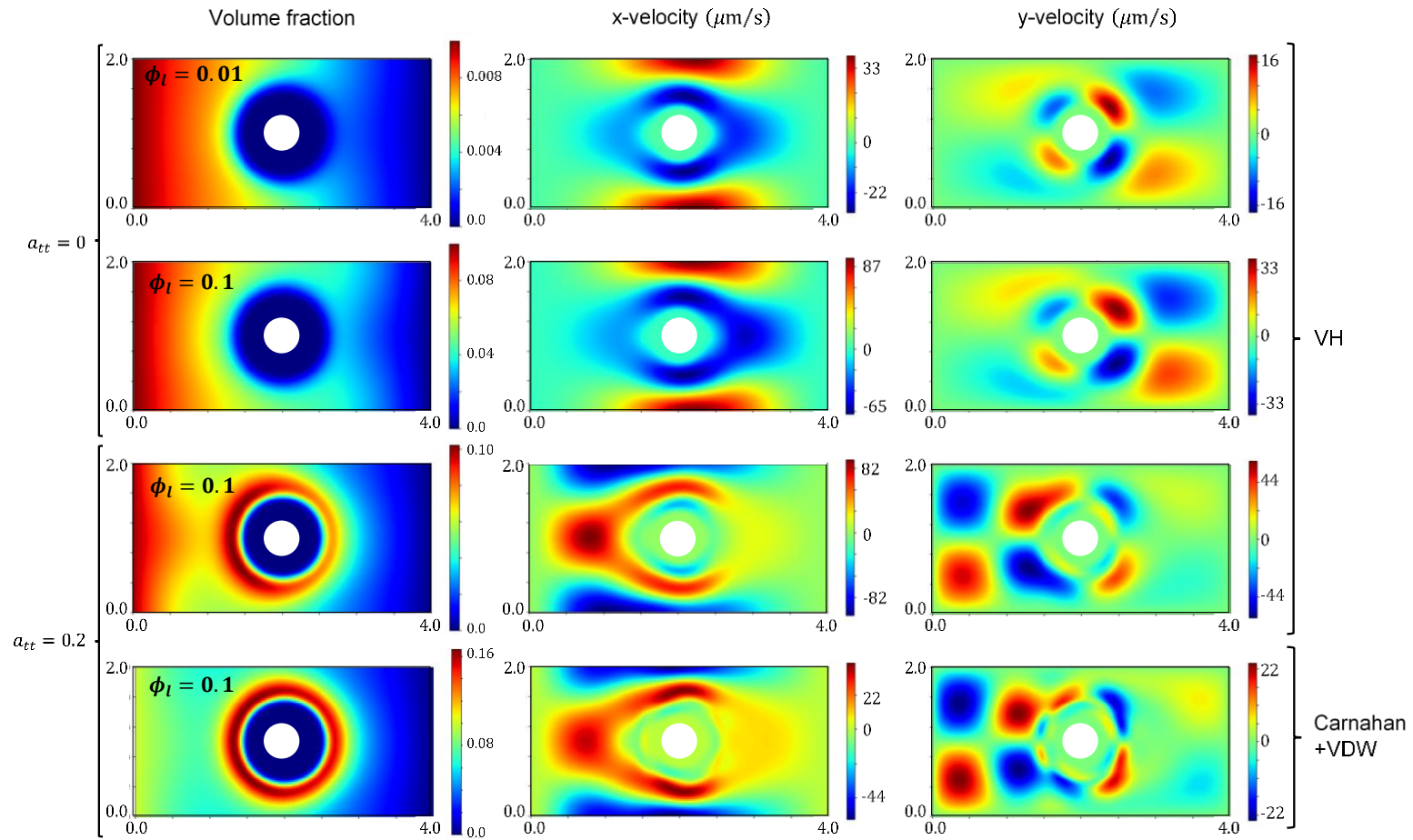


Figure III.12 – Colloid and velocity profiles at advection – osmosis equilibrium. Simulations are performed for different concentration differences, different colloid-cylinder interactions (by changing the parameter  $a_{tt}$ ) and for different EoS for colloids, which include a van 't Hoff (VH) or Carnahan repulsion term and a Van der Waals (VDW) attraction term.

### Chapter III. Numerical study of diffusioosmosis and diffusiophoresis

Finally, the last line of Figure III.12 displays results when using the Carnahan-Starling + VDW EoS (III.15). It shows that the profiles change significantly according to how the colloids interact with each other. When the van 't Hoff EoS is used to describe the colligative properties of colloids (lines 1-3), one neglects the impact of colloid – colloid interactions on the effective diffusion coefficient. Indeed, van 't Hoff law implies a constant diffusion coefficient (eq. (III.12)). When Carnahan-Starling + VDW EoS are used (line 4), colloid interactions are described with a more complex repulsive term. In this case, the effect of the colloid – colloid interactions on the diffusivity is captured by the derivative of the particle pressure with respect to  $\phi$  (eq. (III.16)).

In particular, the diffusivity close to the left boundary of the domain ( $\phi = 0.1$ ) is higher than the diffusivity at the right boundary ( $\phi = 0$ ). This difference generates some colloid accumulation in the domain. Indeed, we observe that the average colloid concentration  $\phi$  in the channel increases from 0.0576 (line 3) to 0.0638 (line 4). As a result, the colloid ring formed around the cylinder becomes much more pronounced. Colloid concentration peaks at  $\phi_{max} \approx 0.16$  in that area, which corresponds to a 60 % increase with respect to the concentration at the left boundary. At higher volume fractions, that could result in the formation of cakes around the cylinder.

The velocity profiles reflect this change in colloid distribution. When Carnahan + VDW EoS are used to model the particle interactions, the colloid distribution around the cylinder is nearly symmetric. In other words, colloid concentration can be approximated as a function of the distance to the cylinder ( $\phi \approx \phi(d)$ ) in the region  $d < 3.5R$ , with  $R$  being the radius of the cylinder. Furthermore, eq. (III.25) shows that  $\Pi_{ic}$  depends only on the distance  $d$ . Therefore, the body force term  $\phi \underline{\nabla} \Pi_{ic}$  in eq. (III.30) is almost radial close to the cylinder. This means that it can be approximated as a gradient of some function in the range  $d < 3.5R$ . Hence, this force can be balanced by the pressure profile, in the same way that pressure balances the gravitational force in a water bottle. This explains why the absolute velocity values decrease from the third to the fourth lines. Pressure drop changes as well, from -13.85 Pa with van 't Hoff EoS to -11.40 Pa using Carnahan + VDW EoS.

#### III.7 Diffusiophoresis results and discussion

This section discusses simulation results for the diffusiophoretic case study in Section III.2.2, obtained according to the models described in Section III.4.



III.7.1 Influence of initial conditions on long-time behaviour of the system

The transient formulations TEF (Section III.4.1) and TFCV (Section III.4.2) correspond to slightly different physical systems. TEF corresponds to a particle set free in a stagnant suspension. Its velocity changes according to the forces exerted on its surface, as indicated by the third equality in eq. (III.36). And as the name suggests, transient formulation at constant velocity (TFCV) assumes that particle velocity remains the same.

A question that arises when studying the motion of a particle in a mixture is whether the system “forgets” its initial state after a large enough time. This statement translates to both transient formulations as follows. Imagine two systems A and B under the same imposed far-field solute concentration gradient. Each of them contains a spherical particle of radius  $R$ , and at time  $t = 0$  these particles may be in different positions. The position of the spheres can be tracked by the far-field solute concentration  $\phi_m$ , so the initial positions will be named  $\phi_m^{A,0}$  and  $\phi_m^{B,0}$ . Without loss of generality, let us say these particles are moving right, and the sphere in system B starts ahead of the sphere in A. Eventually, these particles will reach a position  $\phi_m^{final}$ , though they will not reach this position at the same time. Still, is it possible to distinguish one system from another when they are at position  $\phi_m^{final}$ ? Figure III.13 illustrates the above discussion.

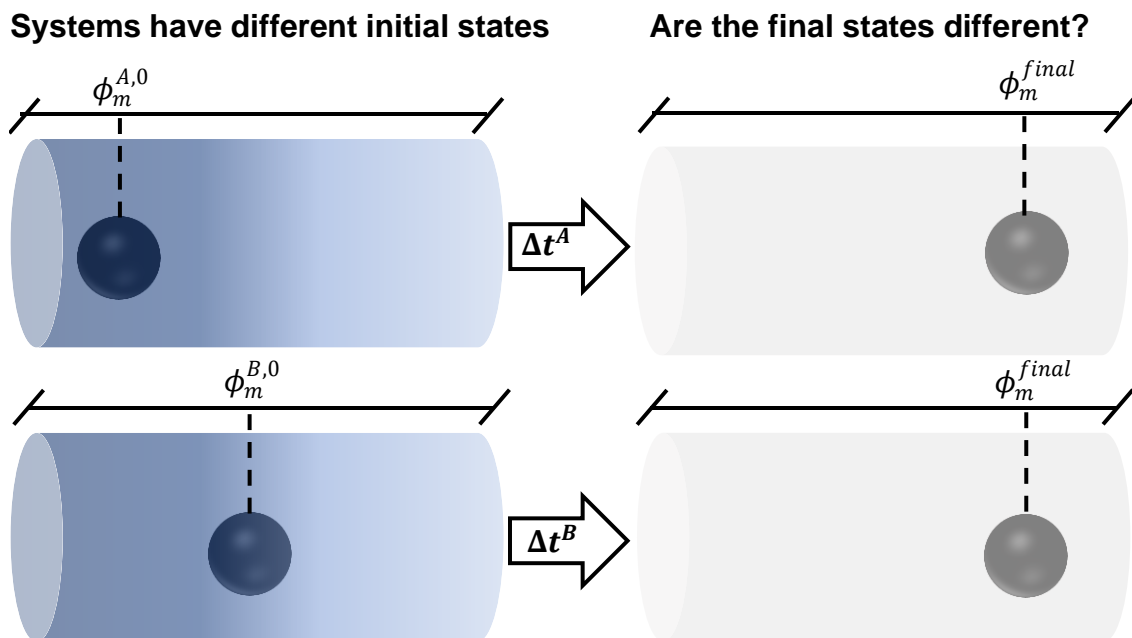


Figure III.13 – 2 particles that move under the same far-field solute concentration profile, but start at different positions. When the particles reach the position  $\phi_m^{final}$  far from their initial positions, will the solute concentration and velocity profiles look the same? In other words: does the state of a diffusiophoretic system depend on the initial conditions?

### Chapter III. Numerical study of diffusioosmosis and diffusiophoresis

The formal mathematical statement for the question depicted in Figure III.13 is given as follows. If the profiles  $\phi^A(\underline{x}, t)$ ,  $\underline{u}^A(\underline{x}, t)$  and  $\phi^B(\underline{x}, t)$ ,  $\underline{u}^B(\underline{x}, t)$  are solutions of eqs. (III.33)–(III.36), or eqs. (III.45)–(III.48), with same boundary conditions but with different initial conditions, then:

$$\lim_{t \rightarrow \infty} [\phi^A(\underline{x}, t + t') - \phi^B(\underline{x}, t)] \stackrel{?}{=} 0$$

$$\lim_{t \rightarrow \infty} [\underline{u}^A(\underline{x}, t + t') - \underline{u}^B(\underline{x}, t)] \stackrel{?}{=} \underline{0}$$
(III.61)

where  $t'$  is such that:

$$\phi_m^A(t + t') = \phi_m^B(t) \quad (III.62)$$

If eq. (III.61) is true, we can say that the system reaches a fully-developed state. That does not mean its properties will not change with respect to time, but rather that they become independent of the initial state.

The complexity and non-linearity of the PDE system describing diffusiophoresis make it extremely difficult to find a rigorous mathematical proof of eq. (III.61). However, numerical simulations can shed light on the validity of this equation. At first, one can investigate the evolutions of two systems A and B using the TFCV formulation described in Section III.4.2. Velocity  $\underline{v}_0$  in eq. (III.48) is set to 14.6  $\mu\text{m/s}$ . Besides, a diffusion coefficient of 21.8  $\mu\text{m}^2/\text{s}$  is considered. Both systems are under a linear far-field solute concentration profile with  $\nabla\phi^\infty = -6.25 \times 10^{-4} \mu\text{m}^{-1}$ . Further,  $\phi_m^{A,0} = 0.0065$  and  $\phi_m^{B,0} = 0.0059$  (i.e., particles start at different positions). The initial concentration profile  $\phi_0(\underline{x})$  is linear in both systems, with  $\underline{\nabla}\phi^A(\underline{x}, 0) = \underline{\nabla}\phi^B(\underline{x}, 0) = \nabla\phi^\infty \underline{e}_z$ . Figure III.14a shows how the forces in each system change with respect to the position  $\phi_m$  of the particle. Figure III.14b and Figure III.14c show two other pairs A, B with different diffusion coefficients (respectively 218 and 2180  $\mu\text{m}^2/\text{s}$ ) and particle velocities (81.5 and 203  $\mu\text{m/s}$  respectively). All simulations considered  $k_{ic} = 100$ ,  $l_{ic} = 0.1\mu\text{m}$  and  $a_{tt} = 0$ .

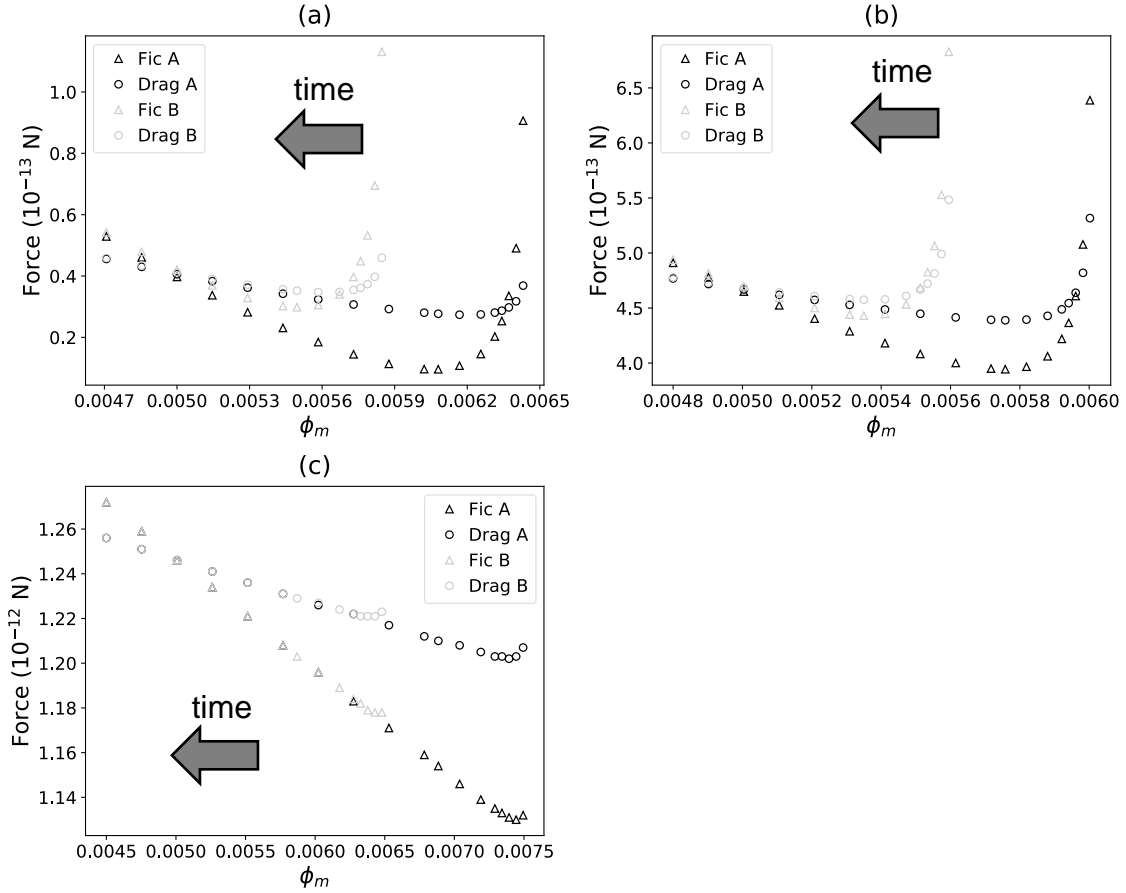


Figure III.14 – Colloid – interface force (triangles) and drag force (circles) acting on the particle in different pairs of systems A and B, in transition to fully-developed state according to TFCV predictions

The time arrow shows the direction of the particle movement (towards lower colloid concentrations). Note that in the range  $\phi_m \in (0.0059, 0.0065)$ , the plot in Figure III.14a only shows data for system A. That is because the particle in B starts at  $\phi_m^{B,0} = 0.0059$  and moves towards smaller values of  $\phi_m$ . All the systems included in Figure III.14 reach an equilibrium of forces ( $|F_{drag}| = |F_{ic}|$ ) when  $\phi_m = 0.005$ . Further, forces in each pair A,B tend to the same values as  $\phi_m$  gets smaller (i.e., as  $t \rightarrow \infty$ ). Such result suggests that eq. (III.61) is true, at least for the set of parameters used in these simulations. This conclusion is confirmed when comparing the concentration and velocity profiles for systems A and B in Figure III.14. For each pair, when  $\phi_m = 0.005$ , concentration and velocity profiles (not shown here for brevity) are identical everywhere, within the numerical accuracy.

Results for TEF modelling in Section III.4.1 show a similar behaviour. Let us consider two systems A and B with the same boundary conditions and initial velocity 0, but starting

### Chapter III. Numerical study of diffusioosmosis and diffusiophoresis

at different positions ( $\phi_m^{A,0} \neq \phi_m^{B,0}$ ). As the particles move away from their initial positions, we observe that the velocities and forces on each particle tend to the same values. Further, colloid concentration and velocity profiles converge to the same values, indicating that eq. (III.61) is valid in the transient exact formulation. Figure III.15 illustrates this behaviour for one particular pair of systems, with  $D = 2180 \mu\text{m}^2/\text{s}$ ,  $\nabla\phi^\infty = -625\text{m}^{-1}$ ,  $k_{ic} = 100$ ,  $l_{ic} = 0.1 \mu\text{m}$ , and  $a_{tt} = 0$ . The initial positions for A and B are  $\phi_m^{A,0} = 0.0065$  and  $\phi_m^{B,0} = 0.0061$ .

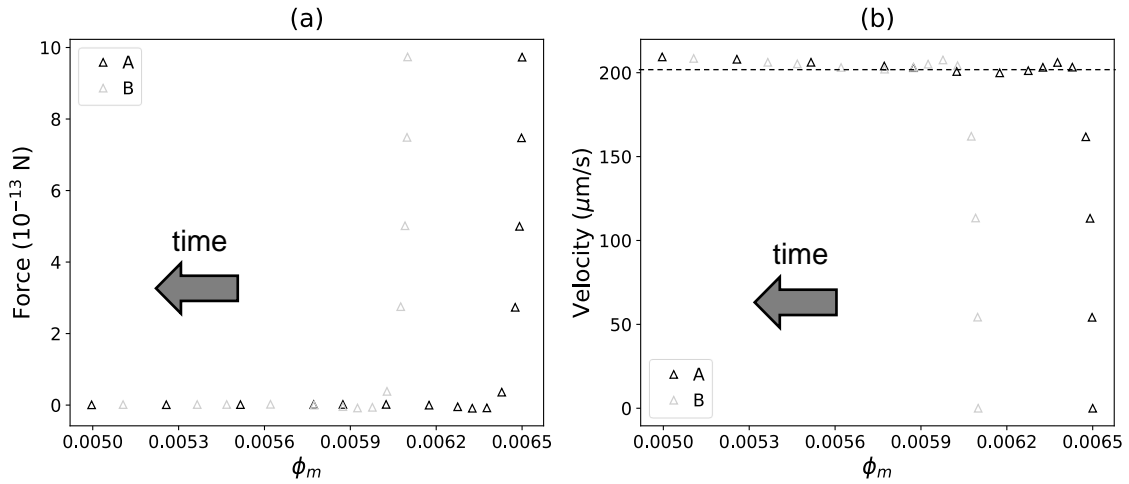


Figure III.15 – Resultant force (a) and particle velocity (b) for a pair of systems A,B in transition to fully-developed state according to TEF predictions; the dashed line corresponds to the diffusiophoretic velocity predicted by TFCV for  $\phi_m = 0.005$

#### III.7.2 Separation of particles via diffusiophoresis

Apart from showing the existence of fully-developed out-of-equilibrium states, TEF simulations also highlighted an interesting application of diffusiophoresis in particle separation (Velegol et al., 2016). Eq. (III.56), obtained in the high diffusion limit, suggests that particles immersed in the same mixture will have different  $v_{DP}$  according to their size and to the interface-solute interactions each of them generates. Therefore, particles with different size or with different surface properties may be separated via diffusiophoresis. Figure III.16 illustrates this phenomenon for two particles with the same size  $R = 0.2 \mu\text{m}$ , but different interaction potentials  $\Pi_{ic}$  (both given by eq. (III.25);  $a_{tt} = 0.1$  for the particle at the left and  $a_{tt} = 0$  for the particle at the right). The particle at the left moves towards the region with higher solute concentration, whereas the particle at the right moves towards the region with lower solute concentration.

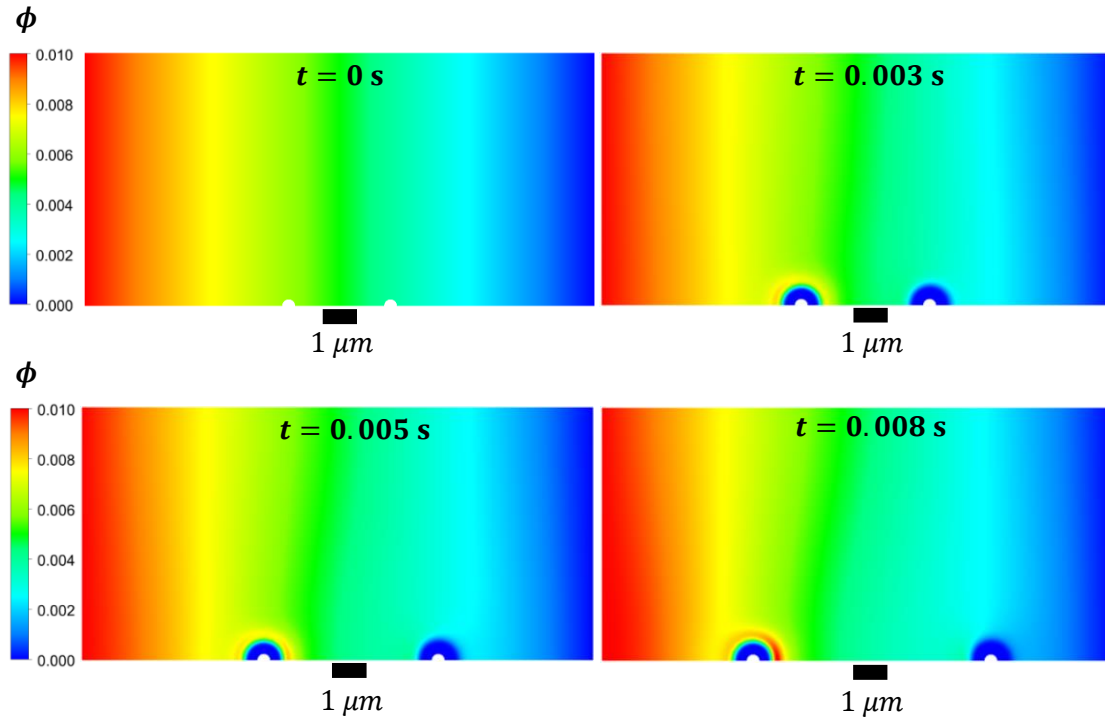


Figure III.16 – Evolution of solute concentration profile and particle position, illustrating particle separation via diffusiophoresis

### III.7.3 Influence of solute concentration, diffusivity and concentration gradient on diffusiophoretic velocities

Note that none of the systems discussed so far is permanently at equilibrium. Indeed, the drag forces and solute-interface forces in Figure III.14 equilibrate each other at  $\phi_m = 0.005$  only. Furthermore, the velocities of the diffusiophoretic particles in Figure III.15 never reach a plateau: they increase at a low rate even by the end of the simulation. This happens because the equilibrium velocity (i.e., the velocity for which drag and solute-interface forces equilibrate each other) generally depends on  $\phi_m$ .

There are a few limit cases for which the equilibrium velocity does not depend on the far-field solute concentration  $\phi_m$ . This is true for the high diffusion limit (see eq. (III.56)), for steric repulsion when interaction range is much smaller than particle radius (Khair, 2013), and for adsorptive interactions when the range of solute – particle interactions and the adsorption length are much smaller than the particle radius (Anderson and Prieve, 1984, 1991). However, other systems have been described for which equilibrium diffusiophoresis velocity depends on the position of the particle with respect to the far-field solute concentration. For example, the equilibrium velocity  $v_{DP}$  of a charged particle

### Chapter III. Numerical study of diffusioosmosis and diffusiophoresis

in an electrolyte solution is proportional to  $\nabla\phi^\infty/\phi_m$  (Anderson, 1989). This velocity depends not only on the imposed far-field electrolyte concentration gradient  $\nabla\phi^\infty$ , but also on the position of the particle with respect to this far-field ( $\phi_m$ ). We expect  $v_{DP}$  to change as the particle moves through the solution, since  $\phi_m$  does not remain constant.

Diffusiophoresis velocity also depends on the position of the particle if adsorption lengths are not negligible compared to the particle radius. Anderson and Prieve (1984, 1991) derived an expression for the diffusiophoresis velocity in this case, assuming that the range of solute-particle interaction (not to be confused with the adsorption length) is much smaller than the particle radius. Their results showed that  $v_{DP}$  is proportional to  $[1 + (1 + l_1 \phi_m/D) K/R]^{-1} \nabla\phi^\infty$ , where  $K$  is the adsorption length and  $l_1$  depends on the interaction potential, temperature, and viscosity.

Simulation results in Table III.4 show that the TFCV model presented in Section III.4.2 accounts for the velocity dependency on the position featured by  $\phi_m$ . All these simulations were performed according to the solute – interface interaction potential in eq. (III.25). The first row in this table gives the equilibrium velocity for a reference set of parameters ( $a_{tt} = 0$ ,  $l_{ic} = 0.1 \mu\text{m}$ ,  $k_{ic} = 100$ ,  $\phi_m = 0.005$ ,  $D = 218 \mu\text{m}^2/\text{s}$  and  $\nabla\phi^\infty = -625\text{m}^{-1}$ ). Simulations 9 – 29 prove that velocity is a function of  $\phi_m$ . Further, results for  $l_{ic} = 0.01 \mu\text{m}$  or  $k_{ic} = 10$  (see eq. (III.25)) show how this dependency is affected by the solute – interface interaction potential. As the interaction width  $l_{ic}$  decreases from 0.1 to 0.01  $\mu\text{m}$  (simulations 23 – 29 in Table III.4), the relative change in velocity with respect to  $\phi_m$  is less significant. This is in agreement with previous results obtained for short-range steric repulsions (Khair, 2013). Besides, velocity variation with respect to  $\phi_m$  decreases when the potential magnitude  $k_{ic}$  decreases from 100 to 10 (simulations 17 – 22).

Another important feature, shown by simulations 4 – 7, is that as  $D \rightarrow \infty$  the equilibrium velocity approaches the value of 242  $\mu\text{m}/\text{s}$  obtained assuming HDL (simulation 8). Further, simulations 1 – 3 show that velocity is a linear function of  $\nabla\phi^\infty$ . This result is in agreement with the various studies on diffusiophoresis cited in this chapter (Anderson and Prieve, 1984, 1991; Churaev et al., 1987; Anderson, 1989; Marbach et al., 2020; Ramírez-Hinestrosa et al., 2020; Rasmussen et al., 2020). Finally, simulations 9 – 16 suggest that the velocity depends on the factor  $D/\phi_m$ , as predicted by Anderson and Prieve (1984, 1991) in the limit of small solute – particle interaction range.

### Chapter III. Numerical study of diffusioosmosis and diffusiophoresis

Table III.4 – Equilibrium velocities obtained with TFCV for different sets of parameters

Number	$v_{DP}$ ( $\mu\text{m/s}$ )	$a_{tt}$	$l_{ic}$ ( $\mu\text{m}$ )	$k_{ic}$	$\phi_m$	$D$ ( $\mu\text{m}^2/\text{s}$ )	$\nabla\phi^\infty$ ( $\text{m}^{-1}$ )
1	80.9	0	0.1	100	0.005	218	-625
2	51.8	0	0.1	100	0.005	218	<b>-400</b>
3	26.0	0	0.1	100	0.005	218	<b>-200</b>
4	14.5	0	0.1	100	0.005	<b>21.8</b>	-625
5	80.9	0	0.1	100	0.005	218	-625
6	200	0	0.1	100	0.005	<b>2180</b>	-625
7	238	0	0.1	100	0.005	<b>21800</b>	-625
8 <sup>†</sup>	242	0	0.1	100	0.005	$\infty$	-625
9	80.9	0	0.1	100	0.005	218	-625
10	82.3	0	0.1	100	<b>0.05</b>	<b>2180</b>	-625
11	14.5	0	0.1	100	0.005	<b>21.8</b>	-625
12	14.6	0	0.1	100	<b>0.05</b>	218	-625
13	238	0	0.1	100	0.005	<b>21800</b>	-625
14	237	0	0.1	100	<b>0.0005</b>	<b>2180</b>	-625
15 <sup>†</sup>	242	0	0.1	100	0.005	$\infty$	-625
16 <sup>‡</sup>	231	0	0.1	100	<b>0</b>	218	-625
17	80.9	0	0.1	100	0.005	218	-625
18	29.1	0	0.1	100	<b>0.02</b>	218	-625
19	14.6	0	0.1	100	<b>0.05</b>	218	-625
20	46.5	0	0.1	<b>10</b>	0.005	218	-625
21	27.9	0	0.1	<b>10</b>	<b>0.02</b>	218	-625
22	16.5	0	0.1	<b>10</b>	<b>0.05</b>	218	-625
23 <sup>‡</sup>	231	0	0.1	100	<b>0</b>	218	-625
24	80.9	0	0.1	100	0.005	218	-625
25	29.1	0	0.1	100	<b>0.02</b>	218	-625
26	14.6	0	0.1	100	<b>0.05</b>	218	-625
27	1.07	0	<b>0.01</b>	100	0.005	218	-625
28	1.06	0	<b>0.01</b>	100	<b>0.02</b>	218	-625
29	1.03	0	<b>0.01</b>	100	<b>0.05</b>	218	-625

<sup>†</sup> Use of HDL model instead of TFCV model

<sup>‡</sup> This result is purely mathematical and has no physical significance, since  $\phi_m = 0$  and  $\nabla\phi^\infty \neq 0$  implies negative solute concentrations in the simulation domain

### Chapter III. Numerical study of diffusioosmosis and diffusiophoresis

Table III.4 – Equilibrium velocities obtained with TFCV for different sets of parameters (cont.)

Number	$v_{DP}$ ( $\mu\text{m/s}$ )	$a_{tt}$	$l_{ic}$ ( $\mu\text{m}$ )	$k_{ic}$	$\phi_m$	$D$ ( $\mu\text{m}^2/\text{s}$ )	$\nabla\phi^\infty$ ( $\text{m}^{-1}$ )
30	200	<b>0</b>	0.1	100	0.005	<b>2180</b>	-625
31	62.8	<b>0.061</b>	0.1	100	0.005	<b>2180</b>	-625
32	-3.66	<b>0.086</b>	0.1	100	0.005	<b>2180</b>	-625
33	-237	<b>0.4</b>	0.1	100	0.005	<b>2180</b>	-625
34	-143	<b>0.7</b>	0.1	100	0.005	<b>2180</b>	-625
35	-252	<b>0.9</b>	0.1	100	0.005	<b>2180</b>	-625
36	-390	<b>1.1</b>	0.1	100	0.005	<b>2180</b>	-625

With these observations, a suitable fitting function could be derived, which approximates the diffusiophoretic velocity in the range of values  $\phi_m$ ,  $D$  and  $\nabla\phi^\infty$  shown in Table III.4. This function is given by eq. (III.63), and the comparison between fitted and simulated velocity values is shown in Figure III.17. All numerical values (385298, 69708 and 20509) in eq. (III.63) have units of  $\mu\text{m}^2/\text{s}$ . Note that this regression was made considering only the simulations with  $k_{ic} = 100$ ,  $l_{ic} = 0.1 \mu\text{m}$  and  $a_{tt} = 0$ . In general, these numerical values will change with respect to these parameters.

$$v_{DP} = -385298 \nabla\phi^\infty \exp\left(-\frac{69708}{D/\phi_m + 20509}\right) \quad (\text{III.63})$$

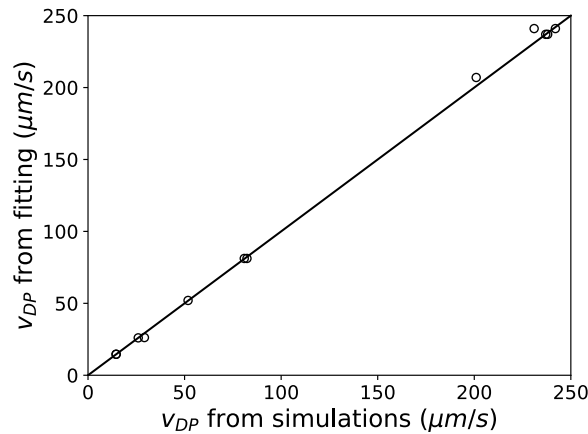


Figure III.17 – Comparison between diffusiophoretic velocities obtained via simulation (x-axis) and via the fitting equation (III.63) (y-axis) for  $k_{ic} = 100$ ,  $l_{ic} = 0.1 \mu\text{m}$  and  $a_{tt} = 0$



### Chapter III. Numerical study of diffusioosmosis and diffusiophoresis

To confirm the validity of eq. (III.63), a random set of values within the ranges shown in Table III.2 were assigned for  $\nabla\phi^\infty$  ( $-504\text{m}^{-1}$ ),  $\phi_m$  (0.0054) and  $D$  ( $186\ \mu\text{m}^2/\text{s}$ ). The velocity calculated according to eq. (III.63) is  $54.6\ \mu\text{m}/\text{s}$ , corresponding to a relative error of only  $-2.0\%$  when compared to the velocity obtained from simulations ( $55.7\ \mu\text{m}/\text{s}$ ). Hence, this equation successfully concludes one of the objectives listed in Section III.2: to derive an expression for the diffusiophoretic velocity as a function of the problem parameters. Despite being limited to one specific solute – solvent interaction potential, it gives a great insight into how the other physical quantities affect diffusiophoresis. Besides, this equation is derived without assuming infinite diffusivity, thin interaction layer or weak interaction strength. To the best of the author’s knowledge, no explicit relation for diffusiophoretic velocities has been derived before without at least one of these assumptions.

At this point, it is important to recall that the diffusiophoretic velocities in Table III.4 and eq. (III.63) correspond to null-force equilibrium states obtained using the TFCV model. However, it was shown in Figure III.14 that such states are instantaneous: as soon as the particle moves away from the  $\phi_m$  position corresponding to equilibrium, the sum of forces acting on the particle becomes non-zero. This suggests that in the actual diffusiophoretic system, described by TEF, the only possible stable equilibrium state corresponds to  $v_{DP} = 0$ . That is because the equilibrium velocities generally change with respect to  $\phi_m$ , but stable equilibrium states imply constant velocity. The only constant velocity that ensures constant  $\phi_m$  value is  $v_{DP} = 0$ .

Such a configuration could evolve as follows: the particle placed at  $\phi_m$  accelerates towards its equilibrium location. As it approaches such a location, it eventually starts to slow down until it stops right on the equilibrium position. Another hypothesis is that it would oscillate around its equilibrium location with decreasing oscillation amplitudes at each passage, until it eventually stops. Unfortunately, neither of these phenomena could be observed from the several simulations that were carried out. Even though there are suitable choices of  $a_{tt}^*$ ,  $\phi_m^*$  and other parameters for which  $v_{DP} = 0$ , the equilibrium in these cases is unstable: if the particle is placed slightly off the position  $\phi_m^*$ , it starts moving away from it. Perhaps with other types of solute-interface interaction potentials, stable equilibrium could be reached.

III.7.4 Influence of solute – interface interactions on diffusiophoretic velocity

The last set of simulations in Table III.4 (30-36) shows the variation of  $v_{DP}$  with respect to the attraction parameter  $a_{tt}$  modulating the solute-interface interactions. For purely repulsive interactions, the sphere moves against solute concentration gradient. However, as  $a_{tt}$  increases this tendency is inverted. Note that the effect of this parameter on the diffusiophoretic velocity is non-monotonic:  $v_{DP}$  decreases from  $a_{tt} = 0$  to  $a_{tt} = 0.4$ , increases from  $a_{tt} = 0.4$  to  $a_{tt} = 0.7$ , and decreases again for  $a_{tt} > 0.7$ . A similar behaviour is mentioned in Section III.1.3, when the paper by Ramírez-Hinestrosa et al. (2020) is discussed. Figure III.18 compares the variations in particle mobility as a function of  $a_{tt}$  (present study) and as a function of the solute–monomer dispersion energy  $\epsilon_{ms}$  (Ramírez-Hinestrosa et al., 2020).

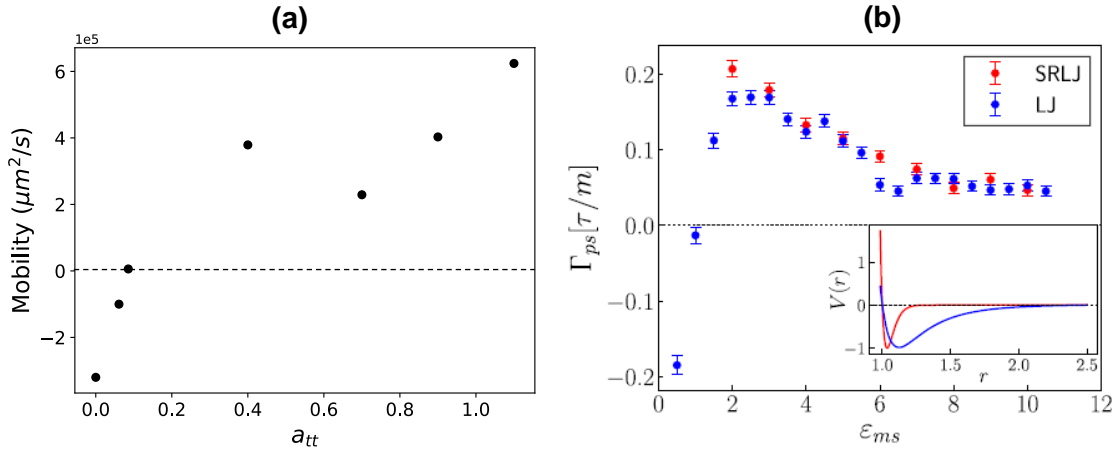


Figure III.18 – (a) Particle mobility vs attraction parameter, according to fluid simulation results in Table III.4; (b) particle mobility vs solute – monomer dispersion energy  $\epsilon_{ms}$ , according to molecular simulations (extracted from Ramírez-Hinestrosa et al. (2020) with permission from AIP)

The definition of mobility changes slightly between both works: whereas the present manuscript defines mobility as  $\Gamma = v_{DP}/\nabla\phi^\infty$ , Ramírez-Hinestrosa et al. (2020) sets  $\Gamma = v_{DP}/F_s$ , where  $F_s$  is an external force acting on the solute particles. However, this difference does not prevent a comparison between the results, as the external force considered in the molecular simulations mimics the effect of explicit concentration gradients.

### Chapter III. Numerical study of diffusioosmosis and diffusiophoresis

Both plots in Figure III.18 show an initial increase in mobility as the solute-interface attraction becomes stronger. When repulsion dominates over attraction (small  $a_{tt}$  and  $\epsilon_{ms}$  values), the particle moves towards lower solute concentrations, and  $\Gamma < 0$ . Zero mobility is attained for  $a_{tt} = 0.086$  (Figure III.18a) and for  $\epsilon_{ms} = 1\epsilon_0$  (Figure III.18b), where  $\epsilon_0$  is a reference energy. The latter result is almost trivial after a closer look into the paper by Ramírez-Hinestrosa et al. (2020). In this paper, the authors simulate solute-solute, solute-solvent, solvent-solvent, solvent-monomer and solute-monomer interactions via a 12-6 Lennard-Jones potential, setting all the binary interaction lengths to  $\sigma_0$ . Further, all dispersion energies are set to  $1\epsilon_0$ , except possibly for solute-monomer interactions  $\epsilon_{ms}$ . When  $\epsilon_{ms} = 1\epsilon_0$ , the monomers are indistinguishable from solute and solvent molecules, and diffusiophoresis no longer takes place. The same is not true for the macroscopic approach that generated Figure III.18a. Indeed, even when  $v_{DP}$ , and thus mobility, approaches 0 (simulation 32 in Table III.4), the effect of the interface on the mixture was very pronounced. It changes solute distribution significantly near the sphere and drives diffusioosmotic flow (profiles not shown for brevity).

When attraction dominates over repulsion, the interface tends to move towards higher solute concentrations, and  $\Gamma > 0$ . Particle mobility continues to increase with respect to  $a_{tt}$  and  $\epsilon_{ms}$  until it reaches a maximum value at  $a_{tt} = 0.4$  and  $\epsilon_{ms} \approx 2.5\epsilon_0$ . A possible reason for this local maximum is given by Ramírez-Hinestrosa et al. (2020): as the adsorption interactions get stronger, the solute particles surrounding the sphere become immobilized, hindering diffusiophoresis. Reasoning in mathematical terms for the case study in Figure III.8, the solute distribution around the interface becomes more symmetric as the attraction parameter increases, decreasing the resultant force exerted by the solute on the sphere.

The systems start to behave differently for large attraction parameters: whereas Ramírez-Hinestrosa et al. (2020) predict an asymptotic decay for the mobility, this work has found that the mobility reaches a minimum (for  $a_{tt} = 0.7$ ) and then increases indefinitely. Some possible explanations for this discrepancy are listed below:

- i) Ramírez-Hinestrosa et al. (2020) considers a truncated potential, whereas in this work the interface can interact with the solute everywhere in the domain. To understand how this may affect the behaviour of the curves in Figure III.18, let us briefly summarize the discussion from the previous paragraphs. As the

### Chapter III. Numerical study of diffusioosmosis and diffusiophoresis

adsorption strength increases, the strength of solute-interface attraction increases, and the interface tends to move faster and faster towards higher solute concentrations. However, after a certain threshold this increment in the individual interaction forces is offset by the increasing symmetry of the solute concentration profile, and mobility starts decreasing. This explains the local maximum at  $a_{tt} = 0.4$  and  $\epsilon_{ms} \approx 2.5\epsilon_0$ . In the paper by Ramírez-Hinestrosa et al. (2020), the monomer-solute interaction potential is truncated at a certain distance  $\sigma$ . If  $\epsilon_{ms}$  is large enough, the entire range of interaction  $\sigma$  may be immobilized, and  $\Gamma$  will decrease asymptotically according to Figure III.18b. On the other hand,  $\Pi_{ic}$  used in this work is not truncated, and an increase in  $a_{tt}$  will also increase the range of interaction between the sphere and the solute. For  $a_{tt} > 0.7$ , this effect probably overcomes the increasing symmetry of the solute distribution, and the mobility starts increasing again with respect to  $a_{tt}$ .

- ii) In the models described in Section III.4, even though solute concentration is given in terms of volume fraction, solute – solute interactions are neglected. However, the size of the solute particles in the mixture is accounted for in molecular simulations via the solute – solute Lennard-Jones potential, which limits solute accumulation around the polymer. These solute – solute interactions surely play an important role in Ramírez-Hinestrosa et al. (2020), since solute molar fraction in the bulk was set to 0.5 in their work. Other simplifying assumptions in the models described in this work, such as incompressible fluid and constant viscosity (i.e., viscosity independent of solute concentration) may also contribute to the discrepancies seen in Figure III.18.
- iii) The small size of the polymer in the molecular simulations by Ramírez-Hinestrosa et al. (2020) makes the problem fundamentally different from the case study investigated here (Figure III.8). For large ratios between molecular mean free path and characteristic length of the system, molecular simulations are generally in agreement with the governing (continuum) equations for fluid dynamics and solute transport (Zhang and Ma, 2020). However, in the work by Ramírez-Hinestrosa et al. (2020) the representative physical length scale for the phenomenon is the size of the polymer, which is close to the mean free path of the solvent molecules. Indeed, Figure III.18b considers a polymer

### Chapter III. Numerical study of diffusioosmosis and diffusiophoresis

made of 30 monomers; when  $\epsilon_{ms} = 8\epsilon_0$ , the equivalent hydrodynamic radius of the polymer is  $R_p \approx 2.4\sigma_0$ , comparable to the mean free path  $l_{free} \approx \sigma_0$  of solvent molecules (the length parameter in the Lennard-Jones potential). It is recalled that the representative physical length scale in the case study shown in Figure III.8 (and used to obtain the points in Figure III.18a) is  $R = 0.2\mu\text{m}$ . This length scale is several orders of magnitude higher than the molecular spacing in liquid water. It is possible that this difference in the orders of magnitude makes the works incomparable. Still, it is interesting to notice that, as  $\epsilon_{ms}$  decreases, the hydraulic radius of the polymer increases (e.g.,  $R_p \approx 4.8\sigma_0$  when  $\epsilon_{ms} = 1.5\epsilon_0$ ). And it is precisely in the region of low  $\epsilon_{ms}$  (and low  $a_{tt}$ ) that qualitative agreement exists between the curves in Figure III.18. This could be because the higher hydraulic radius at low  $\epsilon_{ms}$  makes the polymer diffusiophoresis phenomenon more “continuum-like”.

#### III.8 Summary

This chapter has covered various aspects of diffusioosmosis and diffusiophoresis through numerical simulations. First, the effect of colloid concentration difference  $\Delta\phi$ , colloid-interface interactions and equations of state for colloid – colloid interactions were investigated in the context of suspension flow through a membrane. The membrane was modelled as an array of cylindrical obstacles in a channel connecting two reservoirs, and the advection-osmosis equilibrium (when there is no net flow between the reservoirs) was the target of this study. Membrane selectivity is modelled via the energy map  $\Pi_{ic}$  in eq. (III.25) that describes colloid-interface interactions.

Numerical results show that higher concentration differences increase velocity in the channel. Further, these higher concentration differences require higher pressure drops to prevent the mixture from flowing between the reservoirs. This agrees qualitatively with classic results for membranes. However, the reflection coefficients  $\sigma_0$  calculated from numerical simulations differ from those reported in the literature. More specifically, the simulations performed in Section III.6 show a dependency of  $\sigma_0$  on colloid concentration difference  $\Delta\phi$  between the reservoirs, despite many theoretical works on membrane separation claiming the opposite. Presumable reasons for this discrepancy are the difference in the geometry of the membranes and a number of simplifying assumptions in the literature that are not accounted for in the present simulations. For example,

### Chapter III. Numerical study of diffusioosmosis and diffusiophoresis

(Marbach et al., 2017) modelled a membrane with a 1D geometry to derive eq. (III.23). Further, to derive eq. (III.20), Anderson and Malone (1974) assume a cylindrical pore geometry, neglect the gradient of the radial velocity in the momentum balance of the fluid along the radial direction, and neglect axial variations of the axial velocity in the momentum balance of the fluid along the axial direction. The authors also assume that solute concentration follows a Boltzmann distribution along the radial direction.

This result could have an impact in membrane separation processes. For example, let us assume a hypothetical membrane filtration whose efficiency is lower when particle concentration in the retentate side higher. Engineers may attribute this behaviour to particle – particle interactions, which is the common explanation for reflection coefficients depending on concentration differences (Adamski and Anderson, 1983; Marbach et al., 2017). And since these forces cannot be tuned or controlled, engineering solutions would likely focus on additional separation steps to separate the mixture. However, the simulations performed in this thesis suggest that reflection coefficients might depend on particle concentration even in the absence of particle – particle interactions (when VH EoS holds). As discussed previously, this could be due to the geometry of the membrane. Hence, alternative solutions using different membrane structures may be viable and even preferred over the inclusion of additional separation steps.

After  $\Delta\phi$ , the next aspect of the system to be investigated was the energy map  $\Pi_{ic}$ . The inclusion of long-range attraction (by setting  $a_{tt} = 0.2$  in eq. (III.25)) creates an adsorption zone around the cylinder. This result, also reported in Bacchin et al. (2019), suggests that long-range colloid – interface attraction could accelerate cake formation by increasing solute concentration near the membrane. Overall, the flow becomes more complex, with several vortices forming in the domain, and the pressure drop can be inverted if the attraction is sufficiently strong. This inversion characterizes the anomalous osmosis that was described earlier in Section III.1.2.

Finally, it was found that using the van 't Hoff model in eq. (III.11) for colloid-colloid interactions underestimates the increase in colloid concentration around the cylinder. This is because colloid diffusivity in such a model does not depend on absolute colloid concentration, whereas in reality this diffusivity increases with respect to colloid concentration in the low  $\phi$  range ( $\phi < 0.35$  considering Carnahan + VDW EoS). Because

### Chapter III. Numerical study of diffusioosmosis and diffusiophoresis

of this dependency, the boundary richer in colloid has higher colloid diffusivity, resulting in an average colloid concentration higher than the one predicted with the van 't Hoff model. This larger average concentration is the reason for the higher concentration peak ( $\phi_{max} \approx 0.16$ ) in the last row of Figure III.12, which considers Carnahan-Starling + VDW EoS. For larger concentration differences and/or stronger attraction interactions, van 't Hoff model will underestimate the potential for cake formation due to these concentration peaks. Hence, modelling of membrane processes prone to fouling should use appropriate equations of state for particle – particle interactions. That concludes the summary of the numerical work on diffusioosmosis.

For the diffusiophoretic case study, a different geometry was adopted. It consists of a spherical obstacle placed under a gradient of solute concentration. Three different models were used to achieve different goals. The Transient Exact Formulation (TEF) was used to assess the actual dynamics of a diffusiophoretic system. From this model it was found that diffusiophoresis is a valid mechanism for particle separation, as depicted in Figure III.16. The Transient Formulation at Constant Velocity (TFCV) was used in combination with TEF to demonstrate that diffusiophoretic systems “forget” their initial state after a certain amount of time (see Figure III.14 and Figure III.15). Further, they were used together to retrieve unstable equilibrium states as follows. Fine tuning of  $\phi_m$  and  $a_{tt}$  was performed to retrieve  $v_{DP} = 0$  from TFCV simulations. After that, TEF simulations were run to show that if the particle is placed at  $\phi_m + \epsilon$  it moves away from equilibrium towards higher solute concentrations, and if it is placed at  $\phi_m - \epsilon$  it moves away from equilibrium towards lower solute concentrations.

TFCV alone was employed to regress the mathematical expression (III.63) that relates the diffusiophoretic velocity to  $\phi_m$ ,  $D$  and  $\nabla\phi^\infty$ . The equation shows that velocity is proportional to  $\nabla\phi^\infty$ , as predicted by various authors cited in this chapter. Further, it suggests that the dependency of  $v_{DP}$  on  $D$  and  $\phi_m$  is captured by the joint term  $D/\phi_m$ . The dependency of  $v_{DP}$  on this term was found before by Anderson and Prieve (1984, 1991), but in the limit of infinitely thin solute-interface interaction layers. In fact, all the explicit equations for  $v_{DP}$  provided in the literature reviewed for this thesis were derived assuming infinite diffusivity, thin interaction layer or weak interaction strength.

TFCV was also used to investigate the effect of long-range solute-interface attraction on the particle mobility. This study was performed by varying the parameter  $a_{tt}$  in eq.

### Chapter III. Numerical study of diffusioosmosis and diffusiophoresis

(III.25). It was found that the mobility changes with respect to  $a_{tt}$  in a non-monotonic way, as illustrated by Figure III.18a. The results were compared with those from a benchmark work on molecular simulations applied to diffusiophoresis (Ramírez-Hinestrosa et al., 2020). Both studies agree in the range of small attraction forces, showing an inversion of particle mobility after a certain attraction threshold, followed by a peak of maximum phoretic mobility and a subsequent decrease (Figure III.18). However, discrepancies arise as attraction forces are further increased. Ramírez-Hinestrosa et al. (2020) predict that mobility decreases asymptotically in the limit of strong attraction interactions, whereas the present study predicts that mobility reaches a local minimum and then increases indefinitely as  $a_{tt} \rightarrow \infty$ . Probable reasons for this discrepancy are listed by the end of Section III.7.4.

Finally, the High Diffusion Limit (HDL) was used first to validate the mesh used for simulations. This was done by setting  $\Pi_{ic}$  according to eq. (III.58). Such a suitable choice results in the fully analytic expression (III.60) for diffusiophoretic velocity, which can be compared to  $v_{DP}$  obtained via numerical simulations. Besides, HDL can be used to verify whether the TFCV implementation behaves properly at high  $D$  values, according to simulations 4-8 in Table III.4.

The discussion presented here regarding diffusiophoresis clarifies various aspects of this phenomenon, benefitting its modelling and global understanding. This may be particularly useful in microfluidics, where particle separation via diffusiophoresis is a topic of great interest (Shin, 2020).





---

## Chapter IV. Rebuttal of Ziegler's MaxEP principle

---

The Maximum Entropy Production (MaxEP) was proposed by Ziegler (1961, 1983a) as an attempt to generalize the Onsager's reciprocal relations for far-from-equilibrium systems. MaxEP has found wide acceptance in the literature, with many authors advocating for it. However, there are some flaws and severe limitations to this principle, which are raised here. More specifically, this chapter aims to refute the MaxEP demonstration as proposed by Ziegler (1970), and to show a simple example for which the principle fails to predict the thermodynamic fluxes of the system. Section IV.1 gives the concepts and principles in thermodynamics that will assist in the understanding and rebuttal of Ziegler's principle. Three different nonequilibrium thermodynamic theories are discussed in this section: Onsager's reciprocal relations, Prigogine's Minimum Entropy Production (minEP) principle and Ziegler's MaxEP principle. Section IV.2 reproduces in detail the derivation of the orthogonality principle, from which the MaxEP principle stems. It also highlights the main flaws and limitation in this derivation. The next section discusses a reactive system that violates MaxEP. Section IV.4 brings other criticisms of MaxEP, and attempts to refute some of the counterarguments of those who advocate for it. Finally, Section IV.5 summarizes the main findings of this chapter.

### IV.1 Literature review

#### IV.1.1 Onsager's reciprocal relations

Onsager's reciprocal relations were briefly discussed in Section I.3. These relations are applied to linear non-equilibrium thermodynamics, and they state that, under certain assumptions, the matrix of phenomenological coefficients relating fluxes and forces is symmetric. For example, one may recall the coupling described in Section I.3 between heat conduction and diffusive flux in a continuous system when only one solute species is present in solution:

$$\underline{q} = \overbrace{L_{qq} \nabla \left( \frac{1}{T} \right)}^{\text{Fourier's law}} + \overbrace{L_{qj} \frac{1}{M_1 T} \nabla^T \mu_1}^{\text{Dufour effect}} \quad (\text{IV.1})$$

$$\underline{J}_1 = \overbrace{\frac{L_{jj}}{M_1 T} \nabla^T \mu_1}^{\text{Fick's law}} + \overbrace{L_{jq} \nabla \left( \frac{1}{T} \right)}^{\text{Soret effect}} \quad (\text{IV.2})$$

## Chapter IV. Rebuttal of Ziegler's MaxEP principle

In eqs. (IV.1) and (IV.2),  $\underline{q}$  and  $\underline{J}_1$  are respectively the heat and diffusive flux,  $L_{qq}$  is the linear ratio linking the heat flux to the gradient of  $1/T$ , and  $L_{jj}$  is the ratio linking the diffusive flux to the gradient of chemical potential (in the absence of temperature gradients). Further,  $L_{jq}$  and  $L_{jq}$  are the coupling coefficients linking both phenomena. In this simple case, Onsager's theorem states that  $L_{jq} = L_{qj}$ . For a general thermodynamic coupling between processes  $k$  and  $l$ :

$$L_{kl} = L_{lk} \quad (\text{IV.3})$$

Eq. (IV.3) holds for phenomena with the same parity under time-reversal. The generalization of this equation to phenomena with different parities was given in eq. (I.19c).

In this section, Onsager's relations are rigorously derived following an approach similar to the developments of de Groot and Mazur (1984). Let us consider an isolated system with well-defined number of molecules ( $N$ ), volume ( $V$ ) and energy ( $E$ ). We denote  $\Omega$  the number of microstates compatible with the macrostate  $(N, V, E)$ . In other words,  $\Omega$  is the degeneracy of the energy level  $E$ . Other properties of the system, such as pressure, may vary according to the microstate.

Let us then focus on a set  $\underline{A}$  of  $n$  mechanical variables of interest, where *mechanical variables* are functions of the microstate of the system. The ergodic hypothesis states that an isolated system will spend equal amounts of time in each of the available microstates (Hill, 1986). Therefore, the probability of finding the system in a certain macrostate  $\underline{A}^*$  is given by:

$$p(\underline{A} = \underline{A}^*) = \frac{\Omega(\underline{A}^*)}{\Omega} \quad (\text{IV.4})$$

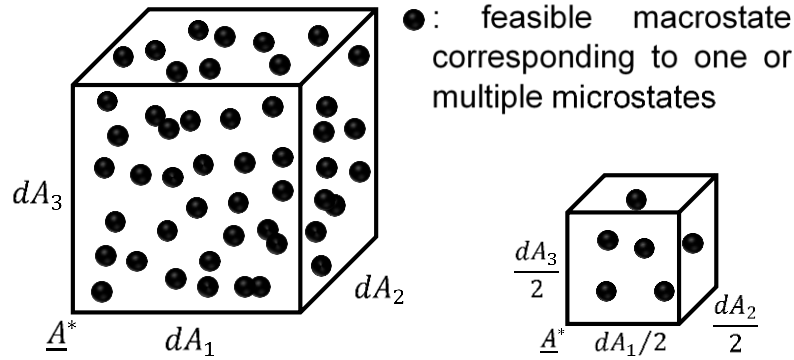
where  $\Omega(\underline{A}^*)$  is the total number of microstates corresponding to the macrostate  $\underline{A}^*$ .

Analogously, one can write the expression for the probability of finding the system  $(N, V, E)$  at a certain state within  $\underline{A}^*$  and  $\underline{A}^* + d\underline{A}$ :

$$p(\underline{A} \in [\underline{A}^*, \underline{A}^* + d\underline{A}]) = \sum_{i: \underline{A}^i \in [\underline{A}^*, \underline{A}^* + d\underline{A}]} \frac{\Omega(\underline{A}^i)}{\Omega} \quad (\text{IV.5})$$

## Chapter IV. Rebuttal of Ziegler's MaxEP principle

In eq. (IV.5),  $[\underline{A}^*, \underline{A}^* + d\underline{A}]$  corresponds to a hyperrectangle in the macrostate space, and the sum in the right-hand side is taken over all the states  $\underline{A}^i$  within this hyperrectangle. In what follows, it shall be assumed that the sum in the right-hand side is proportional to the volume of the hyperrectangle. This is equivalent to assuming that, in the limit of small volumes  $dA_1 dA_2 \dots dA_n$ , the possible microstates are evenly distributed in the hyperrectangle (see Figure IV.1). Such an assumption is true if the number of molecules in the system is sufficiently high so that the mechanical variables are practically continuous, even at this small scale. Figure IV.1 is only an illustration of the assumption, and it depicts each macrostate as a single point in the state space. In reality, there are  $\Omega(\underline{A}^i)$  coincident points at any feasible state  $\underline{A}^i$ , since multiple microstates may correspond to the same macrostate  $\underline{A}^i$ .



*Figure IV.1 – Hypothesis of homogeneous distribution of microstates over two cuboids originating from  $\underline{A}^*$ . The density of points (accounting for the multiple coincident points due to degeneracy) is the same in both cases.*

Assuming the mechanical variables take continuous values, eq. (IV.5) is rewritten as:

$$p(\underline{A} \in [\underline{A}^*, \underline{A}^* + d\underline{A}]) = f(\underline{A}^*) dA_1 dA_2 \dots dA_n \quad (\text{IV.6})$$

where  $f(\underline{A}^i)$  is a probability density function.

As an extra assumption, one shall write this function as Gaussian distribution, given by eq. (IV.7):

$$f(\underline{A}) = \sqrt{\frac{\det(\underline{K})}{(2\pi k_B)^n}} \times \exp\left[-\frac{1}{2k_B} (\underline{A} - \underline{A}^{eq}) \cdot \underline{K} \cdot (\underline{A} - \underline{A}^{eq})\right] \quad (\text{IV.7})$$

## Chapter IV. Rebuttal of Ziegler's MaxEP principle

Here,  $\underline{A}^{eq}$  corresponds to the equilibrium values for the mechanical variables under consideration, and the covariance matrix  $\underline{K}$  is symmetric and positive definite. The validity of eq. (IV.7) will be discussed later in this section.

The macrostate fluctuations  $\underline{\alpha}$  mentioned in Section I.3 are defined as the differences between the instantaneous values of the mechanical variables  $\underline{A}$  and their equilibrium (or mean) values:

$$\underline{\alpha} = \underline{A} - \underline{A}^{eq} \quad (\text{IV.8})$$

Replacing eq. (IV.8) into eq. (IV.7) yields:

$$f(\underline{\alpha}) = \sqrt{\frac{\det(\underline{K})}{(2\pi k_B)^n}} \times \exp\left[-\frac{1}{2k_B} \underline{\alpha} \cdot \underline{K} \cdot \underline{\alpha}\right] \quad (\text{IV.9})$$

Eq. (IV.9) is the probability distribution of the fluctuations  $\underline{\alpha}$ . The fact that it is a Gaussian centred at  $\underline{0}$  indicates that the mean fluctuation, as well as the most likely fluctuation, is  $\underline{0}$ . In order to complete the demonstration of Onsager's reciprocal relations, one needs to establish a relationship between  $f(\underline{\alpha})$  and  $S(\underline{\alpha})$ , the entropy at the macrostate  $\underline{\alpha}$ .

For a system  $(N, V, E)$  at equilibrium, the entropy  $S$  can be defined as a quantity proportional to the logarithm of the number of microstates compatible with the macroscopic quantities  $N, V$  and  $E$ , according to the Boltzmann entropy postulate:

$$S^{eq} = k_B \ln(\Omega) \quad (\text{IV.10})$$

This definition applies to the microcanonical statistical ensemble ( $N, V$  and  $E$  constant) at equilibrium. However, an out-of-equilibrium entropy may be defined in statistical mechanics in a similar way. For example, for the system at a macrostate  $(N, V, E, \underline{\alpha})$ , this quantity may be written as:

$$S(\underline{\alpha}) = k_B \ln[\Omega(\underline{\alpha})] \quad (\text{IV.11})$$

Note that, in general,  $S(\underline{\alpha} = \underline{0}) < S^{eq}$ . The inequality arises because the degeneracy  $\Omega$  in eq. (IV.10) accounts for all microstates compatible with  $N, V, E$ , including those states where  $\underline{\alpha} \neq \underline{0}$ . However, in fluctuation theory one usually assumes that the probability of observing an equilibrium system at  $\underline{\alpha} \approx \underline{0}$  is much higher than the probability of observing it at some other state  $\underline{\alpha}^*$  far from  $\underline{0}$ . This approximation can be proven

## Chapter IV. Rebuttal of Ziegler's MaxEP principle

rigorously for energy fluctuations in the closed isothermal  $(N, V, T)$  canonical system (Hill, 1986). In this case, if  $N$  is large then the energy probability distribution resembles a sharp gaussian around the mean value  $\bar{E}$ , and the ratio between the standard deviation  $\sigma_E$  and  $\bar{E}$  is of order  $N^{-1/2}$  ( $7.76 \times 10^{-11}$  if the system contains 1 mol of molecules). If one assumes that the fluctuations of any mechanical variable resemble a very sharp gaussian, then:

$$S(\underline{0}) \approx S^{eq} \quad (\text{IV.12})$$

To relate  $f(\underline{\alpha})$  in eq. (IV.9) to the entropy  $S(\underline{\alpha})$ , one can recalculate the probability of finding the system  $(N, V, E)$  at some macrostate  $\underline{\alpha}^*$  using eq. (IV.11):

$$\begin{aligned} p(\underline{\alpha} = \underline{\alpha}^*) &= \frac{\Omega(\underline{\alpha}^*)}{\Omega} \stackrel{(\text{IV.11})}{\Rightarrow} \\ \Rightarrow p(\underline{\alpha} = \underline{\alpha}^*) &= \frac{1}{\Omega} e^{S(\underline{\alpha}^*)/k_B} \end{aligned} \quad (\text{IV.13})$$

According to eq. (IV.13), the most likely macrostate is the one corresponding to the highest entropy. This equation is obtained assuming a discrete number of microstates  $\Omega(\underline{\alpha})$ . In the limit of large number of molecules, one may again assume that the mechanical fluctuations  $\underline{\alpha}$  take continuous values. The continuous form of eq. (IV.13) is:

$$f(\underline{\alpha}) \sim e^{S(\underline{\alpha})/k_B} \quad (\text{IV.14})$$

Defining  $\Delta S = S(\underline{\alpha}) - S(\underline{0})$ , eq. (IV.14) implies:

$$f(\underline{\alpha}) = f(\underline{0}) \times e^{\Delta S/k_B} \quad (\text{IV.15})$$

Eq. (IV.15) is the relation between the probability distribution of the macrostates and the entropy of the system. Because the most likely macrostate is the one where fluctuations are  $\underline{0}$ ,  $\Delta S \leq 0$  and eq. (IV.15) shows that the only appreciable fluctuations are those for which  $|\Delta S| = O(k_B)$ .

## Chapter IV. Rebuttal of Ziegler's MaxEP principle

Comparing eqs. (IV.9) and (IV.15) yields:

$$f(\underline{0}) = \sqrt{\frac{\det(\underline{K})}{(2\pi k_B)^n}} \quad (\text{IV.16})$$

$$\Delta S = -\frac{1}{2} \underline{\alpha} \cdot \underline{K} \cdot \underline{\alpha} \quad (\text{IV.17})$$

The entropy is a quadratic function of the fluctuations with a negative sign. Hence, it is concave everywhere. This relation was derived assuming that the mechanical variables follow a Gaussian distribution, as in eq. (IV.7). Alternatively, one could assume that the second-order Taylor expansion of the entropy around  $\underline{A} = \underline{A}^{eq}$  is a satisfactory approximation, and use eqs. (IV.15) and (IV.17) to derive eq. (IV.7) (Prigogine, 1962).

The next steps in the derivation of Onsager's law involve defining a new joint distribution  $f^U(\underline{\alpha}, \underline{\alpha}'; \tau)$ . This distribution is related to the probability of observing the system in the range  $[\underline{\alpha}, \underline{\alpha} + d\underline{\alpha}]$  at time 0, and later observing this system within the range  $[\underline{\alpha}', \underline{\alpha}' + d\underline{\alpha}']$  at time  $\tau$ . Some relations between  $f^U$  and  $f$  can be promptly derived. First, the probability of finding a system in the range  $[\underline{\alpha}^*, \underline{\alpha}^* + d\underline{\alpha}]$  at time 0, and later observing this system at any possible fluctuation is:

$$P\{\underline{\alpha}(t=0) \in [\underline{\alpha}^*, \underline{\alpha}^* + d\underline{\alpha}] \wedge \underline{\alpha}(t=\tau) \text{ is free}\} = D_{\alpha} \int f^U(\underline{\alpha}^*, \underline{\alpha}'; \tau) D_{\alpha'} \quad (\text{IV.18})$$

In eq. (IV.18), the integration in the right-hand side is taken over all possible microstates  $\underline{\alpha}'$ . The terms  $D_{\alpha}$  and  $D_{\alpha'}$  are the volume forms in the state space, given by:

$$D_{\alpha} = d\alpha_1 d\alpha_2 \dots d\alpha_n ; D_{\alpha'} = d\alpha'_1 d\alpha'_2 \dots d\alpha'_n \quad (\text{IV.19})$$

The probability in eq. (IV.18) (observe the system in the range  $[\underline{\alpha}^*, \underline{\alpha}^* + d\underline{\alpha}]$  at time 0, and later observe it at any possible fluctuation) is obviously equivalent to the probability of observing the system in the range  $[\underline{\alpha}^*, \underline{\alpha}^* + d\underline{\alpha}]$ . Therefore, the probability in eq. (IV.18) can be written by means of  $f(\underline{\alpha}^*)$ :

$$\begin{aligned} P\{\underline{\alpha}(t=0) \in [\underline{\alpha}^*, \underline{\alpha}^* + d\underline{\alpha}] \wedge \underline{\alpha}(t=\tau) \text{ is free}\} &= P\{\underline{\alpha} \in [\underline{\alpha}^*, \underline{\alpha}^* + d\underline{\alpha}]\} \stackrel{(\text{IV.6}), (\text{IV.18})}{\Rightarrow} \\ &\Rightarrow f(\underline{\alpha}^*) = \int f^U(\underline{\alpha}^*, \underline{\alpha}'; \tau) D_{\alpha'} \quad (\text{IV.20}) \end{aligned}$$

Similarly:

$$f(\underline{\alpha}') = \int f^U(\underline{\alpha}, \underline{\alpha}'; \tau) D_{\alpha} \quad (\text{IV.21})$$

The principle of microscopic reversibility states that, for a system at equilibrium, and for some Hamiltonian dynamics describing its evolution, the probability of observing a change from microstate A to microstate B after a time interval  $\tau$  is the same as the probability of observing a change from the microstate B to the microstate A after time  $\tau$  in a system under time-reversed dynamics. It results that, if the mechanical variables  $\underline{\alpha}$  are invariant under time-reversal:

$$f^U(\underline{\alpha}, \underline{\alpha}'; \tau) = f^U(\underline{\alpha}', \underline{\alpha}; \tau) \quad (\text{IV.22})$$

In classic mechanics, the time-reversal transformation consists in inverting (i.e., multiplying by -1) the time variable and the momenta of all the particles in the system. Derivation of eq. (IV.22) using this classical approach can be found in de Groot and Mazur (1984).

Let us study the evolution of a system at an initial macrostate  $\underline{\alpha}_0$  with the help of the previous results. The exact state of the system at time  $t$  is unknown, but one can calculate its average macrostate  $\tilde{\alpha}(t; \underline{\alpha}_0)$  according to the following equation:

$$\tilde{\alpha}(t; \underline{\alpha}_0) = \int \underline{\alpha} \times f^c(\underline{\alpha} | \underline{\alpha}_0; t) D_{\alpha} \quad (\text{IV.23})$$

In eq. (IV.23),  $f^c(\underline{\alpha} | \underline{\alpha}_0; t)$  is the conditional probability density associated with the probability of observing the system at macrostate  $\underline{\alpha}$  at time  $t$ , given that its initial macrostate was  $\underline{\alpha}_0$ . To write  $f^c(\underline{\alpha} | \underline{\alpha}_0; t)$  in terms of the previously enounced distributions, let us consider the probability of observing a system at  $\underline{\alpha} \in [\underline{\alpha}^*, \underline{\alpha}^* + d\underline{\alpha}]$  after time  $t$ , given that the system was in some state  $\underline{\alpha}_0 \in [\underline{\alpha}_0^*, \underline{\alpha}_0^* + d\underline{\alpha}_0]$ :

$$\begin{aligned} P(\underline{\alpha} \in [\underline{\alpha}^*, \underline{\alpha}^* + d\underline{\alpha}] | \underline{\alpha}_0 \in [\underline{\alpha}_0^*, \underline{\alpha}_0^* + d\underline{\alpha}_0]; t) &= \frac{P\{\underline{\alpha}(t) \in [\underline{\alpha}^*, \underline{\alpha}^* + d\underline{\alpha}] \wedge \underline{\alpha}(0) \in [\underline{\alpha}_0^*, \underline{\alpha}_0^* + d\underline{\alpha}_0]\}}{P\{\underline{\alpha}(0) \in [\underline{\alpha}_0^*, \underline{\alpha}_0^* + d\underline{\alpha}_0]\}} \Rightarrow \\ \Rightarrow P(\underline{\alpha} \in [\underline{\alpha}^*, \underline{\alpha}^* + d\underline{\alpha}] | \underline{\alpha}_0 \in [\underline{\alpha}_0^*, \underline{\alpha}_0^* + d\underline{\alpha}_0]; t) &= \frac{f^U(\underline{\alpha}_0^*, \underline{\alpha}^*; t) D_{\alpha_0} D_{\alpha}}{f(\underline{\alpha}_0^*) D_{\alpha_0}} = \frac{f^U(\underline{\alpha}_0^*, \underline{\alpha}^*; t) D_{\alpha}}{f(\underline{\alpha}_0^*)} \Rightarrow \\ \Rightarrow f^c(\underline{\alpha}^* | \underline{\alpha}_0^*; t) &= \frac{f^U(\underline{\alpha}_0^*, \underline{\alpha}^*; t)}{f(\underline{\alpha}_0^*)} \end{aligned} \quad (\text{IV.24})$$



## Chapter IV. Rebuttal of Ziegler's MaxEP principle

The fluxes of the mechanical variables  $\underline{\alpha}$  are defined in eq. (I.20a) as the time derivatives of their average fluctuations:

$$J_i = \frac{\partial \tilde{\alpha}_i}{\partial t} \quad (\text{IV.25})$$

Near equilibrium, experiments show that these fluxes are usually linear functions of the average fluctuations:

$$\frac{\partial \tilde{\alpha}(t; \underline{\alpha}_0)}{\partial t} = -\underline{M} \cdot \tilde{\alpha}(t; \underline{\alpha}_0) \quad (\text{IV.26})$$

where  $\underline{M}$  is a matrix of coefficients. In eq. (IV.26) it is implied that the flux of a given variable  $\alpha_i$  may be coupled to other fluctuations  $\alpha_{j \neq i}$ . Further, the linear differential equation with negative sign at the right-hand side indicates that fluctuations are damped exponentially. Indeed, the solution for eq. (IV.26) is:

$$\tilde{\alpha}(t; \underline{\alpha}_0) = e^{-\underline{M}t} \cdot \underline{\alpha}_0 \quad (\text{IV.27})$$

Taking the left dyadic product by  $f(\underline{\alpha}_0)\underline{\alpha}_0$  on both sides of eq. (IV.27) and integrating the equation over  $\underline{\alpha}_0$  yields:

$$\begin{aligned} & \int f(\underline{\alpha}_0)\underline{\alpha}_0 \tilde{\alpha}(t; \underline{\alpha}_0) D_{\alpha_0} = \int f(\underline{\alpha}_0)\underline{\alpha}_0 e^{-\underline{M}t} \cdot \underline{\alpha}_0 D_{\alpha_0} \stackrel{(\text{IV.23})}{\Rightarrow} \\ \Rightarrow & \int f(\underline{\alpha}_0)\underline{\alpha}_0 \left( \int \underline{\alpha} \times f^c(\underline{\alpha}|\underline{\alpha}_0; t) D_{\alpha} \right) D_{\alpha_0} = \int f(\underline{\alpha}_0)\underline{\alpha}_0 e^{-\underline{M}t} \cdot \underline{\alpha}_0 D_{\alpha_0} \Rightarrow \\ \Rightarrow & \int \int f(\underline{\alpha}_0)\underline{\alpha}_0 \underline{\alpha} \times f^c(\underline{\alpha}|\underline{\alpha}_0; t) D_{\alpha} D_{\alpha_0} = \int f(\underline{\alpha}_0)\underline{\alpha}_0 e^{-\underline{M}t} \cdot \underline{\alpha}_0 D_{\alpha_0} \end{aligned}$$

Replacing  $f(\underline{\alpha}_0)f^c(\underline{\alpha}|\underline{\alpha}_0; t)$  by its expression from eq. (IV.24) yields:

$$\begin{aligned} & \int \int f^U(\underline{\alpha}_0, \underline{\alpha}; t) \underline{\alpha}_0 \underline{\alpha} D_{\alpha} D_{\alpha_0} = \int f(\underline{\alpha}_0)\underline{\alpha}_0 e^{-\underline{M}t} \cdot \underline{\alpha}_0 D_{\alpha_0} \Rightarrow \\ \Rightarrow & \int \int f^U(\underline{\alpha}, \underline{\alpha}_0; t) \underline{\alpha} \underline{\alpha}_0 D_{\alpha_0} D_{\alpha} = \int f(\underline{\alpha}_0)\underline{\alpha}_0 e^{-\underline{M}t} \cdot \underline{\alpha}_0 D_{\alpha_0} \stackrel{(\text{IV.22})}{\Rightarrow} \\ \Rightarrow & \int \int f^U(\underline{\alpha}_0, \underline{\alpha}; t) \underline{\alpha} \underline{\alpha}_0 D_{\alpha_0} D_{\alpha} = \int f(\underline{\alpha}_0)\underline{\alpha}_0 e^{-\underline{M}t} \cdot \underline{\alpha}_0 D_{\alpha_0} \stackrel{(\text{IV.24})}{\Rightarrow} \\ \Rightarrow & \int \int f(\underline{\alpha}_0)f^c(\underline{\alpha}|\underline{\alpha}_0; t) \underline{\alpha} \underline{\alpha}_0 D_{\alpha_0} D_{\alpha} = \int f(\underline{\alpha}_0)\underline{\alpha}_0 e^{-\underline{M}t} \cdot \underline{\alpha}_0 D_{\alpha_0} \end{aligned}$$

## Chapter IV. Rebuttal of Ziegler's MaxEP principle

With the help of eq. (IV.23), the left-hand side integrand can be written as a function of the average macrostate  $\underline{\tilde{\alpha}}(t; \underline{\alpha}_0)$ :

$$\begin{aligned}
 \int f(\underline{\alpha}_0) \underline{\tilde{\alpha}}(t; \underline{\alpha}_0) \underline{\alpha}_0 D_{\alpha_0} &= \int f(\underline{\alpha}_0) \underline{\alpha}_0 e^{-\underline{M}t} \cdot \underline{\alpha}_0 D_{\alpha_0} \stackrel{(IV.27)}{\Rightarrow} \\
 \Rightarrow \int f(\underline{\alpha}_0) \left( e^{-\underline{M}t} \cdot \underline{\alpha}_0 \right) \underline{\alpha}_0 D_{\alpha_0} &= \int f(\underline{\alpha}_0) \underline{\alpha}_0 \left( e^{-\underline{M}t} \cdot \underline{\alpha}_0 \right) D_{\alpha_0} \Rightarrow \\
 \Rightarrow e^{-\underline{M}t} \cdot \left\{ \int f(\underline{\alpha}_0) \underline{\alpha}_0 \underline{\alpha}_0 D_{\alpha_0} \right\} &= \left\{ \int f(\underline{\alpha}_0) \underline{\alpha}_0 \underline{\alpha}_0 D_{\alpha_0} \right\} \cdot e^{-\underline{M}^T t} \quad (IV.28)
 \end{aligned}$$

In eq. (IV.28),  $\underline{M}^T$  is the transpose of matrix  $\underline{M}$ . The integral appearing in both sides of this equation is the expected value of the dyadic  $\underline{\alpha}_0 \underline{\alpha}_0$ . Because the probability density  $f(\underline{\alpha})$  is given by the Gaussian function in (IV.9), the expected value of the dyadic product is (Gut, 2009):

$$E(\underline{\alpha} \underline{\alpha}) = k_B \underline{K}^{-1} \quad (IV.29)$$

where  $\underline{K}^{-1}$  is the inverse of matrix  $\underline{K}$ . Inserting eq. (IV.29) into eq. (IV.28) yields:

$$e^{-\underline{M}t} \cdot \underline{K}^{-1} = \underline{K}^{-1} \cdot e^{-\underline{M}^T t} \quad (IV.30)$$

Eq. (IV.30) is true for any time  $t$ . Therefore, the following relation must hold:

$$\underline{M}^k \cdot \underline{K}^{-1} = \underline{K}^{-1} \cdot \left( \underline{M}^T \right)^k \quad \forall k \in \mathbb{N} \quad (IV.31)$$

It can be shown via induction that eq. (IV.31) is equivalent to:

$$\underline{M} \cdot \underline{K}^{-1} = \underline{K}^{-1} \cdot \underline{M}^T \quad (IV.32)$$

For later convenience, let us define  $\underline{L} \equiv \underline{M} \cdot \underline{K}^{-1}$ . Because  $\underline{K}$  is symmetric, eq. (IV.32) can be re-written in terms of  $\underline{L}$  as:

$$\underline{M} \cdot \underline{K}^{-1} \equiv \underline{L} = \underline{L}^T \quad (IV.33)$$

## Chapter IV. Rebuttal of Ziegler's MaxEP principle

Now it shall be shown that the matrix  $\underline{\underline{L}}$  defined in eq. (IV.33) is the matrix of linear coefficients relating fluxes and forces, according to eq. (I.17):  $\underline{J} = \underline{\underline{L}} \cdot \underline{X}$ . First, let us re-write here the definition of the thermodynamic forces, according to eq. (I.20b):

$$X_i = \frac{\partial \Delta S}{\partial \alpha_i} \quad (\text{IV.34})$$

For convenience, the derivative of the entropy  $S$  in eq. (I.20b) has been replaced by the derivative of the entropy variation  $\Delta S$  from equilibrium. Inserting eq. (IV.17) into eq. (IV.34) yields:

$$\underline{X} = -\underline{\underline{K}} \cdot \underline{\alpha} \quad (\text{IV.35})$$

Now, inserting eq. (IV.33) into eq. (IV.26):

$$\begin{aligned} \frac{\partial \underline{\underline{\alpha}}(t; \underline{\alpha}_0)}{\partial t} &= -\underline{\underline{L}} \cdot \underline{\underline{K}} \cdot \underline{\underline{\alpha}}(t; \underline{\alpha}_0) \stackrel{(\text{IV.23})}{\Rightarrow} \\ \Rightarrow \frac{\partial \underline{\underline{\alpha}}(t; \underline{\alpha}_0)}{\partial t} &= -\underline{\underline{L}} \cdot \int \underline{\underline{K}} \cdot \underline{\alpha} f^c(\underline{\alpha} | \underline{\alpha}_0; t) D_{\alpha} \end{aligned}$$

Replacing  $\underline{\underline{K}} \cdot \underline{\alpha}$  according to its expression in eq. (IV.35):

$$\begin{aligned} \frac{\partial \underline{\underline{\alpha}}(t; \underline{\alpha}_0)}{\partial t} &= \underline{\underline{L}} \cdot \int \underline{X} f^c(\underline{\alpha} | \underline{\alpha}_0; t) D_{\alpha} \Rightarrow \\ \Rightarrow \frac{\partial \underline{\underline{\alpha}}(t; \underline{\alpha}_0)}{\partial t} &\stackrel{(\text{IV.25})}{\equiv} \underline{\underline{J}} = \underline{\underline{L}} \cdot \underline{\underline{X}}(t; \underline{\alpha}_0) \end{aligned} \quad (\text{IV.36})$$

In eq. (IV.36),  $\underline{\underline{X}}(t; \underline{\alpha}_0)$  is the average evolution of the forces for a system that was initially in the macrostate  $\underline{\alpha}_0$ . This equation shows that matrix  $\underline{\underline{L}}$  is indeed the matrix of phenomenological coefficients describing the average behaviour of the system. Hence, eq. (IV.33) is indeed Onsager's reciprocal relations. Instead of assuming linear flux-fluctuation relations (IV.26) and later retrieving the linear flux-forces relations in eq. (IV.36) along with Onsager's reciprocal relations, one could assume (IV.36) to be true and derive the reciprocal relations from it (Onsager, 1931b; Prigogine, 1962).

The derivation of Onsager's reciprocal relations in this section followed the developments shown in de Groot and Mazur (1984). It was important to reproduce it here because there are some similarities between this demonstration and Ziegler's developments leading to the Orthogonality Principle (Ziegler, 1958), which will be discussed in Section IV.2. Two

## Chapter IV. Rebuttal of Ziegler's MaxEP principle

important corollaries regarding Onsager's reciprocal relations are listed next. The first one is the extension of Onsager's reciprocal relations when some of the fluctuations are anti-symmetric under time-reversal, as shown in eqs. (I.19b) and (I.19c). The second corollary is the validity of Onsager's reciprocal relations for continuous systems, where fluxes and forces are defined according to eqs. (I.21a) and (I.21b). De Groot and Mazur (1984) derive eqs. (I.19b) and (I.19c) rigorously, and they prove the validity of the reciprocal relations for two continuous cases: anisotropic heat conduction in a crystal and heat conduction coupled with diffusion in an isotropic fluid.

Finally, several assumptions had to be made in order to derive the Onsager's reciprocal relations shown in eq. (IV.33). These assumptions are listed and briefly discussed below:

1. The fluctuations associated to the fluxes are mechanical variables, i.e. quantities defined for any given microstate. For example, heat and diffusive fluxes are associated respectively to internal energy and concentration; both these quantities are well-defined for any given microstate.
2. The number of molecules in the system is sufficiently large so that the fluctuations are continuous-like. As a hypothetical example of a closed system violating this rule, imagine a mixture of 3 molecules of water and 3 molecules of some acid HA. The system undergoes ionization according to the following reaction:  $\text{HA} + \text{H}_2\text{O} \rightleftharpoons \text{A}^- + \text{H}_3\text{O}^+$ . The fluctuations here are associated to the reaction extent, which can only take 4 discrete values.
3. At equilibrium, fluctuating mechanical variables follow a Gaussian distribution, according to eq. (IV.7). Hill (1986) and de Groot and Mazur (1984) prove it for the energy fluctuations in an isothermal closed system. More generally, de Groot and Mazur (1984) give a sufficient condition for this assumption to hold: if the mechanical variable corresponds to the sum of some property of the individual molecules, and if these individual properties are mutually independent and follow the same probability distribution, then the mechanical variable will follow a Gaussian distribution in the neighbourhood of its mean value. An alternative assumption is: the second-order Taylor expansion of the entropy around  $\underline{\alpha} = \underline{0}$  is a satisfactory approximation. In this case, eq. (IV.17) replaces eq. (IV.7) as the assumption.

## Chapter IV. Rebuttal of Ziegler's MaxEP principle

4. Microscopic reversibility holds. In classic mechanics, this is equivalent to saying that the equations of motion for the particles composing the system are invariant under time-reversal. Any conservative system obeys this principle.
5. The dynamics of the average fluctuations are given by the linear differential equations in eq. (IV.26). This linear flux-fluctuation relationship is observed experimentally for various systems, including reactions near equilibrium and pairs of subsystems exchanging heat and mass. However, these experimental measures are taken for systems out of equilibrium, since the small fluctuations of a system at equilibrium are hard to capture. One has to assume that the same dynamics observed experimentally for large fluctuations holds in the limit  $\underline{\alpha} \underline{\alpha} = O(k_B \underline{K}^{-1})$ . Alternatively, one could assume eq. (IV.36) instead of eq. (IV.26).

### IV.1.2 Prigogine's Minimum Entropy Production Principle

The principle of Minimum Entropy Production (minEP) concerns systems with  $n$  distinct fluctuations, in which  $m$  forces ( $X_1, X_2, \dots, X_m$ ) are held constant, and  $n - m$  forces ( $X_{m+1}, \dots, X_n$ ) are free to change. For example, two reservoirs separated by a membrane can exchange heat and mass ( $n = 2$ ). If the reservoirs are jacketed vessels, then their temperature (and therefore the temperature difference between them) can be held fixed ( $m = 1$ ). Prigogine shows that, if the Onsager's reciprocal relations hold for such systems, then they evolve in such a way that they reach a minimum of entropy production at steady state (Prigogine, 1962). This statement is illustrated in Figure IV.2 for  $X_1$  (temperature difference) fixed and  $X_2$  (concentration difference) free, with associated fluxes  $J_1$  and  $J_2$ . Note that here steady state does not mean equilibrium state: if at least one of the  $m$  forces is fixed at a value different from 0, then the system will always be out of equilibrium.

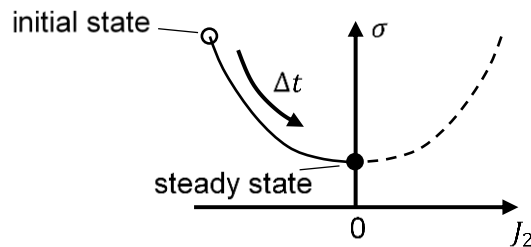


Figure IV.2 – Illustration of Prigogine's minEP principle when a system is subjected to a fixed force  $X_1$  and a free force  $X_2$ ; the system reaches a minimum of entropy production at steady state, when  $J_2 = 0$

## Chapter IV. Rebuttal of Ziegler's MaxEP principle

To prove his principle, Prigogine replaces the linear flux-force relationships in eq. (I.17) ( $J_k = \sum_j L_{kj}X_j$ ) into the bilinear entropy production expression in eq. (I.11) to obtain:

$$\sigma = \sum_{i,j} L_{ij}X_iX_j \quad (\text{IV.37})$$

Because there are  $m$  forces being held constant, the evolution of the entropy production in the system depends only on the  $n - m$  remaining forces. Differentiation of (IV.37) with respect to a force  $X_k$  that is not held constant yields:

$$\begin{aligned} \frac{\partial \sigma}{\partial X_k} &= \sum_i L_{ik}X_i + \sum_j L_{kj}X_j \stackrel{(\text{IV.3})}{\Rightarrow} \\ \Rightarrow \frac{\partial \sigma}{\partial X_k} &= 2 \sum_j L_{kj}X_j, \quad k = m + 1, m + 2, \dots, n \end{aligned} \quad (\text{IV.38})$$

At the steady state, the fluxes ( $J_{m+1}, \dots, J_n$ ), corresponding to the  $n - m$  forces that are free to change, will disappear. Replacing eq. (I.17) into eq. (IV.38) then yields:

$$\begin{aligned} \frac{\partial \sigma}{\partial X_k} &= 2J_k \Rightarrow \\ \Rightarrow J_k &= 0 \Leftrightarrow \frac{\partial \sigma}{\partial X_k} = 0, \quad k = m + 1, m + 2, \dots, n \end{aligned} \quad (\text{IV.39})$$

Eq. (IV.39) shows that the steady state corresponds to a critical point of the surface  $\sigma(X_{m+1}, X_{m+2}, \dots, X_n)$ . Further, eq. (IV.37) shows that  $\sigma$  is quadratic and positive definite with respect to the forces. Therefore, the unique critical point in eq. (IV.39) corresponds to a minimum of entropy production, and that establishes the minEP principle.

### *IV.1.3 Ziegler's Maximum Entropy Production Principle*

One of the key benefits from the Onsager's reciprocal relations is allowing the prediction of the system evolution based solely on the entropy production function  $\sigma(\underline{X})$ . Close to equilibrium,  $\sigma(\underline{X})$  is expected to be a quadratic function of the forces:

$$\sigma = \sum_{i=1}^n \sum_{j=i}^n P_{ij}X_iX_j \quad (\text{IV.40})$$

Note that eq. (IV.40) is slightly different from eq. (IV.37), the difference being that in eq. (IV.40) the sum over the second index ( $j$ ) starts at  $i$ , so that each product  $X_aX_b$  only

## Chapter IV. Rebuttal of Ziegler's MaxEP principle

appears once in the expression for the entropy production. Comparing equations (IV.40) and (IV.37) for an initial set of forces  $\underline{X}$  yields:

$$\begin{aligned} \sigma &= \sum_{i=1}^n \sum_{j=i}^n P_{ij} X_i X_j = \sum_i \sum_j L_{ij} X_i X_j \quad (IV.33) \\ &\Rightarrow \begin{cases} L_{ii} = P_{ii} \\ L_{ij} = L_{ji} = P_{ij}/2, \forall i, j > i \end{cases} \quad (IV.41) \end{aligned}$$

Eq. (IV.41) shows that the phenomenological matrix  $\underline{L}$  relating the fluxes to the forces is entirely determined by the quadratic expression of  $\sigma(\underline{X})$ . I.e., the fluxes  $J_k = \sum_j L_{kj} X_j$  (c.f. eqs. (I.17) and (IV.36)) at any given instant can be calculated as a function of the forces. As explained in Section I.3, these fluxes are either the time derivatives of state variables  $x$ , or the actual fluxes appearing in the transport equations for these variables. Knowing these fluxes at some time  $t$  means being capable of predicting the state of the system at time  $t + dt$ . And because the thermodynamic forces can generally be calculated from the state of the system, this suffices to predict the evolution of the system.

Note that Onsager's reciprocal relations are only meaningful when linear flux-force relationships can be assumed (c.f. eq. (I.17) or eq. (IV.36)). This is generally true close to equilibrium, but far-from-equilibrium systems may present more complex behaviours. One example is the large deformation of a non-Newtonian body (Ziegler, 1958). Another example is the deviation from the Fourier law of heat conduction under very large temperature gradients, as observed in the context of laser-driven plasmas (Jou et al., 2010).

Ziegler (1958, 1968) proposed a generalization of Onsager's reciprocal relations for these far-from-equilibrium systems. It was first introduced as an orthogonality principle (Ziegler, 1958), and later reformulated as a variational principle (Ziegler, 1961, 1968). In Ziegler's generalization of Onsager's law, the assumptions (3) and (5) given by the end of Section IV.1.1 are relaxed, as both these assumptions were linked to the near-equilibrium hypothesis. Indeed, assumption (3) states that fluctuating mechanical variables follow a Gaussian distribution, which is only true for small fluctuations (i.e., near equilibrium). Further, assumption (5) regarding linear flux-fluctuation relationships (eq. (IV.26)) is only true near equilibrium.

## Chapter IV. Rebuttal of Ziegler's MaxEP principle

The new assumptions that replace (3) and (5) for Ziegler's MaxEP principle are:

- 3'. The entropy production can be expressed as a function of the fluxes alone, or as a function of the fluxes and the instantaneous values of some state variables.
- 5'. There is a one-to-one correspondence between fluxes and forces. I.e., a system can neither have two different sets of forces  $(\underline{X}, \underline{X}')$  compatible with the same set of fluxes  $\underline{J}$ , nor have two different sets of fluxes  $(\underline{J}, \underline{J}')$  compatible with the same set of forces  $\underline{X}$ .

If these hypotheses, along with hypotheses (1), (2) and (4) by the end of Section IV.1.1, are satisfied, then the Orthogonality Principle states that the thermodynamic fluxes represented on the flux space are perpendicular to the isosurfaces of the entropy production. A more detailed statement of the Orthogonality Principle is given in the beginning of Section IV.2.

Its variational counterpart, the Maximum Entropy Production (maxEP) principle, states that, for some prescribed forces  $\underline{X}^*$ , the fluxes are "chosen" by the system so as to maximize the entropy production. Mathematically, if the surface  $\sigma(\underline{J})$  is known, and if the thermodynamic forces at some time  $t$  are known and equal to  $\underline{X}^*$ , then the fluxes  $\underline{J}^*$  can be calculated by the following variational procedure (Ziegler, 1968):

$$\begin{aligned} \underline{J}^* &= \max_{\underline{J}} \{ \sigma(\underline{J}) \} \\ \text{s. t. } \sigma(\underline{J}) &= \underline{X}^* \cdot \underline{J} \end{aligned} \quad (\text{IV.42})$$

The constraint shown in eq. (IV.42) comes from eq. (I.11), which gives the entropy production as a bilinear expression involving the fluxes and the forces. Solving eq. (IV.42) via Lagrange multipliers yields the following system of equations that can be solved for  $\underline{J}$  (Ziegler, 1968):

$$X_i^* \frac{1}{\sigma} \sum_k \frac{\partial \sigma}{\partial J_k} J_k = \frac{\partial \sigma}{\partial J_i} \quad (\text{IV.43})$$

This principle is a direct consequence of the Orthogonality Principle (Ziegler, 1961), whose derivation is reviewed later in Section IV.2. The discussion hereafter is limited to some key consequences of Ziegler's MaxEP principle. Firstly, it is important to highlight



## Chapter IV. Rebuttal of Ziegler's MaxEP principle

that, when the function  $\sigma(\underline{J})$  is quadratic, Onsager's reciprocal relations can be derived from Ziegler's maxEP principle. Indeed, assuming a quadratic  $\sigma(\underline{J})$ :

$$\begin{aligned} \sigma(\underline{J}) &= \sum_{j=1}^n \sum_{l=j}^n Q_{jl} J_j J_l \stackrel{(IV.43)}{\Rightarrow} \\ \Rightarrow \frac{X_i^*}{\sum_{j=1}^n \sum_{l=j}^n Q_{jl} J_j J_l} \left[ \sum_{k=1}^n J_k \left( \sum_{l=k}^n Q_{kl} J_l + \sum_{j=1}^k Q_{jk} J_j \right) \right] &= \sum_{l=i}^n Q_{il} J_l + \sum_{j=1}^i Q_{ji} J_j \quad (IV.44) \end{aligned}$$

Eq. (IV.44) can be greatly simplified by defining the symmetric matrix  $\underline{\underline{Q'}}$  such that:

$$\begin{aligned} Q'_{jl} &= Q'_{lj} = \frac{1}{2} Q_{jl} \quad \forall l > j \\ Q'_{jj} &= Q_{jj} \end{aligned} \quad (IV.45)$$

Replacing eq. (IV.45) into eq. (IV.44):

$$\begin{aligned} X_i^* \frac{1}{\sum_{j=1}^n \sum_{l=1}^n Q'_{jl} J_j J_l} \left[ \sum_{k=1}^n \left( J_k \times 2 \sum_{j=1}^n Q'_{jk} J_j \right) \right] &= 2 \sum_{j=1}^n Q'_{ij} J_j \Rightarrow \\ \Rightarrow X_i^* &= \sum_{j=1}^n Q'_{ij} J_j \quad (IV.46) \end{aligned}$$

Because the function  $\sigma(\underline{J})$  must be positive definite, the matrix  $\underline{\underline{Q'}}$  must be invertible.

Hence, one can write the fluxes as a function of the forces according to eq. (IV.47):

$$\underline{\underline{J}}^* = \underline{\underline{Q'}}^{-1} \cdot \underline{\underline{X}}^* \quad (IV.47)$$

Note that  $\underline{\underline{Q'}}^{-1}$  is the phenomenological matrix  $\underline{\underline{L}}$  that gives the fluxes as a function of the forces in the linear regime. And because  $\underline{\underline{Q'}}$  is symmetric (see eq. (IV.45)), its inverse  $\underline{\underline{Q'}}^{-1}$  must also be symmetric. Hence, we derive Onsager's reciprocal relations (eq. (IV.33)) from Ziegler's MaxEP principle.

It is not surprising that Onsager's relations are a consequence of the MaxEP principle. As a matter of fact, Ziegler's principle is an attempt to generalize Onsager's law. So it is only natural that the former must stem from the latter near equilibrium.

Finally, some confusion may arise regarding the compatibility of MaxEP and minEP. These principles are actually not contradictory: the system maximizes entropy production at every *instant* (MaxEP), but its *evolution in time* decreases entropy production (minEP) (Martyushev and Seleznev, 2006). Figure IV.3 illustrates this statement for an out-of-equilibrium system with only two fluxes,  $J_1$  and  $J_2$ . The orange surface in this figure corresponds to the surface  $\sigma = \sigma(J_1, J_2)$ , and the blue plane corresponds to the plane  $\sigma = X_1^*J_1 + X_2^*J_2$ .

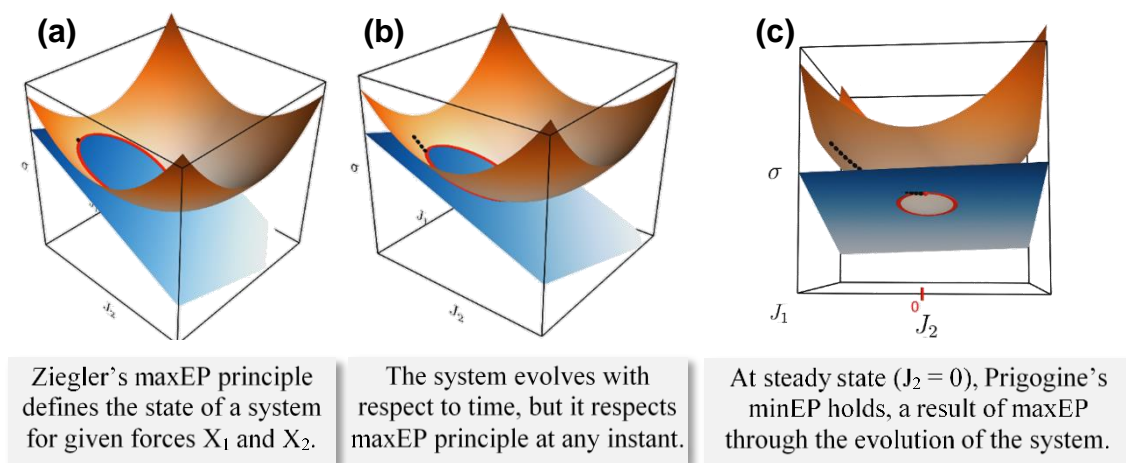


Figure IV.3 – Prigogine's minEP principle as a consequence of Ziegler's maxEP principle

The red contour is the intersection between these surfaces, and it corresponds to the set of points satisfying the constraint in eq. (IV.42). The values of  $J_1^*$  and  $J_2^*$  corresponding to the maximum of  $\sigma$  along this red curve give the state of the system according to Ziegler's principle. Assuming that the force  $X_1^*$  is fixed, whereas  $X_2^*$  is free to change, the evolution of the system is tracked by rotating the plane. Each value that  $X_2^*$  takes will correspond to some inclination of the blue plane. At any time, Ziegler's principle can be applied to find the instantaneous state of the system. Finally, when the system reaches steady state ( $J_2 = 0$ ), the entropy production reaches a minimum in the trajectory of states. This minimum is depicted by the red dot in Figure IV.3c.

## IV.2 Derivation of the Orthogonality Principle

The MaxEP principle discussed in Section IV.1.3 is a direct consequence of the so-called Orthogonality Principle (OP) (Ziegler, 1961). The proof of the equivalence between OP and MaxEP is straightforward, and it was already covered in Ziegler (1961). Therefore, it is omitted from this section. A rigorous statement of OP is given next.

**Orthogonality Principle (OP):** Let us assume a thermodynamic system satisfying the following restrictions, discussed by the end of Sections IV.1.1 (H1, H2, H4) and IV.1.3 (H3, H5):

H1. The fluctuations associated to the fluxes are mechanical variables, i.e. quantities defined for any given microstate.

H2. The number of molecules in the system is sufficiently large so that the fluctuations are continuous-like.

H3. The entropy production can be expressed as a function of the fluxes alone, or as a function of the fluxes and the instantaneous values of some state variables.

H4. Microscopic reversibility holds.

H5. There is a one-to-one correspondence between fluxes and forces.

For such a system, if the entropy production surface is represented by  $\sigma(\underline{J}, \underline{x})$ , where  $\underline{J}$  are the fluxes and  $\underline{x}$  are the state variables, then the forces are perpendicular (orthogonal) to the level sets of  $\sigma(\underline{J}, \underline{x})$  in the velocity state. In other words (c.f. eq. (IV.43)):

$$\underline{X} = f(\underline{J}, \underline{x}) \underline{\nabla}^J \sigma \quad (\text{IV.48})$$

where  $\underline{\nabla}^J$  indicates that the gradient is taken with respect to the flux space.

Eq. (IV.48) can be better understood with geometrical reasoning. Imagine there are only two fluxes  $J_1$  and  $J_2$  in the system. For any given set of state variables  $\underline{x}^*$ , one can draw the surface  $\sigma(\underline{J}, \underline{x}^*)$  in the flux space. The forces  $\underline{X}$ , if drawn in the same flux space, will be perpendicular to the level sets of the surface. Figure IV.4 illustrates this geometrical reasoning. In this figure, the force vectors are depicted for three arbitrary pairs of fluxes corresponding to the same level set  $\sigma = \sigma_l$ .

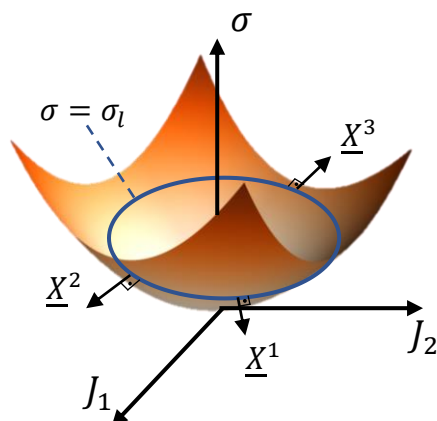


Figure IV.4 – Illustration of the OP, with vectors  $\underline{X}^1, \underline{X}^2, \underline{X}^3$  perpendicular to the level set  $\sigma = \sigma_l$

Ziegler has attempted a few times to prove the OP (Ziegler, 1958, 1970, 1983b). These demonstrations share some common ideas and arguments. However, the developments in the 1958 work focused on the rheological problem, which restricts the proof to a specific case study. Further, Ziegler himself stated that his 1958 work was a rudimentary version of the more formal proof given in 1970 (Ziegler, 1970). Between the two remaining proofs (Ziegler, 1970, 1983), the latter is much more detailed. Besides, the 1983 demonstration was published in a subsection of a book chapter, whereas the one from 1970 is in an article whose purpose was to prove OP. For these reasons, only the 1970 paper will be discussed in the remaining of the section.

For his analysis, Ziegler assumes a thermodynamic system with a large number of degrees of freedom (H2). Further, he assumes that the evolution of the system (in a microscopic sense) can be described by a Hamiltonian. The microscopic coordinates  $\underline{q}$  in this case can be defined as either the quantum states of the several molecules in the system (the quantum approach), or the positions of these molecules (the classical approach). Ziegler uses the latter approach in his derivation.

He later claims that the Hamiltonian depends on  $\underline{q}, \underline{p}$  (the momenta corresponding to  $\underline{q}$ ) and on the state variables  $\underline{x}$  used to describe the macroscopic state of the system (a priori, it could be the temperature, pressure, and so on). I.e.:

$$\mathcal{H} = \mathcal{H}(\underline{q}, \underline{p}, \underline{x}) \quad (\text{IV.49})$$

## Chapter IV. Rebuttal of Ziegler's MaxEP principle

Eq. (IV.49) is the first questionable step in Ziegler's derivation. The dynamics of the microsystem do not necessarily depend on the state variables  $\underline{x}$ . For example, the mechanical variables mentioned in Section IV.1.1 (during the derivation of Onsager's relations) are a category of state variables that are entirely determined by the microstate of the system  $(\underline{q}, \underline{\dot{q}})$ . Therefore, the evolution of the mechanical variables is a property that stems from the Hamiltonian of the system, and not the opposite. Still, there is merit to eq. (IV.49) since temperature, chemical potentials and other non-mechanical variables may influence the dynamics of the microsystem without being entirely defined at specific microstates. Further, external coordinates (e.g. strain components in a plastic body generated by external forces) may also affect the dynamics of the system. In both cases ( $\underline{x}$  being nonmechanical state variables and/or external coordinates), it will be assumed that their dynamics  $\underline{x}(t)$  are known. Otherwise, if the trajectories  $\underline{x}(t)$  were to be determined, conjugate variables of  $\underline{x}$  would have to be included in the Hamiltonian, and that would undermine the rest of Ziegler's proof.

To avoid confusion, eq. (IV.49) is re-written as:

$$\mathcal{H} = \mathcal{H}(\underline{q}, \underline{p}, \underline{a}(t)) \quad (\text{IV.50})$$

where  $\underline{a}$  are nonmechanical state variables and/or external coordinates.

For conservative systems, the Hamiltonian in eq. (IV.50) equals the energy of the microsystem. The average of this energy over small time scales corresponds to a macroscopic property called internal energy  $U$ . In other words:

$$U = \overline{\mathcal{H}} \quad (\text{conservative systems}) \quad (\text{IV.51})$$

The small time scale mentioned above makes it possible to average over several microstates while holding  $\underline{a}$  constant.

The internal energy in eq. (IV.51) can be written as a function of Helmholtz free energy  $F$ , temperature, and entropy according to the following well-known relation:

$$U = F + TS \quad (\text{IV.52})$$

The time derivative of (IV.52) yields:

$$\dot{U} = \dot{F} + \dot{T}S + T\dot{S} \quad (\text{IV.53})$$

## Chapter IV. Rebuttal of Ziegler's MaxEP principle

The derivative of the entropy with respect to time is usually written as the sum of two terms: the variation due to exchanges with the surroundings ( $\dot{S}_e$ ) and the so-called entropy production ( $\dot{S}_i$ ). For adiabatic closed systems,  $\dot{S}_e = 0$  and  $\dot{S} = \dot{S}_i$ . Note that adiabatic closed systems are not necessarily isolated. For example, an insulated closed piston can exchange energy with its surroundings through work. Further, the entropy production in an adiabatic closed system is not necessarily zero. For example, an isolated reactive system that is out-of-equilibrium will have  $\dot{S} > 0$  until equilibrium is reached.

As mentioned in Section IV.1.3, the MaxEP principle (and also the OP) establishes fluxes relationships from the entropy production written as a function of the fluxes. Therefore, it is suitable to further develop eq. (IV.53), which contains the entropy production term  $\dot{S}$ .

To do this, let us first write the statistical definition of entropy (Hill, 1986):

$$S = -k_B \sum_j P_j \ln(P_j) \quad (\text{IV.54})$$

where  $P_j$  is the probability of observing the system at a certain microstate  $j$ . Eq. (IV.54) shows that entropy is not defined for a single microstate. Instead, it is an averaged quantity. Further, note that this definition is different from the definition in eq. (IV.11). However, they are not contradictory. Rather, eq. (IV.54) implies eq. (IV.11) for  $(N, V, E)$  systems, since all the  $\Omega$  possible microstates in those systems have the exact same probability  $P_j = 1/\Omega$ .

The careful reader will notice a disagreement between eq. (IV.54) and the classical approach for statistical mechanics. Indeed, the microstates  $j$  in eq. (IV.54) are discrete, whereas classical statistical mechanics assumes the microscopic coordinates  $\underline{q}$  are continuous. Despite this difference, both approaches yield the same results. The discrete approach is used here for the sake of simplicity, and because this approach was used earlier in Section IV.1.1.

The probabilities in eq. (IV.54) depend on the energy  $E_j$  of the microstate  $j$  and on the temperature of the system according to the following relation (Gibbs, 1948; Hill, 1986):

$$P_j = e^{\frac{F-E_j}{k_B T}} \quad (\text{IV.55})$$

## Chapter IV. Rebuttal of Ziegler's MaxEP principle

where  $F$  is the Helmholtz free energy, not defined for a specific microstate. Even though eq. (IV.55) is derived for the canonical  $(N, V, T)$  ensemble, it also applies to other closed systems. For example, a  $(N, V, E)$  system has  $P_j = 1/\Omega$ . Further, its entropy is given by  $S = k_B \ln(\Omega)$  according to eq. (IV.10). These two equations, along with eq. (IV.55), show that  $F$  appearing in eq. (IV.55) is the same quantity as the free energy that appears in eq. (IV.52) even for a  $(N, V, E)$  system.

For later convenience, a quantity  $\psi$  shall be defined for each microstate as follows:

$$\psi_j \equiv k_B \ln(P_j) = \frac{F - E_j}{T} \quad (\text{IV.56})$$

Isolating  $E_j$  in eq. (IV.56) and taking its time derivative yields:

$$\dot{E}_j = \dot{F} - \dot{T}\psi_j - T\dot{\psi}_j \quad (\text{IV.57})$$

As mentioned in the beginning of this section, the Hamiltonian of the system gives the energy of its microstate. Hence:

$$\mathcal{H} = \dot{F} - \dot{T}\psi - T\dot{\psi} \quad (\text{IV.58})$$

The subscript  $j$  was omitted in eq. (IV.58) because the Hamiltonian is assumed to take continuous values, as the microscopic coordinates also take continuous values in the phase space. Hence, the above derivation of eq. (IV.58) is not completely rigorous. Still, the discrete approach is simpler as it avoids integrals to calculate averages, and is similar to the one used in Section IV.1.1. For another derivation of eq. (IV.58) using classical statistical mechanics, the reader can refer to Ziegler (1970).

The average of the time derivative in eq. (IV.58) over short periods of time is given by:

$$\overline{\mathcal{H}} = \dot{F} - \dot{T}\overline{\psi} - T\overline{\dot{\psi}} \quad (\text{IV.59})$$

The short period of time captures microscopic fluctuations while guarding  $\dot{F}$ ,  $\dot{T}$  and  $T$  constant.

Eq. (IV.59) is not yet in a suitable form, as it contains the unknown terms  $\overline{\dot{\psi}}$  and  $\overline{\psi}$ . The term  $\overline{\dot{\psi}}$  can be written as a function of the entropy in the system. Indeed, replacing  $\ln(P_j)$  in eq. (IV.54) by its expression in eq. (IV.56) yields:

## Chapter IV. Rebuttal of Ziegler's MaxEP principle

$$\begin{aligned}
 S &= - \sum_j P_j \psi_j \Rightarrow \\
 &\Rightarrow \bar{\psi} = -S
 \end{aligned} \tag{IV.60}$$

Finally, the average of the time derivative of  $\psi$  can be found using its definition from eq. (IV.56):

$$\begin{aligned}
 \dot{\psi}_j = \frac{k_B}{P_j} \dot{P}_j \Rightarrow \bar{\dot{\psi}}_j &= \sum_j k_B \dot{P}_j = k_B \frac{d}{dt} \sum_j P_j \Rightarrow \\
 &\Rightarrow \bar{\dot{\psi}} = 0
 \end{aligned} \tag{IV.61}$$

Inserting eqs. (IV.60) and (IV.61) into eq. (IV.59) yields:

$$\bar{\dot{\mathcal{H}}} = \dot{F} + \dot{T}S \tag{IV.62}$$

From eq. (IV.62) and (IV.53):

$$\dot{U} = \bar{\dot{\mathcal{H}}} + T\dot{S} \tag{IV.63}$$

Eq. (IV.63) is a simplified formula relating the time derivative of the internal energy (a macroscopic quantity) to the Hamiltonian describing the dynamics of the system and to two other macroscopic quantities: the temperature and the entropy production. The total time derivative of the Hamiltonian in eq. (IV.50) for trajectories  $\underline{q}(t)$ ,  $\underline{p}(t)$  is given by:

$$\dot{\mathcal{H}} = \sum_i \left( \frac{\partial \mathcal{H}}{\partial q_i} \dot{q}_i + \frac{\partial \mathcal{H}}{\partial p_i} \dot{p}_i \right) + \sum_k \frac{\partial \mathcal{H}}{\partial a_k} \dot{a}_k \tag{IV.64}$$

Physical trajectories satisfy Hamilton's equations:

$$\dot{q}_i = \frac{\partial \mathcal{H}}{\partial p_i}; \quad \dot{p}_i = - \frac{\partial \mathcal{H}}{\partial q_i} \tag{IV.65}$$

Inserting eq. (IV.65) into eq. (IV.64) yields:

$$\dot{\mathcal{H}} = \sum_k \frac{\partial \mathcal{H}}{\partial a_k} \dot{a}_k \tag{IV.66}$$

The average of eq. (IV.66) over short periods of time yields:

$$\bar{\dot{\mathcal{H}}} = \sum_k \overline{\frac{\partial \mathcal{H}}{\partial a_k}} \dot{a}_k \tag{IV.67}$$



## Chapter IV. Rebuttal of Ziegler's MaxEP principle

The quantities  $a_k$  (and their time derivatives) are macroscopic properties which can be held constant in the time scale of microscopic variations.

Finally,  $\overline{\mathcal{H}}$  in eq. (IV.63) can be replaced by its expression in eq. (IV.67), resulting in the following expression for the time derivative of internal energy:

$$\dot{U} = \sum_k \frac{\overline{\partial \mathcal{H}}}{\partial a_k} \dot{a}_k + T\dot{S} \quad (\text{IV.68})$$

The rate of change in internal energy according to eq. (IV.68) has two contributions: a reversible contribution from the averaged partial derivatives of the Hamiltonian with respect to the external coordinates, and an irreversible contribution from  $T\dot{S}$ . For the sake of simplicity, let us define forces  $Y_k^r$  such that:

$$Y_k^r \equiv \frac{\overline{\partial \mathcal{H}}}{\partial a_k} \quad (\text{IV.69})$$

The physical meaning of this force will be discussed later in the section. For now, note that this force is not necessarily equal to the one defined in eq. (IV.34).

An alternative expression for  $\dot{U}$  can be obtained if one recalls that the systems under study are adiabatic and closed. Hence, any change in internal energy comes from the external forces applied to the system. In other words:

$$\dot{U} = \sum_k \frac{\partial U}{\partial a_k} \dot{a}_k \quad (\text{IV.70})$$

Here, new forces  $Y_k$  shall be defined such that:

$$Y_k = \frac{\partial U}{\partial a_k} \quad (\text{IV.71})$$

From this definition, eq. (IV.70) takes a simpler form:

$$\dot{U} = \sum_k Y_k \dot{a}_k \quad (\text{IV.72})$$

The meaning of the external coordinates becomes clearer with the above expression. If the system consists of gas and a piston moving along the  $x$ -direction under the influence of an external force,  $Y$  is the force,  $a$  is the position of the piston (along the  $x$ -direction) and (IV.72) is simply the expression of the First Law of Thermodynamics. The same

## Chapter IV. Rebuttal of Ziegler's MaxEP principle

applies to a rubber band being stretched:  $Y$  is again the external force,  $a$  is the deformation of the rubber band, and eq. (IV.72) represents the First Law of Thermodynamics.

Inserting eqs. (IV.72) and (IV.69) into eq. (IV.68) yields:

$$\begin{aligned} \sum_k Y_k \dot{a}_k &= \sum_k Y_k^r \dot{a}_k + T\dot{S} \Rightarrow \\ \Rightarrow \sum_k (Y_k - Y_k^r) \dot{a}_k &= T\dot{S} \end{aligned} \quad (\text{IV.73})$$

The difference  $Y_k - Y_k^r$  can be seen as the irreversible contribution of the force  $Y_k$ , responsible for the entropy production in the system. To clarify this statement, let us reconsider the system consisting of gas in a cylinder with cross-sectional area  $A$ . The gas can be compressed/expanded by applying a force  $Y$  on a piston. Assuming that at any moment the pressure  $p$  inside the cylinder is homogeneous, the reversible work exerted on the system is  $-pAdx$ , so that  $Y^r = -pA$ . The difference  $Y_k - Y_k^r$  therefore denotes an excess force, which is responsible for the entropy production in the system. This force shall be named  $Y_k^i$ :

$$Y_k^i \equiv Y_k - Y_k^r \quad (\text{IV.74})$$

Hence, an expression is derived for the product  $T\dot{S}$  as a function of  $\dot{a}_k$  and  $Y_k^i$ , which Ziegler considers to be respectively the thermodynamic fluxes and forces of the system:

$$T\dot{S} \equiv D = \sum_k Y_k^i \dot{a}_k \quad (\text{IV.75})$$

The quantity  $D$  defined above is called the dissipation function. Note that eq. (IV.69) gives the reversible contribution  $Y_k^r$  as a function of the average of the partial derivative of the Hamiltonian. However, such expression is not suitable for practical calculations since a macroscopic observer does not know the Hamiltonian of the microscopic system. In other words, he does not know the exact expression of eq. (IV.50).

To obtain  $Y_k^r$  as a function of macroscopic quantities, one can look again at eq. (IV.68). This equation relates the rate of change in internal energy to the rate of change in  $\underline{a}$  and to the rate of change in  $S$ . Note that knowing  $\underline{a}$  alone is not enough to determine the state of the system. Indeed, looking back at the gas-in-a-cylinder example, knowing the position of the piston is not enough to determine its state. If the gas is compressed by  $\Delta x$

## Chapter IV. Rebuttal of Ziegler's MaxEP principle

through the action of a reversible force, its final internal energy will be lower than the one obtained if the force is irreversible. However, knowing both  $\Delta x$  and the entropy suffices to determine the state of this system. For example, the internal energy of a monoatomic gas is related to its entropy, volume and number of molecules via the Sackur-Tetrode equation (Schroeder, 2000).

The above discussion can be generalized to a higher number of forces. For instance, the state of an insulated elastic body being stretched on the  $x$  and  $y$ -directions is determined from  $\Delta x, \Delta y$  and the entropy of the system, despite how much each force (individually) contributed to entropy variation. Therefore, the following equation holds:

$$U = U(\underline{a}, S) \quad (\text{IV.76})$$

Finally, eqs. (IV.76) and (IV.68) together yield:

$$\overline{\frac{\partial \mathcal{H}}{\partial a_k}} \equiv Y_k^r = \frac{\partial}{\partial a_k} U(\underline{a}, S) \quad (\text{IV.77})$$

$$T = \frac{\partial}{\partial S} U(\underline{a}, S) \quad (\text{IV.78})$$

Eq. (IV.77) is one possible way to write the reversible contributions in terms of the state variables. Alternatively, one could compare eqs. (IV.68) and (IV.53) to obtain:

$$\begin{aligned} \sum_k \overline{\frac{\partial \mathcal{H}}{\partial a_k}} \dot{a}_k + T \dot{S} &= \dot{F} + \dot{T} S + T \dot{S} \Rightarrow \\ \Rightarrow \dot{F} &= \sum_k \overline{\frac{\partial \mathcal{H}}{\partial a_k}} \dot{a}_k - S \dot{T} \end{aligned} \quad (\text{IV.79})$$

The above equation suggests that the reversible contributions to the forces can be obtained from Helmholtz free energy if the state variables chosen to represent the system are  $\underline{a}$  and  $T$ . In this case:

$$\overline{\frac{\partial \mathcal{H}}{\partial a_k}} \equiv Y_k^r = \frac{\partial}{\partial a_k} F(\underline{a}, T) \quad (\text{IV.80})$$

$$S = -\frac{\partial}{\partial T} F(\underline{a}, T) \quad (\text{IV.81})$$

Note that the additional state variables ( $S$  or  $T$ ) needed to determine the reversible contribution to the forces do not undermine the form of the Hamiltonian written in eq.

## Chapter IV. Rebuttal of Ziegler's MaxEP principle

(IV.50). These quantities will appear “naturally” during the averaging of  $\partial\mathcal{H}/\partial\alpha_k$ , since the probability distribution of the microstates depends on  $T$  (see eq. (IV.55)) and is related to  $S$  via eq. (IV.54).

The developments so far were essentially the preliminary steps in the derivation of OP. The remaining development, which is the cornerstone of the OP proof, is done in 20 lines of convoluted text in Ziegler (1970). These are replicated *ipsis litteris* below, except for notations and references to equations, which were updated according to the conventions used in this chapter. From Ziegler (1970), p. 859:

*Let the state of a macrosystem, together with the macro-force  $Y_m$ , be given at time  $t$ , and let us ask for the corresponding velocity  $\dot{a}$ . According to the equation (IV.77),  $Y_m^r$  is a state variable. Thus,  $Y_m^r$  is given and it follows from (IV.74) that also the vector  $Y_m^i$  is known. This is essential for what follows.*

*According to (IV.65) and (IV.50),  $\dot{a}_m$  does not enter the differential equations of the motion of the microsystem. If, therefore,  $\dot{a}_m$  is varied at time  $t$  by the amount  $\delta\dot{a}_m$ , this variation is of arbitrarily small influence on the motion, during a sufficiently short time interval  $t \dots t + \delta t$ , of the various microsystems corresponding to the given macrosystem. In the irreversible case, though, there is also a flux in phase space, and the corresponding change of  $\psi$  in the layers bounded by  $H$ -surfaces may be different for the velocities  $\dot{a}_m$  and  $\dot{a}_m + \delta\dot{a}_m$ . However, for variations  $\delta\dot{a}_m$  which do not affect the two sides of the last equality in (IV.75), the first equality in (IV.75) and equation (IV.60) show that  $\dot{S} = -\dot{\psi}$  is the same. It follows that not only a single velocity  $\dot{a}_m$  is compatible with the force  $Y_m$  or - equivalently - with its irreversible part  $Y_m^i$  but also all those varied velocities  $\dot{a}_m + \delta\dot{a}_m$  for which the dissipation function and hence also the scalar product with  $Y_m^i$  remain unchanged. However, this is possible only if  $Y_m^i$  is orthogonal to the tangential plane of the dissipation surface passing through the end point of  $\dot{a}_m$ .*

*We have thus proved that, for systems with conservative microforces, whether nongyroscopic or with gyroscopic forces of the type (2.4)<sup>†</sup>, (2.5)<sup>†</sup>, the irreversible force  $Y_m^i$  corresponding to the velocity  $\dot{a}_m$  is orthogonal to the dissipation surface in the end point of  $\dot{a}_m$ .*

<sup>†</sup>These equations describe the specific type of gyroscopic forces for which Hamilton's approach still holds

## Chapter IV. Rebuttal of Ziegler's MaxEP principle

In what follows, the above final steps will be discussed in full detail, and the mistake made in the demonstration will be put in evidence.

First, let us take another look at eq. (IV.75). The product  $T\dot{S}$ , and hence the dissipation function  $D$ , cannot be entirely determined based on the state of the system ( $\underline{a}$  and  $T$ ). Even if  $\underline{a}$  and  $T$  are known, that is not enough to determine how the system will *evolve* after an infinitesimal interval  $\delta t$ . However, if the state *and* the instantaneous velocities  $\underline{\dot{a}}$  are known, then the instantaneous  $T\dot{S}$ , and hence the instantaneous value  $D$  is entirely determined. Therefore, one can write:

$$D = D(T, \underline{a}, \underline{\dot{a}}) \quad (\text{IV.82})$$

For a given state  $(T^*, \underline{a}^*)$ , the dissipation function defines a surface in the velocity space:

$$D^*(\underline{\dot{a}}) = D(T^*, \underline{a}^*, \underline{\dot{a}}) \quad (\text{IV.83})$$

If the state of the macrosystem and the forces  $\underline{Y}$  are known, then  $\underline{Y}^r$  is known, since it is a state function according to eqs. (IV.77) and (IV.80). Therefore,  $\underline{Y}^i$  can be determined from eq. (IV.74).

However, the state and the forces alone do not suffice to determine the dynamics of the system. Indeed, note that the velocities cannot be determined from eq. (IV.75) alone, since there are multiple variables  $\underline{\dot{a}}$  and only one equation. Phenomenological laws are hence necessary to find  $\underline{\dot{a}}$  and fully describe the dynamics of the macrosystem.

Let us assume that the velocities  $\underline{\dot{a}}^*$  corresponding to the state  $(T^*, \underline{a}^*)$  and to the forces  $\underline{Y}^{*i}$  were somehow calculated. The dissipation of the microsystem in this case is denoted  $D = D(T^*, \underline{a}^*, \underline{\dot{a}}^*) = D_0$ . The cornerstone for the proof of OP is essentially the following question:

*Q1: Assume a system defined by the state  $(T^*, \underline{a}^*)$  and by the forces  $\underline{Y}^{*i}$ . Assume there exist velocities  $\underline{\dot{a}}^*$  corresponding to this system, and let  $\delta^{D_0}\underline{\dot{a}}$  be an incremental displacement along the isosurface  $D^*(\underline{\dot{a}}) = D_0$  (c.f. Figure IV.5). In this case, are the velocities  $\underline{\dot{a}}^* + \delta^{D_0}\underline{\dot{a}}$  also compatible with the same system?*

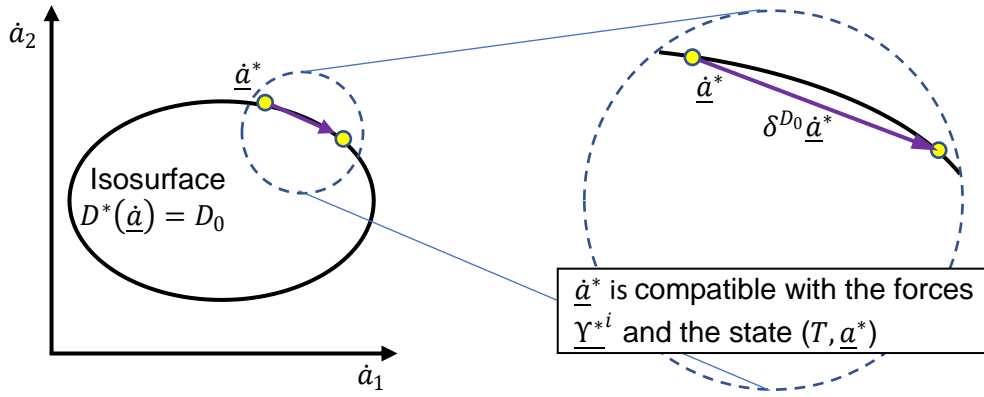


Figure IV.5 – Change in velocities following the isosurface  $D^*(\underline{\dot{a}}) = D_0$ , for a system with only two forces

In Q1, two velocities  $\underline{\dot{a}}_1^*$  and  $\underline{\dot{a}}_2^*$  are said to be compatible with the same system if, for its given macrostate and forces, the corresponding fluxes can be equal to  $\underline{\dot{a}}_1^*$  or  $\underline{\dot{a}}_2^*$ . According to Ziegler, given that  $\underline{\dot{a}}^*$  is compatible with the state  $(T^*, \underline{a}^*)$  and the forces  $\underline{\Upsilon}^{*i}$ ,  $\underline{\dot{a}}^* + \delta^{D_0} \underline{\dot{a}}^*$  will also be compatible with these conditions if and only if (Ziegler, 1970, p. 859):

(a) the increment  $\delta^{D_0} \underline{\dot{a}}^*$  is of arbitrarily small influence on the motion during a short interval  $\delta t$ ;

and

(b) the probability distribution of the microstates is not affected by this increment.

Proving that the answer to Q1 is yes would also prove OP. However, Ziegler does not answer the above question. Instead, he finds a necessary and sufficient condition for a positive answer. This is the crucial mistake in Ziegler's derivation: he claims that finding a condition equivalent to Q1 is the proof that Q1 is true. This logical flaw shall be clarified in the following paragraphs.

To prove (a), one can use the Taylor expansion of the Hamiltonian in eq. (IV.50) to evaluate the difference in the motion of a microsystem whose external velocities  $\underline{\dot{a}}^*$  fluctuate by  $\delta^{D_0} \underline{\dot{a}}^*$ :

$$\mathcal{H}_1(\underline{q}, \underline{p}, \underline{a}^* + t \underline{\dot{a}}^*) = \mathcal{H}(\underline{q}, \underline{p}, \underline{a}^*) + \sum_k \frac{\partial}{\partial a_k} \mathcal{H}(\underline{q}, \underline{p}, \underline{a}) \Big|_{\underline{a}^*} \times t \dot{a}_k^*$$

$$\mathcal{H}_2(\underline{q}, \underline{p}, \underline{a}^* + t(\underline{\dot{a}}^* + \delta^{D_0} \underline{\dot{a}}^*)) = \mathcal{H}(\underline{q}, \underline{p}, \underline{a}^*) + \sum_k \frac{\partial}{\partial a_k} \mathcal{H}(\underline{q}, \underline{p}, \underline{a}) \Big|_{\underline{a}^*} \times t(\dot{a}_k^* + \delta^{D_0} \dot{a}_k^*)$$

Hence:

$$\mathcal{H}_2 - \mathcal{H}_1 = \sum_k \frac{\partial}{\partial a_k} \mathcal{H}(\underline{q}, \underline{p}, \underline{a}) \Big|_{\underline{a}^*} \times t \times \delta^{D_0} \dot{a}_k^* = O(\delta t \|\delta^{D_0} \dot{a}^*\|) \quad (\text{IV.84})$$

Eq. (IV.84) shows that small fluctuations in the external velocities do not affect the motion of the microsystem during short time intervals. This concludes the proof of (a).

Statement (b) cannot be discussed using the discrete probability distribution given in eq. (IV.55). Indeed, the phase space  $(\underline{q}, \underline{p})$  used to describe the motion of the microsystems takes continuous values. Hence, the probability of finding a system within a certain range  $[\underline{q}^0, \underline{q}^0 + d\underline{q}]$  and  $[\underline{p}^0, \underline{p}^0 + d\underline{p}]$  is written by means of a probability density function  $g$ :

$$P(\underline{p} \in [\underline{p}^0, \underline{p}^0 + d\underline{p}] \wedge \underline{q} \in [\underline{q}^0, \underline{q}^0 + d\underline{q}]) = g D_q D_p \quad (\text{IV.85})$$

In eq. (IV.85),  $D_q = d_{q_1} d_{q_2} \dots d_{q_n}$  and  $D_p = d_{p_1} d_{p_2} \dots d_{p_n}$ . Besides, the continuous version of eq. (IV.55) is (Gibbs, 1948):

$$P(\underline{p} \in [\underline{p}^0, \underline{p}^0 + d\underline{p}] \wedge \underline{q} \in [\underline{q}^0, \underline{q}^0 + d\underline{q}]) = C \times e^{\frac{F - \mathcal{H}(\underline{q}^0, \underline{p}^0, \underline{a})}{k_B T}} D_q D_p \quad (\text{IV.86})$$

where  $C$  is a constant. From eqs. (IV.85) and (IV.86), the continuous probability distribution can be written as a function of  $\underline{q}$ ,  $\underline{p}$ ,  $\underline{a}$  and  $T$ :

$$g = C \times e^{\frac{F(\underline{a}, T) - \mathcal{H}(\underline{q}, \underline{p}, \underline{a})}{k_B T}} \quad (\text{IV.87})$$

Eq. (IV.87) should be used to evaluate the probability distribution over the phase space of a system with given  $\underline{a}$  and  $T$ . The quantity  $\psi$  defined in eq. (IV.56) for the discrete microstates can be redefined for the probability density in eq. (IV.87) as follows:

$$\psi \equiv k_B \ln(g/C) = \frac{F - \mathcal{H}}{T} \quad (\text{IV.88})$$

With this definition, eq. (IV.60) still holds (Gibbs, 1948). Eqs. (IV.60) and (IV.75) together yield the following result with and without velocity fluctuations:

$$\begin{aligned} \dot{\bar{\psi}}_1 &= -\frac{1}{T} \sum_k Y_k^i \dot{a}_k^* \\ \dot{\bar{\psi}}_2 &= -\frac{1}{T} \sum_k Y_k^i (\dot{a}_k^* + \delta^{D_0} \dot{a}_k^*) \end{aligned} \quad (\text{IV.89})$$

## Chapter IV. Rebuttal of Ziegler's MaxEP principle

Ziegler then argues that  $\dot{\bar{\psi}}_1 = \dot{\bar{\psi}}_2$  if and only if  $\sum_k \Upsilon_k^i \delta^{D_0} \dot{a}_k^* = 0$ , which is true. However, he claims that  $\dot{\bar{\psi}}_1 = \dot{\bar{\psi}}_2$  is equivalent to stating that the probability distribution is unaffected by the velocity fluctuation, and this is the first flaw in his proof. This flaw is summarized in equation (IV.90).

$$\overbrace{\sum_k \Upsilon_k^i \delta^{D_0} \dot{a}_k^* = 0}^{\text{OP}} \stackrel{\text{True}}{\Leftrightarrow} \dot{\bar{\psi}}_1 = \dot{\bar{\psi}}_2 \stackrel{\text{False}}{\Leftrightarrow} \text{(b)} \quad (\text{IV.90})$$

The first equality in eq. (IV.90) is OP itself, as shown in Figure IV.4. Recall that this is the very property Ziegler wishes to prove. The second equality in this equation,  $\dot{\bar{\psi}}_1 = \dot{\bar{\psi}}_2$  indicates that the average value of the quantity  $\psi$  will remain invariant over a short period of time  $\delta t$ . However, that does not mean that distribution itself will remain invariant. Indeed, if  $\bar{\psi}_1 = \bar{\psi}_2$  during the interval  $[0, \delta t]$ , eqs. (IV.88) and (IV.85) yield:

$$\begin{aligned} \int k_B \ln\left(\frac{1}{C} g_1\right) g_1 D_q D_p &= \int k_B \ln\left(\frac{1}{C} g_2\right) g_2 D_q D_p \Rightarrow \\ \Rightarrow \int \ln\left(\frac{1}{C} g_1\right) g_1 D_q D_p &= \int \ln\left(\frac{1}{C} g_2\right) g_2 D_q D_p \end{aligned} \quad (\text{IV.91})$$

But the equality (IV.91) does not imply that the functions  $g_1$  and  $g_2$  are identical over time.

The second flaw in Ziegler's demonstration is that he concludes his proof with (IV.90). However, eq. (IV.90) is simply a re-statement of (b). Even if OP statement was equivalent to statement (b), neither of them is proved.

### IV.2.1 Summary of the main flaws and limitations

The development by Ziegler (1970) has two main logical flaws, and is severely limited. Its limitation comes from the fact that the system under consideration is assumed to be closed and insulated. Therefore, any variation in its internal energy comes necessarily from mechanical work exerted on/by the system. This means that the external variables  $\underline{a}$  in the above development can only be strain components or deformations, so phenomena such as heat flow, diffusion and reaction are all a priori excluded from OP. It is very important to highlight this limitation, as it invalidates the widespread idea that OP (and hence MaxEP) is a generalization of Onsager's reciprocal relations (Ziegler, 1968; Martyushev and Seleznev, 2006; Yang et al., 2013; Seleznev and Martyushev, 2014).



## Chapter IV. Rebuttal of Ziegler's MaxEP principle

Apart from the above restriction, two logical flaws in Ziegler's demonstration undermine his principle. These are:

- 1) The second equivalence in eq. (IV.90), which he establishes during his demonstration, is false. Indeed, the fact that  $\bar{\psi}_1 = \bar{\psi}_2$  for a certain interval of time does not imply that  $\psi_1 = \psi_2$  during this interval. In general, there exist distribution probabilities  $g_1$  and  $g_2 \neq g_1$  for which eq. (IV.91) is true.
- 2) Even if that equivalence was true, it does not prove Ziegler's Orthogonality Principle. It only shows that OP is equivalent to statement (b), but one would still need to prove that the phenomenological laws of nature work in such a way that (b) is always true.

### IV.3 A counterexample: coupled reactions far from equilibrium

Section IV.2 does not disprove Ziegler's MaxEP principle. It only invalidates its demonstration. Still, its simple formulation and practicality are very appealing, especially in the field of far-from-equilibrium thermodynamics, where concepts and theories are still being developed. Hence, other researchers could be inclined to accept Ziegler's MaxEP principle as a conjecture. This section will show that Ziegler's principle fails to predict the kinetics of coupled reactions, and therefore cannot be used neither as a theorem nor as a conjecture.

An important disclaimer before proceeding: Bataille et al. (1978) have also used a reactional system to disprove the MaxEP principle. However, the argument that will be presented below was made without knowledge of said article. Bataille et al. (1978) considered a general reactional system with  $r$  reactions and  $n$  chemicals, which is more general than the system that will be considered here (with 2 reactions and 3 chemicals). Still, one counterexample suffices to disprove a theorem, regardless of how specific the example is, as long as it satisfies the conditions for which said theorem can be applied. Further, choosing a specific case study with a defined number of chemicals and reactions helps with the calculations and representation of the results.

*IV.3.1 Preliminary study – assessing the applicability of Onsager's reciprocal relations to a reaction system*

Since Ziegler's MaxEP principle is supposedly an extension of Onsager's reciprocal relations to far-from-equilibrium systems, one may be inclined to examine the applicability of Onsager's reciprocal relations first. This is the objective of the present section.

Let us consider an isolated system of two types of molecules  $A$  and  $B$ , which undergo isomerization according to the following reaction:



For convenience, the above reactions (forward and backward) are considered first-order with respect to  $A$  and  $B$  respectively; see Yuan and Chen (2001) for examples of first-order reversible isomerization.

Because the reactions in eq. (IV.92) are first-order, one may assume that the rate-determining steps of the mechanisms involve only one molecule. That is, even if the mechanism of  $A \rightarrow B$  takes several steps, the slowest one is a transformation that a molecule  $A$  undergoes without the interference of other molecules  $A$  or  $B$ . The same can be said for the  $B \rightarrow A$  reaction: its rate-determining step involves one molecule of  $B$  alone.

This system has a well-defined equilibrium state (when forward and backward reaction velocities are the same). Further, its fluctuations (i.e., deviations from the mean equilibrium state) are captured by the reaction extent  $\xi$ . This means that, according to eqs. (IV.25) and (IV.34), the thermodynamic flux of the process is the reaction rate  $\dot{\xi}$ , and the corresponding force is  $X = A_1/T$ , where  $A_1 = \mu_A - \mu_B$  (difference in chemical potential of the species) is the chemical affinity of eq. (IV.92). Hence, one could ask whether reaction systems with multiple reactions will follow the Onsager's reciprocal relations discussed in Sections I.3 and IV.1.1.

The answer to this question is affirmative if the system satisfies the 5 conditions listed at the end of Section IV.1.1. Here they shall be re-stated again, each condition followed by a discussion on whether or not it is satisfied.

1. *The fluctuations associated to the fluxes are mechanical variables, i.e. quantities defined for any given microstate. For example, heat and diffusive fluxes are*

## Chapter IV. Rebuttal of Ziegler's MaxEP principle

*associated respectively to internal energy and concentration; both these quantities are well-defined for any given microstate.*

This is indeed true. The reaction extent can be measured for any given microstate as  $\xi = N_A^{eq} - N_A$ , where  $N_A$  is the number of moles of molecule A, and  $N_A^{eq}$  is the expected value of  $N_A$  at equilibrium.

- 2. The number of molecules in the system is sufficiently large so that the fluctuations are continuous-like. As a hypothetical example of a closed system violating this rule, imagine a mixture of 3 molecules of water and 3 molecules of some acid HA. The system undergoes ionization according to the following reaction:  $HA + H_2O \rightleftharpoons A^- + H_3O^+$ . The fluctuations here are associated to the reaction extent, which can only take 4 discrete values.*

Because this case study is hypothetical, one can simply assume that the number of molecules in the system is in the order of 1 mol, so that condition (2) is true.

- 3. At equilibrium, fluctuating mechanical variables follow a Gaussian distribution, according to eq. (IV.7). Hill (1986) and de Groot and Mazur (1984) prove it for the energy fluctuations in an isothermal closed system. More generally, de Groot and Mazur (1984) give a sufficient condition for this assumption to hold: if the mechanical variable corresponds to the sum of some property of the individual molecules, and if these individual properties are mutually independent and follow the same probability distribution, then the mechanical variable will follow a Gaussian distribution in the neighbourhood of its mean value. An alternative assumption is: the second-order Taylor expansion of the entropy around  $\underline{\alpha} = \underline{0}$  is a satisfactory approximation. In this case, eq. (IV.17) replaces eq. (IV.7) as the assumption.*

This is a delicate condition that will be discussed in detail here. Imagine the total number of molecules in the reaction system (IV.92) is  $N$ . Each molecule can be at the state A or B. Let us assume that the probability of a molecule being at state A is  $p$ , so the probability of it being at state B is  $(1 - p)$ . One can define a random variable  $\chi$  such that:

$$\chi = \begin{cases} 1 & \text{if molecule is at state A} \\ 0 & \text{if molecule is at state B} \end{cases} \quad (\text{IV.93})$$

## Chapter IV. Rebuttal of Ziegler's MaxEP principle

This variable is the individual property of the molecules mentioned in condition (3). The probability distribution for this variable is:

$$\begin{aligned} P(\chi = 1) &= p \\ P(\chi = 0) &= 1 - p \end{aligned} \tag{IV.94}$$

The random variables associated to the various particles in the system are independent, and their sum  $N_A = \sum \chi$  corresponds to the number of molecules  $A$  in the system. This sum follows a binomial distribution:

$$P(N_A = n) = C_n^N p^n (1 - p)^{N-n} \tag{IV.95}$$

Note that  $N_A$ , the sum of the individual properties  $\chi$ , is the mechanical variable mentioned in condition (3). The expected value of the sum,  $E[N_A]$ , is equal to the sum of the expected values for each variable  $\chi$ , so that:

$$E(N_A) = Np \tag{IV.96}$$

Hence, the equilibrium constant of this reaction,  $K_{eq} = E(N_B)/E(N_A)$ , takes the form:

$$K_{eq} = \frac{(1 - p)}{p} \tag{IV.97}$$

According to the third assumption in Onsager's reciprocal relations, the random variable  $N_A$  should follow a Gaussian (or normal) distribution. And indeed, the de Moivre – Laplace theorem, a special case of the central limit theorem, states that the distribution of the random variable  $S_N = (N_A - Np)/\sqrt{Np(1 - p)}$  approaches the standard normal distribution as  $N \rightarrow \infty$  (Nascimento Magalhães, 2006). Although the distribution  $S_N$  does converge to the standard normal distribution, the argument is slightly more complicated for  $N_A$ . That is because  $N_A$  converges to a normal distribution with mean  $Np$  and standard deviation  $\sqrt{Np(1 - p)}$  only around its mean value  $Np$  (Thamattoor, 2018). When one approaches the tail of the binomial distribution, it no longer resembles a Gaussian. But how far from the mean  $Np$  the approximation is still valid? Thamattoor (2018) proves that the distribution of  $N_A$  in eq. (IV.95) converges to a Gaussian for  $n \in [Np - c\sqrt{Np(1 - p)}, Np + c\sqrt{Np(1 - p)}]$ , with  $c$  being a finite and arbitrary real number. However, his demonstration would remain valid for  $n \in [Np - o(N), Np +$

## Chapter IV. Rebuttal of Ziegler's MaxEP principle

$o(N)$ ]. In other words, in the limit  $N \rightarrow \infty$ , the distribution of the random variable  $N_A$  approaches a normal distribution in any interval centred at  $Np$  and with length of  $o(N)$ .

In a reaction system however, the difference  $N_A - Np$  can take values of order  $O(N)$ . In a hypothetical example, the reaction (IV.92) could be driven towards the left at very low temperatures. The system could then be quickly brought to a higher temperature, so that at the beginning of the equilibration process the number of molecules A is  $N_A \approx N$ , at a distance  $N(1 - p)$  from the mean value  $E(N_A)$ . The distribution does not follow a Gaussian in this case, so one can say that condition (3) only holds if the reaction system is close to equilibrium.

To verify this statement, one can look at the expression of the reaction velocity as a function of its affinity, given below (Prigogine, 1962):

$$v = v^f \left( 1 - e^{-\frac{A_1}{RT}} \right) \quad (\text{IV.98})$$

where  $v^f$  is the velocity of the forward reaction  $A \rightarrow B$ . The traditional near-equilibrium condition for a reaction system is written as:

$$|A_1/RT| \ll 1 \quad (\text{IV.99})$$

Hence, a near-equilibrium reaction obeys the following kinetics (Prigogine, 1962):

$$v = v_{eq}^f \left( \frac{A_1}{RT} \right) \quad (\text{IV.100})$$

Note that in eq. (IV.100) the flux (reaction velocity  $v$ ) is proportional to the force  $A_1/T$ . The condition for linear flux-force relationship is therefore given by eq. (IV.99). Affinity  $A_1$  can be rewritten in terms of  $N_A$  and  $K_{eq}$ , so that eq. (IV.99) takes the following form:

$$\left| \ln \left( K_{eq} \frac{N_A}{N - N_A} \right) \right| \ll 1 \quad (\text{IV.101})$$

Replacing  $K_{eq}$  in eq. (IV.101) by its expression in eq. (IV.97) and setting  $N_A = n$  yields:

$$\left| \ln \left( \frac{(1-p)}{p} \frac{n}{N-n} \right) \right| \ll 1 \quad (\text{IV.102})$$

## Chapter IV. Rebuttal of Ziegler's MaxEP principle

If  $n = Np + o(N)$  and  $N \rightarrow \infty$ :

$$\begin{aligned} \lim_{N \rightarrow \infty} \left| \ln \left( \frac{(1-p)}{p} \frac{Np}{N - Np - o(N)} \right) \right| &= \lim_{N \rightarrow \infty} \left| \ln \left( \frac{N}{N - o(N)/(1-p)} \right) \right| = \\ &= \lim_{N \rightarrow \infty} \left| \ln \left( \frac{1}{1 - [o(N)/N]/(1-p)} \right) \right| \Rightarrow \\ &\Rightarrow \lim_{N \rightarrow \infty} \left| \ln \left( \frac{(1-p)}{p} \frac{Np}{N - Np - o(N)} \right) \right| = 0 \end{aligned} \quad (\text{IV.103})$$

However, when  $n = Np + O(N)$  (say  $n = kN$ ):

$$\lim_{N \rightarrow \infty} \left| \ln \left( \frac{(1-p)}{p} \frac{kN}{N - kN} \right) \right| = \ln \left( \frac{1-p}{p} \frac{k}{1-k} \right) \neq 0 \quad (\text{IV.104})$$

The above developments show the connection between condition (3) and the well-known condition for linear flux-force relationships given by eq. (IV.99). The conclusion is that Onsager's reciprocal relations are not applicable for reactions very far from equilibrium, because condition (3) is violated. Near equilibrium, the reciprocal relations hold (Prigogine, 1962).

4. *Microscopic reversibility holds. In classic mechanics, this is equivalent to saying that the equations of motion for the particles composing the system are invariant under time-reversal. Any conservative system obeys this principle.*

This is true as well. In theory, all isolated systems have time symmetry. See (Onsager, 1931a) for an interesting application of microscopic reversibility in the kinetics of coupled reactions.

5. *The dynamics of the average fluctuations are given by the linear differential equations in eq. (IV.26). This linear flux-fluctuation relationship is observed experimentally for various systems, including reactions near equilibrium and pairs of subsystems exchanging heat and mass. However, these experimental measures are taken for systems out of equilibrium, since the small fluctuations of a system at equilibrium are hard to capture. One has to assume that the same dynamics observed experimentally for large fluctuations holds in the limit  $\underline{\alpha} \underline{\alpha} = O(K_B \underline{K}^{-1})$ . Alternatively, one could assume eq. (IV.36) instead of eq. (IV.26).*

## Chapter IV. Rebuttal of Ziegler's MaxEP principle

This condition (5) is virtually impossible to confirm, as the dynamics of a system at equilibrium will look steady for a macroscopic observer. Regardless, condition (3) is violated for a reaction system far from equilibrium, which is enough to reject the reciprocal relations for such a system.

But Ziegler's MaxEP principle does rely upon conditions (3) and (5), which are replaced by conditions (3') and (5'). So the question now is of whether this principle can be applied to a reaction system. The necessary conditions for using such a principle are (1), (2), (4) listed above (which were shown to be satisfied), as well as (3') and (5') in Section IV.1.3. The following section will show that, even though (3') and (5') are satisfied, MaxEP fails to predict the kinetics of a coupled reaction system.

### IV.3.2 Attesting the inadequacy of Ziegler's MaxEP for coupled reactions

Let us consider an isolated system with three components  $A$ ,  $B$  and  $C$ . Two reversible reactions happen in this system, according to the equation below:



For simplification purposes, it shall be assumed that the heat of reaction is negligible in both reactions. Alternatively, one could assume that reactive concentrations are negligible compared to the amount of solvent in solution, so that the temperature of the system remains the same. Further, all reactions are of first order. Their affinities are therefore given by the following expressions (Prigogine, 1962):

$$\begin{aligned} A_1 &= RT \ln \left( K_{eq}^1(T) \frac{C_A}{C_B} \right) \\ A_2 &= RT \ln \left( K_{eq}^2(T) \frac{C_B}{C_C} \right) \end{aligned} \tag{IV.106}$$

where  $C_A$  and  $C_B$  are respectively the molar concentrations of  $A$  and  $B$ , and where the equilibrium constants  $K_{eq}^1$  and  $K_{eq}^2$  can depend on the temperature.

Because the system is isolated, its mass is conserved:

$$C_A + C_B + C_C = C_0 \tag{IV.107}$$

## Chapter IV. Rebuttal of Ziegler's MaxEP principle

From eqs. (IV.106) and (IV.107), it is possible to write  $C_A$  and  $C_B$  as a function of  $A_1$  and  $A_2$ :

$$C_A = C_0 \frac{e^{\frac{A_1+A_2}{RT}}}{K_{eq}^1 \left( K_{eq}^2 + e^{\frac{A_2}{RT}} \right) + e^{\frac{A_1+A_2}{RT}}} \quad (IV.108)$$

$$C_B = C_0 \frac{1}{\left[ \left( K_{eq}^2 e^{-\frac{A_2}{RT}} + 1 \right) + \frac{e^{\frac{A_1}{RT}}}{K_{eq}^1} \right]}$$

The kinetics of first-order reactions can be written as a function of concentrations and affinities:

$$v_1 = k_1^f C_A \left( 1 - e^{-\frac{A_1}{RT}} \right) \quad (IV.109)$$

$$v_2 = k_2^f C_B \left( 1 - e^{-\frac{A_2}{RT}} \right)$$

where  $v_1$  and  $v_2$  are the velocities (in moles per volume) of the first and second reactions, and  $k_1^f$  and  $k_2^f$  are the forward rate constants. Inserting eq. (IV.108) into eq. (IV.109) yields the velocities as a function of the affinities:

$$v_1 = k_1^f C_0 \frac{e^{\frac{A_1+A_2}{RT}} \left( 1 - e^{-\frac{A_1}{RT}} \right)}{K_{eq}^1 \left( K_{eq}^2 + e^{\frac{A_2}{RT}} \right) + e^{\frac{A_1+A_2}{RT}}} \quad (IV.110)$$

$$v_2 = k_2^f C_0 \frac{1 - e^{-\frac{A_2}{RT}}}{\left[ \left( K_{eq}^2 e^{-\frac{A_2}{RT}} + 1 \right) + \frac{e^{\frac{A_1}{RT}}}{K_{eq}^1} \right]}$$

Eq. (IV.110) can be inverted to give the affinities as functions of the velocities:

$$\frac{A_1}{T} = -R \ln \left[ \frac{-\frac{k_1^b}{k_1^f} v_1 + \frac{k_1^b}{k_2^b} v_2 + C_0 k_1^b}{\left( 1 + \frac{k_2^f}{k_2^b} \right) v_1 + \frac{k_1^b}{k_2^b} v_2 + C_0 k_1^b} \right] \quad (IV.111)$$

$$\frac{A_2}{T} = -R \ln \left[ \frac{-k_2^f v_1 - (k_1^f + k_1^b) v_2 + C_0 k_1^f k_2^f}{-k_2^f v_1 + k_1^f k_2^f / k_2^b \times v_2 + C_0 k_1^f k_2^f} \right]$$

where all the equilibrium constants are replaced by the ratio between forward and backward reactions. Note that eqs. (IV.110) and (IV.111) together guarantee a one-to-one



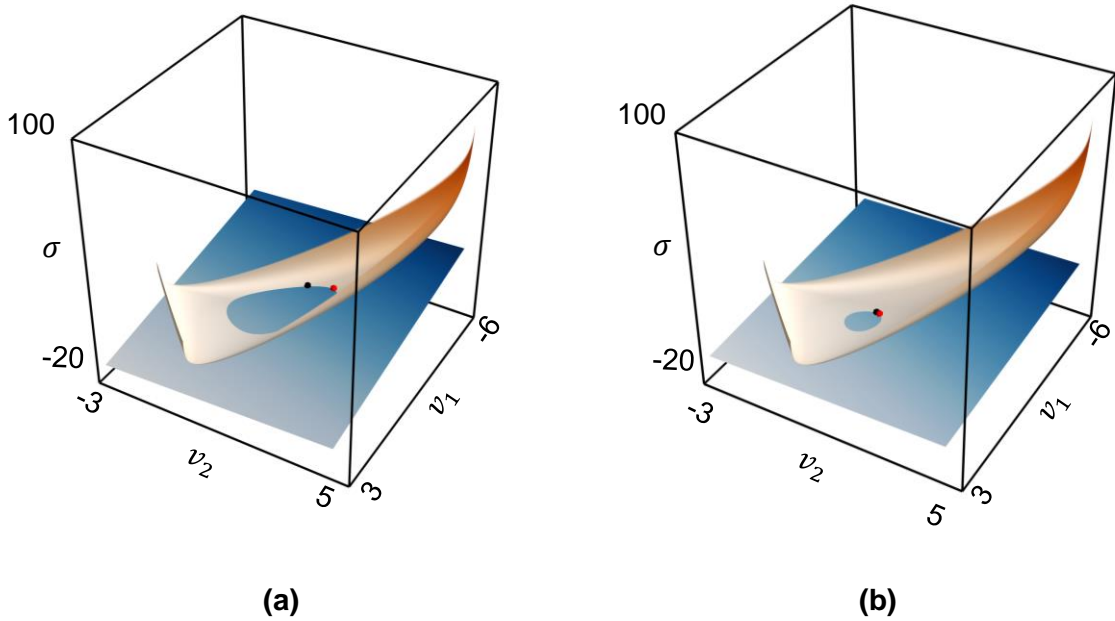
## Chapter IV. Rebuttal of Ziegler's MaxEP principle

correspondence between fluxes  $v_j$  and forces  $A_j/T$ . Therefore, the necessary condition (5') to apply MaxEP is met.

Now, since the forces  $\frac{A_1}{T}, \frac{A_2}{T}$  are known functions of the fluxes  $v_1$  and  $v_2$ , the entropy production itself can be written as a function of  $v_1$  and  $v_2$  by means of the bilinear expression  $\sigma = \sum X_k J_k$  in eqs. (I.11):

$$\sigma = -Rv_1 \ln \left[ \frac{-\frac{k_1^b}{k_1^f} v_1 + \frac{k_1^b}{k_2^b} v_2 + C_0 k_1^b}{\left(1 + \frac{k_2^f}{k_2^b}\right) v_1 + \frac{k_1^b}{k_2^b} v_2 + C_0 k_1^b} \right] - Rv_2 \ln \left[ \frac{-k_2^f v_1 - (k_1^f + k_1^b) v_2 + C_0 k_1^f k_2^f}{-k_2^f v_1 + k_1^f k_2^f / k_2^b \times v_2 + C_0 k_1^f k_2^f} \right] \quad (\text{IV.112})$$

Eq. (IV.112) shows that the entropy production can be expressed as a function of the fluxes, so that condition (3') in Section IV.1.3 is satisfied. Hence, one could use the MaxEP in eq. (IV.42) to find the velocities  $v_1^Z, v_2^Z$  corresponding to certain forces  $A_1^*/T$  and  $A_2^*/T$ . If the MaxEP is correct, the result must be in agreement with the one obtained via eq. (IV.110). Figure IV.6 shows that this is not the case.



*Figure IV.6 – (a) Far from equilibrium, and (b) near equilibrium comparison between the reaction velocities found from reaction kinetics theory (black dot) and from Ziegler's MaxEP principle (red dot)*

In this figure, the blue plane corresponds to the constraint  $\sigma = v_1 A_1^*/T + v_2 A_2^*/T$ , while the orange surface is the graph of function  $\sigma(v_1, v_2)$  given by eq. (IV.112). Further, the black dot corresponds to the point  $(v_1^*, v_2^*)$  found using eq. (IV.110), whereas the red dot is the solution  $(v_1^Z, v_2^Z)$  found using the MaxEP principle in eq. (IV.42). For convenience,

## Chapter IV. Rebuttal of Ziegler's MaxEP principle

the dimensions are defined so that  $R = 1$  and  $T = 1$ . The values of the reaction constants in the two scenarios are the same:  $k_1^f = 1$ ,  $k_1^b = 2$ ,  $k_2^f = 1.5$ ,  $k_2^b = 0.9$ . Table IV.1 gives the velocities and forces for (a) and (b), as well as for an extra case (c) even closer to equilibrium. The units are omitted on purpose, as the convention  $R = 1$  (corresponding to  $8.314 \text{ J/K.mol}$ ) and  $T = 1$  (corresponding to  $298 \text{ K}$ ) do not match any known set of units.

*Table IV.1 – Reaction velocities from MaxEP principle and from kinetics theory for three different pairs of forces*

	$A_1^*/T$	$A_2^*/T$	$v_1^*$	$v_1^Z$	$v_2^*$	$v_2^Z$	$\sigma^*$	$\sigma^Z$
(a)	-2.1401	0.6360	-2.500	-2.707	1.000	1.756	5.9862	6.9101
(b)	-0.7444	0.3285	-1.000	-0.976	0.400	0.498	0.8754	0.8901
(c)	-0.0771	0.0404	-0.100	-0.099	0.040	0.041	0.0093	0.0093

Figure IV.6 and Table IV.1 show that Ziegler's MaxEP principle fails to predict the phenomenological flux-force relations for a reaction system far from equilibrium. However, as the system approaches equilibrium (i.e., as  $A_1^*/T$  and  $A_2^*/T$  decrease), MaxEP predictions approach the actual reaction velocities. This is not surprising: near-equilibrium, the MaxEP principle converges to Onsager's reciprocal relations, as mentioned in Section IV.1.3. And the reaction system described above respects these reciprocal relations near equilibrium. Indeed, if  $A_1/RT \ll 1$  and  $A_2/RT \ll 1$ , the first-order expansion of eqs. (IV.109) or (IV.110) yields a relation where both coupling coefficients are 0 (i.e., where  $v_i$  depends on  $A_i$  alone, and not on  $A_j$ ):

$$v_1 = k_1^f C_A^{eq} \frac{A_1}{RT} \tag{IV.113}$$

$$v_2 = k_2^f C_B^{eq} \frac{A_2}{RT}$$

### IV.4 Other criticisms

Other researchers, such as Bataille et al. (1978) and Poletini (2013), have made pertinent critics to the MaxEP principle. These pertinent critics were often met with vague replies, which either do not have enough evidence to debunk the critic, use some type of circular reasoning to conclude against the criticism, or make wrong use of terms and concepts.

## Chapter IV. Rebuttal of Ziegler's MaxEP principle

For example, it has been recognized that MaxEP sometimes yields fluxes and forces different from the ones originally defined and used to calculate  $\sigma$  in eq. (I.11). For example, for given fluxes  $J_1$  and  $J_2$ , the forces found using Ziegler's MaxEP principle and those originally defined for the system are the same if and only if (Martyushev and Seleznev, 2006):

$$X_2(J_1, J_2) \frac{\partial \sigma(J_1, J_2)}{\partial J_1} = X_1(J_1, J_2) \frac{\partial \sigma(J_1, J_2)}{\partial J_2} \quad (\text{IV.114})$$

Eq. (IV.114) is true for instance when  $\sigma(J_1, J_2)$  is quadratic and the reciprocal relations hold. However, we have seen in Section IV.3.2 that MaxEP does not yield the same fluxes and forces as the ones originally defined for a reaction system far from equilibrium.

This discrepancy is related to the so-called non-uniqueness of the choice of fluxes and forces ( Martyushev and Seleznev, 2006; Janečka and Pavelka, 2017). To circumvent this issue, some authors advocating for MaxEP assume the principle as a postulate, and define the forces according to the  $\underline{X} - \underline{J}$  orthogonality equation (IV.43). This could for example justify the values  $v_1^Z$  and  $v_2^Z$  in Table IV.1: they are different from  $v_1^*$  and  $v_2^*$  because the forces  $A_1^*/T$  and  $A_2^*/T$  have a different meaning (other than affinity divided by temperature) in MaxEP. However, note that this re-interpretation of fluxes and forces goes against the definitions of  $J$  and  $X$  given respectively by eqs. (IV.25) and (IV.34). Further, using Ziegler's theory to redefine thermodynamic forces renders the theory itself hollow.

To illustrate this hollowness, let us imagine an arbitrary variational principle, the Maximization of Something (MaxSmth), which yields the phenomenological relations between fluxes and forces according to the following maximization:

$$\begin{aligned} \max_{\underline{X}} \{ \|\underline{X}\|^2 \xi(\underline{X}) \} \\ \text{s. t. } \xi(\underline{X}) - \underline{J} \cdot \underline{X} = 0 \end{aligned} \quad (\text{IV.115})$$

where  $\xi(\underline{X})$  is the entropy production given as a function of the forces.

## Chapter IV. Rebuttal of Ziegler's MaxEP principle

Solving the above problem allows one to find the fluxes as a function of the forces (i.e., some phenomenological relations):

$$\underline{J} = \frac{2(\underline{\xi} - \underline{X} \cdot \underline{\xi}_{\underline{X}})\underline{\xi}}{(\underline{X} \cdot \underline{X})(2\underline{\xi} + \underline{X} \cdot \underline{\xi}_{\underline{X}})}\underline{X} + \frac{3(\underline{X} \cdot \underline{X})\underline{\xi}}{(\underline{X} \cdot \underline{X})(2\underline{\xi} + \underline{X} \cdot \underline{\xi}_{\underline{X}})}\underline{\xi}_{\underline{X}} \quad (\text{IV.116})$$

where  $\underline{\xi}_{\underline{X}} = [\partial\underline{\xi}/\partial X_1, \partial\underline{\xi}/\partial X_2, \dots]$ .

To overcome the non-uniqueness paradox, one could postulate that the fluxes shall always be defined according to MaxSmth. However, the quantities  $\underline{J}$  found using eq. (IV.116) have no physical meaning. And this is precisely why Ziegler's theory becomes hollow once it is postulated and used to redefine thermodynamic forces. Instead of using variational principles that may result in meaningless fluxes or forces, one should use respectively eqs. (IV.25) and (IV.34) to define these quantities.

Another argument against the MaxEP is made in Polettini (2013). The author considers the fluid flow in two different pipes; in one of them, the flow is laminar, whereas turbulent flow takes place in the other. In such a system, the thermodynamic forces are proportional to the pressure drops. In laminar flow, the pressure drop is proportional to the fluid flowrate  $J_l$ , whereas in turbulent flow the pressure drop is proportional to  $J_t|J_t|$ , with  $J_t$  being the flowrate in the turbulent pipe. Therefore, one can write separate entropy production rates for each pipe following eq. (I.11):  $\sigma_l = M_l J_l^2$  and  $\sigma_t = M_t J_t^3$  (only positive values of  $J_t$  are considered for convenience). The entropy production of the global system containing the two pipes is (Polettini, 2013):

$$\sigma = M_l J_l^2 + M_t J_t^3 \quad (\text{IV.117})$$

Polettini (2013) shows that the MaxEP applied to eq. (IV.117) does not yield the correct flux-forces relationship, which a priori could be another evidence against Ziegler's theory. However, Ziegler (1983b) restricts MaxEP to systems whose entropy production  $\sigma(\underline{J})$  cannot be separated as a sum of independent contributions (the so-called non-compound systems). For example, a system whose entropy production function has a cross-term  $M_{lt} J_l J_t$  ( $M_{lt} \neq 0$ ) is non-compound. Because the system described by Polettini (2013) is compound, his argument against Ziegler's theory is not entirely valid (Martyushev and Seleznev, 2014).

## Chapter IV. Rebuttal of Ziegler's MaxEP principle

A variation of Poletini's argument can be conceived if one considers an arbitrarily small coupling between the two flows. One can of course argue that such a coupling is impossible if the flows take place in different pipes. However, the exact nature of the phenomena, and how the coupling actually happens, is superficial in the next steps. One can assume two hypothetical phenomena  $l$  and  $t$ . If only  $l$  takes place in the system,  $X_l = M_l J_l$  and  $\sigma_l = M_l J_l^2$ . On the other hand, if only  $t$  takes place, then  $X_t = M_t J_t^2$  and  $\sigma_t = M_t J_t^3$  (assuming only positive  $J_t$  values). If both phenomena take place at the same time, it shall be assumed that an infinitesimal coupling takes place. The most general way of representing such system is:

$$\begin{aligned} X_l &= M_l J_l + \epsilon_1 f_1(\underline{J}) \\ X_t &= M_t J_t^2 + \epsilon_2 f_2(\underline{J}) \end{aligned} \quad (\text{IV.118})$$

$$\sigma = M_l J_l^2 + \epsilon_1 J_l f_1(\underline{J}) + \epsilon_2 J_t f_2(\underline{J}) + M_t J_t^3$$

where  $\epsilon_1$  and  $\epsilon_2$  are arbitrarily small,  $f_1|_{J_t=0} = 0$  and  $f_2|_{J_l=0} = 0$ . For the entropy production in eq. (IV.118), MaxEP yields the following relations:

$$\begin{aligned} X_l &= \lambda(\underline{J}) \left[ 2M_l J_l + \epsilon_1 \left( f_1 + J_l \frac{\partial f_1}{\partial J_l} \right) + \epsilon_2 J_t \frac{\partial f_2}{\partial J_l} \right] \\ X_t &= \lambda(\underline{J}) \left[ 3M_t J_t^2 + \epsilon_2 \left( f_2 + J_t \frac{\partial f_2}{\partial J_t} \right) + \epsilon_1 J_l \frac{\partial f_1}{\partial J_t} \right] \end{aligned} \quad (\text{IV.119})$$

where  $\lambda$  appears from the Lagrange multipliers method, and can be determined from the constraint in eq. (I.11):

$$\lambda(\underline{J}) = \frac{M_l J_l^2 + \epsilon_1 J_l f_1(\underline{J}) + \epsilon_2 J_t f_2(\underline{J}) + M_t J_t^3}{\left[ 2M_l J_l + \epsilon_1 \left( f_1 + J_l \frac{\partial f_1}{\partial J_l} \right) + \epsilon_2 J_t \frac{\partial f_2}{\partial J_l} \right] J_l + \left[ 3M_t J_t^2 + \epsilon_2 \left( f_2 + J_t \frac{\partial f_2}{\partial J_t} \right) + \epsilon_1 J_l \frac{\partial f_1}{\partial J_t} \right] J_t} \quad (\text{IV.120})$$

Now the idea of arbitrarily small coupling will prove itself useful. Such weak couplings can be obtained by a careful choice of system. For example, weak heat-diffusion coupling occurs for a solution of toluene in chlorobenzene (Demirel and Gerbaud, 2019). There surely are a large number of other solute-solvent combinations with even weaker coupling strengths. So weak in fact that the coupling might go unnoticed, and the system might be treated as compound.

## Chapter IV. Rebuttal of Ziegler's MaxEP principle

These hypothetical systems are not listed as an exception to MaxEP (Ziegler, 1983b ; Martyushev and Seleznev, 2014). Nevertheless, eqs. (IV.119) and (IV.120) are not in agreement with eq. (IV.118). Indeed, the 0-th approximations of  $X_l$  and  $X_t$  in eq. (IV.120) are:

$$X_l \approx 2M_l J_l \frac{M_l J_l^2 + M_t J_t^3}{2M_l J_l^2 + 3M_t J_t^3} \tag{IV.121}$$

$$X_t \approx 3M_t J_t^2 \frac{M_l J_l^2 + M_t J_t^3}{2M_l J_l^2 + 3M_t J_t^3}$$

This result is clearly different from the 0<sup>th</sup>-order approximation of the forces in eq. (IV.118). The reasoning shown above can be extended to any phenomena  $l$  and  $t$ , as long as the driving force for one phenomenon is analytic on the flux when the other phenomenon does not take place. The conclusion is either: (i) MaxEP is inaccurate; or (ii) infinitely weak coupling between two phenomena whose forces are represented by polynomial series of different orders cannot exist in nature. The second proposal implies the existence of some minimum coupling strengths  $\epsilon_i \neq 0$  for these phenomena, which seems unlikely.

Another work that deserves attention is Ziegler's reply to the article that shows the inadequacy of MaxEP for chemical reactions (Bataille et al., 1978; Ziegler, 1983a). Ziegler makes several flaws in his attempt to discredit Bataille's counterexample. But the most important one is assuming that the entropy production is a quadratic function of the velocities (see eqs. (4.14) and (4.20) in Ziegler (1983a)). This assumption is false even if there is only one reaction taking place, rendering all of the arguments in the paper groundless. For example, an extract in page 842 reads:

*We have stressed that maximal rate of entropy production has not been used in the derivation of (4.13). This equation and hence also (6.3) are based on nothing else than classical Thermodynamics. Since (6.5), obtained from the standard equation, cannot be reconciled with (6.3), the standard equation violates the laws of Thermodynamics and hence must be rejected.*

But eq. (6.3) in Ziegler (1983a) uses the assumption that the entropy production is quadratic on the velocities, and hence is not based on classical thermodynamics alone. Further, the standard equation (better known as the law of mass action) was discovered

## Chapter IV. Rebuttal of Ziegler's MaxEP principle

more than 150 years ago (Ferner and Aronson, 2015), and it has been widely validated ever since. Differently from what was stated by Ziegler, the law of mass action is in agreement with thermodynamics, and the first-order rate equation can be derived for gases from statistical thermodynamics (Hill, 1986).

Finally, the end of this section will discuss an undeserved praise for MaxEP. Many authors seem to commend MaxEP due to the fact that it yields Onsager's reciprocal relations near equilibrium (Ziegler, 1983b; Martyushev and Seleznev, 2006; Bordel, 2010; Herbert et al., 2013; Seleznev and Martyushev, 2014). However, the principle of MaxEP came as an attempt to generalize Onsager's reciprocal relations to nonlinear thermodynamics (Ziegler, 1958). Praising MaxEP because it yields Onsager's reciprocal relations is unreasonable, since MaxEP was itself conceived so that it would agree with the reciprocal relations near equilibrium. Any other attempt to generalize Onsager's principle, regardless of how baseless and incorrect, would of course yield the reciprocal relations as well.

### IV.5 Summary

This chapter shows the inadequacy of the Maximum Entropy Production principle proposed by Ziegler (1958, 1961, 1968, 1970, 1983a) as a generalization of Onsager's reciprocal relations far from equilibrium. First, the derivation of the Orthogonality Principle (precursor of MaxEP) as given in Ziegler (1970) was reproduced with more details, so that its flaws could be seen more clearly. There were two main mistakes in this demonstration: concluding that two functions are equal because their integrals over a certain range have equal values, and using circular reasoning (i.e., assuming the principle is true in order to prove it).

Once these flaws were highlighted, Section IV.3 discussed a simple reaction system that does not obey MaxEP. Although the counterexample was found independently in the course of this thesis, a very similar one had already been discussed more than 40 years ago (Bataille et al., 1978). The advantage of the instance presented here is that the calculations are simpler, and the results can be easily represented in a 3D plot. Finally, Section IV.4 criticizes some of the classic arguments in favour of MaxEP.

Nevertheless, it remains that MaxEP can be seen an elegant formulation of Onsager's reciprocal relations. Further, it provides physical insight on the phenomenological laws

## **Chapter IV. Rebuttal of Ziegler's MaxEP principle**

of coupling: near equilibrium, given the thermodynamic forces at any instant, the system “chooses” the fluxes so that the rate of dissipation (entropy production) is maximized.





---

## Chapter V. Conclusion and recommendations for future work

---

### V.1 Conclusions

To elucidate the mechanisms behind nature's efficiency and resiliency, Gerbaud et al. (2020) proposed a non-equilibrium thermodynamics (NET) framework. This framework was conceived as an analogue of a nature-inspired chemical engineering framework introduced by Coppens (2012). It contemplates three NET concepts for innovation in chemical engineering, as illustrated in Figures I.1 and I.4. NET1 (*equipartition of entropy production + Constructal Law*) is suitable to improve energy efficiency of processes and to optimize flow structures in general. NET2 (*thermodynamic coupling*) provides alternative mechanisms for unit operations, such as performing mass transfer via temperature gradients. Finally, NET3 (*dissipative structures*) exploits the concept of bifurcation in the presence of large thermodynamic forces, such as the emergence of Bénard convection cells in a liquid subjected to high temperature gradients. For instance, bifurcation in the form of switch to different production lines was used to improve the resilience of biorefineries that must cope with variability of feed, demand, and operating conditions (Houngbé et al., 2019).

The first research project derived from this framework is presented in Chapter II, and it concerns the modelling and assessment of a new liquid distributor (Meyer and Rouzineau, 2020) whose design is justified by NET1. The second and third projects are on interface-driven phenomena (Chapter III) and on the rebuttal of Ziegler's Maximum Entropy Production (MaxEP) principle (Ziegler, 1968) (Chapter IV). Both these projects stemmed from NET2. Indeed, in diffusiophoresis and diffusioosmosis phenomena, a gradient in solute concentration drives the flux of another substance. Besides, thermodynamic coupling is at the heart of Ziegler's theory, since it attempts to generalize Onsager's reciprocal relations for coupled phenomena.

The tree-like distributor, illustrated in Figure II.6, improves on the classic orifice-pan internal by adding wire layers that branch and split the liquid coming from the holes on the distributor plate. The configuration with 6 layers and 13 initial irrigation points was

## Chapter V. Conclusion and recommendations for future work

found to decrease the theoretical maldistribution factor  $M_f$  significantly. Indeed, for the collection zones shown in Figure II.22,  $M_f$  decreases from 0.236 (with the classic orifice-pan distributor) to 0.136 (with the retrofitted design). This improvement reflects in the performance of packed distillation columns when the packing is more sensitive to initial liquid distribution. For example, the HETP of the Tetra Spline structured packing (Kawas et al., 2021) discussed in Section II.3.3 decreases from 0.45m to 0.27m when the new distributor is employed.

Such a decrease in HETP also decreases capital cost per theoretical stage for packed columns. Besides, given that distillation is responsible for a great part of the energy consumption in chemical industry, any progress towards increasing distillation efficiency is also progress towards sustainability. Finally, the original and creative design of the liquid distributor depicted in Figure II.6 may motivate other researchers to continue innovating on well-established transport architectures, such as classic heat exchangers and mass transfer devices. For an example of innovative mass transfer device, see the gas supply system proposed by Kjelstrup et al. (2010) for a membrane fuel cell.

After the assessment of the tree-like liquid distributor, diffusioosmosis and diffusiophoresis were studied via numerical simulations in Chapter III. This chapter featured an attempt to model membrane filtration through interface forces alone, i.e. without an external potential acting on the solute along the direction of the flow. The geometry used to simulate the membrane is similar to the one adopted by Bacchin et al. (2019), and it consists of an array of cylindrical obstacles equally spaced, as depicted in Figure III.7. Further, the model used for simulations is a Euler-Euler mixture model, which uses averaged equations to avoid tracking every colloidal particle in the mixture. Such a model, shown in eqs. (III.29)–(III.32), accounts for colloid – colloid interactions via the particle pressure term  $\Pi_{cc}$ . It also takes interface – colloid interactions into account via the interaction potential  $\Pi_{ic}$  shown in eq. (III.25).

Results showed that a membrane modelled in this way is leaky, with reflection coefficients  $\sigma_0$  varying between 0.128 and 0.0414 for colloid concentration differences (in terms of volume fraction) between 0.01 and 0.1. The coefficient  $\sigma_0$ , defined in eq. (III.19), represents the ratio between hydrostatic pressure drop and osmotic pressure drop across a membrane in the advection-osmosis equilibrium state. It equals 1 for ideal semipermeable membranes, but can vary significantly for real membranes. For example,

## Chapter V. Conclusion and recommendations for future work

reflection coefficients between 0.1 and 1 have been measured for membrane separation of organic pollutants (Agenson et al., 2003).

Apart from showing the change in  $\sigma_0$  with respect to colloid concentration difference, the results for the diffusioosmosis case study stressed the tendency for cake formation and anomalous osmosis when colloid – interface attraction is strong. As a reminder, anomalous osmosis refers to the situations in which the solvent tends to flow from the high solute concentration side to the low solute concentration side.

Finally, comparison between simulations using different equations of state (EoS) for  $\Pi_{cc}$  highlighted the importance of an adequate model for colloid – colloid interactions. Two EoS were compared via simulations: van 't Hoff (VH) and Carnahan-Starling + van der Waals, given by eqs. (III.11) and (III.15) respectively. The former EoS neglects colloid – colloid interactions, whereas the latter combines a hard-sphere repulsion term and a van der Waals attraction term. It was shown that VH may underestimate the potential for fouling and cake formation in the system. Indeed, for an array of cylinders separating two reservoirs of concentrations  $\phi_l = 0.1$  (left) and  $\phi_r = 0$  (right), and for an attraction parameter  $a_{tt}$  of 0.2 (c.f. eq. (III.25)), VH predicts a concentration peak of  $\phi_{max} \approx 0.1$  near the interface. This peak increases to  $\phi_{max} = 0.16$  when Carnahan-Starling + van der Waals EoS is used.

The conclusions drawn from this project could be of use in the membrane research field. For example, this thesis brings up the possibility that osmotic reflection coefficients could depend on colloid concentration difference  $\Delta\phi$  across the membrane, even at low concentrations, as long as membrane geometry does not resemble that of capillary pores. Further numerical and experimental investigation that could confirm this possibility are given in the next section. Apart from that, the Python routine for diffusioosmosis simulations given in Appendix C will hopefully assist other researchers willing to study diffusioosmosis via numerical simulations. Finally, the qualitative agreements between experiments and numerical results may instigate others to adopt the model described in Section III.3 for a better description of particle accumulation and mixture flow near the membrane surface. This model accounts for colloid – colloid and colloid – interface interactions. Further, it is a compromise between oversimplistic models that consider membrane as a barrier of 0 thickness, and overcomplex Lagrangian models that account for the membrane structure but keep track of every colloidal particle in the system.

## Chapter V. Conclusion and recommendations for future work

Still in Chapter III, the diffusiophoresis numerical simulations with two moving particles, as depicted in Figure III.16, showed that particles with different solute – interface interaction potentials may move away from each other. This phenomenon could be applied to separation processes. For example, if the mixture is forced to flow in a channel with solute gradient perpendicular to the direction of the flow, continuous particle separation could be achieved by splitting the end of the channel in two parts. The applicability of diffusiophoretic separation in microfluidics is indeed a trending topic in fluid physics, with many recent theoretical and experimental investigations bringing positive results (Shin, 2020).

The results presented in this thesis clarify various aspects of this phenomenon, benefitting its global understanding and consequently its modelling. One such aspect is the realization that a diffusiophoretic system with a fixed far-field solute concentration gradient “forgets” its initial state as it moves towards/against this gradient. Another aspect investigated here is the effect of solute-interface attraction on diffusiophoretic velocities. This study was conducted by varying the attraction parameter  $a_{tt}$  of the solute-interface interaction potential given in eq. (III.25). The results from macroscopic simulations presented in this thesis confirm the claim by Ramírez-Hinestrosa et al. (2020) that particle mobility is nonmonotonic with respect to the attraction strength of solute-interface interactions (Figure III.18). However, differences between these works arise in the limit of high attraction strengths. Whereas Ramírez-Hinestrosa et al. (2020) predict an asymptotic decay in mobility, macroscopic simulations predict an unbounded increase in mobility as the attraction forces increase. Most likely, this discrepancy appears because the former study considers solute molar fractions of 0.5. Hence, the solute-solute interactions, neglected here under the assumption of small concentrations, probably have a strong impact on the molecular simulation results. Other possible reasons for the differences in the behaviour of particle mobility are given in Section III.7.4.

Still in the context of diffusiophoresis, an expression was regressed that relates diffusiophoretic velocity  $v_{DP}$  to the gradient in solute concentration, absolute solute concentration, and diffusion coefficient (eq. (III.63)). Understanding how all these parameters affect the diffusiophoretic velocity is of particular interest in the research for synthetic microswimmers. As mentioned in Section I.2, these nature-inspired microbodies have several potential applications in biomedicine, including drug delivery and the removal of toxins from the human body (Elgeti et al., 2015).

## Chapter V. Conclusion and recommendations for future work

The equation regressed generalizes a result previously obtained in the limit of short solute-particle interaction range (Anderson and Prieve, 1984, 1991), namely the dependency of diffusiophoretic velocities on the factor  $D/\phi_m$ . However, note that the velocity given by eq. (III.63) is an equilibrium velocity, which is close but not equal to the actual velocity of the particle in a diffusiophoretic system. Indeed, particle velocity in such systems does not remain constant (c.f. Figure III.15), which means that the particle is not at mechanical equilibrium.

Finally, in Chapter IV the research project on Ziegler's MaxEP principle has led to its rejection in the context of far-from-equilibrium systems. The mistakes and questionable assumptions made by Ziegler (1970) in his attempt to prove the MaxEP principle were highlighted in this chapter. A detailed look into Ziegler's 1970 paper revealed that he has only found an equivalent condition for MaxEP, and then concluded that MaxEP was true without actually proving that the equivalent condition was true. Of course, debunking the demonstration of Ziegler's principle is not the same as proving the principle false. The proof that MaxEP is incorrect comes from a counterexample that considers a pair of reactions far from equilibrium. Applying Ziegler's principle to this system leads to kinetics different from the ones obtained via the law of mass action, as depicted in Figure IV.6 and Table IV.1. Once again, it is recalled that a similar system was used by Bataille et al. (1978) in a previous dispute about the validity of MaxEP.

The refutation of MaxEP presented in Chapter IV should lead researchers to acknowledge the limitations of this theory. This is of utmost importance, given the attention and the acceptance it has acquired through recent years (Martyushev and Seleznev, 2006; Houlby, 2014; Janečka and Pavelka, 2017). Ziegler's theory is, in fact, valid in the limit of linear NET, where it is equivalent to Onsager's reciprocal relations. In other words, MaxEP is a more sophisticated statement of the reciprocal relations.

In a broader context, this thesis attests the validity of the two first concepts in the NET framework for chemical engineering. Such a framework can guide innovation in the field, exploiting concepts in NET often neglected by engineers, such as thermodynamic coupling and non-linear dynamics.

### V.2 Future work

Based on the research for this thesis, the following studies are recommended for further investigation:

- Experimental assessment of the maldistribution factor  $M_f$  for the tree-like liquid distributor: The performance of the distributor discussed in Chapter II was evaluated experimentally via its impact on the HETP of distillation columns. Another suitable experiment is the measure of the liquid distribution over the different zones of the cross-section. To do that, one must fabricate a liquid collector divided in 21 zones similar to the ones depicted in Figure II.22, and with outlet tubes leaving from the underside of each zone. Flow measures can then be taken by placing flow sensors inside each of these tubes, as indicated by Lämmermann et al. (2016). With these data, it will be possible to compare the theoretical  $M_f$  values obtained in Section II.4 with the experimental ones. This work is under progress.
- Additional experiments using the tree-like liquid distributor with other types of industrial packing: Section II.5.1 has shown that the new liquid distributor does not have a significant impact on HETP of the industrial packings Pall rings and Mellapak 250Y. However, it might be possible to observe a decrease in HETP for industrial packings that are more sensitive to initial liquid distribution, such as structured packings with large specific surfaces (Olujić and de Graauw, 1990).
- Validation of the membrane geometry and the diffusioosmosis model given in Chapter III in the limit of semi-permeability: The osmotic reflection coefficients derived from numerical simulations are all quite low, peaking at  $\sigma_0 = 0.128$ . Hence, it would be worth showing that the geometry presented in Section III.2.1, along with the model given in Section III.3, can also replicate the behaviour of semipermeable membranes ( $\sigma_0 = 1$ ). This may be achieved by decreasing the distance between the centres of adjacent cylinders (i.e., decreasing  $H$  in Figure III.7). Other possibilities are increasing the radius of these cylindrical obstacles, increasing the magnitude  $k_{ic}$  of the interface-colloid interaction potential in eq. (III.25), and increasing the interaction range  $l_{ic}$  of this potential.
- Inclusion of entropy and energy balance equations to study adsorption – bulk viscosity coupling near a membrane: Colloid adsorption on a surface can be seen

## Chapter V. Conclusion and recommendations for future work

as a chemical reaction. Therefore, this phenomenon might be coupled with other scalar contributions to entropy production. One such contribution exists when the mixture is compressible. In this case, mixture velocity is not divergence-free, and a bulk viscosity term  $\tau^0/T (\underline{\nabla} \cdot \underline{v})$  (see eq. (I.10)) contributes to energy dissipation. Note that reaction and bulk velocity coupling have already been mentioned in the literature for reacting compressible flows and for relativistic reactive gas systems (Hermens et al., 1972; Kustova and Giordano, 2011).

- Experiments to determine the dependency of reflection coefficient on solute/colloid concentration differences at small concentrations: Previous experimental and theoretical evidence suggest that  $\sigma_0$  does not depend on solute/colloid concentration difference across the membrane if concentration is low. However, the numerical results in Chapter III show the opposite. To confirm this prediction, it would be suitable to perform experiments in the limit of low solute/colloid concentrations, using a leaky membrane whose morphology resembles an array of cylinders. Membranes with finger-like structure (Kingsbury and Li, 2009) may be appropriate for this.
- Further numerical simulations to regress a more general expression for the diffusiophoretic velocity: One of the key results from the diffusiophoretic case study is eq. (III.63), which relates diffusiophoretic velocity to gradient in solute concentration, absolute solute concentration, and diffusion coefficient. However, this expression is only valid for the interaction potential shown in eq. (III.25), having attraction strength  $k_{ic} = 100$ , interaction length  $l_{ic} = 0.1$ , and attraction parameter  $a_{tt} = 0$ . An expression valid for any set of interface-solute interaction parameters would be even more useful, as it would enable predictions for various types of interface – solute interactions.
- Review of other attempts to prove Ziegler’s Maximum Entropy Production principle: Convincing the scientific community that MaxEP is inaccurate might be a challenging task, as many researchers have already accepted and used it in their own works. One possible way of doing that is pointing out the mistakes in other works that attempted to prove the principle (Ziegler, 1958, 1983b).
- Review of alleged successful applications of the Maximum Entropy Production principle: Ziegler’s theory would not persist for so long if it had not found successful applications. Indeed, from kinetic theory of gases to the distribution of



## **Chapter V. Conclusion and recommendations for future work**

temperature and longwave radiation on the atmosphere of planets, there are many instances where MaxEP seems to give accurate predictions (Fukumura and Ozawa, 2014; Seleznev and Martyushev, 2014). A critical review of the main works among these instances may elucidate the reasons behind these successes.

---

## Bibliography

---

- Adamski, R.P., Anderson, J.L., 1983. Solute Concentration Effect on Osmotic Reflection Coefficient. *Biophys. J.* 44, 79–90. [https://doi.org/10.1016/S0006-3495\(83\)84279-9](https://doi.org/10.1016/S0006-3495(83)84279-9)
- Agenson, K.O., Oh, J.I., Urase, T., 2003. Retention of a wide variety of organic pollutants by different nanofiltration/reverse osmosis membranes: Controlling parameters of process. *J. Memb. Sci.* 225, 91–103. <https://doi.org/10.1016/j.memsci.2003.08.006>
- Ajdari, A., Bocquet, L., 2006. Giant amplification of interfacially driven transport by hydrodynamic slip: Diffusio-osmosis and beyond. *Phys. Rev. Lett.* 96, 1–4. <https://doi.org/10.1103/PhysRevLett.96.186102>
- Anderson, J., 1989. Colloid Transport By Interfacial Forces. *Annu. Rev. Fluid Mech.* 21, 61–99. <https://doi.org/10.1146/annurev.fluid.21.1.61>
- Anderson, J.L., Malone, D.M., 1974. Mechanism of Osmotic Flow in Porous Membranes. *Biophys. J.* 14, 957–982. [https://doi.org/10.1016/S0006-3495\(74\)85962-X](https://doi.org/10.1016/S0006-3495(74)85962-X)
- Anderson, J.L., Prieve, D.C., 1984. Diffusiophoresis: Migration of Colloidal Particles in Gradients of Solute Concentration. *Sep. Purif. Rev.* 13, 67–103. <https://doi.org/10.1080/03602548408068407>
- Anderson, J.L., Prieve, D.C., 1991. Diffusiophoresis Caused by Gradients of Strongly Adsorbing Solutes. *Langmuir* 7, 403–406. <https://doi.org/10.1021/la00050a035>
- Angrist, S.W., Hepler, L.G., 1967. *Order and chaos: laws of energy and entropy*. Basic Books, New York.
- Ansys Inc, 2013. *ANSYS Fluent UDF Manual*, 15.0. ed. Canonsburg.
- Ansys Inc, 2020. *Ansys Academic Research Mechanical and CFD*.
- Ansys Inc, 2021. *ANSYS Fluent Theory Guide*. Canonsburg.
- Autodesk, 2019. *Autodesk Inventor*.

- Bacchin, P., 2017. An energy map model for colloid transport. *Chem. Eng. Sci.* 158, 208–215. <https://doi.org/10.1016/j.ces.2016.10.024>
- Bacchin, P., Glavatskiy, K., Gerbaud, V., 2019. Interfacially driven transport theory: A way to unify Marangoni and osmotic flows. *Phys. Chem. Chem. Phys.* 21, 10114–10124. <https://doi.org/10.1039/c9cp00999j>
- Bacchin, P., Si-Hassen, D., Starov, V., Clifton, M.J., Aimar, P., 2002. A unifying model for concentration polarization, gel-layer formation and particle deposition in cross-flow membrane filtration of colloidal suspensions. *Chem. Eng. Sci.* 57, 77–91. [https://doi.org/10.1016/S0009-2509\(01\)00316-5](https://doi.org/10.1016/S0009-2509(01)00316-5)
- Balistreri, K.J., 2019. Entropy: Origin of the Second Law of Thermodynamics [WWW Document]. Kathy Loves Phys. Hist. URL <https://www.youtube.com/watch?v=7se7K0mnRaY> (accessed on February 2, 2021).
- Bataille, J., Edelen, D.G.B., Kestin, J., 1978. Nonequilibrium Thermodynamics of the Nonlinear Equations of Chemical Kinetics. *J. Non-Equilibrium Thermodyn.* 3, 153–168. <https://doi.org/10.1515/jnet.1978.3.3.153>
- Bhattacharjee, S., Elimelech, M., Borkovec, M., 1998. DLVO Interaction between Colloidal Particles: Beyond Derjaguin's Approximation. *Croat. Chem. Acta* 71, 883–903.
- Bejan, A., 1996. Street network theory of organization in nature. *J. Adv. Transp.* 30, 85–107. <https://doi.org/10.1002/atr.5670300207>
- Bejan, A., 1997. Constructal-theory network of conducting paths for cooling a heat generating volume. *Int. J. Heat Mass Transf.* 40, 799–816.
- Bejan, A., Lorente, S., 2004. The constructal law and the thermodynamics of flow systems with configuration. *Int. J. Heat Mass Transf.* 47, 3203–3214. <https://doi.org/10.1016/j.ijheatmasstransfer.2004.02.007>
- Bejan, A., Tondeur, D., 1998. Equipartition, optimal allocation, and the constructal approach to predicting organization in nature. *Rev. Gen. Therm.* 37, 165–180. [https://doi.org/10.1016/S0035-3159\(97\)83647-1](https://doi.org/10.1016/S0035-3159(97)83647-1)

- Bessou, V., Rouzineau, D., Prévost, M., Abbé, F., Dumont, C., Maumus, J.P., Meyer, M., 2010. Performance characteristics of a new structured packing. *Chem. Eng. Sci.* 65, 4855–4865. <https://doi.org/10.1016/j.ces.2010.05.029>
- Bonthuis, D.J., Golestanian, R., 2014. Mechanosensitive channel activation by diffusio-osmotic force. *Phys. Rev. Lett.* 113, 148101. <https://doi.org/10.1103/PhysRevLett.113.148101>
- Bordel, S., 2010. Steepest entropy increase is justified by information theory. the relations between Ziegler's principle, Onsager's formalism and Prigogine's principle. *Phys. A Stat. Mech. its Appl.* 389, 4564–4570. <https://doi.org/10.1016/j.physa.2010.06.050>
- Bozzano, G., Dente, M., Manenti, F., Corna, P., Masserdotti, F., 2014. Fluid distribution in packed beds. Part 1. Literature and technology overview. *Ind. Eng. Chem. Res.* 53, 3157–3164. <https://doi.org/10.1021/ie402137z>
- Caretto, L.S., Gosman, A.D., Patankar, S. V., Spalding, D.B., 1973. Two Calculation Procedures for Steady, Three-Dimensional Flows with Recirculation, in: Cabannes, H., Temam, R. (Eds.), *Proceedings of the Third International Conference on Numerical Methods in Fluid Mechanics*. Springer, Berlin, pp. 60–68. <https://doi.org/10.1007/BFb0112677>
- Carnahan, N.F., Starling, K.E., 1969. Equation of state for nonattracting rigid spheres. *J. Chem. Phys.* 51, 635–636. <https://doi.org/10.1063/1.1672048>
- Carnot, S., 1824. *Réflexions sur la puissance motrice du feu et sur les machines propres à développer cette puissance*. Bachelier, Paris.
- Casimir, H.B.G., 1945. On Onsager's Principle of Microscopic Reversibility. *Rev. Mod. Phys.* 17, 343–350. <https://doi.org/10.1103/RevModPhys.17.343>
- Churaev, N.V., Derjaguin, B. V., Muller, V.M., 1987. *Surface Forces*, 1st ed. Plenum Publishing Corporation, New York. <https://doi.org/10.1007/978-1-4757-6639-4>
- Clausen, J.R., 2013. Using the suspension balance model in a finite-element flow solver. *Comput. Fluids* 87, 67–78. <https://doi.org/10.1016/j.compfluid.2012.12.004>
- Clausius, R., 1856. X. On a modified form of the second fundamental theorem in the mechanical theory of heat. *London, Edinburgh, Dublin Philos. Mag. J. Sci.* 12, 81–98.

- CNRS, 2018. Gargantex [WWW Document]. URL [gargantext.org](http://gargantext.org) (accessed on November 16, 2018).
- Coppens, M.O., 2005. Scaling-up and -down in a Nature-Inspired Way. *Ind. Eng. Chem. Res.* 44, 5011–5019.
- Coppens, M.O., 2012. A nature-inspired approach to reactor and catalysis engineering. *Curr. Opin. Chem. Eng.* 1, 281–289. <https://doi.org/10.1016/j.coche.2012.03.002>
- Coppens, M.O., 2021. Nature-Inspired Chemical Engineering for Process Intensification. *Annu. Rev. Chem. Biomol. Eng.* 12, 6.1–6.29. <https://doi.org/10.1146/annurev-chembioeng-060718-030249>
- Coppens, M.O., van Ommen, J.R., 2003. Structuring chaotic fluidized beds. *Chem. Eng. J.* 96, 117–124. <https://doi.org/10.1016/j.cej.2003.08.007>
- Cotignola, M.I., Bordogna, C., Punte, G., Cappannini, O.M., 2002. Difficulties in learning thermodynamic concepts: Are they linked to the historical development of this field? *Sci. Educ.* 11, 279–291. <https://doi.org/10.1023/A:1015205123254>
- Count of Rumford, B., 1798. An Inquiry concerning the Source of the Heat Which is Excited by Friction. *Philos. Trans. R. Soc. London* 80–102. <https://doi.org/10.1098/rstl.1798.0006>
- CrashCourse, 2018. Thermodynamics: Crash Course History of Science #26 [WWW Document]. URL <https://www.youtube.com/watch?v=VpiLucwH-AQ> (accessed on February 25, 2021).
- de Groot, S.R., Mazur, P., 1984. *Non-Equilibrium Thermodynamics*. Dover, New York.
- Dejean, B., Meyer, M., Rouzineau, D., 2020. Design and conception of an innovative packing for separation column—Part I: Hydrodynamic study on wire intersections. *Chem. Eng. Res. Des.* 160, 11–19. <https://doi.org/10.1016/j.cherd.2020.05.006>
- Demirel, Y., Gerbaud, V., 2019. *Nonequilibrium Thermodynamics: Transport and Rate Processes in Physical, Chemical and Biological Systems*, 4th ed. Elsevier, Amsterdam.
- Derjaguin, B. V., Sidorenkov, G.P., Zubashchenkov, E.A., Kiseleva, E.V., 1947. Kinetic Phenomena in Boundary Films of Liquids. *Kolloidn. Zh.* 9, 335–347.

- Derjaguin, B. V., Sidorenkov, G.P., Zubashchenkov, E.A., Kiseleva, E.V., 1993. Kinetic Phenomena in the Boundary Layers of Liquids 1. The Capillary Osmosis. *Prog. Surf. Sci.* 43, 138–152. [https://doi.org/10.1016/0079-6816\(93\)90023-0](https://doi.org/10.1016/0079-6816(93)90023-0)
- Duprat, C., 2009. Instabilités d'un film liquide en écoulement sur une fibre verticale. Université Pierre et Marie Curie - Paris VI.
- Eck, T., Kirsten, K., 2019. Liquid Redistributor. 10,357,740 B2.
- Elgeti, J., Winkler, R.G., Gompper, G., 2015. Physics of microswimmers - Single particle motion and collective behavior: A review. *Reports Prog. Phys.* 78, 56601. <https://doi.org/10.1088/0034-4885/78/5/056601>
- Fan, Z., Zhou, X., Luo, L., Yuan, W., 2009. Numerical Investigation of Constructal Distributors with Different Configurations. *Chinese J. Chem. Eng.* 17, 175–178. [https://doi.org/10.1016/S1004-9541\(09\)60052-5](https://doi.org/10.1016/S1004-9541(09)60052-5)
- Ferner, R.E., Aronson, J.K., 2015. Cato Guldberg and Peter Waage, the history of the Law of Mass Action, and its relevance to clinical pharmacology. *Br. J. Clin. Pharmacol.* 81, 52–55. <https://doi.org/10.1111/bcp.12721>
- Franz, U., Geipel, W., 2019. Liquid Distributor of a Process-Technology Column. 10,272,354 B2.
- Friedman, E., 2021. Triangles in Circles [WWW Document]. URL <https://erich-friedman.github.io/packing/triincir/> (accessed on November 6, 2021).
- Fukumura, Y., Ozawa, H., 2014. Entropy Production in Planetary Atmospheres and Its Applications, in: Dewar, R.C., Lineweaver, C.H., Niven, R.K., Regenauer-Lieb, K. (Eds.), *Beyond the Second Law: Entropy Production and Non-Equilibrium Systems*. Springer, Berlin.
- Gambar, K., Markus, F., 1994. Hamilton-Lagrange formalism of nonequilibrium thermodynamics. *Phys. Rev. E* 50, 1227–1231. <https://doi.org/10.1103/PhysRevE.50.1227>
- Gerbaud, V., Shcherbakova, N., Da Cunha, S., 2020. A nonequilibrium thermodynamics perspective on nature-inspired chemical engineering processes. *Chem. Eng. Res. Des.* 154, 316–330. <https://doi.org/10.1016/j.cherd.2019.10.037>

- Ghodoossi, L., 2004. Conceptual study on constructal theory. *Energy Convers. Manag.* 45, 1379–1395. <https://doi.org/10.1016/j.enconman.2003.09.002>
- Gibbs, J.W., 1948. *The Collected works of J. Willard Gibbs*. Yale University Press, London.
- Glavatskiy, K.S. 2015a. Lagrangian formulation of irreversible thermodynamics and the second law of thermodynamics. *J. Chem. Phys.* 142, 204106. <https://doi.org/10.1063/1.4921558>
- Glavatskiy, K.S. 2015b. Local equilibrium and the second law of thermodynamics for irreversible systems with thermodynamic inertia. *J. Chem. Phys.* 143, 164101. <https://doi.org/10.1063/1.4933431>
- Gut, A., 2009. *An Intermediate Course in Probability*, 2nd ed. Springer, New York. <https://doi.org/10.1007/978-1-4419-0162-0>
- Guyer, J.E., Wheeler, D., Warren, J.A., 2009. FiPy: Partial differential equations with Python. *Comput. Sci. Eng.* 11, 6–15. <https://doi.org/10.1109/MCSE.2009.52>
- Guyer, J.E., Wheeler, D., Warren, J.A., 2012. *FiPy Manual*, Release 3.0.
- Hansch, F., Künzler, M., Renner, M., Rehfeldt, S., Klein, H., 2019. Liquid distributor design for random packed columns. *Chem. Eng. Res. Des.* 147, 689–698. <https://doi.org/10.1016/j.cherd.2019.05.035>
- Herbert, C., Paillard, D., Dubrulle, B., 2013. Vertical temperature profiles at maximum entropy production with a net exchange radiative formulation. *J. Clim.* 26, 8545–8555. <https://doi.org/10.1175/JCLI-D-13-00060.1>
- Hermens, W.T., van Leeuwen, W.A., van Weert, C.G., de Groot, S.R., 1972. On Relativistic Kinetic Gas Theory : VIII. Reciprocal relations for a reactive mixture. *Physica* 60, 472–487. [https://doi.org/10.1016/0031-8914\(72\)90116-4](https://doi.org/10.1016/0031-8914(72)90116-4)
- Hill, T.L., 1986. *An Introduction to Statistical Thermodynamics*. Dover, New York.
- Hoek, P.J., Wesselingh, J.A., Zuiderweg, F.J., 1986. Small Scale and Large Scale Liquid Maldistribution in Packed Columns. *Chem. Eng. Res. Des.* 64, 431–449.
- Houlsby, G.T., 2014. Dissipation Rate Functions, Pseudopotentials, Potentials and Yield Surfaces, in: Dewar, R.C., Lineweaver, C.H., Niven, R.K., Regenauer-Lieb, K.

(Eds.), *Beyond the Second Law: Entropy Production and Non-Equilibrium Systems*. Springer, Berlin.

Houngbé, M., Barthe-Delanoë, A.M., Négny, S., 2019. A systemic approach for agile biorefineries, in: *Computer Aided Chemical Engineering*. Elsevier, Eindhoven, pp. 1519–1524. <https://doi.org/10.1016/B978-0-12-818634-3.50254-X>

Janečka, A., Pavelka, M., 2017. Gradient Dynamics and Entropy Production Maximization. *J. Non-Equilibrium Thermodyn.* 43, 1–19. <https://doi.org/10.1515/jnet-2017-0005>

Jönsson, A.S., Jönsson, B., 1996. Ultrafiltration of colloidal dispersions - A theoretical model of the concentration polarization phenomena. *J. Colloid Interface Sci.* 180, 504–518. <https://doi.org/10.1006/jcis.1996.0331>

Jou, D., Casas-Vázquez, J., Lebon, G., 2010. *Extended Irreversible Thermodynamics, Fourth Edition, 4th ed.* Springer, New York. <https://doi.org/10.1007/978-90-481-3074-0>

Joule, J.P., 1843. On the Calorific Effects of Magneto-Electricity, and on the Mechanical Value of Heat. *London, Edinburgh, Dublin Philos. Mag. J. Sci.* 23, 435–443.

Joule, J.P., 1850. III. On the mechanical equivalent of heat. *Philos. Trans. R. Soc. London* 140, 61–82. [https://doi.org/10.1016/0016-0032\(75\)90283-5](https://doi.org/10.1016/0016-0032(75)90283-5)

Kawas, B., Mizzi, B., Dejean, B., Rouzineau, D., Meyer, M., 2021. Design and conception of an innovative packing for separation column - Part II: Design and characterization of a wire based packing. *Chem. Eng. Res. Des.* 169, 189–203.

Keh, H.J., Ma, H.C., 2007. Diffusioosmosis of electrolyte solutions in a fine capillary tube. *Langmuir* 23, 2879–2886. <https://doi.org/10.1021/la062683n>

Khair, A.S., 2013. Diffusiophoresis of colloidal particles in neutral solute gradients at finite Péclet number. *J. Fluid Mech.* 731, 64–94. <https://doi.org/10.1017/jfm.2013.364>

Kingsbury, B.F.K., Li, K., 2009. A morphological study of ceramic hollow fibre membranes. *J. Memb. Sci.* 328, 134–140. <https://doi.org/10.1016/j.memsci.2008.11.050>

Kister, H.Z., 1990. *Distillation Operation*. McGraw-Hill, New York.



- Kister, H.Z., Mathias, P.M., Steinmeyer, D.E., Penney, W.R., Crocker, B.B., Fair, J.R., 2008. Equipment for Distillation, Gas Absorption, Phase Dispersion, and Phase Separation, in: Green, D.W., Perry, R.H. (Eds.), *Perry's Chemical Engineer's Handbook*. McGraw-Hill, New York.
- Kjelstrup, S., Coppens, M.O., Pharoah, J.G., Pfeifer, P., 2010. Nature-inspired energy- and material-efficient design of a polymer electrolyte membrane fuel cell. *Energy and Fuels* 24, 5097–5108. <https://doi.org/10.1021/ef100610w>
- Kobayashi, H., Lorente, S., Anderson, R., Bejan, A., 2013. Trees and serpentines in a conducting body. *Int. J. Heat Mass Transf.* 56, 488–494. <https://doi.org/10.1016/j.ijheatmasstransfer.2012.09.012>
- Kuddusi, L., Eđrican, N., 2008. A critical review of constructal theory. *Energy Convers. Manag.* 49, 1283–1294. <https://doi.org/10.1016/j.enconman.2007.05.023>
- Kustova, E. V., Giordano, D., 2011. Cross-coupling effects in chemically non-equilibrium viscous compressible flows. *Chem. Phys.* 379, 83–91. <https://doi.org/10.1016/j.chemphys.2010.11.009>
- Lämmermann, M., Schwieger, W., Freund, H., 2016. Experimental investigation of gas-liquid distribution in periodic open cellular structures as potential catalyst supports. *Catal. Today* 273, 161–171. <https://doi.org/10.1016/j.cattod.2016.02.049>
- Laser, D.J., Santiago, J.G., 2004. A review of micropumps. *J. Micromechanics Microengineering* 14, R35–R64. <https://doi.org/10.1088/0960-1317/14/6/R01>
- Lloyd-Jones, J., 2019. Anatomical neon. *Cardiovasc. Diagn. Ther.* 9, S183–S184. <https://doi.org/10.21037/cdt.2018.12.02>
- Loth, E., 2000. Numerical approaches for motion of dispersed particles, droplets and bubbles. *Prog. Energy Combust. Sci.* 26, 161–223. [https://doi.org/10.1016/S0360-1285\(99\)00013-1](https://doi.org/10.1016/S0360-1285(99)00013-1)
- Marbach, S., 2018. S'inspirer du rein pour filtrer l'eau, ou comment réinventer la passoire. *Reflète la Phys.* 58, 20–24. <https://doi.org/10.1051/refdp/201858020>
- Marbach, S., Yoshida, H., Bocquet, L., 2017. Osmotic and diffusio-osmotic flow generation at high solute concentration. I. Mechanical approaches. *J. Chem. Phys.* 146, 194701. <https://doi.org/10.1063/1.4982221>

- Marbach, S., Yoshida, H., Bocquet, L., 2020. Local and global force balance for diffusiophoretic transport. *J. Fluid Mech.* 892. <https://doi.org/10.1017/jfm.2020.137>
- Marcandelli, C., Lamine, A.S., Bernard, J.R., Wild, G., 2000. Liquid Distribution in Trickle-Bed Reactor. *Oil Gas Sci. Technol.* 55, 407–415. <https://doi.org/10.2516/ogst:2000029>
- Martyushev, L.M., Seleznev, V.D., 2006. Maximum entropy production principle in physics, chemistry and biology. *Phys. Rep.* 426, 1–45. <https://doi.org/10.1016/j.physrep.2005.12.001>
- Martyushev, L.M., Seleznev, V.D., 2014. The restrictions of the maximum entropy production principle. *Phys. A Stat. Mech. its Appl.* 410, 17–21. <https://doi.org/10.1016/j.physa.2014.05.014>
- McDermott, J.J., Kar, A., Daher, M., Klara, S., Wang, G., Sen, A., Velegol, D., 2012. Self-generated diffusioosmotic flows from calcium carbonate micropumps. *Langmuir* 28, 15491–15497. <https://doi.org/10.1021/la303410w>
- Merlin, G., Ménézo, C., 2018. *Ingénierie bio-inspirée: Principes et transition énergétique*, 1st ed. Ellipses, Paris.
- Meyer, M., Rouzineau, D., 2020. DISTRILI, distributeur liquide pour les colonnes à garnissages (Patent). BI3 2008668.
- Michelin, S., Lauga, E., 2014. Phoretic self-propulsion at finite Péclet numbers. *J. Fluid Mech.* 747, 572–604. <https://doi.org/10.1017/jfm.2014.158>
- Miller, R.M., Singh, J.P., Morris, J.F., 2009. Suspension flow modeling for general geometries. *Chem. Eng. Sci.* 64, 4597–4610. <https://doi.org/10.1016/j.ces.2009.04.033>
- Moore, F., Rukovena, F., 1987. Liquid and Gas Distribution in Commercial Packed Towers. *CPP Ed. Eur.* 11–15.
- Moroz, A., 2008. On a variational formulation of the maximum energy dissipation principle for non-equilibrium chemical thermodynamics. *Chem. Phys. Lett.* 457, 448–452. <https://doi.org/10.1016/j.cplett.2008.04.050>

- Mount Sinai Health System, 2021. Urine 24-hour volume [WWW Document]. URL <https://www.mountsinai.org/health-library/tests/urine-24-hour-volume> (accessed on December 2, 2021).
- Mulop, N., Yusof, K.M., Tasir, Z., 2012. A Review on Enhancing the Teaching and Learning of Thermodynamics. *Procedia - Soc. Behav. Sci.* 56, 703–712. <https://doi.org/10.1016/j.sbspro.2012.09.706>
- Nascimento Magalhães, M., 2006. *Probabilidade e Variáveis Aleatórias*, 2nd ed. Edusp, São Paulo.
- Nick Moore, 2016. Rayleigh–Bénard convection cells [Youtube Video] [WWW Document]. URL <https://www.youtube.com/watch?v=gSTNxS96fRg> (accessed on March 12, 2021).
- Nott, P.R., Guazzelli, E., Pouliquen, O., 2011. The suspension balance model revisited. *Phys. Fluids* 23. <https://doi.org/10.1063/1.3570921>
- Olujić, Ž., de Graauw, J., 1990. Experimental Studies on the Interaction Between the Initial Liquid Distribution and the Performance of Structured Packings. *Sep. Sci. Technol.* 25, 1723–1735. <https://doi.org/10.1080/01496399008050419>
- Olujić, Ž., Seibert, A.F., Fair, J.R., 2000. Influence of corrugation geometry on the performance of structured packings: An experimental study. *Chem. Eng. Process. Process Intensif.* 39, 335–342. [https://doi.org/10.1016/S0255-2701\(99\)00095-1](https://doi.org/10.1016/S0255-2701(99)00095-1)
- Onsager, L., 1931a. Reciprocal relations in irreversible processes. I. *Phys. Rev.* 37, 405–426. <https://doi.org/10.1103/PhysRev.37.405>
- Onsager, L., 1931b. Reciprocal relations in irreversible processes. II. *Phys. Rev.* 38, 2265–2279.
- Oster, G., Peskin, C.S., 1992. Dynamics of osmotic fluid flow, in: Karalis, T.K. (Ed.), *Mechanics of Swelling*. Springer, Berlin, pp. 731–742. [https://doi.org/10.1007/978-3-642-84619-9\\_44](https://doi.org/10.1007/978-3-642-84619-9_44)
- Pascau, A., 2011. Cell face velocity alternatives in a structured colocated grid for the unsteady Navier – Stokes equations. *Int. J. Numer. Methods Fluids* 65, 812–833. <https://doi.org/10.1002/fld.2215>

- Polettini, M., 2013. Fact-checking Ziegler's maximum entropy production principle beyond the linear regime and towards Steady States. *Entropy* 15, 2570–2584.  
<https://doi.org/10.3390/e15072570>
- Popescu, M.N., Uspal, W.E., Dietrich, S., 2016. Self-diffusiophoresis of chemically active colloids. *Eur. Phys. J. Spec. Top.* 225, 2189–2206.  
<https://doi.org/10.1140/epjst/e2016-60058-2>
- Prigogine, I., 1962. *Introduction à la Thermodynamique des Processus Irréversibles*, 1st ed. Wiley, New York.
- Pruessner, G., 2012. *Self-Organised Criticality: Theory, Models and Characterisation*. Cambridge University Press, Cambridge.
- Ramírez-Hinestrosa, S., Yoshida, H., Bocquet, L., Frenkel, D., 2020. Studying polymer diffusiophoresis with non-equilibrium molecular dynamics. *J. Chem. Phys.* 152, 164901. <https://doi.org/10.1063/5.0007235>
- Rasmussen, M.K., Pedersen, J.N., Marie, R., 2020. Size and surface charge characterization of nanoparticles with a salt gradient. *Nat. Commun.* 11, 1–8.  
<https://doi.org/10.1038/s41467-020-15889-3>
- Russel, W.B., Saville, D.A., Schowalter, W.R., 1989. *Colloidal Dispersions*, 1st ed. Cambridge University Press, New York.
- Sang, L.C., Coppens, M.O., 2011. Effects of surface curvature and surface chemistry on the structure and activity of proteins adsorbed in nanopores. *Phys. Chem. Chem. Phys.* 13, 6689–6698. <https://doi.org/10.1039/c0cp02273j>
- Sasidhar, V., Ruckenstein, E., 1982. Anomalous effects during electrolyte osmosis across charged porous membranes. *J. Colloid Interface Sci.* 85, 332–362.  
[https://doi.org/10.1016/0021-9797\(82\)90003-0](https://doi.org/10.1016/0021-9797(82)90003-0)
- Schroeder, D. V., 2000. *An Introduction to Thermal Physics*. Addison-Wesley, San Francisco.
- Seleznev, V.D., Martyushev, L.M., 2014. Fluctuations, Trajectory Entropy and Ziegler's Maximum Entropy Production Principle, in: Dewar, R.C., Lineweaver, C.H., Niven, R.K., Regenauer-Lieb, K. (Eds.), *Beyond the Second Law: Entropy Production and Non-Equilibrium Systems*. Springer, Berlin.

- Sharifi-Mood, N., Koplik, J., Maldarelli, C., 2013. Diffusiophoretic self-propulsion of colloids driven by a surface reaction: The sub-micron particle regime for exponential and van der Waals interactions. *Phys. Fluids* 25. <https://doi.org/10.1063/1.4772978>
- Shin, S., 2020. Diffusiophoretic separation of colloids in microfluidic flows. *Phys. Fluids* 32, 101302. <https://doi.org/10.1063/5.0023415>
- Smith, C.H., 2013. Alfred Russel Wallace's world of final causes. *Theory Biosci.* 132, 239–249. <https://doi.org/10.1007/s12064-013-0191-6>
- Subawalla, H., González, J.C., Seibert, A.F., Fair, J.R., 1997. Capacity and Efficiency of Reactive Distillation Bale Packing: Modeling and Experimental Validation. *Ind. Eng. Chem. Res.* 36, 3821–3832. <https://doi.org/10.1021/ie9700501>
- SUEZ, 2021. Al Dur seawater reverse osmosis desalination plant (Bahrain) [WWW Document]. URL [www.suezwaterhandbook.com/case-studies/desalination/Al-Dur-seawater-reverse-osmosis-desalination-plant-Bahrain](http://www.suezwaterhandbook.com/case-studies/desalination/Al-Dur-seawater-reverse-osmosis-desalination-plant-Bahrain) (accessed on March 12, 2021).
- Thamattoor, A., 2018. Normal Limit of the Binomial via the Discrete Derivative. *Coll. Math. J.* 49, 216–217. <https://doi.org/10.1080/07468342.2018.1440872>
- Tondeur, D., Fan, Y., Luo, L., 2009. Constructal optimization of arborescent structures with flow singularities. *Chem. Eng. Sci.* 64, 3968–3982. <https://doi.org/10.1016/j.ces.2009.05.052>
- Tondeur, D., Kvaalen, E., 1987. Equipartition of Entropy Production. An Optimality Criterion for Transfer and Separation Processes. *Ind. Eng. Chem. Res.* 26, 50–56. <https://doi.org/10.1021/ie00061a010>
- UCL, 2021. Centre for Nature Inspired Engineering [WWW Document]. URL <https://www.ucl.ac.uk/nature-inspired-engineering/> (accessed on March 12, 2021).
- Van Der Sman, R.G.M., 2009. Simulations of confined suspension flow at multiple length scales. *Soft Matter* 5, 4376–4387. <https://doi.org/10.1039/b915749m>
- Velegol, D., Garg, A., Guha, R., Kar, A., Kumar, M., 2016. Origins of concentration gradients for diffusiophoresis. *Soft Matter* 12, 4686–4703. <https://doi.org/10.1039/c6sm00052e>

- von Helmholtz, H., 2003. The Conservation of Force, in: Hall, N.S. (Ed.), *The Kinetic Theory Of Gases: An Anthology of Classic Papers with Historical Commentary*. Imperial College Press, Singapore, pp. 89–110.  
[https://doi.org/10.1142/9781848161337\\_0008](https://doi.org/10.1142/9781848161337_0008)
- West, G.B., Brown, J.H., Enquist, B.J., 1997. A general model for the origin of allometric scaling laws in biology. *Science* (80). 276, 122–126.  
<https://doi.org/10.1126/science.276.5309.122>
- Wolfram|Alpha, 2020. Wolfram|Alpha [WWW Document]. URL <https://www.wolframalpha.com/> (accessed on November 13, 2020).
- Wong, T.S., Kang, S.H., Tang, S.K.Y., Smythe, E.J., Hatton, B.D., Grinthal, A., Aizenberg, J., 2011. Bioinspired self-repairing slippery surfaces with pressure-stable omniphobicity. *Nature* 477, 443–447. <https://doi.org/10.1038/nature10447>
- Yang, Q., Leng, K., Liu, Y., 2013. On the Structure of Maximum Entropy Production Principle: from Near to far-from Equilibrium, in: *12th Joint European Thermodynamics Conference*. Brescia, pp. 133–138.
- Yuan, J.P., Chen, F., 2001. Kinetics for the reversible isomerization reaction of trans-astaxanthin. *Food Chem.* 73, 131–137. [https://doi.org/10.1016/S0308-8146\(01\)00107-8](https://doi.org/10.1016/S0308-8146(01)00107-8)
- Zhang, J., Ma, W., 2020. Data-driven discovery of governing equations for fluid dynamics based on molecular simulation. *J. Fluid Mech.* 892, A5.  
<https://doi.org/10.1017/jfm.2020.184>
- Zhang, X.H., Lv, N., 2012. Three-dimensional multi-scale fluid distributor assembly minimizing total viscous dissipation. *Int. Commun. Heat Mass Transf.* 39, 1535–1541.  
<https://doi.org/10.1016/j.icheatmasstransfer.2012.09.009>
- Ziegler, H., 1958. An attempt to generalize Onsager's principle, and its significance for rheological problems. *ZAMP Zeitschrift für Angew. Math. und Phys.* 9, 748–763.  
<https://doi.org/10.1007/BF02424793>
- Ziegler, H., 1961. Zwei Extremalprinzipien der irreversiblen Thermodynamik. *Ingenieur-Archiv* 30, 410–416. <https://doi.org/10.1007/BF00531783>

## Bibliography

Ziegler, H., 1968. A Possible Generalization of Onsager's Theory, in: Parkus, H., Sedov, L.I. (Eds.), *Irreversible Aspects of Continuum Mechanics and Transfer of Physical Characteristics in Moving Fluids*. Springer, Viena, pp. 411–424.

Ziegler, H., 1970. Proof of an orthogonality principle in irreversible thermodynamics. *ZAMP Zeitschrift für Angew. Math. und Phys.* 21, 853–863.

<https://doi.org/10.1007/BF01594846>

Ziegler, H., 1983a. Chemical reactions and the principle of maximal rate of entropy production. *ZAMP Zeitschrift für Angew. Math. und Phys.* 34, 832–844.

<https://doi.org/10.1007/BF00949059>

Ziegler, H., 1983b. *An Introduction to Thermomechanics*, 2nd ed. North-Holland, Amsterdam.

---

## Appendix A. Brief history of thermodynamics

---

Undergraduate and graduate students commonly give negative feedback on their learning experience with thermodynamics. This problem motivated several researchers to look for alternative methods for teaching the subject (Mulop et al., 2012). Overall, these methods were found to improve the learning experience, with students performing better at exams and giving more positive feedback by the end of the semester. Nevertheless, many of the articles cited by Mulop et al. (2012) focused on “how can we make students understand the contents we wish to pass to them”. Only a few of them questioned the contents themselves.

Cotignola et al. (2002) recognized that many introductory textbooks on thermodynamics reproduce some types of misconceptions. For example, out of the 7 books reviewed by the authors, 5 refer to heat as a “form of energy” at some point, and only 2 describe Joule’s experiments correctly. This suggests that the confusion and misunderstanding the students experience may not be related exclusively to their capacity to learn. Even the most genius, fast-learner student would be incapable of comprehending a subject if its contents are not logically structured (e.g. if they carry contradictory information). The same student would also be unable to assimilate a subject if its contents are not self-sufficient (e.g., if they make use of quantities which are not defined).

In order to avoid perpetuating misconceptions and improve the quality of thermodynamic classes, Cotignola et al. (2002) propose a historical approach to thermodynamics. Regarding the concept of internal energy, the authors say: *learning about its origin and evolution, as well as the ways it is presented and treated by different textbooks, mainly during the last years, would help us uncover hidden conceptual schemes not only in our students but also in scientists and teachers.*

This historical approach, although time-consuming, seems indeed to be the answer to many problems faced by the students. If concepts in thermodynamics are taken for granted, full learning is never achieved. The best way for students and professors to get rid of misconceptions and preconceptions is to position themselves in a time prior to said conceptions. For example, the idea of temperature is something internalized in people’s minds since they are young. Children playing outside can see the current temperature on



## Appendix A. Brief history of thermodynamics

street thermometers. When they come back home to watch TV, the forecast is announcing what tomorrow's temperature will be. But there was a time when thermometers did not exist, and temperature was a much more abstract concept.

Much longer before the concept of temperature was solidified, humans already knew about hot and cold. Hot is the sensation one has when getting close to a fire, or when stepping on a stone that stayed under the sun for too long. Object 1 is hotter than object 2 if that sensation is stronger upon touching object 1. Cold is what people experience when it is snowing, or when they jump into a river. Object 2 is colder than object 1 if that sensation is stronger upon touching object 2. The temperature is just an entity associated with these sensations of hot and cold. If object 1 is hotter than object 2, its temperature should be higher. If they are both equally hot/cold, their temperature should be the same.

The association described above between temperature and physical sensation has its limitations. If an individual touches a metal spoon and a wood spoon, both at room temperature, the metal spoon will feel colder than the wood one. Putting these spoons in contact with each other for a long time will not change the sensation they produce: the metal spoon will feel as cold as it was before. In other words, some materials seem colder/hotter than others even at the same temperature (nowadays it is known that this is due to a difference in their thermal conductivities). Further, sensations are subjective, and individuals will experience hot and cold in different ways. Clearly, the human "sensation" of hot and cold is not enough to consistently evaluate temperatures.

The first people to find a consistent way of measuring said entity linked the idea of temperature to the idea of mercury dilatation. When a mercury-in-glass device is immersed in a certain system (say cold water), the mercury level in this device will reach a certain level and then remain at this level. If we move the device to hotter water (hotter in the sense described in the previous paragraphs), the mercury level increases and eventually settles. The volume occupied by the mercury in the glass is related to the physical sensations of hot and cold. If two systems made of the same material are equally hot/cold upon touch, the corresponding level of mercury in the mercury-in-glass device will also be the same. Around the year 1724, Daniel Gabriel Fahrenheit devised a scale for temperature by assigning 2 reference values in this device (0 °F for the eutectic equilibrated mixture of ice, water and ammonium chloride; 30 °F for the equilibrated mixture of ice and water). He then graduated his device linearly, so that equal amounts of mercury dilatation correspond to equal increments in the Fahrenheit scale. After seeing

## Appendix A. Brief history of thermodynamics

that the quantity now called temperature is linked to dilatation, Jacques Charles discovery (years later) that temperature and volume of an ideal gas obey a linear relation sounds much more reasonable.

In the second half of the 18<sup>th</sup> century, chemist Antoine Lavoisier debunked the phlogiston theory of combustion, an old theory defending that all flammable substances contained an element called phlogiston. He suggested that combustion was the combination of substances with an active gas (oxygen) in the air. He also advocated for the caloric heat theory, stating that heat was a substance that migrates from warmer to colder bodies.

Lavoisier died in the French Revolution, and his widow married Benjamin Thompson. Thompson, also known as Count Rumford, is famous for his paper entitled *An Enquiry Concerning the Source of the Heat which is Excited by Friction* (Count of Rumford, 1798). In this paper, he describes an experiment in which water is heated by the friction of a blunt borer forced against a rotating metallic object. Heat could be “generated” indefinitely in this insulated experimental device, proving that it could not be a material substance.

It took some time for the scientific community around the world to accept that the caloric heat theory was wrong. In the meanwhile, mechanical engineer Nicolas Carnot used this theory in his study of steam engines. He created a much more abstract model for engines, describing it as a system in contact with a hot source and a cold sink, and from which mechanical work can be extracted. Carnot also introduced the idea of cycle for engines. According to this idea, the working fluid (steam in the case of steam engines) could be brought to the same state after successive operations, such as heating/ expansion/ cooling/ compression. Through his abstract model, Carnot neglected any type of friction that appears in real engines, as well as heat conduction between different parts of the engine. He theorized that, in this case, engine’s efficiency was maximum, and it depended only on the temperatures of the hot and cold bodies in contact with the system.

This postulate was the precursor for the Second Law of Thermodynamics. If it was to be violated, then the Second Law as we know today would be violated as well. To see this, it is important to note that the idealized model for engines proposed by Carnot is nowadays known as a *reversible engine*. A fictitious system can be conceived by coupling an engine more efficient than Carnot’s with a reverse Carnot engine. Both engines share the same hot source and cold sink, and the work produced by the first engine is all used

## Appendix A. Brief history of thermodynamics

by Carnot's reverse engine. The result from this mental construction is a closed system, consisting of the hot and cold bodies, the engine and the reversible Carnot engine, in which heat goes from the cold body to the hot body. That is a violation of the Second Law as we know today.

Seeing that the embryo of the Second Law of Thermodynamics appeared before the First Law can help debunk the misconception that the latter is more "fundamental", or more "intuitive", than the former. In fact, the balance equations Carnot used to model an engine cycle violated the First Law! He thought (not to his discredit) that, after one cycle, the sum of the heat gained and lost by the engine was 0. This comes from the caloric theory view of heat as matter associated to the state of the system.

The First Law of Thermodynamics cannot coexist with the caloric theory. Thus, it is only natural that the early formulations of the First Law would be treated with reluctance and scepticism by scientists in the past. Julius von Mayer is the proof of that. This German physician noted that the venous blood from patients in Java (a tropical island) was brighter red than the venous blood from his patients in Germany. Being acquitted with the works of Lavoisier in chemistry, he concluded that less combustion (oxidation) was required for patients in Java to keep their body temperature. The brighter colour can then be explained by an excess of oxygen in the veins.

He later extrapolated his conclusions, saying that the "heat" (chemical energy) produced by the body should be equal to the heat we lose to the surroundings *plus the mechanical work our body exerts on its surroundings*. He gave a more general statement to his theory: *A force once in existence cannot be annihilated*. Mayer used the word *force* to describe the quantity now known as energy. His theory was dismissed by journals and newspapers at the time, so he looked for ways to prove it experimentally.

It so happens that the experiments supporting his theory had been made around 30 years before, by Gay-Lussac. Gay-Lussac's experiment consisted of two reservoirs, one containing air and the other at vacuum. They were connected by a channel, which was closed by a valve. The entire system was insulated, and thermometers were used to measure the temperature in each reservoir. The valve was then opened, so the air could pass from one reservoir to another, and Gay-Lussac recorded the new temperatures after equilibration. Adepts of the caloric theory would predict a temperature drop, since the caloric substance would spread out from one reservoir to two reservoirs. This was the

## Appendix A. Brief history of thermodynamics

same explanation given at the time for the decrease in temperature observed in gas expansion against a piston. Astonishingly for them, the final equilibrium temperature observed by Gay-Lussac was the same as the system's initial temperature.

Mayer could explain this phenomenon with his new theory: in the piston experiment, *force* (energy) is converted into work exerted on the piston. As a result, the *force* (energy) of the gas decreases, and so does its temperature. However, in Gay-Lussac's experiment, gas expansion takes place without work being exerted on the surroundings. Therefore, the system's *force* (energy) is conserved, and so is the temperature. Mayer used the same reasoning to explain why the specific heat of gas at constant pressure was always higher than the specific heat measured at constant volume. According to him, it was simply because part of the heat provided to a system at constant pressure is converted to work during gas' expansion.

It took years for people to give credit to Mayer for his findings. Another researcher, James Joule, was luckier in his endeavours. Joule first observed that forcing a perforated piston through a cylinder containing water would increase the water's temperature. Using this arrangement, he observed that a work of ~770 ft-lb was necessary to increase the temperature of the water by 1 °F (Joule, 1843). In another series of experiments, Joule used a dynamo to create a current. His dynamo was man-powered, but he was able to measure the work put into the system afterwards by repeating a few cycles using weights as the driving force. The circuit itself was immersed in water, and its ends were connected to a galvanometer to measure the current. Joule had already proposed the law of heating for circuits prior to these experiments, so he expected the water's temperature to increase due to the electrical current. He observed that it was necessary to put ~838 ft-lb of mechanical work to the dynamo in order to increase the temperature of 1 pound of water by 1 °F (Joule, 1843). The way he stated this result was quite revolutionary at the time. He said (bold for emphasis):

*The quantity of heat capable of increasing the temperature of a pound of water by one degree of Fahrenheit's scale is **equal to**, and may be converted to, a mechanical force capable of raising 838lbs. to the perpendicular height of one foot.*

Perhaps to some people living in the 1840's, this statement would sound as unsettling as someone claiming that 1 meter was equal to 1 second. What Joule was proposing is that

## Appendix A. Brief history of thermodynamics

heat is, in essence, equivalent to mechanical work, and hence they could be measured using the same units.

The physicist needed more to prove his bold claims to the scientific community. This led him to devise what is perhaps his most known experiment on the mechanical equivalence of heat. He used a paddle wheel to stir a reservoir full of water, and made use of weights to calculate the work being put to the system. He found that  $\sim 772.7$  ft-lb of mechanical work was necessary to increase the temperature of 1 pound of water by  $1^\circ\text{F}$  (Joule, 1850). With various types of experiments all giving very close results for the mechanical equivalent of heat, this new thesis would replace the caloric theory once and for all.

Joule figured out that same changes in water state could be obtained via mechanical work or via heat. The First Law of Thermodynamics was within reach, and Hermann von Helmholtz was the first to state it (von Helmholtz, 2003). The German physicist was a mind ahead of his time. By postulating that the universe is deterministic and that perpetual machines cannot exist, he shows that all phenomena can be reduced to attraction/repulsion, distance-dependant forces between pairs of particles. And he proves that, for any system with only these distance-dependant forces, a quantity corresponding to the sum of *vires vivae* (kinetic energy) and tensions (potential) should remain the same. For systems that seem to lose *vis viva* without gaining tension (e.g. the collision of inelastic bodies, or frictional systems), Helmholtz argues that heat is released to the surroundings. And following Joule's theory on the mechanical equivalent of heat, the physician concludes that, in these "non-conservative" systems, heat is simply the transfer of *vis viva* to the surroundings. The overall energy (system + surroundings) remains the same.

Another German physicist, named Rudolf Clausius, pinned the First Law of Thermodynamics in the 1850's with a simple statement and a simple equation. His statement:

*The energy of the universe is constant.*

The corresponding equation:

$$\Delta U = Q + W \tag{A1}$$

In eq. A1,  $\Delta U$  refers to the variation of internal energy in a system,  $Q$  is the heat provided to the system, and  $W$  is the work exerted on it.

## Appendix A. Brief history of thermodynamics

Clausius also formulated the Second Law of Thermodynamics as we know today, and wrote the equation that corresponds to it. All the development leading to this law (Clausius, 1856) was based upon an axiom: *Heat can never pass from a colder to a warmer body without some other change, connected therewith, occurring at the same time.* It is a common misconception to believe that the Second Law is purely axiomatic, and that heat flowing from hot to cold is a consequence of this axiom. In truth however, the Second Law itself is derived from the axiom that heat cannot pass from a cold body to a hot body.

Clausius imagined a reversible cycle in which ideal gas enclosed in a cylinder interacts with 3 bodies, K1 (at temperature  $t_1 < t$ ), K2 (at temperature  $t_2 < t_1$ ), and K (at temperature  $t$ ). The gas starts at a temperature  $t$ , and it expands adiabatically until it cools to a temperature of  $t_1$ . The cylinder is then put in contact with body K1, and it expands isothermally. In this isothermal expansion, the cylinder gains some heat  $Q_1$  to the body K1, to compensate the energy that would be lost during its expansion. We assume the bodies K, K1 and K2 to be of great volume, so that their temperatures remain constant during the process.

In the third step of this cycle, the cylinder is insulated and allowed to expand until it reaches temperature  $t_2$ . Afterwards, it is put in contact with K2 and compressed isothermally. The compression continues until the amount of heat imparted to K2 equals  $Q_1$ . The following fifth step is an adiabatic compression of the gas until it reaches temperature  $t$ . It can be shown that the volume of the cylinder at this point is smaller than its original volume, so the cylinder needs to be put in contact with body K and expand isothermally until it restores its volume. In this last isothermal expansion, an amount of heat  $Q$  flows from K to the cylinder.

Overall, the amount of heat the cylinder receives in this cycle is  $Q$ . According to eq. A1, one concludes that the resulting work exerted by the cylinder on its surroundings is equal to  $Q$  (i.e.,  $W = -Q$ ). The amount of heat transferred from K1 to K2 is equal to  $Q_1$ . Clausius states that any other reversible cycle operating through heat transfer between the engine and bodies K, K1, K2, and transforming heat  $Q$  from K into work, would have the same overall heat  $Q_1$  being transferred from K1 to K2. If that was not the case, one could simply perform the cycle for which  $Q_1$  is lower, and then perform the reverse of the cycle

## Appendix A. Brief history of thermodynamics

for which  $Q_1$  is higher. The result from this 2-cycle operation would be a net heat transfer from the colder body  $K_2$  to the hotter body  $K_1$  without any type of “compensation”.

The physician then introduces the concept of equivalent transformations. In a reversible cycle, some operations will change the engine’s state from  $a$  to  $b$ , and other operations will restore the engine back to state  $a$ . If done in reverse, this second set of operations could actually bring the engine from state  $a$  to state  $b$ . Therefore, the first part of the cycle is said to be equivalent to the reverse of the second part. More generally, reversible transformations using the same heat sources/sinks ( $K$ ,  $K_1$  and  $K_2$ ), and capable of bringing the engine from state  $a$  to state  $b$ , are equivalent.

Clausius postulates that there must be a mathematical quantity to be assigned to these transformations such that, when the transformations are equivalent, the corresponding quantities are equal. Looking back at the 6-steps cycle described above, it can be simplified into two types of transformation: heat  $Q$  taken from  $K$  and converted into work; heat  $Q_1$  flowing from  $K_1$  to  $K_2$ . The mathematical quantity associated to the first type of transformation should depend on the temperature  $t$  of body  $K$ , and be proportional to the heat flow  $Q$ . Indeed, taking  $Q/2$  from  $K$  and transforming it into work, and later taking another  $Q/2$  from  $K$  and also transforming it into work, should be equivalent to taking  $Q$  from  $K$  in one shot and transforming it into work. So the transformation “engine takes heat  $Q$  from  $K$  and transforms it into work” has an equivalence value of  $\Delta = -Q \times f(t)$ . The negative sign is used to follow Clausius’ convention. Similarly, the transformation “heat  $Q_1$  flows from  $K_1$  to  $K_2$ ” has an equivalence value of  $\Delta = Q_1 \times F(t_1, t_2)$ . Of course, if  $Q_1$  is transferred from  $K_2$  to  $K_1$ , it is suitable that  $\Delta$  inverts its sign. Therefore,  $F(t_1, t_2) = -F(t_2, t_1)$ . When a cycle is complete, the engine returns to its initial state. So it is reasonable to assume that the sum of the mathematical quantities  $\Delta$  in a cycle will be equal to zero. Hence, for the cycle studied here:  $Q_1 \times F(t_1, t_2) - Qf(t) = 0$ .

Imagine now a similar cycle that uses a body  $K'$  at temperature  $t'$  to replace body  $K$  at temperature  $t$ . The steps that would be changed are: (i) adiabatic compression from temperature  $t_2$  to temperature  $t$  replaced by adiabatic compression from temperature  $t_2$  to temperature  $t'$ ; (ii) isothermal expansion restoring the engine’s initial volume would be performed at temperature  $t'$ , with some amount of heat  $Q'$  being taken from  $K'$ . The sum of the quantities  $\Delta$  in this second cycle should also be equal to 0:  $Q_1 \times F(t_1, t_2) -$

## Appendix A. Brief history of thermodynamics

$Q'f(t') = 0$ . If we subtract this equation from the one written in the previous paragraph, we have:  $Qf(t) = Q'f(t')$ .

Now if the cycle with the body K (at temperature  $t$ ) is followed by the inverse of the cycle with the body K' (at temperature  $t' < t$ ), the result is a process in which the engine takes heat  $Q$  from K and transforms it into work, and then converts some external work  $Q'$  into heat to the body K'. With a few extra steps, one can write the balance equation for the equivalence value in this double cycle as:  $\Delta = -(Q - Q')f(t) + Q'F(t, t') = 0$ . Replacing the equality  $Qf(t) = Q'f(t')$  found previously finally yields:  $F(t, t') = f(t') - f(t)$ .

We have found that the balance equation for the equivalence values of a reversible engine cycle using two bodies at temperatures  $t$  and  $t'$  is:  $\Delta = Qf(t) - Q'f(t') = 0$ . If, instead of only two bodies, the reversible cycle had made use of  $N$  bodies, then:  $\sum_i Q_i f(t_i) = 0$ . Here  $Q_i$  is positive when body  $K_i$  receives heat, and negative when it releases heat. Note that the bodies themselves could change their temperature in the process. For example, if  $K_i$  is a small body, giving heat to the engine should decrease its temperature  $t_i$ . For this step of the cycle to be reversible, the temperature of the engine should follow  $t_i$ . Therefore, the engine must expand fast enough so that, despite the gain of heat, its temperature decreases as fast as  $t_i$ . For reversible cycles having such temperature-changing bodies, the balance equation for  $\Delta$  is:  $\sum_i \int f(t_i) \delta Q_i = 0$ . This equation can be rewritten in terms of the engine's temperature:  $\int f(t) \delta Q = 0$ .

The value  $\sum_i \int f(t_i) \delta Q_i$  cannot be less than 0 for an irreversible cycle, because then it would be possible to combine it with a reversed cycle in such a way that, after both cycles were performed, net heat would be flowing from smaller temperatures to higher temperatures without any type of compensation. Therefore,  $\sum_i \int f(t_i) \delta Q_i \geq 0$  for any cycle, the equality being achieved when the cycle is reversible. However, for the engine we have  $\int f(t) \delta Q = 0$  even for irreversible cycles, just as long as the temperature and pressure inside the engine remain homogeneous throughout the process. Indeed, the evolution of an engine in any irreversible cycle could be replicated by a reversible cycle with infinite bodies  $K_i$  through an infinite amount of successive isothermal and adiabatic expansions/compressions.

The function  $f(t)$  appearing in the expressions above has yet to be found. By assuming that in an isothermal expansion the total heat imparted to the engine is equal to the work



## Appendix A. Brief history of thermodynamics

it produces, Clausius proves that  $f(t) = 1/t$  (as long as  $t$  is given in an absolute scale). The physician noted that his theory could be generalized for any process (not only cycles) in an isolated compound system, just as long as the subsystems (bodies and engines) were always at thermodynamic equilibrium. The mathematical formulation for the Second Law of Thermodynamics was then written as:

$$\Delta S = \int 1/T \delta Q \geq 0 \quad A2$$

where the integral is extended to all bodies and engines in the isolated system.

Clausius called the quantity  $\Delta S$  *entropy variation*. He summarized the Second Law with a short sentence:

*The entropy of the universe tends to a maximum.*

The history of thermodynamics does not end here. Many more interesting discoveries were made in the field since after Clausius' work, specially with the development of statistical mechanics and the progress in nonequilibrium thermodynamics. Nevertheless, most of these remaining developments are taught to a satisfactory degree, and not much would be gained from approaching them in a historical fashion.

For those interested in a more thorough analysis, Angrist and Hepler (1967) is a great recommendation. This book, as well as the videos by CrashCourse (2018) and Balistreri (2019) were the key sources for this Appendix.

---

## Appendix B. The auxiliary tool for distributor design

---

An Excel spreadsheet was developed to assist with the design of tree-shaped liquid distributors. Indeed, as discussed in Section II.4 there are several constraints and variables that need to be taken into account in the design stage. These are not always trivial considerations, hence an automated application that can systematically assess distributor configurations is a valuable tool. A diagram chart illustrating the operating mode of this tool was shown in Figure II.17. Here, the specifics of this Excel spreadsheet will be discussed in detail.

First, let us recall the design variables that determine distributor configuration. These are: the number of layers ( $N_l$ ), the length of the wires ( $l_w$ ), the inclination with respect to the vertical axis ( $\theta$ ), and the diameter of the wires ( $d_w$ ). The user can input these values in the *Setup* tab of the spreadsheet (Figure B1). Alternatively, he/she can set a range for these variables, choose a variation step (“Delta”) for each, and run the “Feasibility analysis”. This macro tries all possible configurations within the given range, and returns which are feasible (i.e., obey all constraints) and which are unfeasible. Note that, if “Wire diameter input” (cell B27) is set to “Automatic”, the diameter of the first layer is calculated via a macro, and the subsequent diameters are obtained according to the “Diameter ratio” specified in cell C9. For example, if the diameter ratio is set to 0.9, then the diameter for layer  $n$  is 0.9 times the diameter from the previous layer. Alternatively, if “Wire diameter input” is set to “Manual”, the user will have to specify wire diameters for all layers in row 32.

Other than the design variables, total liquid flow and column/mixture parameters are also defined in the *Setup* tab. Further, this tab contains the different constraints summarized in Table II.3. The constraint “Side of the proj triangle (m)” in cell F15 is related to the quantity  $L'_\Delta$  defined by eq. (II.15). If its value (cell F16) is higher than the upper limit in cell F18, then the distributor will not fit in the column. Further, constraint “Weber number check” in cell G15 checks whether all the layers of the distributor are in the wetting regime. If that is true, its value is 0.5; otherwise, it is set to 1000. For example, the configurations D1-D3 mentioned Chapter II will all have a “Weber number check” value of 1000, since there are some layers in Figure II.19 placed out of the wetting zone.

## Appendix B. The auxiliary tool for distributor design

Design Variables:		Diameter ratio	Wire length (m)	Angle (°)	Number of layers			
Value		1	0.02	38	3	Feasibility analysis		
Minimum		0.8	0.01	30	3	User-specified		
Maximum		1	0.02	40	6	Calculated		
Delta		0.1	0.001	2	1			
NumX		4						
Constraint		Total height (m)	Diameter min (m)	Diameter max (m)	Side of proj triangle (m)	Weber number check		
Value		0.067280645	0.00436	0.00436	5.82E-02	0.5		
Minimum		0	0.00227	0	0	0		
Maximum		0.2	1	0.00770	4.91E-02	1		
NumC		5						
Parameters		Column diameter (m)	No. of starting points (pts/m <sup>2</sup> )	Liquid flux (m <sup>3</sup> /m <sup>2</sup> .s)	Liquid viscosity (Pa.s)	ρ (Kg/m <sup>3</sup> )	Surface tension (N/m)	Gravity (m/s <sup>2</sup> )
Value		0.15	734	0.0056	0.00033	672	2.01E-02	9.8
Wire diameter input		Manual/Automatic						
Value		Automatic						
Wire diameters (m)		Layer 1	Layer 2	Layer 3	Layer 4	Layer 5	Layer 6	Layer 7
Values (for manual input)		3.0E-03	3.0E-03	3.0E-03	3.0E-03	3.0E-03	3.0E-03	3.0E-03

### Setup

Layer	0	1	2	3	4	5
No. of outlets	1	3	6	10	15	21
No. of wires	1	3	9	18	30	45
Wire diameter (m)	<b>4.36E-03</b>	<b>4.36E-03</b>	<b>4.36E-03</b>	<b>4.36E-03</b>	<b>4.36E-03</b>	<b>4.36E-03</b>
Height (m)	<b>0.02</b>	<b>0.0358</b>	<b>0.0515</b>	<b>0.0673</b>	<b>0.0830</b>	<b>0.0988</b>
Side of the proj triangle (m)	<b>0.0075</b>	<b>0.0244</b>	<b>0.0413</b>	<b>0.0582</b>	<b>0.0750</b>	<b>0.0919</b>
Wire volume per layer (m <sup>3</sup> )	<b>2.99E-07</b>	<b>8.97E-07</b>	<b>2.69E-06</b>	<b>5.38E-06</b>	<b>8.97E-06</b>	<b>1.35E-05</b>
Average flow per wire (m <sup>3</sup> /s)	<b>7.55E-06</b>	<b>2.52E-06</b>	<b>8.39E-07</b>	<b>4.20E-07</b>	<b>2.52E-07</b>	<b>1.68E-07</b>
Film thickness (m)	<b>4.11E-04</b>	<b>2.90E-04</b>	<b>2.03E-04</b>	<b>1.62E-04</b>	<b>1.37E-04</b>	<b>1.20E-04</b>
d*	<b>2.49</b>	<b>2.49</b>	<b>2.49</b>	<b>2.49</b>	<b>2.49</b>	<b>2.49</b>
Weber number	-	<b>2.30E+01</b>	<b>2.56E+00</b>	<b>2.84E-01</b>	<b>7.10E-02</b>	<b>2.56E-02</b>
Weber number min	-	<b>1.07E-01</b>	<b>1.07E-01</b>	<b>1.07E-01</b>	<b>1.07E-01</b>	<b>1.07E-01</b>
Weber number max	-	<b>5.04E+01</b>	<b>5.04E+01</b>	<b>5.04E+01</b>	<b>5.04E+01</b>	<b>5.04E+01</b>
Is We within range? (1=True; 0=False)	1	1	1	1	0	0
Diameter 1st wire (m)	<b>4.36E-03</b>					

	B	C
3 Feasible ?		<b>FALSE</b>
4 Min flow (m <sup>3</sup> /m <sup>2</sup> .s)		0.00340767
5 Max flow (m <sup>3</sup> /m <sup>2</sup> .s)		0.00822206
6 No. of outlets		7356
7 Volume fraction		10%

### Results

### Distributor configuration

	D	E	F	G	S	T	U	V
3 Diameter ratio	Wire length (m)	Angle (°)	Number of layers	Volume (m <sup>3</sup> )	No. of outlets (pts/m <sup>2</sup> )	Feasible?	Constraints violated	
66	1	0.019	32	3	1.15E-04	7356	TRUE	
67	0.8	0.02	32	3	6.72E-05	7356	TRUE	
68	0.9	0.02	32	3	9.06E-05	7356	TRUE	
69	1	0.02	32	3	1.22E-04	7356	FALSE	Side of proj triangle (m)
70	0.8	0.01	34	3	3.64E-05	7356	TRUE	
71	0.9	0.01	34	3	4.91E-05	7356	TRUE	

### Feasibility

Figure B1 – Screenshots of the different tabs in the Excel auxiliary tool for distributor design

For a given combination of decision variables and parameter values, the design tool calculates the geometric features (number of wires, height, ...) and flow characteristics (film thickness, average flowrate and Weber number) on each layer. These are presented in the tab *Distributor configuration* (Figure B1). The fields in bold correspond to the layers that actually exist in a given configuration; for example, if the user specifies a total of 3 layers in the *Setup* tab, only the columns C to F will be in bold in the *Distributor configuration* tab. The number of outlets per layer is calculated according to the equation in Figure II.14, and the number of wires in a given layer is equal to 3 times the number of outlets from the previous layer. The field “Side of the proj triangle (m)” corresponds

## Appendix B. The auxiliary tool for distributor design

to the term  $L'_\Delta$  defined in eq. II.15, and the wire volume per layer is calculated according to eq. II.20.

Furthermore, the macro “Film thickness (m)” shown in the figure calculates the film thickness according to eq. (II.6). The subsequent rows give  $d^*$  and  $We$  in each layer, according to eq. (II.8). The fields “Weber number min” and “Weber number max” take the value  $d^*$  and calculate the minimum and maximum Weber numbers for which the layer will experiment wetting flow. If the actual Weber number for that layer is within this wetting range, the next row (row 34) returns 1; otherwise, it returns 0. Finally, the macro “Diameter 1st wire (m)” suggests a value for the diameter of the wires in the first layer. This value is calculated so that the first layer will be close to the upper limit of the wetting regime. This way, the subsequent layers (with smaller Weber numbers, since the flowrate per wire decreases) are more likely to remain in the wetting regime. The distributor D3 in Figure II.19 illustrates this statement; its first layer is on the upper limit of the wetting regime, and consequently the second and third ones fall in this same zone.

The *Results* tab (Figure B1) summarizes the key results for distributor analysis. First, it tells whether all constraints in Table II.3 are satisfied in the current configuration. Second, it gives the turndown throughput interval (i.e., the minimum and maximum flowrates for which all layers remain in the wetting regime). Third, it gives the total number of outlets and the volume fraction of the distributor zone that is occupied by the wires. Finally, the last tab in the spreadsheet is called *Feasibility*. It assembles the results from the feasibility analysis, telling the user which configurations are feasible and which are not.



---

## Appendix C. Python and C routines for numerical simulations of mixture flow

---

In Chapter III, diffusioosmosis and diffusiophoresis were investigated via numerical simulations. Section III.5 mentioned that it was necessary to do some programming during the numerical implementation of these case studies, as the available models in existing software could not cope with the specificities of these phenomena. The diffusioosmotic case study in Figure III.7 was implemented in Python with the help of the FiPy library (Guyer et al., 2009). The source code used for diffusioosmosis simulations is given below.

*Listing C1 – Python code used to simulate diffusioosmosis*

```

1 import matplotlib
2 matplotlib.use('Agg')
3 from pylab import *
4 import sys
5 import threading, os
6 from fipy import *
7 from fipy.tools import numerix
8 from fipy.tools import serial
9 from scipy import misc
10 import osmotic_pressure_functions as opf
11 import numpy as np
12 import time
13
14 start_time = time.time()
15
16 plt.close("all")
17 #S: plt is an acronym for pyplot, defined in pylab
18
19 fp=open("addresses.txt", "r")
20 lines=fp.readlines()
21 address=lines[1].strip()
22 fp.close()
23 try:
24     os.mkdir(address)
25 except OSError:
26     pass
27 #Creates a folder with address input in addresses.txt
28 #Does nothing if folder already exists
29
30 #DATA
31 viscosity = 5.5555555555555555e-06
32 T=303. #Temperature (K)
33 kB=1.381e-23 #Boltzmann constant (m2.kg.s-2.K-1)
34 AH=1.e-20 #Hamaker constant (J)
35 NA=6.022e23 #Avogadro number
36 ele_charge=1.602e-19 #charge of one electron (C)
37 eps0=8.854e-12 #vacuum permittivity
38
39 fp2=open("parameters.txt", "r")

```

## Appendix C. Python and C routines for numerical simulations of mixture flow

```
40
41 lines2=fp2.readlines()
42 kic=float(lines2[2].strip())
43 lic=float(lines2[4].strip())
44 attrac=float(lines2[6].strip())
45
46 pfi = float(lines2[10].strip()) * 100.
47 lfi=float(lines2[12].strip())
48
49 phi_c=float(lines2[16].strip())
50
51 Pe=float(lines2[20].strip())
52
53 a=float(lines2[24].strip()) #particle radius
54 zn=float(lines2[26].strip()) #nb of neighbours
55 c0=float(lines2[28].strip()) #bulk ion concentration
56 epsilon=float(lines2[30].strip()) #geometric factor
57 phi_cp=float(lines2[32].strip()) #phi for closed packing
58 zeta=float(lines2[34].strip()) #zeta potential
59 Zion=float(lines2[36].strip()) #ion valence
60 epsr=float(lines2[38].strip()) #water permittivity
61
62 entr_model=int(lines2[42].strip()) #model for entropic pressure
63 vdw_model=int(lines2[46].strip()) #model for van der waals pressure
64 electr_model=int(lines2[50].strip()) #model for electrostatic pressure
65
66 dt=float(lines2[53].strip()) #time step
67 steps=int(lines2[56].strip()) #no of steps
68 storage=int(lines2[59].strip()) #no of steps for storage
69
70 fp2.close()
71
72
73
74 entr_cte=3.*kB*T / (4.*numerix.pi*a**3)
75 vdw_cte=-1.*zn*AH / (48.*numerix.pi*a**3)
76 electr_cte=epsilon*NA*kB*T*c0 / zn
77
78
79 #tolerance for momentum and mass balance
80 tol=1.e-6
81 x_tol = tol
82 y_tol = tol
83 resphi_tol = tol
84 pres_tol=tol
85 continuity_tol=tol
86
87 Ly=1.
88 Ny=100
89 Nx=200
90 Lx=2.
91 dL=Ly/Ny
92
93 mesh = Grid2D(nx=Nx, ny=Ny, dx=dL, dy=dL)
94 mesh_for_plot = Grid2D(nx=Nx, ny=Ny, dx=dL, dy=dL, communicator=serial)
95
96 X, Y = mesh.faceCenters
97 x, y = mesh.cellCenters
98
99 #0.8 for pressure and 0.5 for velocity are typical relaxation values for SIMPLE
100 pressureRelaxation = 0.8
101 velocityRelaxation = 0.5
102 #Relaxation is used to solve sparse linear systems
103 #(coming from discretization of pdes)
104
105 rad=0.1
```

## Appendix C. Python and C routines for numerical simulations of mixture flow

```
106 #radius
107
108 #level set function to define the distance to the wall
109 var1 = DistanceVariable(name='distance to center', mesh=mesh, \
110                         value=numerix.sqrt((x-Nx*dL/2.)**2+(y-Ny*dL/2.)**2))
111
112 phi_init=0.
113
114 pressure = CellVariable(mesh=mesh, value = 0., hasOld=True, name='press')
115 pressure_for_plot = CellVariable(mesh=mesh_for_plot, name='pressure')
116
117 pressureCorrection = CellVariable(mesh=mesh, value = 0., hasOld=True)
118
119 xVelocity = CellVariable(mesh=mesh, hasOld=True, name='X vel')
120 xVelocity_for_plot = CellVariable(mesh=mesh_for_plot, name='X velocity')
121
122 yVelocity = CellVariable(mesh=mesh, hasOld=True, name='Y vel')
123 yVelocity_for_plot = CellVariable(mesh=mesh_for_plot, name='Y velocity')
124
125 velocity = FaceVariable(mesh=mesh, rank=1)
126 velocityold = FaceVariable(mesh=mesh, rank=1)
127
128 #Volume fraction of colloids
129 phi = CellVariable(mesh=mesh, hasOld=True, value=phi_init, name='Volume frac')
130 phi_for_plot = CellVariable(mesh = mesh_for_plot, value = phi_init, \
131                             name = 'Volume fraction')
132
133 #BOUNDARY CONDITIONS (no-flux by default)
134 xVelocity.constrain(Pe, mesh.facesLeft | mesh.facesRight)
135 xVelocity_for_plot.constrain(Pe, mesh_for_plot.facesLeft | \
136                              mesh_for_plot.facesRight)
137
138 yVelocity.constrain(0., mesh.facesRight | mesh.facesLeft)
139 yVelocity.constrain(0., mesh.facesTop | mesh.facesBottom)
140 yVelocity_for_plot.constrain(0., mesh_for_plot.facesRight | \
141                              mesh_for_plot.facesLeft)
142 yVelocity_for_plot.constrain(0., mesh_for_plot.facesTop | \
143                              mesh_for_plot.facesBottom)
144
145 pressureCorrection.constrain(0., mesh.facesBottom & (X < dL))
146
147 #mass (no-flux by default)
148 phi.constrain(phi_c, mesh.facesLeft)
149 phi.constrain(0., mesh.facesRight)
150
151 phi_for_plot.constrain(phi_c, mesh_for_plot.facesLeft)
152 phi_for_plot.constrain(0., mesh_for_plot.facesRight)
153
154 #Building the colloid-interface energy map
155 pi_ci = CellVariable(mesh = mesh, value = 0., name = 'Colloid-interface e map')
156 pi_ci.setValue(-attrac * kic * exp(-1. * (var1 - rad)/(2 * lic)) + \
157               (1. + attrac) * kic * exp(-1. * (var1 - rad)/(1. * lic)), \
158               where = (var1 > rad))
159 pi_ci.setValue(kic, where = (var1 <= rad))
160 pi_ci_for_plot = CellVariable(mesh = mesh_for_plot, value = pi_ci.globalValue, \
161                               name='Colloid-interface energy map')
162
163 #Building the fluid-interface energy map
164 pi_fi = CellVariable(mesh=mesh, value=0., name='Fluid-interface e map')
165 pi_fi.setValue(pfi, where=(var1 <= rad))
166 pi_fi_for_plot = CellVariable(mesh=mesh_for_plot, value = pi_fi.globalValue, \
167                               name='Fluid-interface energy map')
168
169 viewer_pi_ci = Viewer(vars=pi_ci_for_plot)
170 viewer_pi_ci.plot(filename = address + '/energy_map.png')
171 viewer_pi_fi = Viewer(vars=pi_fi_for_plot)
```



## Appendix C. Python and C routines for numerical simulations of mixture flow

```

172
173 pre_drop=zeros(steps)
174 osm_drop=zeros(steps)
175 trans=zeros(steps)
176 phi_max=zeros(steps)
177 phi_mean=zeros(steps)
178 flux_in=zeros(steps)
179
180 xFaces=numerix.array([]) #vertical faces
181 yFaces=numerix.array([]) #horizontal faces
182
183 Nx_in_proc = mesh.nx
184 Ny_in_proc = mesh.ny
185
186 for yfcount in range(Nx_in_proc*(1+Ny_in_proc)) :
187     xFaces=numerix.append(xFaces,[False])
188     yFaces=numerix.append(yFaces,[True])
189
190 for xfcount in range(Ny_in_proc*(1+Nx_in_proc)) :
191     xFaces=numerix.append(xFaces,[True])
192     yFaces=numerix.append(yFaces,[False])
193
194 #EQUATIONS
195 xVelocityEq = DiffusionTerm(coeff=viscosity) - pressure.grad.dot([1.,0.]) - \
196     ImplicitSourceTerm(pi_fi) - (phi)*(pi_ci.grad.dot([1.,0.]))
197 yVelocityEq = DiffusionTerm(coeff=viscosity) - pressure.grad.dot([0.,1.]) - \
198     ImplicitSourceTerm(pi_fi) - (phi)*(pi_ci.grad.dot([0.,1.]))
199
200 def pi_cc_entr(x):
201     return {
202         1: opf.vantHoff(x),
203         2: opf.carnahan_starling(x),
204         3: opf.hall_fluid(x),
205         4: opf.hall_solid(x,phi_cp)
206     }[entr_model]
207
208 def pi_cc_vdw(x):
209     return {
210         1: 0.,
211         2: opf.van_der_waals(x,phi_cp,vdw_cte/entr_cte)
212     }[vdw_model]
213
214 #Debye-Huckel parameter
215 kappa = numerix.sqrt((2.*c0*NA*ele_charge**2) / (epsr*eps0*kB*T))
216 zeta_star=zeta*ele_charge*Zion / (kB*T)
217 def pi_cc_electr(x):
218     return {
219         1: 0.,
220         2: opf.electrost(x,electr_cte/entr_cte,kappa*a,zeta_star)
221     }[electr_model]
222
223 def pi_cc(x):
224     return pi_cc_entr(x) + pi_cc_vdw(x) + pi_cc_electr(x)
225
226 diffusioncoeff = misc.derivative(pi_cc,phi.arithmeticFaceValue,dx=1.e-6)
227 diffusioncoeff2 = FaceVariable(mesh=mesh, value=0., name='Diffusion coefficient')
228 hydro_coeff = (6. - 9. * phi.arithmeticFaceValue**(1./3.) + 9. * \
229     phi.arithmeticFaceValue**(5./3.) - 6. * \
230     phi.arithmeticFaceValue**2.) / \
231     (6. + 4. * phi.arithmeticFaceValue**(5./3.))
232
233 eq0 = TransientTerm() + ConvectionTerm(velocity - pi_ci.faceGrad) == \
234     DiffusionTerm(coeff=diffusioncoeff2)
235
236
237 apx = CellVariable(mesh=mesh, value=1.)

```

## Appendix C. Python and C routines for numerical simulations of mixture flow

```

238 apy = CellVariable(mesh=mesh, value=1.)
239 ap = FaceVariable(mesh=mesh, value=1.)
240
241 volume = CellVariable(mesh=mesh, value=mesh.cellVolumes, name='VoLume')
242 contrvolume = volume.arithmeticFaceValue
243 coeff = FaceVariable(mesh=mesh, value=1.)
244 pressureCorrectionEq = DiffusionTerm(coeff=coeff) - velocity.divergence
245
246 #VIEWERS
247 step=0
248 t=0.
249 plt.ion()
250 viewer_pre = Viewer(vars=(pressure_for_plot), colorbar= True)
251 wf, hf = plt.figaspect(1.)
252 fig = plt.figure(figsize=(2*wf, 2*hf))
253 viewer_v = MultiViewer(viewers = \
254     (Viewer(vars = xVelocity_for_plot, colorbar = True , \
255         axes= fig.add_subplot(121)), \
256     Viewer(vars = yVelocity_for_plot, colorbar = True , \
257         axes = fig.add_subplot(122))))
258 viewer_vv = MatplotlibStreamViewer(vars=velocity)
259 viewer_phi = MatplotlibViewer(vars=(phi_for_plot), datamin=0.)
260 xlabel('$z$')
261
262 from mpi4py import MPI
263 comm = MPI.COMM_WORLD
264 rank = comm.Get_rank()
265
266 for step in range(steps):
267     sweep = 0.
268     xres = 1000.
269     yres = 1000.
270     pres = 1000.
271     cont = 1000.
272     pressure.updateOld()
273     pressureCorrection.updateOld()
274     xVelocity.updateOld()
275     yVelocity.updateOld()
276     while (xres > x_tol or yres > y_tol or pres > pres_tol or cont > \
277         continuity_tol) :
278         sweep=sweep+1
279
280         ## solve the Stokes equations to get starred values
281         xVelocityEq.cacheMatrix()
282         xres=xVelocityEq.sweep(var=xVelocity,underRelaxation=velocityRelaxation)
283         xmat = xVelocityEq.matrix
284         yVelocityEq.cacheMatrix()
285         yres = yVelocityEq.sweep(var=yVelocity,underRelaxation=velocityRelaxation)
286         ymat = yVelocityEq.matrix
287
288         apx[:] = -xmat.takeDiagonal()
289         apy[:] = -ymat.takeDiagonal()
290         ap.setValue(apx.arithmeticFaceValue,where=xFaces)
291         ap.setValue(apy.arithmeticFaceValue,where=yFaces)
292
293
294         velocity[0] = (xVelocity.arithmeticFaceValue + \
295             (volume / apx * pressure.grad[0]).arithmeticFaceValue - \
296             contrvolume * (1. / apx).arithmeticFaceValue * \
297             pressure.faceGrad[0] + (1. - velocityRelaxation) * \
298             (velocityold[0] - xVelocity.old.arithmeticFaceValue))
299
300         velocity[1] = (yVelocity.arithmeticFaceValue + \
301             (volume / apy * pressure.grad[1]).arithmeticFaceValue - \
302             contrvolume * (1. / apy).arithmeticFaceValue * \
303             pressure.faceGrad[1] + (1. - velocityRelaxation) * \

```

## Appendix C. Python and C routines for numerical simulations of mixture flow

```

304         (velocityold[1] - yVelocity.old.arithmeticFaceValue)
305
306
307     velocity[1, mesh.facesRight.value] = 0.
308     velocity[1, mesh.facesLeft.value] = 0.
309     velocity[1, mesh.facesBottom.value] = 0.
310     velocity[1, mesh.facesTop.value] = 0.
311     velocity[0, mesh.facesRight.value] = Pe
312     velocity[0, mesh.facesLeft.value] = Pe
313
314     ## solve the pressure correction equation
315     coeff.setValue(contrvolume * (1. / apx).arithmeticFaceValue, where=xFaces)
316     coeff.setValue(contrvolume * (1. / apy).arithmeticFaceValue, where=yFaces)
317     pressureCorrectionEq.cacheRHSvector()
318     pres = pressureCorrectionEq.sweep(var=pressureCorrection)
319     rhs = pressureCorrectionEq.RHSvector
320
321     pressure.setValue(pressure + pressureRelaxation * pressureCorrection )
322     pressure_for_plot.setValue(pressure.globalValue)
323
324     xVelocity.setValue(xVelocity - pressureCorrection.grad[0] / apx * volume)
325     yVelocity.setValue(yVelocity - pressureCorrection.grad[1] / apy * volume)
326
327     velocity[0] = velocity[0] - pressureCorrection.faceGrad[0] * \
328         contrvolume * (1. / apx).arithmeticFaceValue
329     velocity[1] = velocity[1] - pressureCorrection.faceGrad[1] * \
330         contrvolume * (1. / apy).arithmeticFaceValue
331
332     velocity[1, mesh.facesRight.value] = 0.
333     velocity[1, mesh.facesLeft.value] = 0.
334     velocity[1, mesh.facesBottom.value] = 0.
335     velocity[1, mesh.facesTop.value] = 0.
336     velocity[0, mesh.facesRight.value] = Pe
337     velocity[0, mesh.facesLeft.value] = Pe
338
339     velocityold[0] = velocity[0]
340     velocityold[1] = velocity[1]
341
342     xVelocity.updateOld()
343     yVelocity.updateOld()
344     cont=max(abs(velocity.divergence.globalValue))
345
346     if sweep % 10 == 0 :
347         print ('step:', step, 'sweep:', sweep, ', x residual:', xres, \
348             ', y residual:', yres, ', p residual:', pres, \
349             ', continuity:', cont)
350
351
352
353     phi.updateOld()
354     res0 = 1e100
355     t=step*dt
356
357     while res0 > resphi_tol :
358         phi.setValue(0., where=phi<0.)
359         diffusioncoeff2.setValue(diffusioncoeff.value * hydro_coeff.value)
360         diffusioncoeff2.setValue((pi_cc(phi.arithmeticFaceValue.value+1.e-8) - \
361             pi_cc(phi.arithmeticFaceValue.value)) / \
362             1.e-8 * hydro_coeff.value, \
363             where=np.isnan(diffusioncoeff.value))
364         res0 = eq0.sweep(var=phi, dt=dt)
365
366     if (step % 1 == 0) :
367         phi_mat=reshape(phi.globalValue, (Ny,Nx))
368         phi_mat=numerix.flipud(phi_mat)
369         pre_mat=reshape(pressure.globalValue, (Ny,Nx))

```

## Appendix C. Python and C routines for numerical simulations of mixture flow

```

370     pre_mat=numerix.flipud(pre_mat)
371     xv_mat=reshape(xVelocity.globalValue, (Ny,Nx))
372     xv_mat=numerix.flipud(xv_mat)
373
374     mean_gradp=mean(pressure_for_plot.grad.dot([0.,1.]).value)*(Lx*Ly)
375     mean_dpic = mean((phi.globalValue) * \
376                     (pi_ci_for_plot.grad.dot([0.,1.])).value) * (Lx*Ly)
377     phi_for_plot.setValue(phi.globalValue)
378     phigrad_mat=reshape(phi_for_plot.grad[1].value, (Ny,Nx))
379     massfluxin=xv_mat[:,0]*phi_mat[:,0]-phigrad_mat[:,0]
380     upin=massfluxin/phi_mat[:,0]
381     ufin=(xv_mat[:,0]-massfluxin)/(1-phi_mat[:,0])
382     massfluxout=xv_mat[:,Nx-1]*phi_mat[:,Nx-1]-phigrad_mat[:,Nx-1]
383     put(pre_drop,step,mean(pre_mat[:,Nx-1])-mean(pre_mat[:,0]))
384     put(osm_drop,step,mean((phi)*(pi_ci.grad.dot([0.,1.])).value)*(Lx*Ly))
385     put(trans,step,mean(phi_mat[:,Nx-1])/mean(phi_mat[:,0]))
386     put(phi_max,step,amax(phi.globalValue))
387     put(phi_mean,step, mean(phi.globalValue))
388
389     print ('step:', step, ', phi-moy:',mean(phi.globalValue), ', pre_drop:', \
390           mean(pre_mat[:,Nx-1]) - mean(pre_mat[:,0]), 'um_in=', \
391           mean(xv_mat[:,0]), 'um_out=',mean(xv_mat[:,Nx-1]), ', meangardP:', \
392           mean_gradp, 'mean dpic',mean_dpic, 'perm', - \
393           mean(xv_mat[:,Nx-1]) / (mean_gradp+mean_dpic), 'continuity:', \
394           max(abs(velocity.divergence.globalValue)))
395
396     xVelocity_for_plot.setValue(xVelocity.globalValue)
397     yVelocity_for_plot.setValue(yVelocity.globalValue)
398
399     if (step % storage == 0) :
400         viewer_phi.plot(filename = address+'/phi2D'+str('%04d' %step)+'.png')
401         viewer_pre.plot(filename = address+'/pre2D'+str('%04d' %step)+'.png')
402         viewer_vv.plot(filename = address + '/vv2D' + str('%04d' %step) + \
403                        '_proc'+str('%d' %rank)+'.png')
404         viewer_v.plot()
405         timer = fig.text(0.1, 0.9, 't={0:1.2f}'.format(t), fontsize=16, \
406                        bbox={'facecolor':'white', 'alpha':1., 'pad':5.})
407         fig.savefig(address+'/v2D'+str('%04d' %step)+'.png', bbox_inches='tight')
408
409     run_time = time.time() - start_time
410
411     from xlwt import Workbook
412     book = Workbook()
413     feuil1 = book.add_sheet('feuille 1')
414     feuil1.write(0,0,'Pe')
415     feuil1.write(0,1,Pe)
416     feuil1.write(0,2,'Viscosity')
417     feuil1.write(0,3,viscosity)
418     feuil1.write(1,0,'Energy map int-col')
419     feuil1.write(1,2,'int-fluid')
420     feuil1.write(2,0,'time')
421     feuil1.write(2,1,run_time)
422     feuil1.write(3,0,'kic')
423     feuil1.write(3,1,kic)
424     feuil1.write(4,0,'Lic')
425     feuil1.write(4,1,lic)
426     feuil1.write(3,2,'kfi')
427     feuil1.write(3,3,pfi)
428     feuil1.write(4,2,'Lfi')
429     feuil1.write(4,3,lfi)
430     ligne9 = feuil1.row(9)
431     ligne9.write(0,'t')
432     ligne9.write(1,'pre_drop')
433     ligne9.write(2,'osm_drop')
434     ligne9.write(3,'Tr')
435     ligne9.write(4,'phi_max')

```

## Appendix C. Python and C routines for numerical simulations of mixture flow

```
436 ligne9.write(5, 'phi_mean')
437 start=10
438 for step in range(steps) :
439     feuil1.write(step+start,0,step*dt)
440     feuil1.write(step+start,1,pre_drop[step])
441     feuil1.write(step+start,2,osm_drop[step])
442     feuil1.write(step+start,3,trans[step])
443     feuil1.write(step+start,4,phi_max[step])
444     feuil1.write(step+start,5,phi_mean[step])
445 book.save(address+'/result.xls')
446 np.save(address+'/xv_mat', xv_mat)
447 np.save(address+'/phi_mat', phi_mat)
448 np.save(address+'/pre_mat', pre_mat)
449 yv_mat=reshape(yVelocity.globalValue, (Ny,Nx))
450 yv_mat=numerix.flipud(yv_mat)
451 np.save(address+'/yv_mat', yv_mat)
```

The above code is inspired by an example provided in the FiPy manual (Guyer et al., 2012) that solves the Stokes flow in a cavity. The key variables used in the above code are: *xVelocity* (the *x*-component of the velocity), *yVelocity* (the *y*-component of the velocity), *phi* (the volume fraction of colloids), and *pressure* (the pressure of the mixture). The boundary conditions for velocity and colloid concentration are found in lines 134, 138-139 and 148-149. The momentum balance equation (III.30) is declared in lines 195-198 (one equation for the momentum balance along the *x*-direction, and another for the momentum balance along the *y*-direction). The implicit source term in these equations corresponds to the penalization term discussed in Section III.5, which prevents the fluid from entering the cylinder and slipping on its surface.

The next equation declared in the code is the colloid transport equation (III.31), which can be found in lines 233-234. Note that the equation in the script accounts for a transient term, which is not present in eq. (III.31). Indeed, the routine depicted in Listing C1 captures the evolution of the diffusioosmotic system as it approaches steady state. However, only steady state results are discussed in Chapter III, which is why the model shown in Section III.3 does not include the transient term. Finally, the pressure correction equation (III.17) from the SIMPLE procedure is declared in line 244.

Listing C1 implements the SIMPLE algorithm in Figure III.1 as follows. The pressure variable is initialized to 0 in line 114. Inside a *while* loop, the starred velocity profile is computed by solving the momentum balance equations (lines 281-286). Afterwards (lines 288-304), an adaptation of the Rhie-Chow interpolation is used to compute the velocity on the mesh faces (Pascau, 2011). Lines 315-319 are dedicated to solving the pressure correction equation. With the pressure correction term, the pressure field can be updated

## Appendix C. Python and C routines for numerical simulations of mixture flow

(line 321). Further, the velocity fields are updated in lines 324-330 according to eq. (III.18).

Once this sweep is over, the program checks for convergence. If velocity and pressure profiles have not converged, the program does another iteration. Otherwise, it proceeds to solving the colloid transport equation (lines 357-364) and then stores some key results before going to the next time step. Once the calculations are over, final velocity, pressure and colloid concentration profiles are stored in a .npy file, whereas other results such as pressure drop and average colloid concentration are stored in an Excel spreadsheet.

The key aspects of the python routine have been described above. A more detailed description of the listing would be tedious and unfitting in the scope of this thesis, which aims to discuss the results rather than the technicalities of numerical implementations. However, three other interesting points regarding the routine in Listing C1 are worth mentioning. First, all the variables in the code are in their dimensionless form, following the convention adopted by Bacchin et al. (2019). Second, the equations of state (EoS) for colloid-colloid interactions are declared in a separate file called *osmotic\_pressure\_functions.py*, which is imported in line 10. The user can choose which EoS to use in the file *parameters.txt*. In this file the user should also input other problem parameters, such as  $a_{tt}$ ,  $k_{ic}$  and  $l_{ic}$  for the colloid-interface interaction potential in eq. (III.25). All these inputs are read in lines 39-70.

The third and last extra point worth mentioning about Listing C1 is that it models colloid mobility (see eq. (III.7)) via the Happel function (Bacchin et al., 2002). The mobility corresponds to the *hydro\_coeff* variable, whose expression is assigned in lines 228-231. However, all the diffusioosmosis simulations in Chapter III assumed constant mobility (*hydro\_coeff=1*), as mentioned in Section III.1.1a. This happened because the Happel feature was implemented later in the thesis. Future studies will assess the impact of concentration-dependent mobility on the diffusioosmotic flow of suspensions.

Differently from the diffusioosmosis case study discussed above, diffusiophoresis did not require programming from scratch. Instead, ANSYS Fluent software was used for numerical simulations. The software provides several algorithms to solve the Navier-Stokes equations along with solute transport equation. However, it can only account for the extra convective term  $-D\phi\nabla\Pi_{ic}$  in the solute transport equations via user-defined functions (UDF). UDFs are subroutines written in C that can be loaded with Fluent in

## Appendix C. Python and C routines for numerical simulations of mixture flow

order to enhance its features (Ansys Inc, 2013). For this extra convective term, three UDFs are required: one to allocate memory for  $\Pi_{ic}$ , one that assigns the values for  $\Pi_{ic}$  and another that calculates the scalar product of the overall advection field  $\underline{\psi} = -D\nabla\Pi_{ic} + \underline{u}$  with the face normal vectors. These UDFs are given in Listing C2 and Listing C3 for the TFCV formulation in Section III.4.2.

Listing C2 – Allocating memory and assigning  $\Pi_{ic}$  values

```
1 /*****
2 set_pi_ic.c contains two UDFs: an execute on loading UDF that reserves
3 one UDM for libudf and renames the UDM to enhance postprocessing,
4 and an on-demand UDF that sets the initial value of the UDM.
5 *****/
6 #include "udf.h"
7 #define NUM_UDM 1
8 #define x_center 0.
9 #define y_center 0.
10 #define kic 100.
11 #define lic 1.e-7
12 #define att 0.
13 #define rad 2.e-7
14 #define diff_coeff 2.18e-10
15 /* diff_coeff in kg/m-s */
16 /* diff_coeff = D x rho */
17 static int udm_offset = UDM_UNRESERVED; /*makes sure udm_offset from loading
18                                           is the same as udm_offset from
19                                           demand*/
20 DEFINE_EXECUTE_ON_LOADING(allocate_udm_memory, libname)
21 {
22     if (udm_offset == UDM_UNRESERVED)
23         udm_offset = Reserve_User_Memory_Vars(NUM_UDM);
24     if (udm_offset == UDM_UNRESERVED)
25         Message("Undefined UDM");
26     else
27     {
28         Set_User_Memory_Name(udm_offset, "pi_ci_udm");
29     }
30     Message("\nUDM Offset for Current Loaded Library = %d", udm_offset);
31 }
32 DEFINE_ON_DEMAND(set_udm)
33 {
34     Domain* d;
35     Thread* ct;
36     cell_t c;
37     int i;
38     real distance_cell_center;
39     real xc[ND_ND];
40     d = Get_Domain(1); /*Fluid domain; there's only one domain for the
41                       simulation*/
42     if (udm_offset != UDM_UNRESERVED)
43     {
44         Message("Setting UDM\n");
45         for (i = 0; i < NUM_UDM; i++)
46         {
47             thread_loop_c(ct, d)
48             {
49                 begin_c_loop(c, ct)
50                 {
```

## Appendix C. Python and C routines for numerical simulations of mixture flow

```

51         C_CENTROID(xc, c, ct);
52         distance_cell_center = sqrt(ND_SUM(pow(xc[0] -
53             x_center, 2.), pow(xc[1] - y_center, 2.), 0.));
54         C_UDMI(c, ct, udm_offset + i) = (1. + att) * kic *
55             exp(-1. * (distance_cell_center - rad) / lic) -
56             att * kic * exp(-1. * (distance_cell_center - rad)
57                 / (2. * lic));
58         C_UDMI(c, ct, udm_offset + i) =
59             C_UDMI(c, ct, udm_offset + i) * diff_coeff;
60     }
61     end_c_loop(c, ct)
62 }
63 }
64 }
65 else
66     Message("UDMs have not yet been reserved for current library\n");
67 }

```

Listing C3 – Setting solute advection field

```

1  /*****
2  /* UDF that implements a modified advective term in the */
3  /* scalar transport equation */
4  /*****
5  #include "udf.h"
6  #include "sg.h" /*to use INTERIOR_FACE_GEOMETRY*/
7  DEFINE_UDS_FLUX(set_convective_flow,f,t,i)
8  {
9      real A[ND_ND], es[ND_ND], dr0[ND_ND], dr1[ND_ND], A_by_es, ds;
10     cell_t c0, c1 = -1;
11     Thread *t0, *t1 = NULL;
12     real NV_VEC(psi_vec);
13     real flux = 0.0;
14     c0 = F_C0(f,t);
15     t0 = F_C0_THREAD(f,t);
16     F_AREA(A, f, t);
17     real vx;
18     /* If face lies at domain boundary, use face values; */
19     /* If face lies IN the domain, use average of adjacent cells. */
20     if (BOUNDARY_FACE_THREAD_P(t)) /*Most face values will be available*/
21     {
22         real dens;
23         /* Depending on its BC, density may not be set on face thread*/
24         if (NNULLP(THREAD_STORAGE(t, SV_DENSITY)))
25             dens = F_R(f, t); /* Set dens to face value if available */
26         else
27             dens = C_R(c0, t0); /* else, set dens to cell value */
28         NV_DS(psi_vec, =, F_U(f, t), F_V(f, t), F_W(f, t), *, dens);
29         flux = NV_DOT(psi_vec, A); /* flux only comes from velocity */
30         /*flux =0.*/
31     }
32     else
33     {
34
35         c1 = F_C1(f,t); /* Get cell on other side of face */
36         t1 = F_C1_THREAD(f,t);
37         NV_DS(psi_vec, =, C_U(c0,t0), C_V(c0,t0), C_W(c0,t0), *, C_R(c0, t0));
38         vx = C_U(c1, t1) - v0;
39         NV_DS(psi_vec, +=, vx, C_V(c1, t1), C_W(c1, t1), *, C_R(c1, t1));

```



## Appendix C. Python and C routines for numerical simulations of mixture flow

```
40     flux = NV_DOT(psi_vec, A) / 2.0;
41     INTERIOR_FACE_GEOMETRY(f, t, A, ds, es, A_by_es, dr0, dr1);
42     flux = flux - A_by_es * (C_UDMI(c1, t1, 0) - C_UDMI(c0, t0, 0)) / ds;
43     /* Flux from both velocity and Pi_ic */
44 }
45 return flux;
46 }
```

In Listing C2, *DEFINE\_EXECUTE\_ON\_LOADING* is the UDF that allocates memory for the solute-interface interaction potential, and *DEFINE\_ON\_DEMAND* is the UDF that assigns its value. Variable *C\_UDMI* in the second UDF corresponds to  $\Pi_{ic}$ , and its value is set in lines 54-59 according to eq. (III.25). Note that the loops in the second UDF of Listing C2 guarantee that a value is assigned to all cells in all the cell zones of the domain.

In Listing C3, the advection field is calculated differently depending on whether the face is part of the boundaries (lines 20-31) or not (lines 32-44). The main reason for this distinction is that face values of  $\underline{\nabla}\Pi_{ic} \cdot \underline{A}$  (where  $\underline{A}$  is the face area vector) are obtained via differencing between adjacent cells, which is not possible when the face is at a boundary. For boundary faces, it is simply assumed that  $\underline{\nabla}\Pi_{ic} = 0$ . Note that this approximation is correct for the external boundaries of the domain, which are very far from the interface. However,  $\underline{\nabla}\Pi_{ic} = 0$  does not hold on the surface of the sphere. Still, this is not a real issue since the overall solute flux is set to 0 as a boundary condition for the interface.

Apart of the above mentioned UDFs, two other macros are necessary to implement the TEF model discussed in Section III.4.1. The first, named *DEFINE\_ADJUST*, updates  $\Pi_{ic}$  at the beginning of every time step, since the structure of the cells change as the mesh deforms. Further, *DEFINE\_CG\_MOTION* is used to update the velocity of the sphere, according to the following expression:  $v^{new} = v^{old} + F \times \Delta t$ . In this expression,  $v^{new}$  is the updated velocity,  $v^{old}$  is the previous one,  $F$  is the resultant force along the axial direction, and  $\Delta t$  is the interval between two time steps.

The two extra UDFs used for TEF simulations are omitted from this appendix for conciseness. The reader can refer to the UDF manual (Ansys Inc, 2013) for more details regarding these UDFs and the ones used in Listing C2 and Listing C3.